

# Thin-shell concrete floors for sustainable buildings



**William John Hawkins**

Department of Engineering  
University of Cambridge

This dissertation is submitted for the degree of  
*Doctor of Philosophy*



## **Declaration**

The work described in this dissertation was carried out at the University of Bath and the University of Cambridge between September 2015 and June 2019.

The author declares that, except where specific reference is made to the work of others, the contents of this dissertation are original and have not been submitted in whole or in part for consideration for any other degree or qualification at the University of Cambridge, or any other University or similar institution. This dissertation is my own work and contains nothing which is the outcome of collaboration with others, except as specified in the text and acknowledgements.

The length of this dissertation is 276 pages. It contains 140 figures and approximately 63,000 words.

William John Hawkins  
July 2019



## **Acknowledgements**

I am extremely thankful to my supervisors Dr. John Orr, Dr. Paul Shepherd and Professor Tim Ibell, from whom I have learnt much over the last few years. Their time, guidance, inspiration and encouragement have made this project possible.

My gratitude also goes out to Dr. Julie Bregulla, Ed Moseley, Professor Janet Lees, Dr. Juliana Holley, Dr. Chris Williams and Dr. Antony Darby for their valuable thoughts and insight at various stages throughout this research. In addition, I am particularly grateful to Rostislav Chudoba, Tine Tysmans, Sebastian May, Andrew Liew and Caitlin Mueller for welcoming me during my travels and introducing me to the exceptional work of their respective research groups.

Experimental investigations have formed an essential component of this research, and would not have been possible without the advice, assistance and technical expertise of Ian Benford, Will Bazeley, Miles Chambers, Robert Dyer, Lorna Roberts and Martin Touhey. Additional thanks are due to Dr. Daniel Wells of EAB Associates for his invaluable help and guidance regarding foamed concrete.

I am grateful for the support of the EPSRC Centre for Decarbonisation of the Built Environment (dCarb) at the University of Bath, the Building Research Establishment Trust (BRE) Trust and the Cambridge University Department of Engineering for funding this project.

I have been lucky to share workplaces with many inspiring, helpful and supportive colleagues (and others who I like regardless) in both Bath and Cambridge. I hope our paths will cross again. Finally, to my family, house-mates, band-mates, old friends and new, for everything else beyond concrete, thank you.



## Abstract

Rapid urbanisation and population growth is driving unprecedented levels of building construction. Over the next 40 years, approximately 230 billion square meters of new floor area will be constructed globally, a doubling of existing building stock. Already, the production of concrete and steel accounts for a third of worldwide industrial CO<sub>2</sub> emissions, representing a major opportunity, and responsibility, for structural engineers to contribute towards a low-carbon future through efficient design. A significant majority of the structural material in a typical building exists within the floors, making these a prime target for material reductions.

This dissertation shows that thin-shell concrete floors are a viable alternative to typical slabs and beams in multi-storey buildings. Switching the dominant structural behaviour from bending to membrane action increases efficiency, enabling significant embodied carbon reductions.

A system is proposed featuring pre-cast textile reinforced concrete shells of uniform thickness and shallow depth, supported at columns, with a network of prestressed steel tension ties. A lightweight foamed concrete fill is cast above the shells to provide a level top surface and transfer floor loads to the shell. The structural behaviour of this system is explored through a series of computational and experimental investigations, leading to refinement of the design, exploration of construction methods and the development of a complete design methodology incorporating novel theoretical work. The shells feature optimised singly-curved groin vault geometry. This provides efficient structural performance whilst simultaneously minimising construction complexity. Thus, a practical and scalable solution is proposed, which is shown to offer considerable embodied carbon savings over typical concrete and steel floor structures.

This work provides a robust platform for future refinement and large-scale implementation of thin-shell concrete floors for sustainable buildings.





# Table of contents

<b>1</b>	<b>Introduction</b>	<b>1</b>
1.1	Background . . . . .	1
1.2	The potential of thin-shells . . . . .	4
1.3	Aims and objectives . . . . .	5
1.4	Dissertation structure . . . . .	5
<b>2</b>	<b>Literature review</b>	<b>7</b>
2.1	Historical context . . . . .	7
2.1.1	Ancient and medieval master builders . . . . .	7
2.1.2	Fireproof floor construction . . . . .	9
2.1.3	20 <sup>th</sup> century concrete innovation . . . . .	11
2.2	Modern design, materials and manufacturing methods . . . . .	14
2.2.1	Form-finding and structural analysis . . . . .	14
2.2.2	Fabrication . . . . .	17
2.2.3	Materials and reinforcement . . . . .	20
2.3	Quantifying and minimising the environmental impact of buildings . . . . .	25
2.3.1	Embodied carbon of structures . . . . .	26
2.4	Low-carbon floors . . . . .	32
2.4.1	Embodied carbon of typical modern buildings . . . . .	32
2.4.2	Current research in efficient floor design . . . . .	34
2.5	Summary, findings and conclusions . . . . .	40
<b>3</b>	<b>Development and feasibility of a thin-shell flooring system</b>	<b>41</b>
3.1	Introduction . . . . .	41
3.2	Proposed structural system . . . . .	41
3.2.1	Shell and reinforcement . . . . .	41
3.2.2	Columns and ties . . . . .	42
3.2.3	Floor levelling . . . . .	43

3.2.4	Construction . . . . .	43
3.3	Basic behaviour . . . . .	44
3.3.1	Preliminary case study . . . . .	45
3.4	Computational analysis methodology . . . . .	47
3.4.1	Finite element modelling . . . . .	48
3.4.2	Mesh density investigation . . . . .	48
3.4.3	Loads . . . . .	49
3.4.4	Tie pre-strain . . . . .	50
3.4.5	Textile reinforced concrete strength calculation . . . . .	51
3.5	Shell geometry definitions . . . . .	53
3.5.1	Hyperbolic paraboloids . . . . .	53
3.5.2	Parabolic groin vault . . . . .	54
3.5.3	2D form-found groin vault . . . . .	54
3.5.4	Optimised (parametric) groin vault . . . . .	55
3.5.5	Form-finding in 3D . . . . .	58
3.5.6	Fabric-formwork . . . . .	59
3.6	Results . . . . .	60
3.6.1	Self-weight and pre-strain . . . . .	60
3.6.2	Deflection . . . . .	62
3.6.3	Free vibration . . . . .	62
3.6.4	Strain energy . . . . .	63
3.6.5	TRC strength utilisation . . . . .	64
3.6.6	Buckling . . . . .	66
3.7	Discussion . . . . .	67
3.7.1	Comparison of shell geometries . . . . .	67
3.7.2	TRC section design . . . . .	68
3.7.3	FE analysis methodology . . . . .	70
3.7.4	Variable shell thickness investigation . . . . .	71
3.8	Summary, findings and conclusions . . . . .	72
<b>4</b>	<b>Construction, modelling and design of suitable TRC materials</b>	<b>75</b>
4.1	Introduction . . . . .	75
4.2	Experimental investigation . . . . .	76
4.2.1	Materials . . . . .	76
4.2.2	Specimen construction . . . . .	83
4.2.3	Tensile tests . . . . .	83
4.2.4	Four-point bending tests . . . . .	89

---

4.2.5	Eccentric compression tests . . . . .	92
4.2.6	Experimental failure envelope . . . . .	98
4.3	Analytical failure envelope . . . . .	98
4.3.1	Proposed theoretical model . . . . .	99
4.3.2	Comparison with experimental envelope . . . . .	102
4.3.3	Comparison with bi-linear failure envelope . . . . .	105
4.3.4	Practical application for shells . . . . .	105
4.3.5	Limitations and potential extensions . . . . .	106
4.4	Non-linear finite element analysis . . . . .	107
4.4.1	Modelling methodology . . . . .	107
4.4.2	Mesh density . . . . .	109
4.4.3	Compressive behaviour . . . . .	109
4.4.4	Tensile behaviour . . . . .	110
4.4.5	Bending behaviour . . . . .	112
4.4.6	Four-point bending . . . . .	114
4.5	Summary, findings and conclusions . . . . .	115
<b>5</b>	<b>Experimental study of quarter-scale prototypes: Methodology and results</b>	<b>117</b>
5.1	Introduction . . . . .	117
5.2	Specimen design . . . . .	118
5.3	Materials . . . . .	120
5.3.1	Textile reinforcement . . . . .	120
5.3.2	Fine-grained concrete . . . . .	121
5.3.3	Foamed concrete . . . . .	124
5.4	Construction . . . . .	127
5.4.1	Formwork . . . . .	127
5.4.2	Tie rods and corner supports . . . . .	128
5.4.3	Casting the textile reinforced concrete shells . . . . .	129
5.5	Measurement of geometry . . . . .	132
5.5.1	Methodology . . . . .	133
5.5.2	Results . . . . .	135
5.5.3	Discussion . . . . .	137
5.6	Textile reinforced concrete specimen tests . . . . .	139
5.6.1	Tensile . . . . .	139
5.6.2	Four-point bending . . . . .	143
5.6.3	Compression . . . . .	145
5.7	Shell test methodology . . . . .	147

5.7.1	Loading . . . . .	148
5.7.2	Instrumentation . . . . .	149
5.7.3	Test sequence . . . . .	150
5.8	Shell test results . . . . .	152
5.8.1	Shell 1 . . . . .	152
5.8.2	Shell 2 . . . . .	155
5.8.3	Shell 3 . . . . .	160
5.8.4	Comparison between shells . . . . .	164
5.9	Supplementary tests . . . . .	167
5.9.1	Tie rod tests . . . . .	167
5.9.2	Load-spreader assembly tests . . . . .	169
5.10	Summary, findings and conclusions . . . . .	171
<b>6</b>	<b>Experimental study of quarter-scale prototypes: Analysis</b>	<b>173</b>
6.1	Introduction . . . . .	173
6.2	Modelling methodology . . . . .	174
6.2.1	Importing measured geometry . . . . .	175
6.2.2	Materials . . . . .	175
6.2.3	Behaviour and refinement of the model . . . . .	176
6.3	Sensitivity studies . . . . .	185
6.3.1	Concrete flexural strength . . . . .	185
6.3.2	Concrete stiffness and compressive strength . . . . .	187
6.3.3	Tie rod stiffness . . . . .	188
6.3.4	Foamed concrete fill . . . . .	189
6.3.5	Shell geometry and thickness . . . . .	192
6.4	Comparison with experimental results . . . . .	195
6.5	Strength utilisation analysis . . . . .	197
6.5.1	Methodology . . . . .	198
6.5.2	Results and discussion . . . . .	200
6.6	Summary, findings and conclusions . . . . .	204
<b>7</b>	<b>Design refinement and comparative case study</b>	<b>207</b>
7.1	Introduction . . . . .	207
7.2	Methodology . . . . .	207
7.2.1	Analysis and Design . . . . .	208
7.2.2	Loading and deflection criteria . . . . .	211
7.2.3	Materials and embodied carbon . . . . .	212

---

7.3	Minimising embodied carbon . . . . .	217
7.3.1	Optimising shell thickness and tie diameter . . . . .	217
7.3.2	Influence of column dimensions . . . . .	223
7.3.3	Span, depth and embodied carbon . . . . .	225
7.4	Further design considerations . . . . .	228
7.4.1	Minimum reinforcement . . . . .	228
7.4.2	Point loads . . . . .	229
7.4.3	Differential settlement . . . . .	230
7.4.4	Stability . . . . .	232
7.5	Comparative case-study . . . . .	237
7.5.1	Thin concrete shells . . . . .	238
7.5.2	Concrete flat slab . . . . .	239
7.5.3	Composite steel deck . . . . .	242
7.5.4	Performance comparison . . . . .	246
7.6	Summary, findings and conclusions . . . . .	248
<b>8</b>	<b>Conclusions and future work</b>	<b>251</b>
8.1	Proposed structural system . . . . .	251
8.2	Structural behaviour and design . . . . .	253
8.3	Construction . . . . .	254
8.4	Design methodology and theoretical models . . . . .	255
8.5	Thin-shell floors for sustainable buildings . . . . .	256
	<b>References</b>	<b>257</b>



# Chapter 1

## Introduction

### 1.1 Background

Environmental degradation and a warming climate have become the dominant global issues of the generation. Political, societal and business responses are intensifying as the realities of global warming unfold, and the remedial actions required have also become increasingly well defined in recent years.

The 2015 Paris Agreement aims to keep global average temperature less than 2°C above pre-industrial levels, and to pursue efforts for a 1.5°C limit (United Nations, 2015). A recent report by the Intergovernmental Panel on Climate Change (2018) maps potential pathways to meet this 1.5°C target, each of which involves reducing global CO<sub>2</sub> emissions to 45% of 2010 levels by 2030, and to zero by 2050. Compared to 1.5°C, a 2°C warming would expose twice as many people to water shortages and cause an additional 10cm of sea level rise, affecting a further 10 million people (Christensen, 2018). Beyond 2°C, there is a risk of initiating a potentially unstoppable feedback-induced warming scenario. According to Steffen et al. (2018), "widespread, rapid and fundamental transformations" must be made to the present-day socioeconomic system in order to prevent this so-called "Hothouse Earth" scenario.

Concrete is the world's second most consumed material, after water, and the production of Portland cement has nearly trebled over the last 20 years (U.S. Geological Survey, 2018). Today, cement alone is estimated to account for 8% of global CO<sub>2</sub> emissions (Lehne and Preston, 2018). The figure for steel is 9% (IEA, 2008), with around half of this attributed to the construction industry (Wang et al., 2007). Together, concrete and steel production contribute over one-third of all industrial carbon emissions (Allwood et al., 2011).

Buildings are major consumers of these materials, accounting for 83% of cement use in the UK (Shanks et al., 2019). Globally, rapid population growth and urbanisation is driving

ever faster rates of building construction, with a predicted 230 billion new square metres, doubling the total existing floor area over the next 40 years, the equivalent of re-building Paris every week (Abergel et al., 2017). As a result, annual consumption of construction materials will be considerably higher in 2050 than today; by a predicted 12-23% for cement (IEA, 2018) and 42-69% for steel (IEA, 2008; Worldsteel, 2018). This represents a considerable barrier to meeting emissions targets, which improvements in material production efficiency alone cannot overcome (Allwood et al., 2010; Shanks et al., 2019).

Continuing to make buildings using the same quantities of the same materials is incompatible with the transition to a low-carbon economy. To achieve sustainability, the carbon emissions per unit floor area must be significantly reduced, either by reusing existing buildings where possible, switching to alternative low-carbon materials or by finding ways to provide the same function with less, if possible, and structural engineers therefore have a vital role to play.

Most structural material in a typical building exists within its floors (De Wolf et al., 2016a; Foraboschi et al., 2014), making these a prime target for reducing embodied carbon. Typical floors in multi-storey buildings use a combination of steel and concrete to create planar structural elements which resist floor loads through bending and shear forces, examples of which are shown in Figure 1.1.

Flat slabs (Figure 1.1a) are a common floor construction typology favoured for their simple formwork, architectural flexibility and low structural depth. However, the stresses in these reinforced concrete (RC) structures are highly non-uniform. Figure 1.2 shows the results of an investigation featuring a 300mm thick simply supported single-spanning slab with a span of 10m, carrying a uniform load of  $10\text{kN/m}^2$ , a typical design load of a new office building. Stresses were calculated assuming pure bending behaviour. The concrete properties were those of a C40/50 mix, and the reinforcement ratio (0.77%) was chosen such that the strength is fully utilised at the mid-span according to BS EN 1992-1-1 (BSI, 2004a). Figure 1.2 therefore shows a slab theoretically at the point of failure.

The average stress in the concrete is 2.5MPa. This is just 9.4% of the design strength, or 5.2% of the mean (48MPa). Most (61%) of the concrete is cracked and therefore makes very little structural contribution, despite contributing the majority of self-weight. In practice, additional strength capacity is included above code requirements, or the design is instead serviceability governed (Orr, 2018), and therefore the stresses are lower still. This demonstrates the poor material efficiency of beam and slab structures. The introduction of steel beams (Figure 1.1b), voids (Figure 1.1c) or concrete ribs (Figure 1.1d) can increase the sectional efficiency of such structures, however bending remains the primary mode of structural operation in these cases, with high stress variation through the section depth.





Figure 1.1: Typical multi-storey floor structures including a) reinforced concrete flat slabs (photo by Darren Kirby/CC BY-SA 2.0), b) steel composite decking (photo by MTA Capital Construction Mega Projects/CC BY 2.0), c) pre-cast hollow core concrete units (photo by Michael Schmah/CC BY-SA 2.0) and d) waffle slabs (photo by Peka/CC BY-SA 4.0).

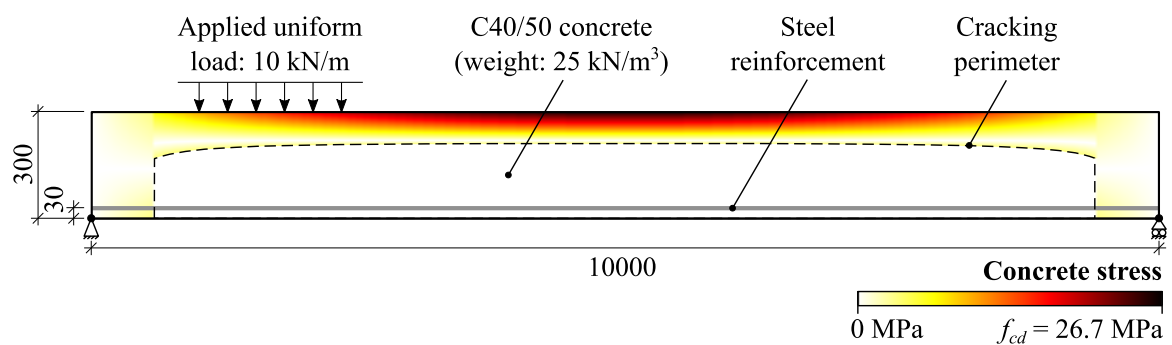


Figure 1.2: Concrete stresses in a single-spanning RC slab at the point of bending failure (all dimensions in mm, diagram not to scale).

The behaviour of real buildings can indicate how these structures might be made more efficient. In tests conducted on flat slabs within full buildings, Ockleston (1958) found that the strength can be up to five times greater than that predicted using yield-line theory. This was due to an arching effect he named "compressive membrane action", which arises as a

result of lateral restraint from neighbouring slabs. This suggests that an alternative approach to concrete floors, designed with arching action in mind, could therefore provide significant material savings.

## 1.2 The potential of thin-shells

For centuries, arches and vaults were the only way to create spanning structures using brittle materials such as stone, brick and unreinforced concrete. These were often highly successful in their functionality and durability. An example of a medieval masonry vault is shown in Figure 1.3a, the undercrofts of the monastery at Ely cathedral, which has stood for over 800 years. The Guastavino company constructed thousands of thin, shallow, tile-vaulted floors across North America between 1889 and 1962, an example of which is shown in Figure 1.3b. This system was economical at the time, has no documented incidents of structural failure, and is celebrated today for its distinctive architectural qualities (Ochsendorf, 2010).



Figure 1.3: Historical example of vaulted floors using brittle materials, including a) masonry undercrofts constructed in the 12th century for the monastery of Ely cathedral and b) tile vaulting in the Boston public library, constructed by Raphael Guastavino in 1895.

Today, advances in materials, manufacturing methods and computational techniques increasingly allow designers to explore non-planar structural geometries. This has enabled the design of complex, organic free-forms iconic of modern architecture. However, in a time of increasing pressure on the natural world, structural engineers must also use these opportunities to reduce resource consumption.

## 1.3 Aims and objectives

This project aims to establish whether thin shells, harnessing membrane action, are a viable, practical and low-carbon alternative to typical floor structures in multi-storey buildings which act primarily in bending.

The objectives are to:

- Understand the construction techniques, structural behaviour and environmental impacts of various materials, and therefore propose a practical and efficient structural system with sustainable potential.
- Explore and interpret the structural behaviour of thin-shell floors and thereby refine the proposal.
- Assess manufacturing methods through physical prototyping.
- Create a safe, reliable and repeatable design methodology suitable for widespread application.
- Quantify the potential embodied carbon reductions compared to existing alternatives.

## 1.4 Dissertation structure

**Chapter 1** has introduced the motivation, aims and objectives of this project.

**Chapter 2** reviews the relevant literature including historical background, modern innovations, environmental context and current research.

**Chapter 3** describes the proposed solution, and presents initial investigations into materials, design methods and structural feasibility. A number of geometric forms for the primary shell structure are explored, and a method for optimising groin vault geometries is developed.

**Chapter 4** investigates the behaviour of textile reinforced concrete (TRC) designed specifically for use in low-carbon compression shells. A series of experimental investigations are described and, based on these results, a novel approach for determining the strength of TRC shells is presented. The non-linear structural response of the material is also replicated in finite element (FE) analysis.

**Chapter 5** details the construction and testing of three physical prototype floor structures, each featuring 18mm thick TRC shells of 2m span.

**Chapter 6** replicates the experimental work of Chapter 5 using an FE model. This enables a detailed assessment of the testing methodology, structural behaviour, and the analytical methods developed in Chapter 4. A parametric study is carried out to determine the influence of several variables, including geometric and material properties, which provides further insight into how the structures might most effectively be designed and analysed.

**Chapter 7** establishes a repeatable design methodology for the proposed floor system, which is used to further refine the design and thus minimise total embodied carbon. A more detailed exploration of the structural requirements for practical use in buildings is also given. Finally, a performance comparison is made with typical floor structures including flat slabs and steel composite decks.

**Chapter 8** provides broad conclusions and considers the further work which might build upon the findings of this project.

# Chapter 2

## Literature review

### 2.1 Historical context

Durable, low-carbon structures are commonplace in historical buildings and infrastructure. This section chronologically explores key developments in the design and construction of compressive structures for buildings.

#### 2.1.1 Ancient and medieval master builders

Whilst the earliest examples of masonry arches date from ancient Greece, it was the Romans who first developed and widely applied the technology, and over 300 Roman masonry arch bridges are still in-use today. These were circular in profile and often contained no mortar, instead relying on precise stone-cutting and friction (O'Connor, 1994). Figure 2.1a shows the bridge at Pont-Saint-Martin in the Italian Alps, spanning 31.4m and constructed by 14AD.

The Romans were also the first to create hydraulic cement, using pozzolanic volcanic ash, and to combine this with aggregate to form concrete. The dome of the Roman Pantheon (Figure 2.1b), constructed from 113-125AD with a span of 43.3m, demonstrates several structural innovations in both form and materials. The density of the concrete shell is reduced at upper levels by using lightweight pumice aggregate. Further reductions in self-weight are achieved through coffering, thickness variations and the inclusion of an oculus. As a result, compressive stresses are very low (Mark and Hutchinson, 1986). The dome exists in a near-pristine state after over 1,900 years of earthquakes and weathering, demonstrating the durability of unreinforced concrete, in this case aided by its high quantity of pozzolans (Jackson et al., 2014).

A thousand years after the Pantheon, Gothic masonry architecture heralded new developments in compression structures, including pointed arches, flying buttresses and ribbed

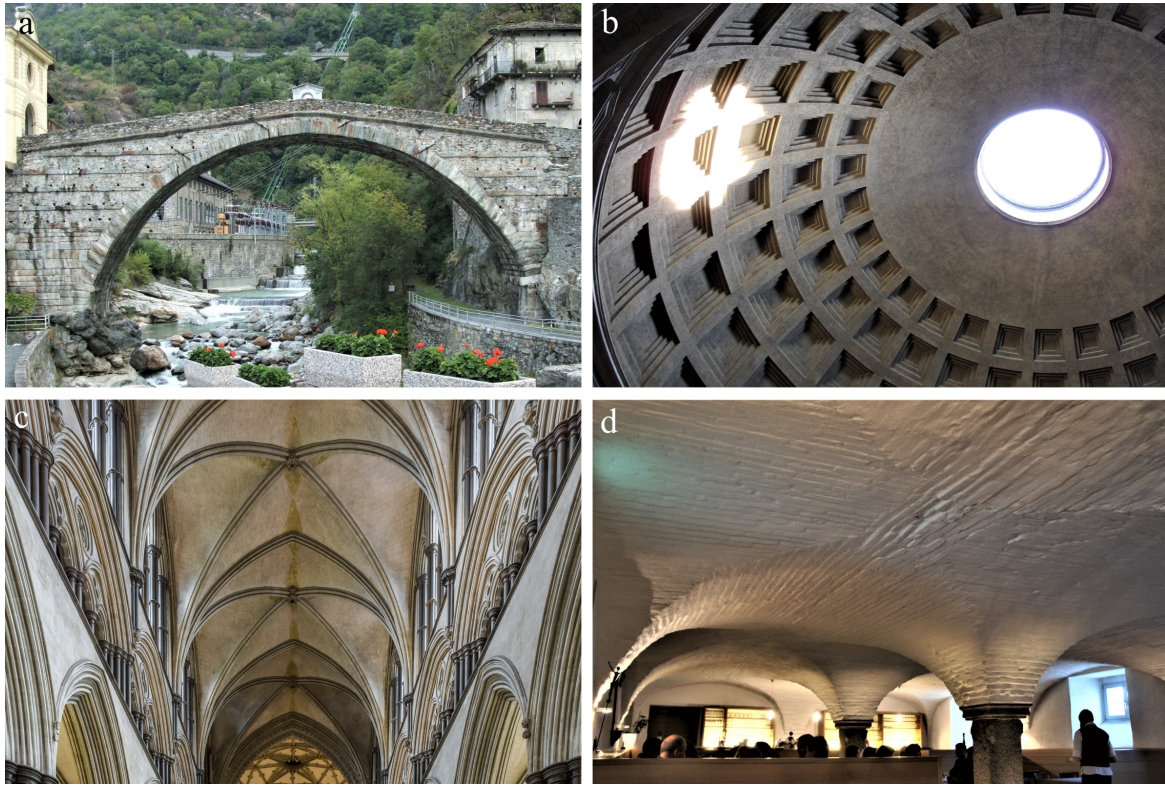


Figure 2.1: Historical examples of durable arch, vault and shell structures including a) the Roman Pont-Saint-Martin masonry arch bridge (photo Twice25, licence: CC BY 2.5), b) the unreinforced concrete Roman Pantheon (photo Poepoe, licence: CC BY 2.0), c) ribbed groin vaults at Salisbury Cathedral (photo David Iliff, licence: CC BY-SA 3.0) and d) a groin-vaulted under-croft in Waldsassen, Bavaria.

vaults. Figure 2.1c shows the ribbed groin vault at Salisbury Cathedral, completed in 1258. The geometry consists of two pointed arch barrel vaults intersecting at right-angles, with each repeated unit supported only at its corners. The ribs were constructed first and used as a stable frame for infilling the surfaces between, thus minimising the use of falsework (Heyman, 2000). However elegant, these costly structures took vast teams of masons many decades to complete.

Even the largest compressive stresses in a cathedral vault are an order of magnitude lower than the crushing strength of the material (Heyman, 2000), and the capacity of masonry vaults is therefore a question of stability only. Analytical and numerical models of masonry assume rigid blocks, with zero allowable tension, and stability is ensured if a purely compressive load path exists within the confines of the material. At the time, master builders understood that self-weight and geometry are key to structural stability, as evidenced by their use of pinnacles, rubble back-fill and large buttresses to keep the line of thrust within the masonry. Cracking

mechanisms can form to accommodate movement of supports (Heyman, 1997). Masonry vaults are therefore not reliably water-tight, necessitating the need for an additional timber roof for weatherproofing. In turn, the stone vault protects the interior from the potential fire hazard created by the flammable roof.

In contrast with roofs and bridges, vaulted floors require a level upper surface. This was commonly achieved through back-filling, which increases self-weight and thrust. For this reason, historic vaulted floors are typically limited to basements and under-crofts where lateral thrust can be resisted directly by the ground, as in Figure 2.1d.

A precise theoretical understanding of arching behaviour would not begin to emerge until the 17<sup>th</sup> century through the work of Hooke and, later, Coulomb. However, using intuition, rules-of-thumb and historical precedent, these examples demonstrate that builders were still able to create elegant, durable and low-carbon spanning structures.

### 2.1.2 Fireproof floor construction

Further innovations in vaulted floors were made from the industrial revolution to the beginning of the 20<sup>th</sup> century, when the superior fire resistance of tile, brick and masonry offered a key advantage over timber.

Catalan tile vaulting has its origins in 14<sup>th</sup> century Valencia. In this method, thin tiles were laid flat along the vault surface, rather than perpendicular to it (as in the preceding Roman system). This allowed the vaults to be much thinner, reducing thrust and hence enabling a much shallower profile. Crucially, by also using a fast-setting mortar, tiles could be placed without the need for falsework. By the 18<sup>th</sup> century, a growing demand for large fireproof buildings led to widespread use of this technique in France. Typically these were thin, singly-curved barrel vaults with a rubble fill. Spans of up to 25ft (7.6m) were common, with span to depth ratios ranging from 6:1 to 12:1 (Bannister, 1968). Figure 2.2a shows an example with five storeys of shallow vaults, constructed by the French engineer Jean-Baptiste Berthier in Versailles, in 1762. According to Bannister (1968), tie rods were not used, with the end vaults instead being oriented perpendicularly to counter the thrust imbalance. This would still leave unresolved forces at the corners, but it is possible that some peripheral ties were included, or that the external walls were sufficiently heavy to resist the thrust themselves.

This style of floor later influenced the construction of multi-storey fireproof mills, factories and warehouses in Britain. A common system was the jack-arch, pioneered by William Strutt and Charles Bage, which featured shallow brick vaults, levelled with sand or rubble, spanning onto a cast-iron frame with iron tie rods (Fitzgerald, 1988). Early examples include the Calico Mill (1793) and Ditherington Flax Mill (1797). A similar example, from 1842, is



Figure 2.2: Examples of tile and brick vaults in fireproof multi-storey buildings, including a) the Office of Foreign Affairs and the Navy in Versailles (photo gbaudouin4, licence: CC BY-NC-SA 2.0), b) Waulk Mill in Manchester (image copyright Urban Splash with permission) and c) the entrance to the City Hall subway station in New York (photo Emil Adiels, licence: CC BY-NC-ND 2.0).

shown in Figure 2.2b. Wermiel (2017) describes several other fireproof floor systems which were later developed across the UK and United States, featuring hollow tiles or concrete arches alongside cast iron.

Many of the most impressive examples of tile vaulting were those of the Guastavino company, and a detailed historical account of their projects is presented by Ochsendorf (2010). Raphael Guastavino gained an international reputation with the construction of the Batlló Factory in Barcelona, completed in 1875, which features extensive tile-vaulted roofs on a regular grid with steel columns and ties. The Boston Public Library (Figure 1.3b), constructed from 1889-1895, was the breakthrough project for Guastavino in North America. The two-way spanning, doubly-curved shells dispensed with the need for costly iron beams, and the absence of falsework enabled fast construction of over 370m<sup>2</sup> per week. The tiled aesthetic also proved hugely popular, leading to use on many grand public buildings, including the



City Hall subway station opened in 1904 (Figure 2.2c). For floors, a typical span to depth ratio was 10:1, with a span to thickness between 24:1 and 48:1 (Guastavino, 1892).

Despite their advantages, the popularity of Guastavino's vaults decreased steadily towards the middle of the 20<sup>th</sup> century. This might have been partially due to changes in aesthetic tastes, with vaults seen as nostalgic, or overly decorative compared to more modern steel and concrete alternatives. Although no examples of structural failure of Guastavino's vaults are documented, the calculations he used were simplistic and often featured incorrect assumptions (Huerta, 2003). Advances in building standards and codes may therefore have started to restrict the use of vaults, with beams and slabs being analysed with greater confidence by engineers. Furthermore, the rising cost of labour, and affordability of steel, eroded the economic advantages of unreinforced tile vaults.

### 2.1.3 20<sup>th</sup> century concrete innovation

Reinforced concrete emerged as the dominant construction material of the 20<sup>th</sup> century, facilitating new architectural movements and widespread, low-cost urban development. Concrete's ability to be moulded into any form was utilised in many structural applications. Although complex geometries required bespoke formwork, the cheap supply of labour in the 1930s (following the Great Depression) enabled early pioneers such as Robert Maillart, Pierre Luigi Nervi and Eduardo Torroja to create radical and intelligent structural forms in concrete, including shells, and Eladio Dieste similarly using post-tensioned brick.

#### Long-span structures

The golden age of concrete shells, in the 1950s and 1960s, was dominated by long-span structures and brought forward developments in both construction and design methods. Heinz Isler's structures, an example of which is shown in Figure 2.3a, were form-found using physical models of hanging or inflated membranes (Isler, 1994). He then used scale models to predict both the stresses within the full-scale structure and its stability. However, these elegant form-finding methods could not be replicated at full-scale, with Isler instead relying on glulam or steel-framed formwork. A reinforcement mesh was placed on this, and concrete sprayed before being trowelled smooth. Chilton (2010) suggests that formwork and falsework would have typically represented half of a shell's total cost at this time.

Felix Candela's famous hyperbolic paraboloid (hypar) shell geometry was influenced directly by formwork considerations (Funes and del Cueto, 2011). Each point on a hypar has negative Gaussian curvature, however the entire surface can be constructed entirely from straight lines. This enables formwork to be constructed using linear elements, such as sawn

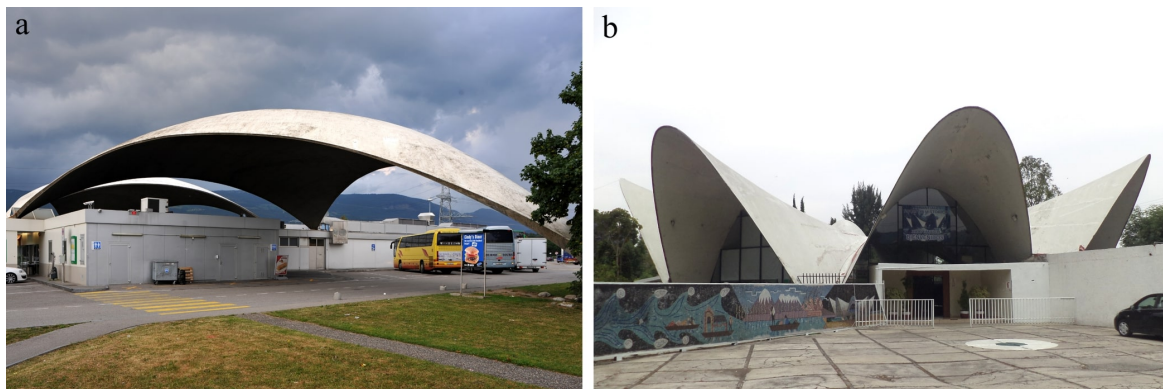


Figure 2.3: Long-span concrete shells, including a) Heinz Isler's 1968 Deitingen motorway service area in Switzerland (photo Chriusha, license: CC BY-SA 3.0) and b) Felix Candela's 1958 Restaurante Los Manantiales in Mexico City (photo Dge, license: CC BY-SA 3.0).

timber, as used in the construction of the Restaurante Los Manantiales in Mexico City, shown in Figure 2.3. Although this doubly curved form was undoubtedly effective, Tomás and Martí (2010a) showed that small changes to the geometry could greatly improve structural performance. The formwork's simplicity therefore comes with a structural efficiency penalty.

### Concrete floors

Shells are well suited to long-span roofs, where ample headroom permits high curvatures, foundations are relatively rigid and self-weight is the dominant load. In contrast, floor structures must remain shallow to maximise headroom, are usually supported by slender columns and carry potentially uneven floor loads. As a result, most innovation in concrete floor design from this era focused on improving the efficiency of bending elements, perhaps most famously in Nervi's ribbed slabs, patented in 1949, which elegantly mirrored principal moment directions (Halpern et al., 2013).

However, some innovative concrete shell floor systems were developed at this time. Figure 2.4a shows an unreinforced concrete vault marketed in Germany under the name "Kelling-decke" (Ministerium für Wirtschaft und Aufbau, 1952), which featured hollow tiles as permanent formwork, a lightweight concrete fill, and spanned up to 3.9m with a total depth of 300mm (Ahnert et al., 1987).

Ramaswamy and Chetty (1960) developed and patented a method of casting pre-fabricated doubly curved shells in fabric. These were inverted, placed on concrete beams and topped with in-situ concrete to create a flooring system used in thousands of buildings, primarily in India.

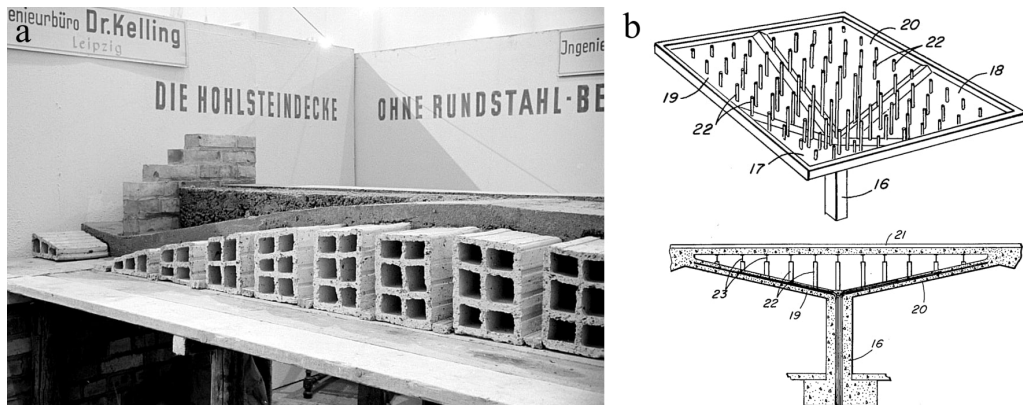


Figure 2.4: Examples of 20<sup>th</sup> century concrete shell floors, including the 1952 "Kelling-Decke" system (photo Deutsche Fotothek, license: CC BY-SA 3.0 DE) and b) a patent by Tully (1979).

Elliptical concrete thin-shell vaults were also recommended as the preferred floor construction solution by Alexander et al. (1977), due to their structural efficiency, use of common compression materials and perceived architectural benefits. A manufacturing method using bent timber lattice strips with hessian fabric as formwork was proposed, enabling vaults to be fitted to any arrangement of columns and beams. An FE analysis of one such shell, spanning 4.9 x 6.1m, was used to justify a thickness of only two inches (51mm), without reinforcement. Today, this use of unreinforced concrete would be difficult to justify due to robustness concerns, particularly in multi-storey buildings.

A patent by Tully (1979), shown in Figure 2.4b, details a thin-shell concrete system with the floor suspended on adjustable props. Leggatt (1980) also proposed a similar modular system comprising a pre-cast fan vault with in-situ concrete fill.

### Decline in use

Although architecturally striking and structurally effective, today concrete shells are rarely considered as a design option. Tang (2015) notes their steady decline in use from the 1970s onwards, and suggests several reasons for this. Economically, the rising cost of labour and falling price of materials favoured simpler forms and faster construction, with less incentive for structural efficiency. Advances in steel, glass and fabric materials made grid-shells and tension structures the preferred choice for large spans, with weight and natural light advantages. Furthermore, the design and behaviour of shells is generally less well understood than beams and slabs, and the lack of design codes creates an impression of high risk to clients. As these structures have faded from use, so has the expertise required to design and construct them.

This section has shown the considerable historical precedent for vaulted floor construction. Whilst these structural typologies have been largely abandoned by modern designers, emerging technologies might enable their rediscovery; a revival of simple, efficient and sculptural forms for low-carbon construction.

## **2.2 Modern design, materials and manufacturing methods**

The construction industry is traditionally seen as slow to change in comparison to other sectors. However, as ever-expanding computational capabilities open up new possibilities in both design and manufacture, innovation in structural engineering research is flourishing. This section explores these recent developments and how they might be applied to the creation of a practical, low-carbon floor system.

### **2.2.1 Form-finding and structural analysis**

Shells are statically indeterminate structures which resist load through membrane and bending forces, the distribution of which depends on geometry, particularly curvature. An efficient shell minimises bending forces, which are associated with large peak stresses and deflections.

Historically, many shell geometries have been mathematically defined using, for example, cylindrical, spherical or hyper surfaces. Before the ubiquity of FE analysis, a mathematical formulation of a surface was prerequisite to its structural analysis. A precise and simple means of defining geometry was also desirable for manual formwork construction. However, the available library of mathematical forms is restricted, and may not offer an efficient geometry in many scenarios. Fortunately, several alternative techniques for defining shell forms are available to designers today.

#### **Form-finding using physical principles**

Funicular geometries are formed by flexible structures with applied forces; the geometry changes in response to loading such that internal membrane forces are in equilibrium with applied loads. If all loads are in the direction of gravity, then a tensile form can be inverted to create a pure compression form. This enables the use of real, physical tensile structures to compute funicular geometries. This approach was adopted by Antoni Gaudi, who used hanging chains to dictate the forms of vaults (Huerta, 2006). Heinz Isler precisely measured hanging models in order to re-create their geometry at full-scale (Chilton and Isler, 2000), and Frei Otto also used a variety of physical models to derive efficient forms (Rasch and Otto, 1996).

Today, this technique can be replicated computationally. This allows designers to create funicular forms in seconds, explore limitless design options and effortlessly extract geometrical data. Several techniques exist to solve this numerical problem:

- **Dynamic Relaxation** finds the equilibrium shape of a system of nodes connected via springs using Newton's second law (Day, 1965; Otter, 1965). An imbalance of forces causes a node to accelerate towards its equilibrium position, and damping is required to converge on equilibrium node locations. This might be viscous, as in a physical system, or kinetic, whereby all velocities are set to zero when the maximum total kinetic energy is detected. Using this method, families of funicular forms can be explored by altering the stiffness, rest length and topology of the particle-spring system.
- **The Force Density Method** uses the ratio of an element's force to its length to linearise the equilibrium equations and hence calculate the equilibrium form of a net structure (Linkwitz and Schek, 1971). Gulentops et al. (2009) and Van Mele and Block (2011) have used this technique for the design of flexibly-formed concrete shells.
- **Thrust Network Analysis** extends the principles of graphic statics into three dimensions to generate funicular forms, and is used in the popular form-finding software RhinoVAULT (Rippmann et al., 2012). Here, the designer is free to modify the arrangement of forces in a structure to explore 3D funicular forms, giving considerable control over the geometry.

Funicular form-finding is a means of generating shell geometry based on justifiable physical principles. However, there are several shortcomings to this approach.

Accuracy is inherently limited by the discretisation of geometry, although this can be overcome through the use of a sufficiently refined mesh. However, the mesh topology (of a particle-spring system, for example) directly influences the flow of forces and hence the resulting form (Kilian and Ochsendorf, 2005; Richardson et al., 2013). Only one funicular form is generated from an infinite number of possibilities, each with its own distribution of membrane forces. Despite this, the inverted geometry is capable of acting in pure compression through a lower bound argument, because a system of pure compressive forces in equilibrium with the applied loads has been found. The true force distribution in the shell structure will however differ, not least because the shell has bending stiffness whereas the flexible membrane does not. For this reason, form-found compression shells still carry bending forces (Elangovan, 1990; Ramm and Mehlhorn, 1991). Furthermore, any funicular form is specific to a single loading arrangement and boundary condition. Any deviation from these, such as variable live loading or movement of supports, will generate bending forces. Finally, there

is no guarantee that a funicular form has good buckling resistance, and a separate stability analysis must therefore be performed (Halpern and Adriaenssens, 2013). In some cases, a purely compressive form may be more prone to buckling than a non-optimal shell. For example, Isler (1994) found that his pneumatic shells, although not funicular in form, had superior buckling resistance to geometries found through inversion of hanging fabric.

In practice, funicular form-finding should therefore be seen simply as an approach to generating a candidate shell geometry, rather than a strict definition of optimality.

### **Parametric optimisation**

Optimisation is the process of selecting the best solution from a user-defined set (design space) based on a numerical measure of performance (fitness). This can be a powerful tool in the design of structures, including the geometry of shells, and has three main steps:

- Firstly, the shell geometry must be defined by a finite set of variables (parametrised). These might be the height of a hyper surface (Tomás and Martí, 2010b), the coordinates of control points for a NURBS surface (Liu et al., 2012; Veenendaal and Block, 2014), or even parameters within a funicular form-finding method (Van Mele and Block, 2011). In all cases, reducing the number of parameters simplifies and speeds up the optimisation process (at the cost of a progressively restricted design space).
- Secondly, the fitness of a candidate geometry must be determined. Often an FE analysis is used to give a structural performance value, such as deflection (Pugnale and Sassone, 2007; Veenendaal and Block, 2014) or total strain energy (Liu et al., 2012; Tomás and Martí, 2010b). Alternatively, the self-weight might be the fitness value, subject to a given structural constraint such as a stress limit (Banichuk et al., 2006; Beghini et al., 2014; Uysal et al., 2007).
- Thirdly, a means of modifying the design parameters in order to maximise fitness is required. This is a highly developed area of engineering mathematics, and the most effective optimisation method depends on the problem. The fitness landscape may be smooth, featuring a single peak, or rough, with multiple sub-optimal peaks. In the former case, gradient methods such as Newton-Raphson are suitable. For more complex design spaces, a number of stochastic methods have been developed which utilise randomness. Examples include Simulated Annealing (Kirkpatrick et al., 1983), Particle Swarm Optimisation (Kennedy and Eberhart, 1995) and Genetic Algorithms (Von Neumann and Burks, 1966).

The power of parametric optimisation lies in its flexibility. The design space can be built to accommodate constraints, perhaps arising from a particular formwork method or a geometric restriction. Multiple design scenarios can also be combined into a single fitness value, allowing various loading arrangements to be considered. However, care should be taken when formulating an optimisation procedure. A parametrised design space is necessarily a restricted one, potentially leading to a sub-optimal solution. Fitness values are also subject to misinterpretation, particularly when relying on FE analysis. Finally, the reliability and repeatability of the chosen optimisation method is not always guaranteed.

### **Structural analysis**

Free-form shells are typically analysed using numerical methods such as FE analysis. A linear model can be used to approximate reinforced concrete providing the stress limits of cracking or crushing are not exceeded, and may therefore be suitable for compression shells (Seracino et al., 2012; Tysmans et al., 2011). Should cracking occur, a more complex non-linear model is required to accurately predict behaviour. Hand et al. (1972) developed a solution for modelling reinforced concrete shells by splitting the section depth into multiple layers, each of which is allowed to crack. This approach is commonly adopted in FE programs. An alternative tool to FE analysis currently being developed for concrete is peridynamic modelling, a mesh-free analysis method which allows realistic replication of cracking (Miranda et al., 2016).

For unreinforced concrete and masonry structures, FE approaches which assume material continuity are not appropriate since cracking is an integral part of structural behaviour. Instead, the plasticity theory of masonry developed by Heyman (1966) can be implemented computationally to determine collapse loads of rigid block mechanisms (Block et al., 2006; Chiozzi et al., 2017).

Shells are particularly sensitive to buckling, and where this might occur, any ultimate limit state assessment therefore requires a geometrically non-linear analysis featuring initial imperfections (Ramm and Mehlhorn, 1991; Verwimp et al., 2016). Often the eigenvectors of a structure are taken as worst-case initial imperfections (Tomás and Tovar, 2012; Veenendaal et al., 2017).

### **2.2.2 Fabrication**

Modern numerical methods and computing power have arguably eliminated structural analysis as the limiting factor in the use of complex structural forms. However, manufacturing processes must also exist to make a structure economically viable.

### **Pre-casting**

Reinforced concrete buildings are typically constructed in-situ, with formwork erection, reinforcement fixing and concrete placement carried out on-site. Pre-casting takes the majority of this activity off-site, significantly reducing construction time, waste, and the number of workers exposed to site hazards. Quality is also improved in a controlled indoor environment, and checks can be made more easily or even automated (Wang et al., 2016). López-Mesa et al. (2009) and Ji et al. (2018) have also shown that pre-cast solutions can have a lower environmental impact than in-situ construction, primarily due to lower material use arising from smaller tolerances and reduced waste.

The growing popularity of pre-casting represents an opportunity to introduce new manufacturing methods into mainstream construction. However, the size of pre-cast components are constrained by road transportation requirements. A standard UK articulated lorry trailer has a maximum width of 2.55m (Butcher, 2009) and, as a result, pre-cast floor structures are almost always single-spanning and therefore require additional beams for support. Pre-cast units also need to be joined together on-site, making connections an important design feature. Examples include adhesive, bolted mechanical connections, post-tensioning, or stitching using small amounts of in-situ concrete to bind together overlapping reinforcement (Eisenbach and Grohmann, 2017).

### **Formwork typologies**

Concrete's fluidity is key to its versatility and ubiquity. Most commonly, wet concrete fills a mould like a fluid, but it is also possible to use single-sided formwork onto which concrete is either sprayed or trowelled. For shell structures, this is potentially a simpler formwork arrangement, although thickness control is a potential concern. Thin concrete shells have been constructed using both filled moulds (Eisenbach and Grohmann, 2017; Liew et al., 2017) and surface moulds (Scholzen et al., 2015a; Seracino et al., 2012; Veenendaal and Block, 2014).

### **Additive manufacturing**

New methods of concrete placement have recently emerged which dispense with formwork entirely, using additive manufacturing (also known as 3D printing). Most methods involve building up successive layers of uniform thickness to create free-form walls, known as 'contour crafting' (Khoshnevis, 2004). Whilst this method is inappropriate for shells, robotic spraying of concrete combined with adaptable formwork is being developed with the potential



to facilitate free-from shell construction (Kloft et al., 2019; Lindemann et al., 2017; Neudecker et al., 2016).

However, several challenges limit the applicability of direct concrete printing at present. Reinforcement is difficult to incorporate, particularly in the direction orthogonal to material deposition (Mechtcherine et al., 2018). There is also a contradiction between the need to pump the concrete through a nozzle, and for it then to stably support itself and subsequent layers, and thus the process is highly sensitive to concrete rheology and setting characteristics (Wolfs et al., 2018). This issue can be overcome by printing formwork instead of the concrete itself. The Digital Building Technologies group at ETH Zürich has pioneered the use of printed formwork consisting of an artificial "sandstone", created from sand with polymer binders (Meibodi et al., 2017). This was used to create a post-tensioned floor slab described by Jipa et al. (2016), shown in Figure 2.5a.

Another material which has been used to create complex formwork is wax, which can be formed, melted and reused multiple times. Mainka et al. (2016) proposes milling of a wax block, whilst Liebringshausen et al. (2017) first sculpted the desired geometry from oil-bonded sand, then cast wax against this to create a mould for thin concrete shells. Wax formwork has also been used commercially for the construction of concrete facade panels. Here, Laing O'Rourke's "FreeFab" system (Gardiner and Janssen, 2014) quickly and approximately 3D prints the wax before milling to the required tolerance.

Additive manufacturing offers geometric freedom, but with a considerable trade-off between precision and construction time. The specialist equipment also adds cost, consumes energy and limits the size of components which can be made.

### **Flexible formwork**

A flexible structure naturally creates a curved form, dictated by its material properties and applied loadings. In principle, this can create a shell forming surface instantaneously with minimal material. Hawkins et al. (2016a) describe the use of this technique in many applications, and an example of a hybrid system incorporating cables and fabric is shown in Figure 2.5b (Liew et al., 2018; Veenendaal and Block, 2014).

The complex behaviour of stressed woven fabrics potentially makes accurate prediction of a component's final geometry challenging, and can create issues of repeatability. Compared to rigid formwork, an additional form-finding step may be required to predict the final form, adding complexity and uncertainty to the design process (Guldentops et al., 2009; Hawkins et al., 2016b; Tysmans et al., 2011; Van Mele and Block, 2011; Veenendaal and Block, 2014).



Figure 2.5: Examples of innovative forming methods for concrete, including a) a ribbed post-tensioned floor slab using 3D printed formwork (image by Tom Mundy, copyright Digital Building Technologies, with permission) and b) hybrid flexible formwork using a cable-net and fabric described by Veenendaal and Block (2014) (image courtesy Diederik Veenendaal, BRG, ETH Zürich).

This section has demonstrated concrete fabrication methods which enable a transition away from prismatic forms. Although currently limited in their application, these might bring considerable opportunities for economical structural optimisation in the future.

### 2.2.3 Materials and reinforcement

Concrete shells, even when acting principally in compression, require reinforcement to provide tensile strength and robustness after cracking. Conventional steel reinforcement can be shaped to follow curved forms only when curvatures are low and bars sufficiently thin and flexible (Seracino et al., 2012). Otherwise, bending of the steel is required. Using ferrous reinforcement also limits the lifespan of concrete, due to carbonation and eventual rusting and spalling. The cover requirements for corrosion protection can add significant thickness to a thin-shell. However, a number of alternative reinforcing strategies are available for shell construction.

#### Fibre reinforcement

The height of fabrication simplicity, particularly for curved and variable section forms, is the incorporation of reinforcement into the concrete mix itself. This allows application of both in a single process. Fibre reinforced concrete (FRC) uses uniformly distributed and randomly orientated fibres to improve shrinkage cracking resistance, ductility and tensile strength (Song and Hwang, 2004). Fibres can be made from steel, glass, polymers or natural

materials, and FRC can be sprayed to create thin-shell structures (Schipper, 2015; Tang, 2012; Torsing et al., 2012; West and Araya, 2012).

However, since fibres are distributed and orientated randomly, only a small proportion will be utilised in crack-bridging. A fibre is also not effective along its entire length, since sufficient bond distance is required on either side of a crack to prevent pull-out.

### **Textile reinforced concrete**

Fibres can also be woven into continuous textile meshes and combined with concrete in layers, creating textile reinforced concrete (TRC). The manufacturing complexity of TRC is greater than that of FRC, since numerous layers of concrete and reinforcement must be applied successively. Accurate construction of thin layers is also challenging, and these can limit maximum aggregate size.

However, TRC offers significant advantages in material efficiency compared to FRC. The reinforcement can be oriented in the direction of tensile stresses and located near the shell surface for improved bending efficiency. Strength is also no longer limited by anchorage. As a result, it is estimated that TRC offers an 80% fibre reduction compared to FRC of similar performance (Butler et al., 2010). TRC therefore offers an ideal solution for the creation of materially efficient concrete shells. Flexible textiles can also easily conform to curved surfaces, such as those created using fabric formwork (Tysmans, 2010; West and Araya, 2012).

TRC was therefore identified as a promising candidate material for a thin-shell flooring system, and its characteristics are explored further in the sections which follow.

### **TRC construction and materials**

In the manufacture of textile reinforcement, fibres are grouped into yarns which are in turn woven or knitted into textile meshes, examples of which are shown in Figure 2.6. Alternating layers of reinforcement and concrete can be built up successively, either through spraying or by hand, or alternatively concrete can be poured around a 3D textile, akin to traditional RC casting (Figure 2.6c).

Gries et al. (2006) provide a detailed overview of the myriad forms of textile reinforcement, which vary in both scale and construction. Often the textile is impregnated with a polymeric matrix material in order to improve load transfer between fibres, bond characteristics and durability. This also adds rigidity to the mesh, potentially restricting the curvatures to which it can be applied.

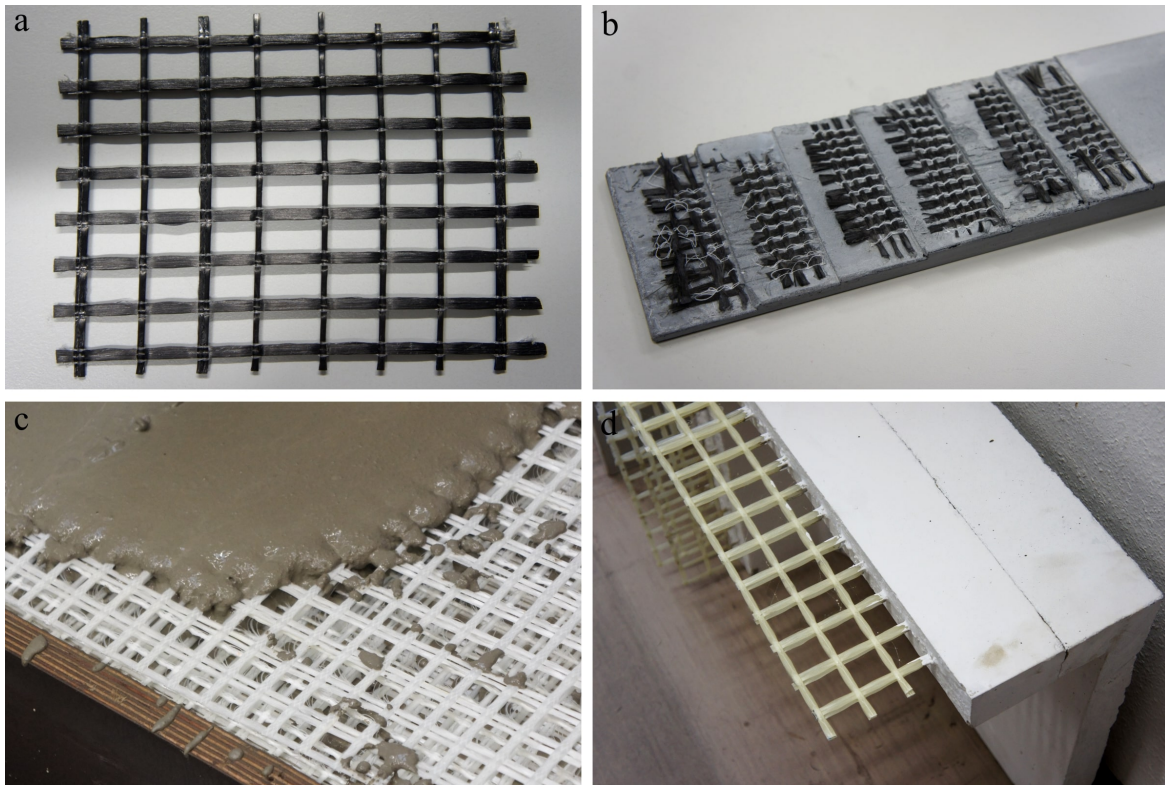


Figure 2.6: Examples of TRC materials and construction, using textiles of a) polymer-impregnated carbon fibres, b) uncoated carbon fibres, c) multi-layered AR-glass fibres with polymer coating and d) a polymer-impregnated AR-glass fibre grid.

Fibre materials used in TRC include carbon, aramid, basalt or alkali-resistant (AR) glass. Carbon typically has a stiffness approximately three times higher than AR-glass or basalt, and twice that of aramid (FIB, 2007), whilst the tensile strength varies significantly between specific products. A comparison of production methods and embodied carbon for these fibre materials is given in Section 2.3.1.

Fibre reinforcement is inherently non-corrosive, offering a major advantage over steel in terms of durability and cover requirements. However, AR-glass fibres in cement matrices exhibit ageing effects due to alkaline corrosion (Larner et al., 1976), delayed failure under sustained load, known as stress corrosion (Jones et al., 1983), and increased brittleness caused by continued bond strength development (Bentur, 2000). Similar time-dependent behaviour is also exhibited by basalt fibres (Hempel et al., 2016; Sim et al., 2005). However, Butler et al. (2010) showed that these phenomena can be greatly mitigated by reducing matrix alkalinity through replacement of Portland cement. Using coatings, as well as large yarns with a lower proportional surface area, also limits fibre exposure for improved durability. In contrast,

carbon fibres are well known for their chemical resistance, making durability is less of a concern (Langlois et al., 2007; Mechtcherine, 2012).

There are a wide variety of matrix materials currently being used in TRC research, as detailed by Mechtcherine et al. (2016). The maximum aggregate size sets a lower limit on thickness between reinforcement layers, and is therefore typically small. This means that a higher binder content is required to achieve the same strength as regular concrete, and can also result in a lower stiffness (Banholzer et al., 2006; Scholzen et al., 2015b; Verwimp et al., 2015).

The performance of TRC in fire is discussed by Krüger and Reinhardt (2006), Bisby (2016) and Kapsalis et al. (2019). The non-combustible inorganic mortars of TRC are a key advantage over fibre-reinforced polymers in terms of fire resistance. However, thin TRC sections would be expected to heat up quickly due to their low thermal mass, and therefore the performance of the fibre at high temperature is critical. In this respect, carbon fibres typically perform better than glass (Bisby, 2016; Krüger and Reinhardt, 2006).

### **Behaviour, modelling and design of TRC**

The structural behaviour of TRC is non-linear and anisotropic due to cracking of concrete and subsequent reinforcement crack-bridging and de-bonding (Mobasher, 2016).

Tensile load-extension curves show three distinct phases; initially uncracked (linear-elastic), a crack-forming phase, and finally a fully-cracked phase which is approximately linear to failure. TRC can be highly robust and exhibit quasi-ductile behaviour, and has been shown to perform well under impact loading (Dey et al., 2015). Compressive behaviour is dominated by the concrete matrix, although the presence of reinforcement can lead to a reduction in strength due to the introduction of discontinuities and subsequent crack initiation (Bochmann et al., 2017).

Design and modelling of TRC is challenging, since the micro-scale interactions between bundles of fibres, coatings and concrete at crack locations has a large influence on the macro-scale behaviour (D'Antino et al., 2014; Raoof et al., 2016; Sneed et al., 2015). Fibres are brittle, and the tensile strength of a yarn or textile is therefore lower than that of individual fibres, due to the variable distribution of flaws (Ashby and Jones, 2012). Non-uniformities in fibre stress also arise due to concrete cracking and delayed shear transfer from outer to inner fibres (Ohno and Hannant, 1994). When the direction of tensile loading is not aligned with the reinforcement, its strength is further reduced due to stress concentrations arising as filaments bridge inclined cracks (Hegger et al., 2006a).

A overview of design models for TRC is given by Hegger and Will (2016). Chudoba et al. (2016) proposes a micro-plane damage model which can be used to predict stress

and deformation through calibration against tensile tests on identical TRC sections. More recently, this has been extended to shells of variable thickness and reinforcement layout (Chudoba et al., 2019). For strength design, a simpler approach is presented by Scholzen et al. (2015b). In this method, a local strength utilisation is calculated based on axial and bending forces. A bi-linear failure envelope is assumed, defined by interpolation between three experimentally determined strengths in pure compression, tension and bending. This linear approximation under tensile loading has been verified experimentally (Scholzen et al., 2015c), however the same assumption is highly conservative in compression (Hawkins et al., 2018). When using a linear FE analysis to calculate forces, further conservatism arises due to the absence of force redistribution caused by cracking (Sharei et al., 2017).

### TRC applications

Scheerer et al. (2017) details recent applications of TRC in Germany, which include bridges, canopies, and strengthening of existing structures. Figure 2.7a shows a hyper roof structure constructed at the university of Aachen (Scholzen et al., 2015a), featuring a 60mm thick TRC section with 12 layers of carbon fibre reinforcement. TRC barrel vaults of 20mm thickness are shown in Figure 2.7b (Sharei et al., 2017).

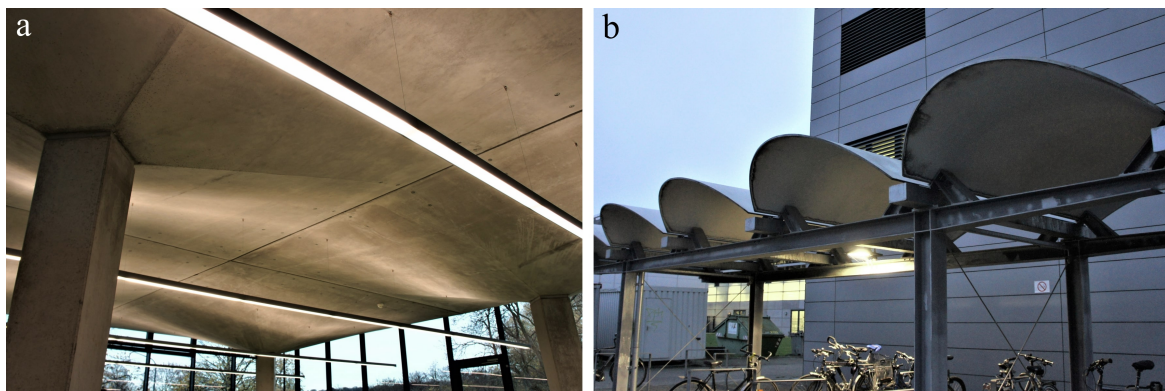


Figure 2.7: Example of TRC structures at the University of Aachen, including a) a 60mm thick glazed pavilion (Scholzen et al., 2015a) and b) 20mm thick barrel vaults (Sharei et al., 2017).

## 2.3 Quantifying and minimising the environmental impact of buildings

The previous section has shown how continued advances in construction methods and materials are creating new opportunities for structural innovation. However, it is vital that this potential is harnessed in an environmentally sustainable way.

Each stage of a building's life impacts the environment, through the extraction and processing of materials, the burning of fossil fuels for energy and modification of local ecosystems, for example (Tukker and Jansen, 2006). Life-cycle assessment (LCA) is a technique used to determine the complete environmental impact of a product or service, including all stages from raw material extraction, transport and processing, transport to site, construction, operation, maintenance, and finally demolition and disposal (McManus and Taylor, 2015). A 'cradle-to-gate' analysis considers only material production itself. Whilst overlooking many important stages, this approach allows general comparison of materials and products by ignoring project specifics. A full LCA is known as "cradle-to-grave", or "cradle-to-cradle" where recycling is also included.

LCAs of buildings and construction materials are becoming more commonplace. This is partly a result of increased recognition and reward in industry. For example, the 2018 incarnation of the popular Building Research Establishment Environmental Assessment Method (BREEAM, 2018) rewards designers for conducting an LCA and "optimising the use of materials". The clarity and consistency of assessment methodologies has also improved with the introduction of the standards BN EN 15804 BSI (2012a) and ISO 14025 ISO (2006), which set out how to produce Environmental Product Declarations (EPDs) for construction products. Slowly, an environment is being created in which building structures are routinely and consistently assessed for their environmental impacts, and this is a vital step towards reducing these. Growing calls for a universal price on carbon might, if implemented, considerably incentivise this action (MacKay et al., 2015).

Improving the operational efficiency of existing buildings is one of the most cost-effective means of reducing the UK's carbon emissions (Committee on Climate Change, 2018). However, Giesekam et al. (2014) determined that focusing on operational performance alone is not enough to meet emission targets since, for new buildings, embodied materials now dominate the life-cycle (Ibn-Mohammed et al., 2013; Sturgis and Roberts, 2010). Across the EU, the Energy Performance of Buildings Directive (European Parliament Council, 2010) states that all new buildings must be "nearly zero energy" after 2021, referring to operation only. In this case, the embodied portion makes up the entire life-cycle impact, and therefore

represents the only means of achieving further reductions. A shift in focus towards materials is the logical next step in sustainable building design.

The structure makes up the majority of embodied carbon in buildings. Kaethner and Burrige (2012) calculate that, of the total embodied CO<sub>2</sub> of a typical new office building, 62% derives from the structural materials, 12% from construction activities, and the remaining portion from non-structural elements. Another study of the Leadenhall Building, a large 48 storey office building in central London, gives similar values of 60% and 7% respectively (UK Green Building Council, 2015). Engineers dictate the form, specification and quantity of these materials, as well as construction methodologies, and therefore exert much control over the total environmental impact.

Of the structure, floors typically make up the majority of material. De Wolf et al. (2016a) estimated that, in a simple 10 storey building with 8m spans, the floors comprise over 90% of the superstructure's mass. Foraboschi et al. (2014) put this figure at 60-81% for concrete-framed buildings of 20-70 storeys. In very tall and slender buildings however, the lateral stability system can begin to dominate (Gan et al., 2017). Shanks et al. (2019) identified floor slabs as the second largest single source of cement consumption in the UK, behind only maintenance and repairs. These are therefore a highly worthwhile target for reductions in cement consumption.

### **2.3.1 Embodied carbon of structures**

Structural engineers wishing to quantify and compare the embodied carbon of structural designs have, at present, no universally adopted methodology for this. There are multitudes of databases and LCA software, each with different approaches and giving sometimes conflicting results (De Wolf et al., 2017). A common, albeit minimal, approach is to multiply the mass of each material in a structure by a single environmental factor. Two units are compared most commonly in structural engineering literature: embodied energy (MJ/kg) and carbon dioxide (kgCO<sub>2</sub>/kg). In the latter case, other greenhouse gasses (including methane and nitrous oxide) are often included, with appropriate factors, to give a carbon dioxide equivalent or global warming potential (kgCO<sub>2</sub>e/kg). Other pollutants and impacts, such as water use, eutrophication and ozone depletion, are included in a full LCA but often ignored in practice (Moncaster and Symons, 2013).

Carbon dioxide emissions are associated with, but not always proportional to, energy use. For example, high grade electrical energy requires more carbon to produce than lower grade heat energy (Vukotic et al., 2010). This presents a difficulty in embodied CO<sub>2</sub> calculations, which correspondingly are highly susceptible to local variations in energy production methods. The embodied carbon associated with a material can also change over time, with potential



for reductions through better energy efficiency, yield improvement, and de-carbonisation of electricity supplies (Allwood et al., 2011). Carbon dioxide can also be emitted separately to the generation of energy, such as in the cement making process. In this regard, considering only the embodied energy can be misleading for some materials. Embodied CO<sub>2e</sub> is therefore considered, in this case, to be a more relevant unit of comparison, despite the additional complexities of its calculation.

Consistency and availability of LCA data for construction materials is vital for comparison of structural systems, and several databases exist which attempt to provide data for several materials, with an overview of these given by De Wolf et al. (2017). A popular reference for many materials is the Inventory of Carbon and Energy (ICE), which provides cradle-to-gate values of CO<sub>2e</sub> with a clear explanation of sources and assumptions, based on data for the United Kingdom (Jones and Hammond, 2019). The Cambridge Engineering Selector (CES) software also gives estimates as part of a comprehensive database of properties for a huge range of engineering materials (Granta Design Ltd., 2018). An increasing number of EPDs are also available in an on-line database, providing detailed information for specific construction products (EPD International, 2018).

Typical values of embodied carbon are compared for a selection of structural materials in Table 2.1, using data primarily from the ICE and CES. Each group of materials is discussed in the sections which follow.

### **Concrete**

Portland cement is the principal source of embodied carbon in concrete. Typically, stronger mixes contain more cement and therefore have higher associated emissions. For this reason, over-specification of concrete strength is a possible target for carbon reductions in industry. Replacing Portland cement with alternative, low-carbon binders is another means of reducing embodied carbon. Fly ash, a by-product of burning coal, and ground-granulated blast furnace slag (GGBS), from steel production, are two cementitious waste materials commonly used as a partial replacement for Portland cement. However, their use at high quantities can have detrimental effects on performance, including slower strength development (Naik and Ramme, 1987). The global availability of these materials is also insufficient to allow widespread use, with the International Energy Agency and The World Business Council for Sustainable Development (2009) estimating a limit of 10% cement carbon reductions using these materials. Another promising cement replacement is calcined clay (metakaolin) and limestone which, according to Antoni et al. (2012), can replace up to 45% of Portland cement without loss of strength.

Table 2.1: Comparison of typical embodied energy and carbon values for a variety of engineering materials. The number of decimal places reflects the data provided by the source. Where a range of values are given, the mid-value is shown.

<b>Material</b>	<b>Embodied carbon [kgCO<sub>2</sub>e/kg]</b>
<b><i>Concrete constituents</i></b>	
Portland cement*	0.912
Fly ash*	0.008
GGBS*	0.083
Aggregate*	0.00747
Water*	0.0008
Superplasticiser‡	1.88
<b><i>Concrete example mixes (CEM I)</i></b>	
C20/25*	0.121
C32/40*	0.149
C40/50*	0.172
<b><i>Metals</i></b>	
Steel reinforcement*	1.99
Hot-rolled steel section*	1.55
Galvanised steel sheet*	2.76
Aluminium extrusions*	6.83
<b><i>Fibre materials</i></b>	
Carbon fibre†	20.3
Aramid fibre†	17.3
Glass fibre†	3.00
Basalt fibre†	0.057
<b><i>Fibre composite matrix materials</i></b>	
Epoxy†	6.60
Vinyl ester†	4.31
Polyester†	2.54

\*Source: Jones and Hammond (2019)

†Source: Granta Design Ltd. (2018)

‡Source: EFCA (2015)

Geopolymer cements are binders which use no Portland cement, instead relying on various combinations of fly ash, GGBS or metakaolin with an alkali activator. As a result, the embodied carbon of geopolymer concretes can be 70-80% less than a Portland cement equivalent (Davidovits, 2005; Rajamane et al., 2012; Wimpenny, 2009). At present, many barriers to widespread commercial adoption exist however, including insufficient availability

and supply infrastructure of the constituent materials (Deventer et al., 2012). Furthermore, hardened geopolymer properties are also highly sensitive to variations in raw material composition and mix proportions, and often require high curing temperatures (Duxson et al., 2007).

Approximately half of the emissions from Portland cement production come from the chemical process, with 40% from the burning of fuel and the remaining 10% split between grinding and transportation (Bosoaga et al., 2009). As a result, the scope for improving production efficiency is limited. Fossil fuels can be replaced with biomass (IEA, 2008; Schneider et al., 2011) and transport can be de-carbonised, but the chemical reaction cannot. It may, however, be possible to overcome this through carbon capture and storage (CCS). Several CCS techniques have been proposed and feasibility studies carried out (Vatopoulos and Tzimas, 2012), with 60% of total CO<sub>2</sub> potentially being captured (Hills et al., 2016). The concentration of CO<sub>2</sub> in the flue gasses of cement plants are greater than that of a coal-fired power station (Bosoaga et al., 2009). However, the technology has not yet progressed beyond pilot studies. Barriers to adoption include unsuitability of current plants and high costs of retrofit, making the technology uneconomical. It has been suggested that carbon prices would need to rise three to six times to make CCS from cement production viable (Kisic et al., 2018).

Throughout the lifetime of a concrete structure, the same cement chemistry acting in reverse absorbs CO<sub>2</sub> from the atmosphere (carbonation). Xi et al. (2016) suggest that this process represents a significant, and growing, carbon sink, estimating that 43% of process-related emissions from cement production between 1930 and 2013 have already been absorbed. Combined with CCS, this hypothetically enables cement to be a carbon-negative product. Regardless, the delay between carbon production and uptake means that a global warming contribution is not avoided. Overall, the environmental argument for reducing concrete consumption remains solid.

The embodied carbon of aggregate, typically the main constituent of concrete, is dominated by transportation and usually very low (see Table 2.1). However, extraction of sand and gravel can cause significant environmental damage depending on local practices. The UK has the world's largest marine aggregate industry (Crown Estate, 2016). Whilst highly abundant (McLaren et al., 1998), the dredging required to collect this material disturbs the seabed, damages the associated benthic ecosystems and can cause re-suspension of contaminated sediments into the water column (Boyd and Rees, 2003). Over-extraction of sand for concrete has also led to severe environmental and societal issues in locations where sand is scarce, including Sri Lanka (Pereira and Ratnayake, 2013), India (Rege, 2016) and Vietnam (Anthony et al., 2015).

## Steel

The steel industry was responsible for 9% of global CO<sub>2</sub> emissions in 2006 (Allwood et al., 2011), and production is projected to approximately double by 2050 (IEA, 2008; Worldsteel, 2018). Müller et al. (2006) note that a lack of availability of raw material is unlikely to curb this consumption for at least another century, although the exhaustion of the most readily accessible reserves may lead to increased costs.

Reducing the environmental impact of steel in line with emissions targets cannot be achieved through production efficiencies alone (Allwood et al., 2010), and recycling rates are already close to an upper limit (Graedel et al., 2011). Demand for steel must therefore be cut through more efficient use. According to Allwood et al. (2012), 42% of all steel is used in building construction, of which 44% is reinforcement for concrete, which therefore represents a considerable opportunity for savings.

## Fibrous reinforcement materials

Embodied energy and carbon varies significantly between fibre materials, as shown in Table 2.1, reflecting differences in raw materials and production methods.

Both carbon and aramid fibres have a very high embodied carbon, each using polymer precursor materials derived from fossil fuels. For carbon, the most common is polyacrylonitrile (PAN), which makes up the majority of total embodied carbon and cost (Duflou et al., 2009; Mainka et al., 2013). This undergoes several high-temperature processes to create a fibre of high purity, which also consumes a significant amount of energy (Chawla, 1998). However, there may be potential to significantly reduce both the embodied carbon and the cost of carbon fibres by replacing PAN with lignin, a renewable waste product from paper production. Baker and Rials (2013) estimates cost savings of 75% compared to typical PAN-based fibres. However, at present the mechanical properties of lignin-based materials are far inferior (Fang et al., 2017).

The main raw material for glass fibres is silica sand, which has a low embodied carbon and high abundance. For use in concrete, zirconium dioxide is added to improve resistance to alkali corrosion (creating AR-glass fibres). The raw materials are heated and drawn in a continuous fibre production operation. According to an LCA by PwC (2016), this melting process contributes two thirds of the total embodied energy, which is significantly lower than that of carbon or aramid fibres.

The production process for basalt fibres is similar to that of glass, albeit with fewer required additives (Chawla, 1998). The only raw material is pure basalt. The value of embodied carbon provided by the CES, included in Table 2.1, is very low, seemingly

contradicting the similarities in production methodology with glass, and it is possible that this only accounts for raw material extraction. More realistically, Williams-Portal et al. (2014) suggest that basalt has an embodied energy around half that of AR-glass fibres, indicating that basalt might be the fibre material with lowest environmental impact.

Raw fibres are often combined with a matrix material to protect them from damage and aid load transfer through the yarn. Thermosetting resins are typically used due to their high stiffness, temperature resistance and ability to penetrate between fibres (Gudonis et al., 2013). Three examples are included in Table 2.1, each of which are derived from fossil fuels and have a high embodied carbon.

Recycling of fibre composites is problematic due to the need to separate the matrix, which often cannot be melted, from fibres, which are sensitive to damage. All approaches to recycling of fibre composite therefore result in a lower quality product than the virgin material (Pickering, 2006).

### **Low-carbon alternatives**

Several building materials offer potential for low-carbon construction. Clay bricks and tiles have a higher embodied carbon than most concretes (Jones and Hammond, 2019), since high temperatures are required in firing (Kumbhar et al., 2014). However, Venkatarama Reddy and Jagadish (2003) propose that stabilised earth blocks, made from compacted soil with a low proportion of cement, can provide an alternative to bricks with 60-70% energy savings. Swapping the cement for a fly ash or GGBS stabiliser further reduces the embodied carbon, or this can be omitted entirely in the case of rammed earth. Stone also has a low embodied carbon, which is usually dominated by transportation (Klemm and Wiggins, 2016).

Timber is often cited as a sustainable building material, however assessing its environmental impact is complex. Processes including planting, fertilising, felling, sawing, kiln-drying and transportation each require energy (Weight, 2011), but atmospheric carbon can also be sequestered within the timber itself. However, if the timber is sent to landfill at end-of-life, its eventual decomposition will re-release this stored carbon. On the other hand, the waste timber might be burned to produce power, displacing the use of a fossil fuel. Changes of land-use are another important factor; in a sustainably managed forest, a felled tree will be replaced with another, whilst in the case of deforestation, decomposition of roots and undergrowth will release significant additional CO<sub>2</sub> (Ostle et al., 2009). Weight (2011) estimates that timber can have an embodied carbon ranging from 7.84kgCO<sub>2</sub>e/kg, for a deforested tree, to -3.11kgCO<sub>2</sub>e/kg with sustainable forest management and incineration at end-of-life providing both heat and power.

At present, many natural and low-carbon materials are not understood well by the design community or affordable enough for widespread use. This may change in future if embodied carbon becomes a higher priority, but today concrete and steel remain dominant.

## 2.4 Low-carbon floors

This section compares common floor structures in terms of embodied carbon, before investigating how researchers and designers are attempting to create more efficient or sustainable alternatives.

### 2.4.1 Embodied carbon of typical modern buildings

Several studies have quantified the embodied carbon, or energy, in typical building structures. These are either based on real projects or, for direct comparison between options, hypothetical designs. This literature gives a benchmark of typical embodied carbon quantities, usually expressed per unit floor area.

De Wolf et al. (2016b) compiled a database of 200 completed building projects, and calculated the total associated cradle-to-gate CO<sub>2</sub>e in the structural materials. For the full structure, typical values ranged significantly, from 150-600kgCO<sub>2</sub>e/m<sup>2</sup>. This database has since been expanded to include over 500 projects (Massachusetts Institute of Technology, 2019). Buildings with a primarily steel structure had the highest average embodied carbon (371kgCO<sub>2</sub>e/m<sup>2</sup>), followed by concrete (361kgCO<sub>2</sub>e/m<sup>2</sup>), composite (355kgCO<sub>2</sub>e/m<sup>2</sup>), masonry (272kgCO<sub>2</sub>e/m<sup>2</sup>) and timber (244kgCO<sub>2</sub>e/m<sup>2</sup>). These figures do not account for variations in height and span, which could be correlated with material choice. The parameter with the greatest influence on embodied carbon is the average span, increasing from 235kgCO<sub>2</sub>e/m<sup>2</sup> at 0-4m, to 384kgCO<sub>2</sub>e/m<sup>2</sup> at 8-12m and 993kgCO<sub>2</sub>e/m<sup>2</sup> at 16-20m. The values at higher spans may be unreliable due to the low numbers of projects featured. Also, since these figures do not separate the structural elements, the proportion within the floors is unclear.

A more reliable comparison of floor designs is given by comparing hypothetical options for the same project. A detailed study of embodied carbon in the structure of a two-storey school building is given by Eleftheriadis et al. (2018). Many designs were generated using an automated design procedure, giving embodied carbon values of 108-127kgCO<sub>2</sub>e/m<sup>2</sup> for composite floors and 73-81kgCO<sub>2</sub>e/m<sup>2</sup> for pre-cast hollow-core designs. In either case, the values are significantly lower than the median values for real projects given by De Wolf et al. (2016b), partly since only the floor is considered, but also because the designs generated

conform precisely to code requirements with no spare capacity, which is almost always included in real projects (Orr, 2018). Moynihan and Allwood (2014) found that average utilisation ratios are below 50% in real structures due to a combination of rationalisation, conservatism and the desire for design flexibility.

Embodied energy, rather than carbon, is sometimes used as a means of comparison between alternative floor structures. Foraboschi et al. (2014) calculated that RC slabs contain 34-44% less embodied energy than equivalent composite floors, but that the use of void-formers in the slab (a system known as BubbleDeck) causes a significant (43-56%) increase. This is because the polyethylene void-formers contain a much higher embodied energy than the concrete they displace. In a case study of a Canadian three-storey office building, Cole and Kernan (1996) showed that a concrete structure contains 24% less embodied energy than a steel equivalent.

Griffin et al. (2010) compared the embodied energy of a range of floor structures for a four-storey building with spans of 4.9-10.9m. These included composite decks, RC flat slabs (with and without column heads), one-way slabs (with beams), ribbed slabs and waffle slabs. The flat slab was found to have a 42% lower energy than the composite floor. The alternative slab designs all had broadly similar values, and contained 17-22% less embodied energy than the flat slab. This indicates the magnitude of potential savings achieved with RC beams and ribs, compared to flat slabs. However, in Kaethner and Burrige (2012) the flat slab gave the lowest carbon of any concrete frame, including post-tensioned slabs and pre-cast single-spanning concrete slabs.

Miller et al. (2015) present two case-studies of concrete buildings in Australia. In the first, a typical office building is designed with both RC and post-tensioned (PT) slabs, demonstrating a reduction in embodied energy of 28-41% for the latter (contrasting with the findings of Kaethner and Burrige (2012)). Using concrete of a higher strength was also shown to increase the overall embodied energy, despite reductions in slab depth. The second case study, of a floor-plate only, indicated that column heads can reduce embodied energy by 8% in a flat slab, and that a one-way beam and slab arrangement has a similar embodied energy to an RC flat slab (without column heads).

A number of conclusions can be drawn from these studies. Reinforced concrete floors have a generally lower embodied energy and carbon than steel. Timber might present a more sustainable option, however fire safety concerns continue to limit its use in high-rise construction (Gerard et al., 2013). Of the common concrete floor types, flat slabs without column heads are the least materially efficient. The addition of beams and ribs can lead to a small increase in efficiency, however the benefits of post-tensioning are potentially greater.

Reducing material quantity through efficient structural design directly reduces costs, as well as environmental impact. However, construction methods are a major driver in structural decision-making because labour and speed are dominant cost considerations. As a result, most structural designers value construction simplicity over material efficiency (Orr, 2018), which also reduces the risk of costly errors on-site. Solutions for which the required construction equipment, skills and knowledge are already widespread are therefore strongly favoured.

### **2.4.2 Current research in efficient floor design**

This section explores recent projects which aim to create sustainable floors through structural optimisation, focusing primarily on concrete.

#### **Functionally graded concrete**

The non-uniform distribution of stress in concrete slabs was highlighted previously in Figure 1.2. One approach to optimising these structures is to vary the material properties spatially in response to local stresses, using functionally graded concrete.

Herrmann and Sobek (2017) describes two approaches to creating concrete beams and slabs with variable density. The first is through layered casting, where different concrete mixes are poured in discreet horizontal layers. The second, graded spraying, uses two nozzles with mixes of maximum and minimum density which, through automated control of the flow rates in each, can be blended to create a continuously variable density. Using the first method, Herrmann and Sobek (2017) created sandwich beams with a lightweight concrete interior. Compared to a regular beam of equivalent structural performance, weight savings of 34% and 43% were achieved using steel and carbon fibre reinforcement respectively. The minimum density of the middle layer was dictated by premature shear failure. Two-way spanning slabs with steel reinforcement and a similar layered construction were tested by Frenzel and Curbach (2017), demonstrating a 15% weight reduction compared to a solid slab.

Further savings can potentially be achieved by grading material in both horizontal and vertical directions, however careful design of concrete mixes and casting processes are required to prevent mixing prior to setting (Torelli and Lees, 2019).

These proposals demonstrate potential for material reduction whilst retaining the geometry of a flat slab, along with its simple formwork and architectural flexibility. However, using multiple mixes and automated placement are likely to present practical challenges for widespread use. The weight savings so far achieved are similar in magnitude to those of



post-tensioned slabs, pre-cast hollow-core units or ribbed/waffle slabs, all of which already have established production and design methodologies. This might indicate the limit of achievable savings using prismatic bending elements.

### Efficient concrete forms using flexible formwork

Flexible forming techniques have been used to create non-prismatic forms which reflect the force distributions within them.

Beams have so far been the primary focus of comparative studies using fabric formwork, and have also been demonstrated in full-scale projects (Morrow, 2018). Lee (2011) calculated embodied energy savings of 20-40% compared to traditional prismatic beams. Orr et al. (2011) presents a pre-cast T-beam with a 35% concrete reduction in the downstand portion (Figure 2.8a), however since a significant majority of the material exists within the top flanges, which remain prismatic, the overall saving of the floor system is smaller. Removing material from beams always reduces stiffness, and hence serviceability requirements potentially limit the potential savings of this approach (Tayfur et al., 2019).

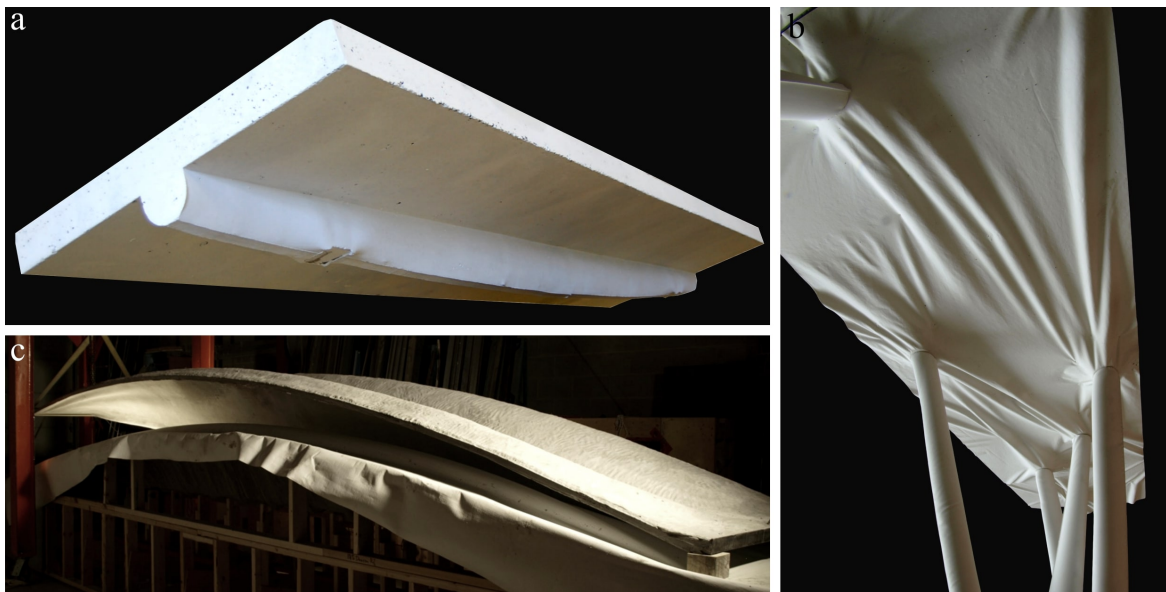


Figure 2.8: Examples of flexibly-formed concrete floor structures, including a) a T-beam with variable cross-section (image courtesy of John Orr), b) a floor slab with ribbed capitals and c) a pre-cast thin-shell flooring unit with stiffening rib (images courtesy of Mark West).

Some examples of thin-shell fabric-formed floor structures have been demonstrated by West and Araya (2012). Figure 2.8b shows model floor slab where the buckling of the fabric formwork has been utilised to create ribbed capitals, thus increasing the local strength and stiffness at the support points. In Figure 2.8c, a pre-cast single-spanning concrete shell unit is

formed using prestressed fabric with a large buckled mid-section. This leads to an increased effective section depth. Combined with glass-fibre textile reinforcement, which provides tensile strength and robustness, this is potentially an elegant means of producing efficient structural forms.

However, as noted previously, the complex behaviour of woven materials under prestress and loading from wet concrete potentially makes accurate geometry prediction challenging, and could create issues of repeatability. The range of available forms is also limited by the use of a tensile membrane, possibly leading to sub-optimal solutions.

### Advanced materials and manufacturing

A lightweight flooring system consisting of a single-spanning pre-cast shell with carbon reinforcement is described by May et al. (2018). This was constructed using rigid timber formwork. A low structural depth of 185mm was used over a span of 4.5m, approximately similar to that of a conventional slab albeit with a 70% weight reduction (or 50% with the required addition of a lightweight concrete fill). However, the high-strength concrete (approximately 90MPa) and large amounts of carbon fibre would come with a considerable embodied carbon cost, likely countering these weight savings. Since the structure is single-spanning, additional material would also be required for beams.

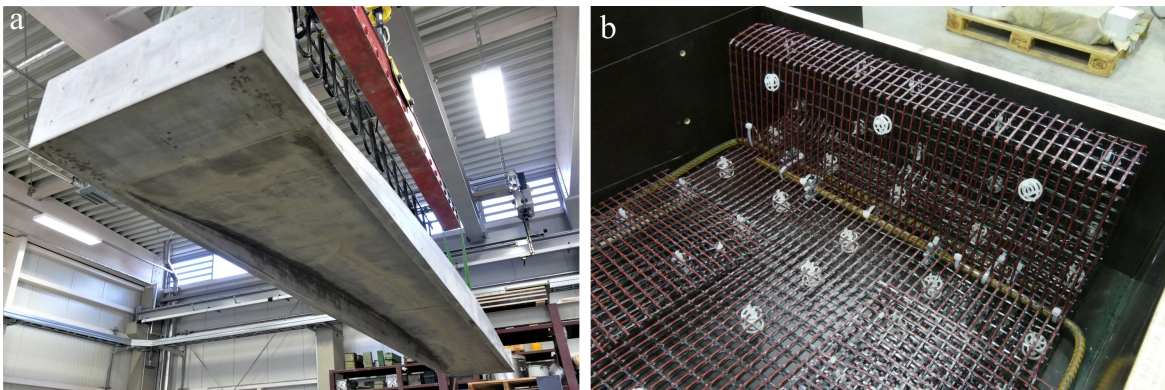


Figure 2.9: Thin-shell TRC flooring system described by May et al. (2018), showing a) shallow-vaulted design and b) extensive carbon fibre textile reinforcement (photos courtesy of Sebastian May).

Another approach to optimising a complete floor system is presented by Liew et al. (2017) and López et al. (2014), and shown in Figure 2.10. The design features a form-found vault with stiffening ribs projected from the top surface, which create a level floor-plane. The prototype has a span of 2.58-2.80m, and total depth of 160mm, whilst a full-scale system with average spans of 5.5m features in the Nest HiLo project (Block Research Group, 2019).

In the prototype, a thickness of 20mm for both the vault and ribs was chosen to limit the maximum tensile stress to 1.5MPa. The structure was cast as a single unit using steel fibre reinforced concrete, and the formwork consisted of a timber case with wire-cut expanded polystyrene (EPS) blocks with a latex coating. In the full-scale system, the upper foam pieces become permanent insulation (Lydon et al., 2017).

Liew et al. (2017) describe the structural testing of the prototype floor structure, which was supported rigidly at the corners and subject to symmetric (serviceability) and asymmetric (to failure) line-loads. The maximum deflection at the serviceability load was small (0.9mm). At failure, a single crack was visible (Figure 2.10) but the steel fibres created some ductility. In the full-scale structure, the rigid lateral supports are replaced with peripheral steel ties, and this will reduce the overall stiffness and strength.

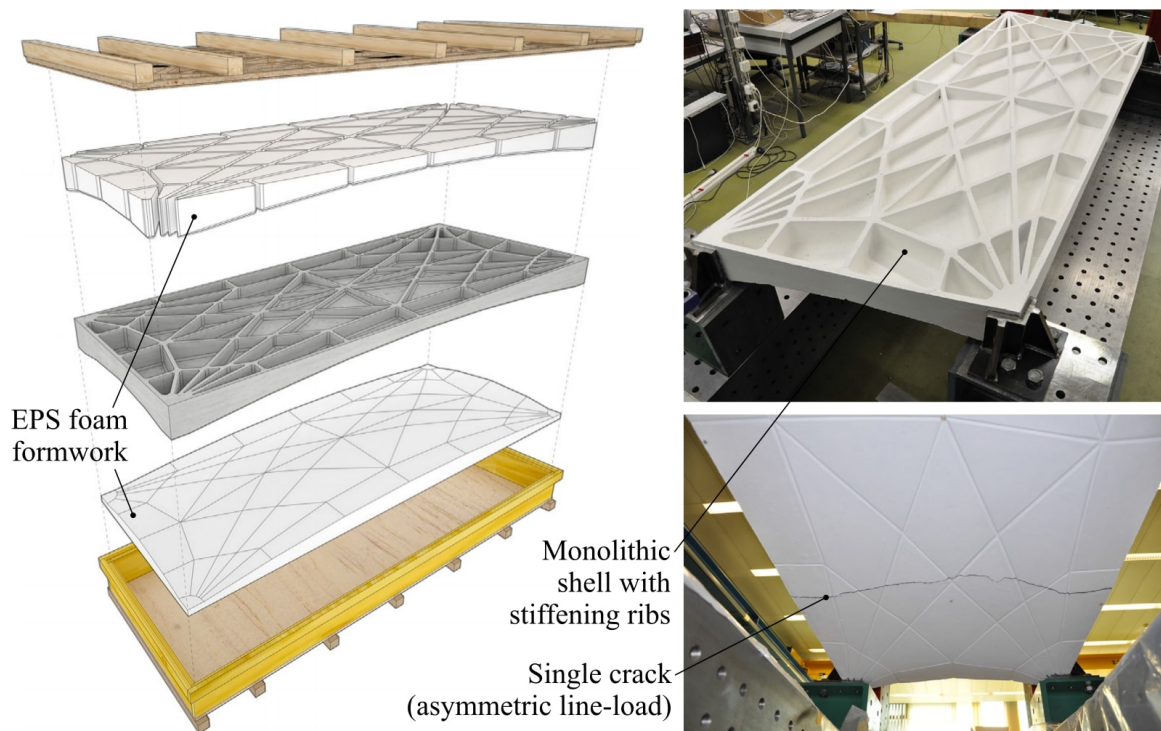


Figure 2.10: Vaulted, rib-stiffened, pre-cast, fibre-reinforced concrete floor structure developed at ETH Zürich (adapted with permission from Liew et al. (2017)).

An environmental analysis of this project was undertaken by Agustí-Juan and Habert (2017). Despite the high embodied carbon of the fibre-reinforced concrete, a value of approximately  $47\text{kgCO}_2\text{e/m}^2$  was calculated for the prototype structure. Whilst this compares favourably with the typical floors presented in the Section 2.4.1, the average span of 2.69m is very small. It is therefore likely that the full-scale structure will have a considerably higher embodied carbon, although the relationship between thickness and span is not discussed in

published literature. The analysis also neglects the EPS foam used in the formwork, which has a high embodied carbon of  $3.29\text{kgCO}_2\text{e/kg}$  (Jones and Hammond, 2019). Assuming a 160mm deep block of EPS with a density of  $30\text{kg/m}^3$ , this would add  $15.8\text{kgCO}_2\text{e/m}^2$  to the total.

The mass of the prototype is very low, at  $119\text{kg/m}^2$  (López et al., 2014). This reflects the high efficiency of the structure, but may have a detrimental impact on the vibration and acoustic performance. The advanced methods required for the design, analysis and construction of the element are also possible barriers to its widespread adoption in the wider construction industry. 3D printed formwork has also been used to create similar vaulted floor slabs of fibre-reinforced concrete (Jipa et al., 2016; Meibodi et al., 2017).

### Tile vaults

It is also possible to create efficient structures without relying on digital fabrication, by looking to past construction methods.

In recent years, tile-vaults have received considerable research interest from both engineers and architects, inspired by the traditional Catalan vaulting techniques discussed previously in Section 2.1.2, but utilising digital form-finding techniques. Whilst the majority of recent projects feature doubly curved roofs with medium to long spans, such as the Mapungubwe National Park Interpretive Centre (Ramage et al., 2010) and Rwanda Cricket Stadium (Ramage et al., 2019), some examples of floor structures have also been constructed.



Figure 2.11: Tile barrel vaulted floor with stiffening ribs (photo Lara Davis, with permission).

Block et al. (2010) describes the construction of a tile barrel-vault for the Sustainable Urban Dwelling Unit (SUDU) project in Ethiopia, shown in Figure 2.11. This structure consists of a singly curved vault of 5.8m span, 500mm depth and 100mm thickness. The catenary profile was determined from a hanging chain, and is therefore funicular under self-weight. The first layer of tiles were placed with quick-setting plaster of Paris, whilst subsequent layers used a stronger cementitious mortar. This eliminated the need for falsework, with only guides required. Slender stiffening ribs were included to provide a load path for asymmetric loads and a semi-rigid fill consisting of lime and pumice was cast above the vault. As well as creating a usable floor surface, this has four structural functions: to provide lateral support to the stiffening ribs, to stiffen the vault under asymmetric loading, to spread concentrated point loads and to increase the dead load (thus reducing the relative influence of asymmetric live loads). Other practical benefits of the fill include increased thermal mass and insulation, acoustic absorption and vibration damping. Steel ties were provided to counter the thrust, and tensioned using turn-buckles.

This structure successfully minimises the use of steel, cement and fired clay by primarily using tiles made from stabilised earth (with 8% cement content) or local stone, and would therefore be expected to have a low embodied carbon. De Wolf et al. (2016a) calculated the embodied carbon of three projects also featuring stabilised earth as a primary structural material, and demonstrated significant savings compared to reinforced concrete buildings.

However, a number of disadvantages potentially limit widespread adoption of this technique. Being labour-intensive, the cost is likely to be high in many parts of the world. The construction time also scales with floor area, making economical application on large-scale projects unlikely. Considerable understanding and experience are required to construct tile-vaults safely, due to the potential instability of incomplete vaults. Whilst stabilised-earth is a proven low carbon construction material, significant experimentation and testing is required to achieve the right structural characteristics due to a high sensitivity to soil properties. It is also not as durable or water-resistant as fired clay (Bahar et al., 2004). Finally, unreinforced masonry vaults can be susceptible to catastrophic failure under seismic loading, particularly if singly-curved, due to the formation of hinges induced by bending. This can, however, be overcome by using reinforcement such as a geotextile between tile layers (Ramage et al., 2019).

## 2.5 Summary, findings and conclusions

This chapter began by giving a historical overview of curved compression structures including arches, shells and vaults, highlighting key innovations and successful floor systems. The current state-of-the-art in concrete shells, including design methods, construction technologies and materials, was then explored. Consideration was then given to the environmental impact and assessment of buildings, construction materials and common floor structures. Finally, examples of structurally efficient floor systems in current research were examined.

Key findings from the literature review are given below:

- There is considerable historical precedent for strong, durable and low-carbon structures utilising curved geometries.
- The analysis and construction complexities which led to the decline of concrete shells in the late 20<sup>th</sup> century are today being overcome through advances in design, manufacture and materials.
- Structural engineers have an essential role to play in the transition to a low-carbon society, particularly as worldwide construction activity accelerates. It is therefore imperative that these new opportunities are harnessed to this aim.
- Floors represent an important opportunity for material savings, and many common systems are structurally inefficient, causing unnecessary environmental damage.
- Reductions in material use have been recently demonstrated by several innovative floor structures, with shells offering particularly large weight savings over bending structures. However, existing approaches either rely on high-carbon materials, use complex design and fabrication methods, or have practical barriers to economic application at large scales.

### Conclusions: Chapter 2

There exists a gap in the research for a floor system which is not only structurally efficient, but can also be constructed using materials with a low environmental impact, is compatible with an economical construction process and can be designed using a reliable, simple and repeatable methodology.

# Chapter 3

## Development and feasibility of a thin-shell flooring system

### 3.1 Introduction

This chapter describes the proposed flooring system, including construction processes, materials and the layout of structural components. The process of evaluating behaviour and feasibility is begun with simplified hand calculations. A computational investigation is then carried out to provide a more detailed assessment of structural behaviour and investigate the influence of shell geometry on performance. A range of options are explored, with each requiring a different formwork approach. As well as refining the design space, the results highlight key questions to be addressed in later investigations.

### 3.2 Proposed structural system

#### 3.2.1 Shell and reinforcement

In the proposed system, pre-cast concrete shells span between columns to create a vaulted ceiling, as shown in Figure 3.1. A shell without stiffeners simplifies manufacture, enabling the use of single-sided formwork. Services can also be integrated within the structural depth without obstruction, both above and below the shell. This frees up vertical space to maximise the total depth, thus minimising thrust.

Although the shell is designed to act primarily in compression, reinforcement is required to increase tensile capacity and provide robustness in the event of accidental loading. A TRC shell is therefore proposed. The flexibility of textile reinforcement facilitates curved geometries, and the low cover leads to a thin and efficient shell section.

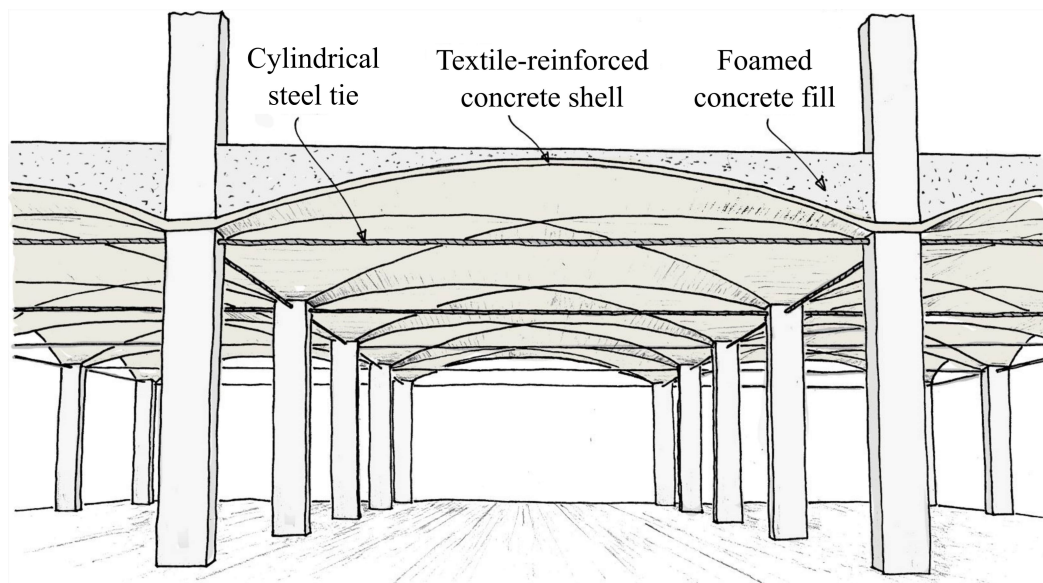


Figure 3.1: Proposed flooring system.

### 3.2.2 Columns and ties

Shallow vaults generate considerable lateral thrust when operating under membrane action. This can be balanced by neighbouring spans at interior columns, however, at the perimeter, an imbalance of force must be addressed. Various options for this are shown in Figure 3.2.

Historic masonry vaults often relied on external buttresses to provide lateral support. This may be feasible in some scenarios, but is likely to require significant space and material for multi-storey buildings, since the maximum moment scales with the number of storeys squared. Replacing the edge spans with a laterally stiff slabs could also provide the necessary restraint, although these might make up the majority of the floor area in all but the largest buildings. Exterior cable structures could also be used, either in a vertical or horizontal plane, although again these require additional space. The forces in the cables will also be very large if the change of angle (on plan) at each column is small.

The chosen option is a network of ties spanning between columns at each level. In this case, the support structure lies within the building envelope, reducing exposure to corrosion but requiring protection in the event of fire. The lateral stiffness is maximised by directly aligning the compressive and tensile forces. This also means that each column experiences no overall bending force. In practice, the tie height could be adjusted vertically from this location if required, at the expense of bending forces in the columns. For example, the ties might be located just above the vault, hiding them from view and mitigating the need for fire protection.



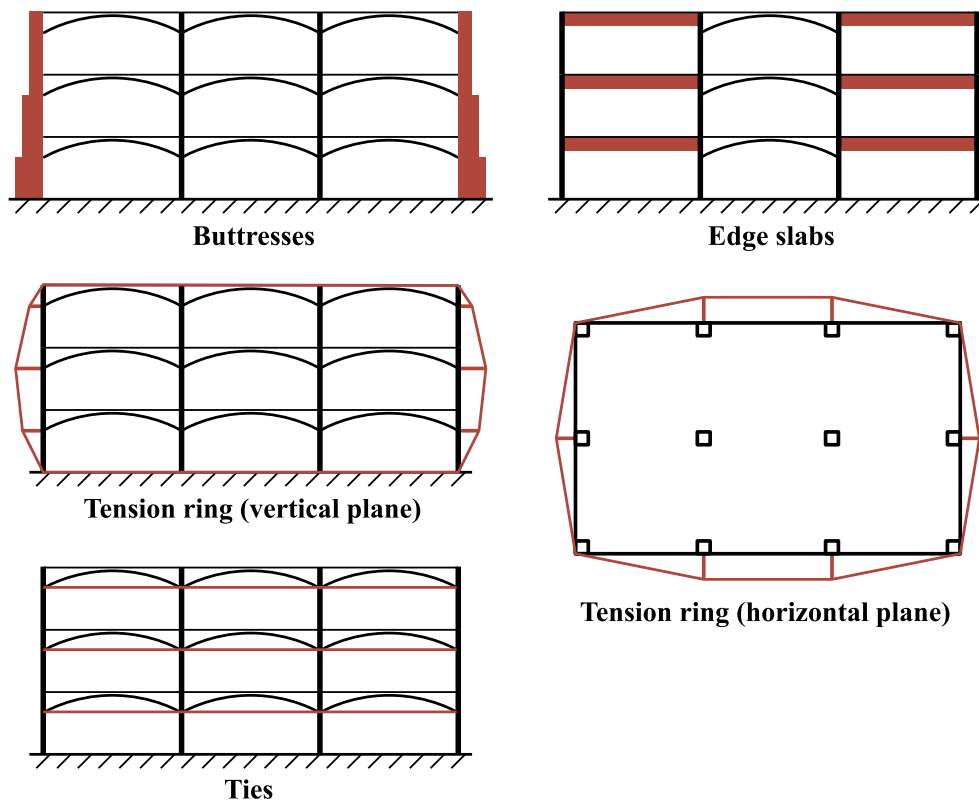


Figure 3.2: Structural options for lateral thrust restraint.

### 3.2.3 Floor levelling

The assumed structural requirement of the fill is only to transfer floor loads to the shell. It might therefore be possible to use an aggregate material such as rubble, however in this instance low density foamed concrete is proposed to minimise weight. This can also be cast quickly in large volumes, is self-levelling and provides thermal and acoustic insulation (Jones and McCarthy, 2005; Zhang et al., 2015).

### 3.2.4 Construction

The pre-cast TRC shells would be used in combination with pre-cast columns and walls for rapid assembly. The proposed construction sequence for each storey is as follows:

1. Ties fixed to columns.
2. Shells located on columns.
3. Columns for floor above positioned.

4. Foamed concrete cast in-situ and levelled.
5. Tie pre-strain applied, using turn-buckles or threaded column connections.

The tie pre-strain is applied after casting of the fill, since the additional dead-load is advantageous (limiting maximum uplift experienced by the shell). Casting the shells in units the size of a full column bay would likely make them too large to be transported by road. The proposal is therefore to manufacture these on-site. The shells could be produced during substructure construction and stored efficiently through stacking ready for fast superstructure assembly. This would allow re-use of formwork, and storage would enable hardening and shrinkage of the concrete to take place prior to assembly and loading. This method does, however, require space on site for manufacturing and storage.

### 3.3 Basic behaviour

This section uses a simplified model to explore the basic structural behaviour of the proposed system. Figure 3.3 shows a simple groin vault with four parabolic segments of uniform thickness  $t$ , spanning a distance  $l$  in each direction and with a mid-span height  $h$ . Flat, square sections in each corner sit directly on the columns below, sharing the space with neighbouring shells where necessary.

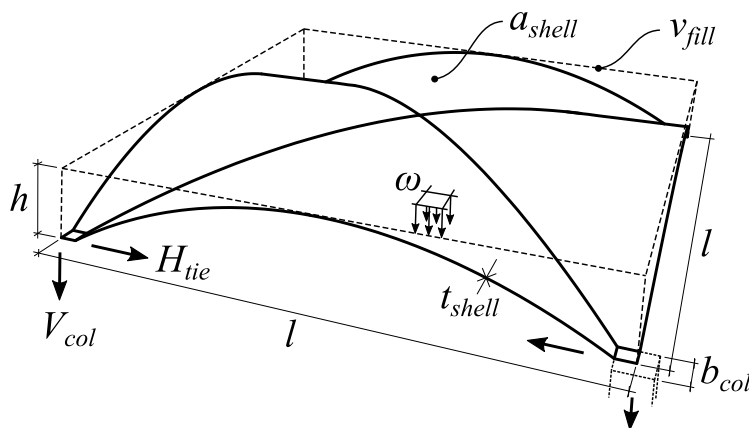


Figure 3.3: Simplified model for initial investigation into structural behaviour, assuming a groin vault with parabolic segments acting in pure compression.

The shell area ( $a_{shell}$ ) and fill volume ( $v_{fill}$ ) are given in Equations 3.1 and 3.2 respectively, assuming small corner support areas. This allows the average self-weight to be calculated from unit weights of the shell ( $\gamma_{shell}$ ) and fill ( $\gamma_{fill}$ ). Although the fill depth is variable, the

self-weight is assumed uniform over the floor surface as a simplification. The total load ( $\omega$ , Equation 3.3) is the self-weight plus the applied load ( $\omega_{floor}$ ).

$$a_{shell} = \left( \frac{l^2}{3} - \frac{l^4}{24h^2} \right) \left( \frac{16h^2}{l^2} + 1 \right)^{\frac{1}{2}} + \frac{l^3}{4h} \sinh^{-1} \left( \frac{4h}{l} \right) + \frac{l^4}{24h^2} \quad (3.1)$$

$$v_{fill} = \frac{hl^2}{6} \quad (3.2)$$

$$\omega = \frac{\gamma_{fill}v_{fill} + \gamma_{shell}a_{shell}t_{shell}}{l^2} + \omega_{floor} \quad (3.3)$$

The vertical column force  $V_{col}$  is simply the total load divided amongst the four corners. The horizontal thrust  $H_{tie}$  is calculated according to Equation 3.4 by isolating one quarter of the shell and taking moments about the apex. This model assumes that the shell acts in pure compression.

This analysis allows preliminary sizing of a cylindrical tie, with diameter  $d_{tie}$  and stiffness  $E_{tie}$ , and estimation of maximum tie extension ( $\delta_{tie}$ ) from Equation 3.5.

$$H_{tie} = \frac{\omega l^3}{16h} \quad (3.4)$$

$$\delta_{tie} = \frac{4H_{tie}l}{\pi d_{tie}^2 E_{tie}} \quad (3.5)$$

The tie force is inversely proportional to the height, and might therefore be very large for shallow vaults, based on this model.

### 3.3.1 Preliminary case study

A case study was carried out, using this model, to estimate tie sizes, concrete stresses and deformations.

#### Loads

The assumed floor loads include a superimposed dead load (SDL) of 1.0kN/m<sup>2</sup> for finishes and services, with a 3.5kN/m<sup>2</sup> live load accounting for typical office use in the UK (2.5kN/m<sup>2</sup>) plus partitions (1.0kN/m<sup>2</sup>) (BSI, 2002a). These were combined without factors and applied uniformly over the floor area. Unit weights of  $\gamma_{shell} = 24\text{kN/m}^3$  and  $\gamma_{fill} = 8\text{kN/m}^3$  were assumed in the estimation of self-weight.

### Dimensions and materials

The chosen span was  $l = 8\text{m}$ , a moderate value for a commercial building. An efficiently designed flat slab would be 300mm deep for these loads, based on deflection requirements at end-spans (Goodchild, 2009). Approximately 500mm would be required beneath a flat slab's soffit for services, deflections and tolerances, giving a total height of 800mm. It is proposed that these could be integrated within the depth of a groin vault, thus a height of  $h = 800\text{mm}$  is assumed. This gives a span to height ratio of 10:1, which is similar to that of historical tile vaulted systems of 12:1 (Bannister, 1968) and 10:1 (Guastavino, 1892), more recent tile vaults of 11.6:1 (Block et al., 2010) and the Kelling-Decke concrete floor system of 13:1 (Ahnert et al., 1987). It should be noted that the total height of the system would be larger than this due to the thickness of the shell, the ties beneath and the minimum depth of the fill at the apex. The assumed shell thickness is  $t_{shell} = 60\text{mm}$ , matching the TRC section used in the construction of a TRC pavilion as described by Scholzen et al. (2015a), and shown previously in Figure 2.7a.

### Results

The total self-weight of the shell and fill is  $2.53\text{kN/m}^2$ . This is 65% less than that of an equivalent 300mm flat slab ( $7.20\text{kN/m}^2$  for  $\gamma = 24\text{kN/m}^3$ ). The total floor load is  $\omega = 7.03\text{kN/m}^2$ , corresponding to a tie force of  $H_{tie} = 281\text{kN}$ . Where a single tie is used for two neighbouring shells at the floor's edge, this force doubles to 562kN. A tie of  $d_{tie} = 50\text{mm}$  therefore gives has corresponding stress of 286MPa, which is viable for high-strength steel under serviceability loading. The tie extension is  $\delta_{tie} = 10.9\text{mm}$  for  $E_{tie} = 210\text{GPa}$ .

Spreading of the supports causes the apex of the parabolic vault to drop in height, if a constant arc length is assumed (ignoring axial shortening of the shell). This allows an estimate of the corresponding vertical displacement to be calculated as shown in Figure 3.4.

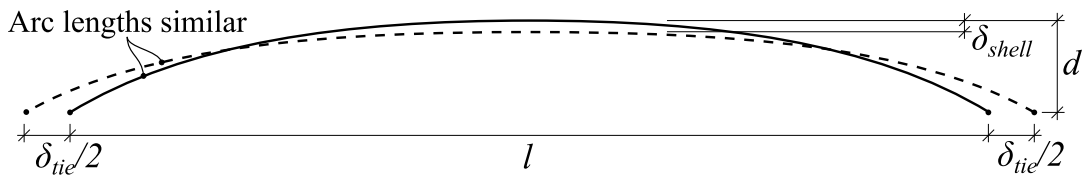


Figure 3.4: Simplified method for calculating maximum vertical displacement ( $\delta_{shell}$ ) from the tie extension ( $\delta_{tie}$ ) by assuming equal parabolic arc lengths.

For the geometry of this investigation, the resulting vertical displacement is  $\delta_{shell} = 21.1\text{mm}$ . This is almost twice the tie extension, highlighting the sensitivity of shallow vaults to lateral support stiffness. The true deflection will be larger once deformation of the shell

itself is also taken into account. It is therefore proposed to prestress the ties to limit the total deflection by creating an initial uplift, effectively pre-cambering the structure. This also reduces the maximum of deformation experienced by the shell, potentially minimising bending forces.

The vertical column reaction at each corner is  $V_{col} = 112\text{kN}$ . The maximum compressive stress in the shell ( $\sigma_{shell,max}$ ) estimated by dividing the vector sum of the horizontal and vertical reactions by the shell area at the column interface, as in Equation 3.6.

$$\sigma_{shell,max} = \frac{(V_{col}^2 + (2H_{tie})^2)^{\frac{1}{2}}}{b_{col}t_{shell}} \quad (3.6)$$

Assuming a column width of  $b_{col} = 500\text{mm}$ , the serviceability concrete stress is  $19.1\text{MPa}$ . This is approximately acceptable for concrete with a cylinder strength of  $f_{ck} = 40\text{MPa}$ , suggesting that  $60\text{mm}$  might be a realistic thickness in this scenario. However, additional stresses from bending forces are as yet unknown.

## Conclusions

Although simplistic in its approach, this preliminary investigation has highlighted several important structural aspects:

- Lateral movement of the supports, caused by large horizontal thrust, creates considerable vertical displacement at mid-span. The stiffness of the horizontal support structure is therefore critical, and deflections can be minimised through prestressing the ties.
- Concentration of compressive stresses at the column interface do not necessarily preclude the use of low shell thicknesses.
- The self-weight is significantly smaller than an equivalent flat slab.

## 3.4 Computational analysis methodology

A more detailed investigation was undertaken using an FE analysis. This was used to evaluate and compare the structural performance of possible shell geometries in order to narrow the design space. The balance of axial, bending and tensile forces within the shell can also be determined in this way, informing the design of a materially efficient TRC section.

The same floor dimensions as in Section 3.3.1 were adopted:  $l = 8\text{m}$ ,  $h = 800\text{mm}$ ,  $t_{shell} = 60\text{mm}$  and  $d_{tie} = 50\text{mm}$ . The strength and stiffness properties of the TRC shell match the

60mm section described by Scholzen et al. (2015a), chosen due to the availability of data and proven application in a real-world project (Figure 2.7a).

### 3.4.1 Finite element modelling

Linear FE analysis was carried out using the software Karamba (Preisinger, 2013), which is integrated with the Grasshopper parametric modelling environment for Rhino. The Young's moduli were 30.4GPa (with a Poisson's ratio of 0.2) for the shell material and 210GPa for the steel ties. Loads were applied directly to the shell, conservatively ignoring the foamed concrete fill.

The shell was meshed into regular triangular plate elements adhering to Kirchoff-Love plate theory, with out-of-plane shear deformations ignored (Love, 1888). Elements were grouped in fours into approximate squares, a mirror of the form-finding methodology described in Section 3.5.5. The behaviour of this element pattern was verified in a simple cantilever test, and confirmed a rapid convergence with beam-theory predictions as the element density was increased.

A shell spanning a single bay was modelled, and assumed to be structurally isolated from its neighbours. In each corner, the nodes at the shell-column interface could move rigidly together to simulate a stiff column. These groups of nodes were fixed vertically but free to slide horizontally, thus conservatively ignoring the lateral stiffness of columns. However, the column-heads were rotationally fixed about both horizontal axes, since this was found to conservatively maximise corner bending moments.

### 3.4.2 Mesh density investigation

A preliminary study was carried out to explore the influence of mesh density. In this investigation, three maximum element edge lengths were chosen: 250mm, 125mm and 62.5mm corresponding to 4080, 16320 and 65280 total elements respectively. For this study, the parabolic groin vault geometry (Figure 3.3) was analysed under a uniform load without tie prestress.

Variations in average compressive stress and mid-span displacement were small between the three meshes; less than 1.5% and 1.2% respectively. However, the peak stress was mesh-dependent. This occurs at the re-entrant corner of the shell-column interface, as shown in Figure 3.5. Refinement of the mesh does not indicate convergence, and such a stress singularity might be expected at a re-entrant corner (Williams, 1952). A large vertical reaction force is also present at this node. In a real structure, non-rigid supports and softening of the concrete would act to redistribute this peak stress.

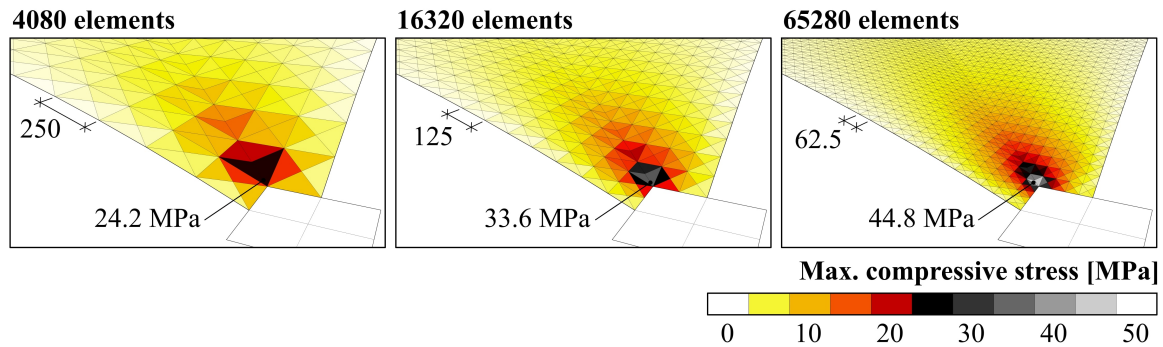


Figure 3.5: Comparison of maximum principal compressive stress at the corner support with increasing mesh density.

The subsequent investigations of this chapter feature the intermediate mesh size (125mm), chosen to balance accuracy and detail with computation speed, and it is noted that peak corner stresses are not representative of true behaviour.

### 3.4.3 Loads

The various loads carried by the shell were modelled differently depending on their origin and spatial distribution.

The self-weight of the shell was assumed to act in the direction of gravity, with the load on each node proportional to the area of surrounding elements, the shell thickness, and specific weight of  $24\text{kN/m}^3$ . The dead load from the fill also acted vertically, and was proportional to the local depth below the fill surface (level with the top of the shell). The assumed specific weight of the foamed concrete was  $8\text{kN/m}^3$ . Typical imposed loads for a UK office were assumed, as described previously in Section 3.3.1. These were applied to each node in proportion to the area projected onto the horizontal (floor) plane.

The loads were variously combined for ultimate (ULS) or serviceability (SLS) limit states according to Eurocode 1 (BSI, 2002a). Load factors are summarised in Table 3.1. ULS is split into unfavourable (maximum) and favourable (minimum) combinations. These were used alongside in the case of pattern loadings, where asymmetry might be expected to increase bending in the shell.

#### Live load patterns

Live loads can, in principle, be distributed in any arrangement. Each part of the structure should therefore be designed for the worst-case scenario. For slabs, critical patterns often feature maximum and minimum loadings on alternate bays, in order to maximise hogging or

Table 3.1: Factors used for combination of dead and live loads.

	Dead	Live
SLS (characteristic)	1.00	1.00
ULS (unfavourable)	1.35	1.50
ULS (favourable)	1.00	0.00

sagging in a specific region. However, the critical patterns are not immediately obvious for a curved shell surface.

The comprehensive way to determine critical loading arrangements is to construct influence surfaces for each region of the structure, analysing in-turn the effect of a point load applied at every location and thus requiring significant computational effort (Clarke and Cope, 1984). However, Timoshenko and Woinowsky-Krieger (1959) note the similarities between influence surfaces and natural vibration modes for irregular plates. This approach was therefore adopted to determine the load patterns used in this investigation. The first few natural vibration modes of each candidate shell geometry were calculated, revealing common patterns of deformation. The resulting load patterns are illustrated in Figure 3.6. Patterns 2-6 are rotationally symmetric and cover one half of the floor area. In addition, both the minimum (Pattern 1) and maximum (Pattern 7) uniform loads were applied, since these result in extremes of lateral extension of the ties.

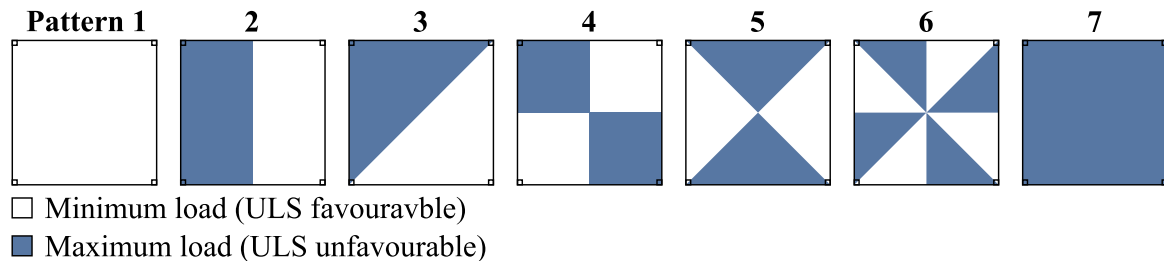


Figure 3.6: Live load patterns analysed for ULS strength analysis of the shell geometries, based on natural free vibration modes.

The same loading patterns were used for all shell geometries. In the case of strength design (discussed in Section 3.4.5), an envelope of the highest local utilisation factors was constructed from each pattern and all symmetrical permutations.

### 3.4.4 Tie pre-strain

Tie extension has a significant impact on the overall deformation of the shell, as shown previously in Section 3.3.1. It is therefore proposed to prestress the ties during construction



in order to limit total deflections and flexure of the shell. The amount of prestress was quantified through an initial pre-strain ( $\epsilon_{tie}$ ), in units of mm/m.

Extremes of lateral movement occur under maximum and minimum total applied loading (Patterns 1 and 7 in Figure 3.6). The proposed strategy was therefore to set the amount of pre-strain such that there is zero tie extension at a uniform load mid-way between the two extremes (factors of 1.175 and 0.750 for dead and live loads respectively). This means that the maximum uplift and settlement are approximately balanced. The amount of pre-strain is unique to each shell geometry.

### 3.4.5 Textile reinforced concrete strength calculation

A strength design methodology for TRC proposed by Scholzen et al. (2015b) was adopted for this investigation. The local utilisation ( $\eta$ ) is expressed as the sum of the ratios of the applied axial ( $n_{Ed}$ ) and bending ( $m_{Ed}$ ) forces and the corresponding design resistances. This effectively creates a bi-linear failure envelope in  $n - m$  space, linearly interpolated between three strengths in pure compression ( $n_{c,Rd}$ ), tension ( $n_{t,Rd}$ ) and bending ( $m_{Rd}$ ).

$$\eta = \max \left( \frac{n_{Ed}}{n_{c,Rd}}, \frac{n_{Ed}}{n_{t,Rd}} \right) + \frac{|m_{Ed}|}{m_{Rd}} \leq 1.0 \quad (3.7)$$

Hegger et al. (2006b) demonstrated that the tensile strength of textile reinforcement is reduced due to stress concentrations arising in the outer filaments when the reinforcement bridges inclined cracks. This introduces an additional step into the design process for shells where internal forces are not always aligned with reinforcement. Further uncertainty is also added, since the true orientation of the forces in a shell can only be known approximately. The corresponding crack-orientation reduction factor  $k_\alpha$ , as given by Scholzen et al. (2015b) for an angle of  $\alpha$  relative to the reinforcement, is as follows:

$$k_\alpha = 1 - \frac{|\alpha|}{90^\circ} \quad \text{for } 0^\circ \leq \alpha < 90^\circ \quad (3.8)$$

The direction-dependent strengths are then the sum of contributions from both the  $0^\circ$  and  $90^\circ$  reinforcement directions.

$$n_{t,Rd} = n_{t,Rd,0^\circ} \cos(\alpha) k_\alpha + n_{t,Rd,90^\circ} \sin(\alpha) (1 - k_\alpha) \quad (3.9)$$

$$m_{Rd} = m_{Rd,0^\circ} \cos(\alpha) k_\alpha + m_{Rd,90^\circ} \sin(\alpha) (1 - k_\alpha) \quad (3.10)$$

The forces in the shell are expressed by a pair of principal in-plane axial forces ( $n_1, n_2$ ), a pair of principal bending moments ( $m_1, m_2$ ), and the angles of each pair relative to the

reinforcement ( $\alpha_n, \alpha_m$ ), as shown in Figure 3.7. In this case, local  $x$  and  $y$  axes are assumed orientated with the reinforcement in the  $0^\circ$  and  $90^\circ$  directions respectively (as well as the column grid of the floor-plan).

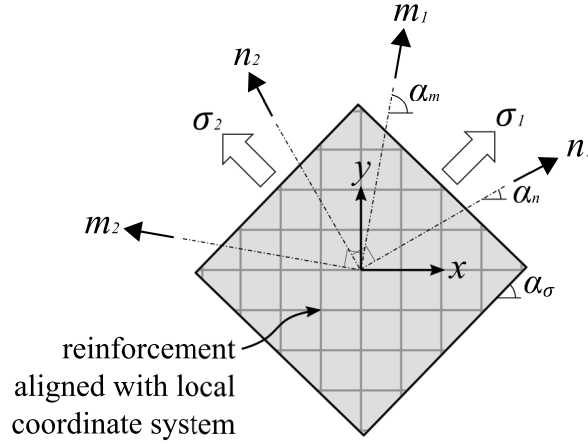


Figure 3.7: Principal axial forces, bending moments and stresses acting on a shell element

The critical direction of loading was assumed to be that of principal tensile or compressive stress at the top or bottom face of the shell. This is because if the reinforcement fails in tension, the crack direction is governed by the principal tensile stress. Similarly, if the concrete fails in compression, it does so in the direction of the largest principal compressive stress.

For a shell of thickness  $t$ , the stress at the top or bottom face is given by Equation 3.11.

$$\sigma(\alpha) = \frac{1}{t} \left( \frac{n_1 + n_2}{2} + \frac{n_1 - n_2}{2} \cos(2\alpha - 2\alpha_n) \right) \pm \frac{6}{t^2} \left( \frac{m_1 + m_2}{2} + \frac{m_1 - m_2}{2} \cos(2\alpha - 2\alpha_m) \right) \quad (3.11)$$

By setting the derivative of this equation with respect to  $\alpha$  to zero, an expression for the principal stress angles  $\alpha_\sigma$  can be obtained:

$$\alpha_\sigma = \frac{1}{2} \tan^{-1} \left( \frac{\frac{n_1 - n_2}{d} \sin 2\alpha_n \pm \frac{6(m_1 - m_2)}{d^2} \sin 2\alpha_m}{\frac{n_1 - n_2}{d} \cos 2\alpha_n \pm \frac{6(m_1 - m_2)}{d^2} \cos 2\alpha_m} \right) \quad (3.12)$$

This is then substituted ( $\alpha = \alpha_\sigma$ ) into Equations 3.8, 3.9 and 3.10 to find the local bending and tensile strengths. In this investigation, basic strength values of  $n_{c,Rd} = 2200\text{kN/m}$ ,  $n_{t,Rd,0^\circ} = n_{t,Rd,90^\circ} = 539\text{kN/m}$  and  $m_{Rd,0^\circ} = m_{Rd,90^\circ} = 8.3\text{kNm/m}$  were assumed, which correspond to the 60mm thick carbon-fibre reinforced section described in Scholzen et al.

(2015b). These are experimentally determined characteristic values, and include partial material factors of 1.5.

## 3.5 Shell geometry definitions

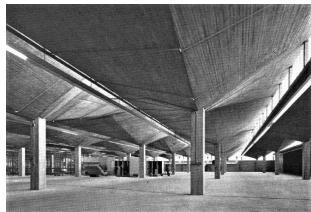
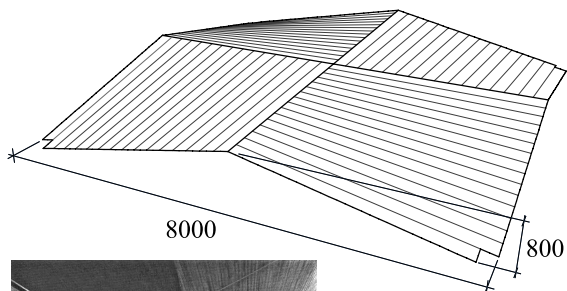
This section introduces a variety of candidate shell forms and the methodologies used to define them. In most instances, these are proposed with a simple formwork strategy in mind. However, the performance of free-form shells is also assessed, although these would require a computer-controlled process to form.

### 3.5.1 Hyperbolic paraboloids

Two hypar shells are considered in this investigation, both of which feature four adjacent hypar surfaces with curvature discontinuities, or creases, at their intersections. The first (Geometry 1) features square hypars on-plan, whilst those of the second (Geometry 2) are triangular, as illustrated in Figure 3.8. Both are similar to several of Felix Candela's projects, examples of which are also shown.

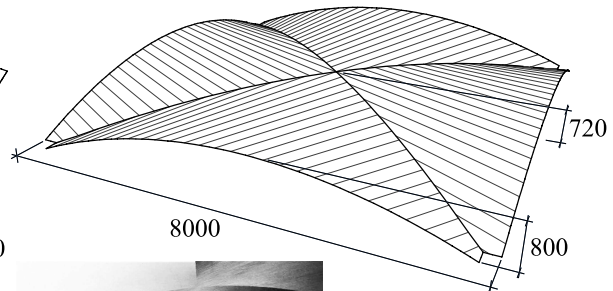
The surface of Geometry 2 is lower at the mid-span than at the edge, and this offset is a variable parameter which describes a family of similar geometries. A small dip of 10% (80mm) was chosen in this case, to avoid an excessive fill volume.

**Geometry 1: Hypar quadrants**



**Felix Candela**  
Warehouse  
1963  
Stevenage, UK

**Geometry 2: Hypar segments**



**Felix Candela**  
Bottling plant  
1961  
Mexico City

Figure 3.8: Shell geometries constructed from hypar surfaces, and similar structures designed by Felix Candela including the John Lewis warehouse (photo Chris James, license: CC BY-SA 2.0) and Bacardi bottling plant (photo HAKEBRY1, license: CC BY-SA 4.0).

### 3.5.2 Parabolic groin vault

Bringing the mid-span of Geometry 2 level with the edge creates a parabolic groin vault with single curvature (Geometry 3). The surface is again constructed from straight lines, but is also developable from a flat sheet in this case, potentially simplifying formwork construction. Two further groin vaults were also tested, as described in the following sections.

### 3.5.3 2D form-found groin vault

The concept of funicularity is central in the analysis and design of masonry structures, whereby a line (or surface) of pure compression must lie within the structure to ensure stability. A shell's thickness allows multiple loading arrangements to be carried in this way. In principle, a shell geometry matching the funicular form of a dominant load pattern will therefore reduce bending.

As noted in Section 3.3, a parabola is the 2D funicular form matching a uniformly distributed load. However, the groin vault is a more complex 3D structure than a simple arch, and also carries the non-uniform self-weight of itself and the fill.

A paper by the author describes a computational form finding method which uses a stepping procedure adapted from Foster (2010) in order to find a 2D funicular shape under hydrostatic loading (Hawkins et al., 2016b). This same technique was adapted to find funicular curves under arbitrary loads.

Starting from the apex, the algorithm advances along the curve in equal length segments, calculating the curvature at each node which satisfies horizontal and vertical equilibrium. An iterative procedure is used to determine the both initial value of compressive force and total curve length which are required to meet the boundary conditions.

The methodology was tested against three analytical solutions; pure self-weight (catenary), floor load (parabolic) and uniform pressure (circular). In each case, the correct profile was obtained, confirming the reliability of the method. The segment size was set to give an accuracy within 0.01mm.

The resulting form-found curve is shown in Figure 3.9, labelled as Geometry 4, and was form-found under a SLS (characteristic) loading combination. Compared to a parabola, the curvature is greater nearer the support and smaller at the apex. This is largely a result of the non-uniform self-weight of the fill, and has the effect of slightly reducing the total fill volume.

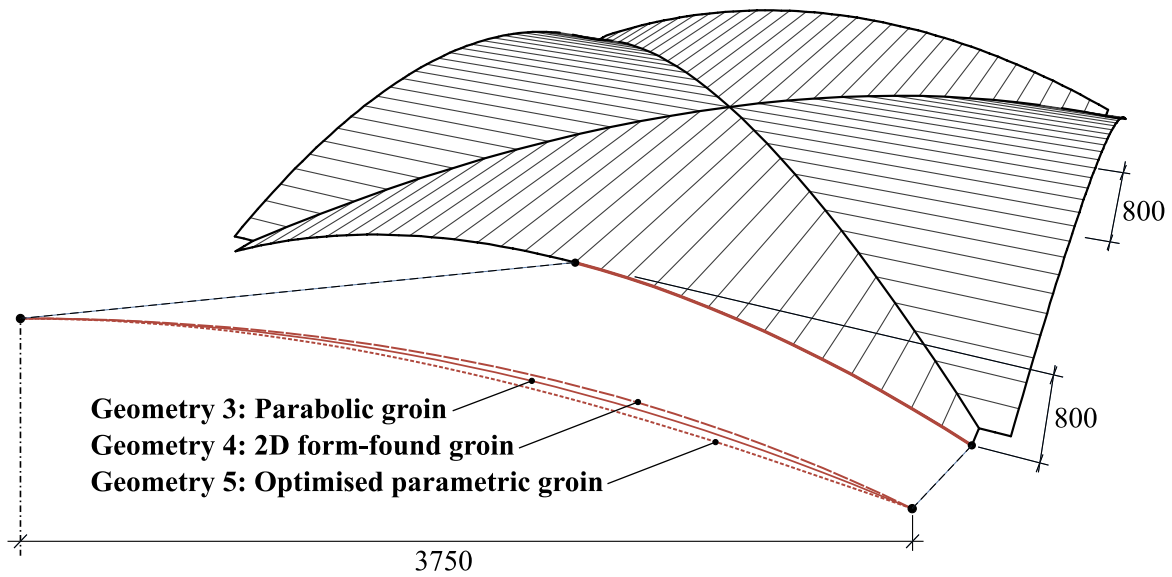


Figure 3.9: Parabolic, 2D form-found and optimised (parametric) groin vault profiles.

### 3.5.4 Optimised (parametric) groin vault

The previous 2D form-finding method considers the groin vault to be spanning in one direction, as for a barrel vault. In the groin vault, however, the question arises of whether funicularity is maintained at the diagonal intersections between the four segments.

The resultant force from the two funicular segments meeting at the diagonal crease is the vector sum of both compressive reactions, which meet at a right-angle on plan. This has both a vertical and horizontal component but is not aligned with the shell surface, and therefore must cause bending of the shell. This result was confirmed using the numerical 2D form-finding technique previously described, by showing that the funicular form of a curve carrying the same loads as the diagonal does not match that formed at the intersection. As a result, a groin vault (without ribs along the diagonals) cannot be funicular, regardless of the curve definition.

Furthermore, a funicular form can only exist for a single set of loading and boundary conditions. In a floor however, a range of loading scenarios must be considered and elastic displacement of the supports is also expected, as noted previously in Section 2.2.1. An alternative approach was therefore explored in which the groin vault profile was parametrised and optimised.

### Fitness parameter

The optimal geometry is dependent on the definition of fitness, which might concern serviceability (maximum displacement or natural frequency, for example) or strength (section utilisation). It was hypothesised that minimising bending forces within the shell is advantageous for all scenarios.

The chosen fitness parameter was the envelope of bending strain energy, over all loading patterns shown previously in Figure 3.6. Compared to the section utilisation, strain energy can be calculated with fewer assumptions on material behaviour, needing only the thickness and stiffness to be defined. In preliminary investigations, it was confirmed that bending strain energy was strongly correlated with average section utilisation; optimising for either gave similar results. Correspondingly, the required thickness, concrete strength and reinforcement are also minimised.

### Parametrisation strategy

Each variable used to define the 2D curve increases the dimension of the optimisation problem, and thus it is desirable to minimise the number of parameters in order to reduce computation time and complexity, albeit without restricting the design space.

For parametrisation, a Bézier curve was used with four control points defined by the span ( $l$ ), height ( $h$ ) and non-dimensional parameters  $a$  and  $b$ , as shown in Figure 3.10. This was selected from several alternative optimisation strategies in a preliminary study. Despite using only two parameters, this approach was able to match circular, catenary and parabolic test curves to within maximum deviations of 0.03mm, 0.02mm and 0.05mm respectively, when setting  $a$  and  $b$  to three significant figures. The discrepancy in bending strain energy was below 0.5%.

The previously described strategy for setting the tie pre-strain ( $\epsilon_{tie}$ ) cannot be easily integrated with this approach because the optimal shell geometry depends on  $\epsilon_{tie}$ , and vice versa. An iterative approach would therefore be needed, requiring the optimisation routine to be run several times. Instead,  $\epsilon_{tie}$  was included as a third parameter to be optimised.

The optimisation was carried out using the Galapagos evolutionary solver within Grasshopper (Rutten, 2013). Parameters  $a$ ,  $b$  and  $\epsilon_{tie}$  were each optimised to three significant figures.

### Results

The optimal parameters, for the design scenario considered, were  $a = 0.439$ ,  $b = 0.363$  and  $\epsilon_{tie} = 0.577\text{mm/m}$ . This curve (Geometry 5) is included in Figure 3.9.

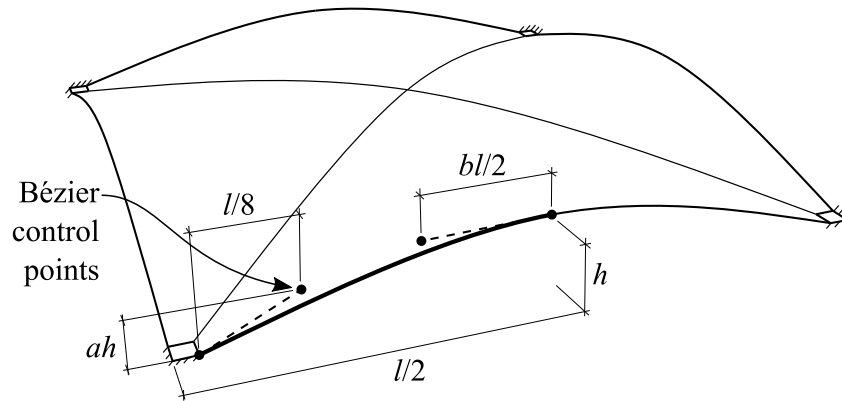


Figure 3.10: Definition of singly-curved groin vault geometry using a Bézier curve with four control points and two non-dimensional parameters  $a$  and  $b$ .

The total bending strain energy envelope was 241Nm. This compares to 302Nm and 391Nm for the parabolic and 2D form-found groin vaults respectively, calculated using an identical methodology. The large range highlights the optimisation procedure's effectiveness, as well as a high sensitivity to small changes in geometry.

The fitness surface for variables  $a$  and  $b$  is shown in Figure 3.11, with the optimal tie pre-strain. The smooth variation of bending strain energy observed across the design space indicates that the optimisation routine finds the global rather than a local optimum solution. The variation of bending strain energy with  $\varepsilon_{tie}$  was similarly smooth.

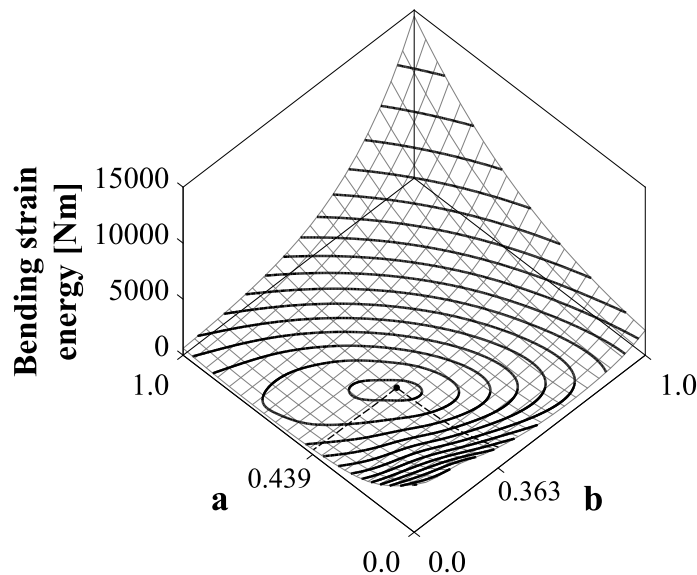


Figure 3.11: Fitness surface showing smooth variation of the bending strain energy envelope with the geometric parameters  $a$  and  $b$ . Contour lines are spaced logarithmically for clarity.

### 3.5.5 Form-finding in 3D

The concept of funicular form-finding was introduced in Section 2.2.1, and explored in Geometry 4 using a 2D method. However, since the shells are intended to span in both directions, a 3D form-finding technique which allows double curvature might be more effective. This approach does not necessarily reflect any particular formwork system, and hence a free-form mould would be required, perhaps utilising 3D printing or milling.

#### Methodology

A form-finding method was developed featuring two grids of springs in both the  $0^\circ/90^\circ$  and  $45^\circ/135^\circ$  directions, and is also described in Hawkins et al. (2017). This topology matches the triangular mesh used for FE analysis. Inverted shell loads are applied at the nodes where these (initially) flat grids intersect, creating a curved surface which is, in principle, a compression-only form for that specific loading. To find the equilibrium shape, a dynamic relaxation algorithm was implemented in Grasshopper using the Kangaroo physics engine (Piker, 2013). The applied loads were updated at each time-step to account for changing geometry. The nodes at the column interface were fully pinned. To maintain a square plan form, those along the edges were also constrained in one direction. This represents a discrepancy with the FE model, where edges are unconstrained, which is however necessary to create the desired form.

The model's reliability was tested in a separate investigation featuring barrel vault geometry. Floor, self-weight and pressure loadings were modelled, and the resulting forms compared to the respective parabolic, catenary and circular theoretical solutions. These were successfully recreated to within a vertical tolerance of 0.6mm.

#### Exploration of form-found geometries

The magnitude of vertical displacement is dictated by the spring stiffnesses. An infinite number of funicular surfaces exist for a given loading, each with a unique distribution of membrane forces. Using dynamic relaxation, the force distribution can be influenced via the stiffness of individual springs (analogous to modifying the force diagram in thrust network analysis). This potentially creates limitless possibilities for a designer to explore.

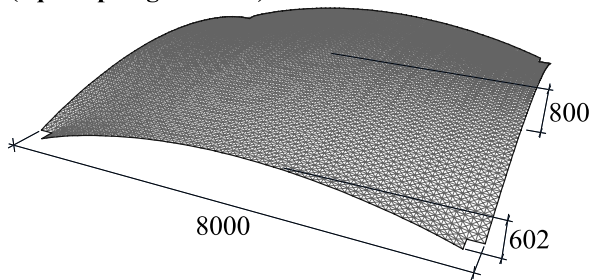
As a simplification, only two stiffness values were used in this case;  $k_{0^\circ,90^\circ}$  for springs aligned with the column grid and  $k_{45^\circ,135^\circ}$  along the diagonals. Including only the former was found to create dome-shaped forms, whilst the latter produces a flatter profile. Adjusting the relative magnitudes traverses a continuous design space between these two extremes.



## Results

Two form-found geometries were included in this investigation, as illustrated in Figure 3.12. In both cases, SLS (characteristic) loads were used to generate the forms.

**Geometry 6: Form-found  
(equal spring stiffness)**



**Geometry 7: Form-found  
(equal rise)**

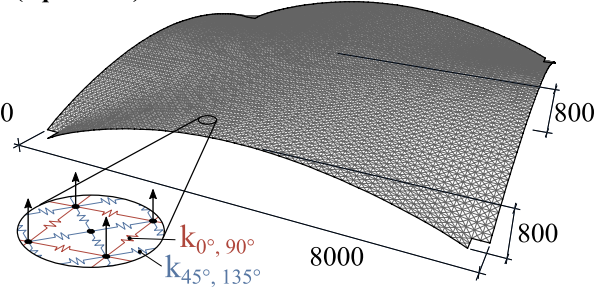


Figure 3.12: Form-found geometries created by applying SLS loads to an initially flat elastic cable-net.

Geometry 6 features similar spring stiffnesses in all directions. The resulting shell form reaches the maximum 800mm height at the middle, and the apex falls to 602mm along the column grid. In Geometry 7,  $k_{0^{\circ}, 90^{\circ}}$  and  $k_{45^{\circ}, 135^{\circ}}$  were adjusted to level both these points at 800mm. This has the advantage of maximising headroom and minimising the required volume of fill.

### 3.5.6 Fabric-formwork

The same form-finding method was adapted to simulate the geometry arising from fabric formwork.

A simplified model of a woven orthogonal fabric was obtained by setting one of  $k_{0^{\circ}, 90^{\circ}}$  or  $k_{45^{\circ}, 135^{\circ}}$  to zero, assuming linear elasticity in the warp and weft directions with zero shear stiffness. The potential for optimisation of the form through control of prestress in the fabric and modification of cutting patterns is not explored in this case. Figure 3.13 shows the resulting shell geometries with the fabric oriented on the  $0^{\circ}$  and  $45^{\circ}$  directions. The results highlight the significant effect of fabric orientation: Geometry 8 is dome-like whilst Geometry 9 is highest at the edges.

In this case, the form-finding load was only that of the shell itself (simulating the weight during casting). This construction method therefore requires inversion of the hardened shell. Alternatively, a hardening resin could be applied to the fabric in this state which could be more easily inverted and then used as formwork at the correct orientation, a method used by

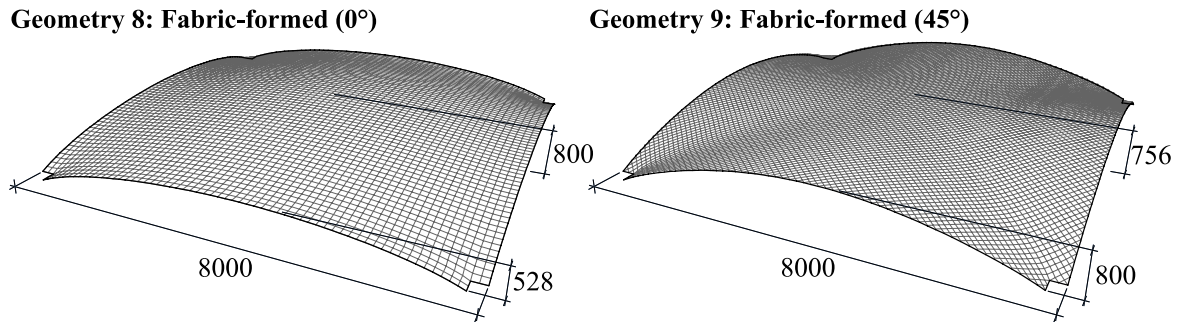


Figure 3.13: Shell forms created through casting onto fabric formwork, with an orthogonal weave orientated at  $0^\circ$  (Geometry 8) or  $45^\circ$  (Geometry 9) relative to the column grid.

West (2009). Lateral support would also be required to maintain straight edges, for example by insertion of a stiff element within the fabric.

## 3.6 Results

This section compares the structural behaviour of each shell geometry, considering both serviceability and strength, determined using the FE analysis methodology described in Section 3.4.

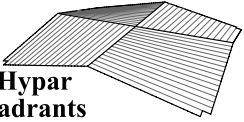
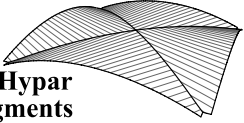
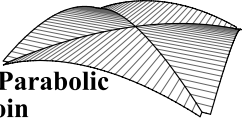
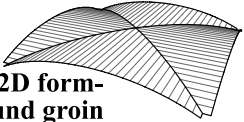
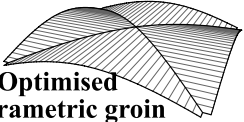

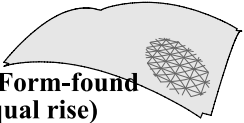
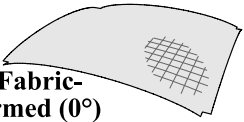
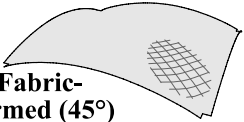
### 3.6.1 Self-weight and pre-strain

The self-weight of each geometry, including both the shell and fill, is shown in Table 3.2. The variation of shell surface area was less than 0.5%, and therefore the differences between geometries result predominantly from the variable fill volume. Shell geometries which maximise headroom also minimise fill volume and have a correspondingly low self-weight. These include all the groin vaults, with the 2D form-found profile giving the lowest self-weight of all. The same principle applies to the form-found and fabric-formed geometries, where the flatter forms of Geometries 7 and 9 offer a significant weight reduction compared to the dome-like forms of Geometries 6 and 8.

A lower self-weight reduces loading on columns and foundation, as well as the shell itself, and the embodied  $\text{CO}_2$  would also decrease.

The tie pre-strain is closely correlated with the self-weight, because a higher load requires more force to offset. The tie, of 50mm diameter, makes only a small contribution to the total self-weight ( $0.08\text{kN/m}^2$  assuming a density of  $7840\text{kg/m}^3$ ).

Table 3.2: Structural comparison of shell geometries.

Geometry	Self-weight [kN/m <sup>2</sup> ]	Tie pre-strain [mm/m]	Live-load deflection [mm]	Strain energy [Nm] (uniform SLS load)		
				$U_c$	$U_t$	$U_b$
1: Hypar quadrants 	3.14	0.64	10.8	423.7	11.8	170.4
2: Hypar segments 	2.98	0.65	14.6	445.7	1.6	27.3
3: Parabolic groin 	2.66	0.56	12.7	339.2	1.0	19.5
4: 2D form-found groin 	2.56	0.56	13.8	378.4	3.6	46.1
5: Optimised parametric groin 	2.78	0.58	11.8	319.4	0.3	6.7
6: Form-found (equal stiffness) 	3.25	0.69	11.5	473.9	5.8	93.9
7: Form-found (equal rise) 	2.61	0.58	15.6	426.2	11.9	124.7
8: Fabric-formed (0°) 	3.40	0.77	13.8	615.1	16.5	350.3
9: Fabric-formed (45°) 	2.67	0.62	19.5	556.1	30.0	237.3

### 3.6.2 Deflection

The total deflection is dependent on the amount of pre-strain in the ties, since this causes uplift. For a better comparison, the deflection under live loading only ( $3.5\text{kN/m}^2$ ) was considered, which is independent of pre-strain and self-weight.

The initial investigation in Section 3.3.1 indicated that tie extension alone might contribute significantly to vertical deflection. However, the variability of deflections shown in Table 3.2 indicate that deformation of the shell geometry is also a factor, at least in some cases.

The stiffest structure was Geometry 1 (hypar quadrants). It is hypothesised that the creases at the apex of the structure create additional bending stiffness around the mid-span. The double curvature of Geometry 2 did not create a higher stiffness than the three groin vaults, of which Geometry 5 was stiffest. The least stiff shell was Geometry 9. Here, the mid-span region has low curvature and was observed to deform in bending. Similar behaviour was noted in Geometry 7.

A deflection limit of  $\text{span}/500$  for loads applied after construction is suggested by Eurocode 2 (BSI, 2004a), which is 16mm in this case. All the shells except Geometry 9 are below this limit, which indicates that the design of the proposed flooring system is unlikely to be governed by deflection. If required, vertical stiffness could be increased by using a larger tie.

### 3.6.3 Free vibration

Vibration, caused by footfall, is a serviceability issue which can influence the design of lightweight flooring systems. Increased mass is an advantage in this situation, and vibration is therefore seldom a consideration for concrete slabs. Typical walking frequencies lie between 1.8Hz and 2.2Hz (De Silva and Thambiratnam, 2009), and problematic resonance can occur where this matches the structure's natural frequency. However, most floor structures which satisfy deflection requirements are stiff enough to have a natural frequency higher than this. It is desirable to maximise natural frequency, since this shifts resonance to a higher harmonic of footfall and hence significantly reduces the magnitude of vibration.

The first and second vibration modes (and corresponding frequencies) for each geometry are shown in Figure 3.14, computed using the linear FE model described in Section 3.4.1. In all cases, the first mode has a wavelength of twice the span; the columns act as nodes with a single anti-node at mid-span. This creates a symmetrical deformed shape similar to the displacement under a uniform load, with lateral spreading of column supports. Correspondingly, the natural frequency of the first mode is negatively correlated with the live-load deflection given in Table 3.2. Again, the hypars and groin vaults perform better than the form-found

and fabric-formed geometries. This mode of vibration creates a change in the length of the tie, and hence the frequencies might increase with tie stiffness. Restraint from neighbouring spans could also have a dampening and stiffening effect (which is ignored in this model).

The second mode has half the wavelength, with two anti-nodes within the shell. However, the natural frequency is not twice that of the first (as might be expected in simpler vibration problems) but quite similar to the first mode, making it potentially influential on performance. A greater variation between shell geometries is apparent than for the first mode, although the groin vaults again perform well and Geometry 5 has the highest natural frequency.

This investigation provides a brief exploration of vibration behaviour and a comparison between geometries. A more detailed analysis would be required for practical implementation. The fill material, ignored in this instance, would be expected to favourably increase stiffness, damping and mass.

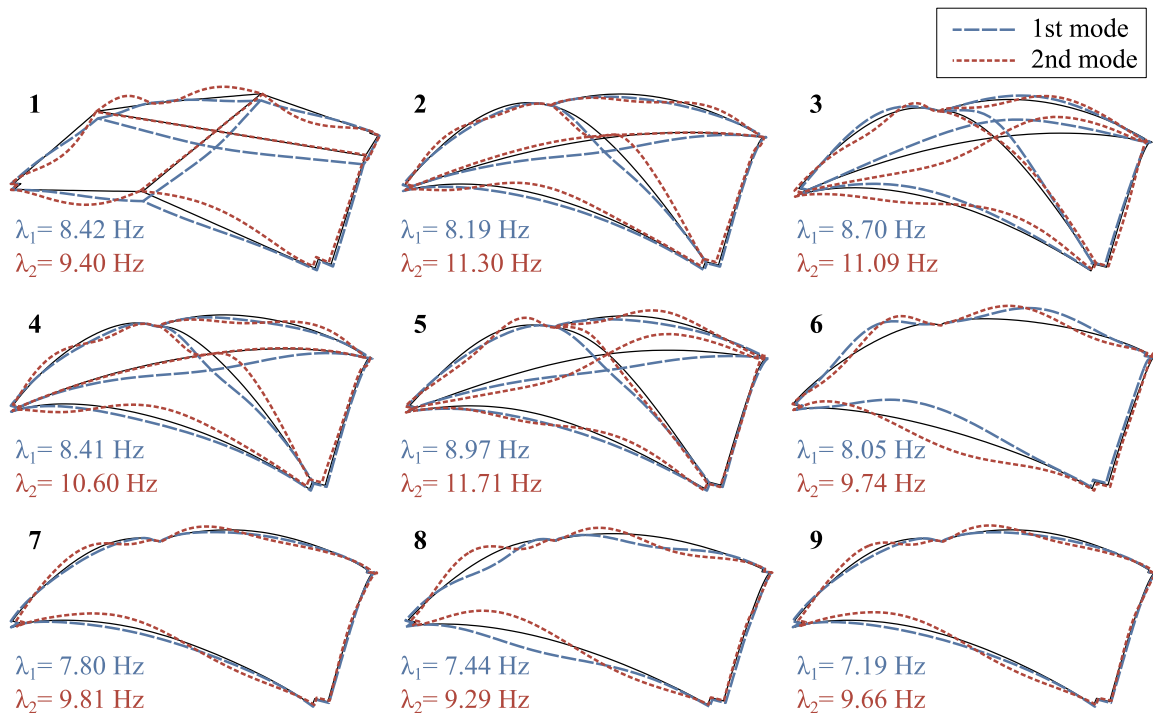


Figure 3.14: Comparison of first and second natural frequencies and mode shapes between shell geometries.

### 3.6.4 Strain energy

The strain energy within each shell was calculated under a uniform SLS load, the same loading under which form-finding was undertaken for Geometries 4, 6 and 7. The total strain

energies arising due to compressive ( $U_c$ ), tensile ( $U_t$ ) and bending ( $U_b$ ) forces are included in Table 3.2, with smaller values suggesting a more efficient design, requiring less material. Compression forces dominate across all the shells. Tension and bending are also present, albeit in significantly varying amounts.

Both the hyper shells have negative Gaussian curvature, and therefore tension might be expected in one direction. However, Geometry 2 experiences significantly less tension and bending than Geometry 1, suggesting greater dominance of arching action.

Compared to Geometry 2, the parabolic groin vault (Geometry 3) shows a reduction in strain energy for all forces. Changing the groin profile to a form-found curve results in a significant increase in both tension and bending, indicating that this is not an effective strategy. However, the parametric groin (Geometry 5) shows considerable improvement; the lowest energies of all shells across compression, bending and tension are achieved, even though this form was optimised for bending energy only and also considers other loading patterns.

Both Geometries 6 and 7 experience significant bending, despite this analysis featuring the same loading as for form-finding. This might be due to the mismatch of support conditions caused by free edges and sliding supports. Geometry 7 has a flatter profile in the mid-span and this appears to cause more bending. The largest strain energies are found in the fabric-formed shells, demonstrating that these are inherently inefficient forms for this application.

Compared to the uniform SLS load used in this comparison, asymmetric loads are likely to create significantly more bending forces across all the geometries. These effects are included in the ULS assessment discussed below.

### 3.6.5 TRC strength utilisation

The calculation of local strength utilisation ( $\eta$ ) was described previously in Section 3.4.5. In a real design, the strength of the TRC section must be sufficient ( $\eta \leq 1.0$ ) throughout the shell at the ultimate limit state.

Envelopes of maximum elemental utilisation were calculated using all ULS loading patterns. These are shown graphically in Figure 3.15, and the same data is also given in the form of a cumulative distribution in Figure 3.16. Where  $\eta \geq 1.0$ , this indicates that an increase in strength would be required above that of the assumed section (from Scholzen et al. (2015b)). Significant variation in both the magnitude and distribution of utilisation can be seen between the shell geometries, and the average is strongly correlated with the bending strain energy given in Table 3.2, indicating that bending dominates section utilisation.

Geometry 1 has a large mean utilisation, caused by significant bending moments throughout the structure. Both form-found geometries perform significantly better than the fabric-

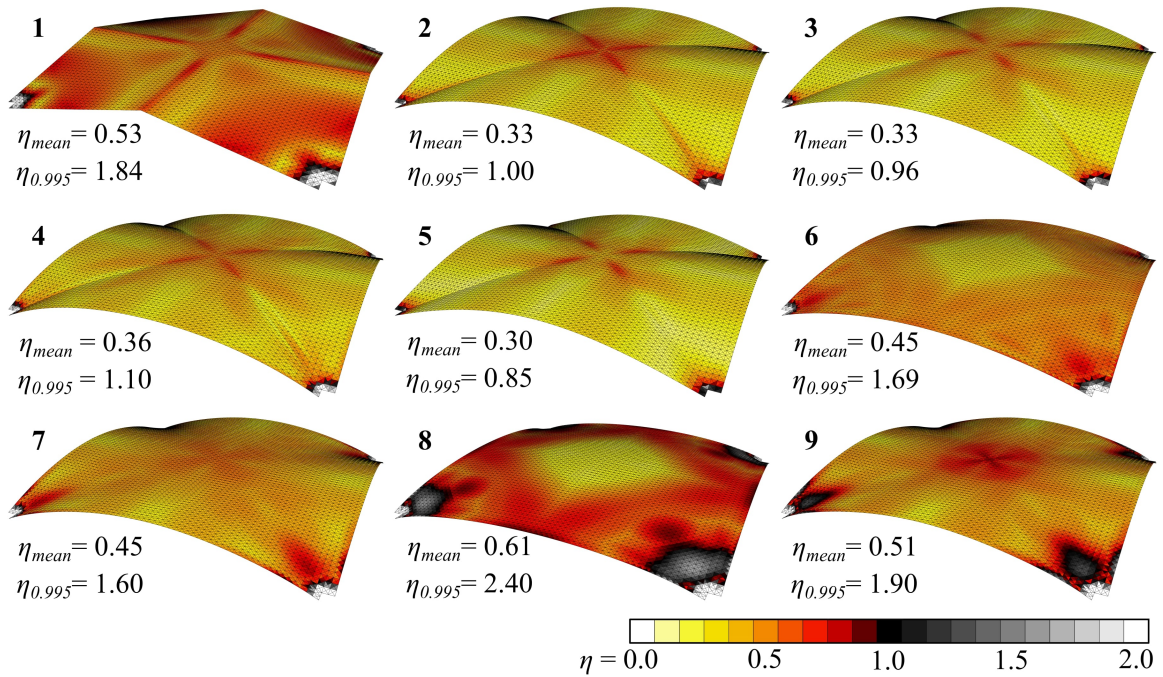


Figure 3.15: Envelopes of maximum utilisation across all loading patterns for each shell geometry. The mean ( $\eta_{mean}$ ) and 99.5th ( $\eta_{0.995}$ ) percentile of utilisation are also shown.

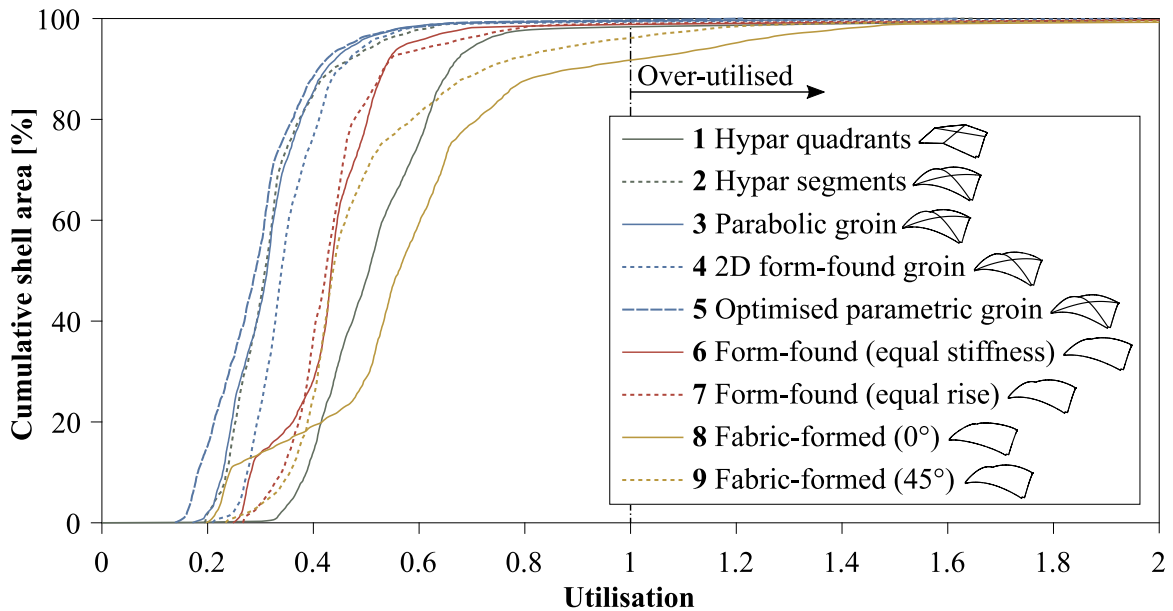


Figure 3.16: Cumulative distribution of maximum element utilisation across the surface area of each shell geometry.

formed options, again due to the presence of significant bending forces. The best performing shells are again the groin vaults. Geometry 5 has the lowest utilisation across the full area distribution, and would thus require the least material in a real design.

As described in Section 3.4.5, the tensile and bending strength of the TRC depends on the direction relative to the reinforcement, which is oriented with the column grid in this case. This potentially favours certain shell geometries over others, depending primarily on the orientation of principle moments. However, the strong correlation between average utilisation and bending strain energy (Table 3.2) suggests that this affect has limited influence in this case.

In each case the most highly utilised elements occur at the shell-column interface, where large compressive and bending forces are concentrated. A corresponding spike in utilisation is visible in Figure 3.16. As established previously in Section 3.4.2, the peak forces in this region are mesh-dependent. However, since the TRC strength requirements are also dictated by the forces in this region, it is important to correctly interpret these results. To enable a comparison, the utilisation at the 99.5th percentile ( $\eta_{0.995}$ ) was calculated, and is included in Figure 3.15. This area covers approximately 80 elements, and represents a measure of maximum utilisation with low mesh-dependency. Again, the groin vaults are the best performers, indicating a much lower TRC strength requirement. The design of a suitable TRC section is discussed further in Section 3.7.2.

### 3.6.6 Buckling

A simple buckling investigation was carried out using a second order geometrically non-linear analysis in Karamba. The material model for the shell remained linear elastic. A factor of safety against buckling was calculated for each load pattern. The uniform loading (Pattern 7 in Figure 3.6) resulted in the lowest factor of safety for each geometry, and these values are therefore compared in Table 3.3.

Table 3.3: Factors of safety against buckling under uniform ULS loading.

<b>Geometry</b>	1	2	3	4	5	6	7	8	9
<b>Buckling safety factor</b>	6.0	10.3	11.1	10.5	11.7	5.8	8.7	5.4	7.9

The results follow a similar trend to average section utilisation (Figure 3.15), bending strain energy (Table 3.2) and natural frequency (Figure 3.14), showing that some shell geometries are generally more structurally effective than others.

All the values are considerably greater than one, and might therefore be considered safe in a ULS design approach. This analysis is conservative, since the stiffening effect of the



foamed concrete fill has been ignored. However, loss of stiffness due to cracking has been neglected in this case, which could potentially induce instability at a lower load. It is likely therefore that a more sophisticated model, ideally backed up with experimental data, would be required for a implementable design proposal.

## 3.7 Discussion

The previous section has compared the structural performance of nine shell geometries by considering self-weight, deflection, vibration, strain energy, strength utilisation and buckling. This section examines the implications of these results on the design, analysis and feasibility of the proposed flooring system.

### 3.7.1 Comparison of shell geometries

#### Hypars

The advantage of hypar surfaces is that formwork can be constructed using straight elements. However, the first hypar shell (Geometry 1) performed poorly across most criteria. Each quartile region has a low curvature, and this resulted in large bending forces. Geometry 2 (hypar segments) showed generally better structural performance across most categories. However, the dip at the mid-span did not provide a structural advantage over the similar groin vault (Geometry 3), and also increases the required volume of fill.

#### Form-found and fabric-formed shells

Geometries 6 to 9 were found using dynamic relaxation. The guiding principle is the elimination of bending and tensile forces, however this was ineffective in this case. The fabric-formed geometries were consistently poor in all performance indicators. This might be expected of the fabric-formed geometries, due to the mis-match between the form-finding (shell self weight only) and real loads. However, Geometries 6 and 7 were only marginally more effective.

Several causes for the poor performance of the form-found shells are outlined below:

- Non-developable surfaces (with double curvature) must distort to accommodate horizontal movement of supports.
- Form-finding can only be carried out under a single set of loads and boundary conditions. In practice, the shells experience a multitude of loading patterns with non-rigid supports.

- Boundary conditions were not consistent between the dynamic relaxation and FE models, since a horizontal perimeter restraint was required in the former case to ensure straight edges on-plan.
- An arch or vault with bending stiffness will always attract bending forces, tending towards beam-like behaviour as they become shallower, regardless of their form.

### Groin vaults

The three groin vaults were the best performers across all comparisons, with the marginal exception of vertical stiffness. They are also the simplest to construct in terms of formwork, consisting of singly-curved developable surfaces.

There are several possible reasons for their strong performance. The groin vaults might accommodate lateral support movement more easily than the other geometries due to their developable surfaces, in a similar manner to which historic arch bridges and medieval groin vaults adapt to movement of their foundations (Heyman, 1969). Furthermore, the diagonal folds of the groin vault are well positioned to provide additional stiffness for serviceability. Finally, the geometry of the groin vault is efficient in maximising headroom and minimising the required volume of fill, reducing self-weight.

The 2D form-finding method used in Geometry 4 was not effective. This is potentially because the method was overly simplistic in ignoring the interaction between the four segments; a groin-vault without ribs can never be funicular in form.

The optimised parametric groin vault (Geometry 5) had the highest natural frequency, lowest utilisation and greatest buckling resistance, and performed well in self-weight and vertical stiffness. This demonstrates that minimising bending forces leads to generally favourable structural performance, as hypothesised in Section 3.5.4. This methodology was therefore chosen as the basis for future designs.

### 3.7.2 TRC section design

Both the TRC section properties and strength utilisation analysis methodology were adopted from Scholzen et al. (2015b), using a failure envelope linearly interpolated between experimentally determined strengths in compression, tension and bending.

Pairs of forces (in principal stress directions) calculated for each element in the ULS analysis of Geometry 5 are plotted in Figure 3.17, along with the failure envelope. Note that maximum bending and tensile strengths are shown, although these would be reduced based on the direction of loading according to Equations 3.9 and 3.10. Each loading pattern is shown separately.

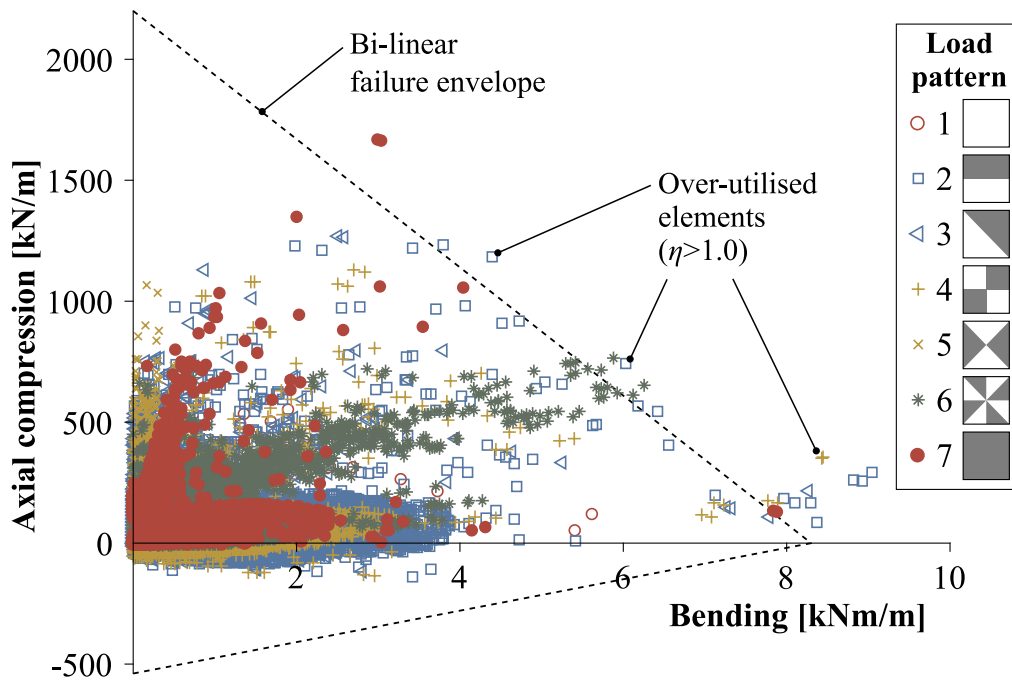


Figure 3.17: Elemental pairs of axial and bending forces calculated for each ULS loading pattern (Geometry 5), plotted against the bi-linear failure envelope used for utilisation calculation (Scholzen et al., 2015b).

The few elements which are over-utilised lie outside the failure envelope, and are located at the shell-column interface (as indicated by Figure 3.15). Significant differences in force distribution between the loading patterns are visible. The highest utilisations occur for the asymmetric loads such as Pattern 6 and, to a greater extent, 2. The maximum uniform load (Pattern 7) gives very few over-utilised elements.

The TRC section described by Scholzen et al. (2015b) has twelve layers of carbon fibre textile reinforcement, evenly distributed throughout the section. This creates a high tensile strength. However, Figure 3.17 shows that the tensile forces throughout the shell are consistently much smaller than the TRC strength, reflecting the predominantly compressive action of the vaults. The peak moments are however of a similar magnitude to the bending strength of the section. It might therefore be possible to improve material efficiency by eliminating fibres from the middle part of the section. This would reduce the tensile strength with only a small impact on the moment capacity, since the outer fibres contribute most significantly to this. Further environmental benefits could also be achieved by swapping carbon fibres for those of AR-glass or basalt which have a considerably lower embodied carbon (see Section 2.3.1).

All the over-utilised elements in Figure 3.17 occur under combined compression and bending, where the bi-linear failure envelope is postulated to be highly conservative. It is proposed that a more realistic failure envelope, which takes into account the behaviour of concrete and textile reinforcement, might therefore provide a more accurate estimation of utilisation. This is addressed in Section 4.3.

### 3.7.3 FE analysis methodology

The FE simulations undertaken so far have featured a linear-elastic material model for the TRC. However, the true behaviour of this material can be non-linear if tensile cracking or compressive softening of the concrete occurs.

The maximum principal ULS surface stress envelopes in both compression and tension are shown in Figure 3.18, for Geometry 5. The mean compressive and tensile strengths for C30/37 concrete are  $f_{cm}=38\text{MPa}$  and  $f_{ctm}=2.9\text{MPa}$  respectively (BSI, 2004a), and are used as a reference values in order to highlight over-stressed regions.

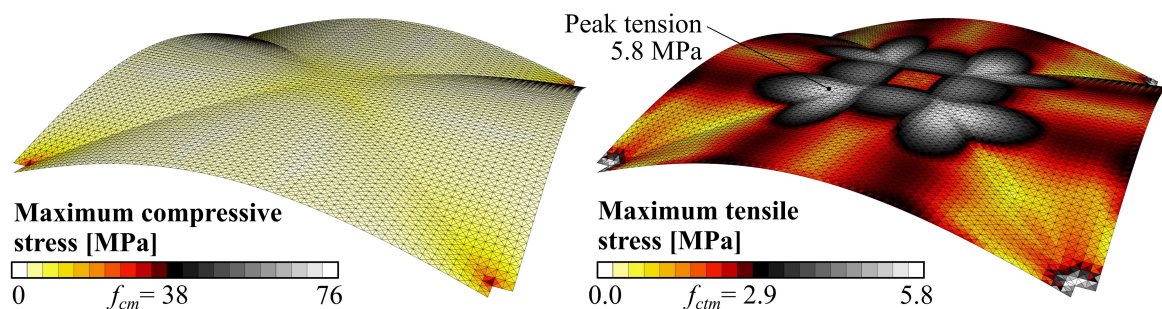


Figure 3.18: Envelopes of maximum principal ULS compressive and tensile stresses for Geometry 5. The scales are set relative to the mean compressive  $f_{cm}$  and tensile  $f_{ctm}$  strengths of C30/37 concrete.

The maximum compressive stresses are mostly very small compared to the concrete strength, with a mean of only 4.8MPa. Throughout the shell, all stresses are below the mean strength of 38MPa.

In contrast, the tensile stress exceeds the concrete strength in multiple locations. Despite the vault being a compression structure, every part of the shell experiences tension in at least one loading pattern, resulting primarily from bending forces. The peak stress occurs at the corner support, although this value is likely to be mesh-dependent (see Section 3.4.2). A significant region across the mid-span also has large tensile stresses, indicating cracking. These were found to be largest and most widespread in load Pattern 2.

In a real TRC structure made using C30/37 concrete, cracking would therefore be expected at ULS loads. The resulting reduction in stiffness would cause some redistribution

of forces and would also alter the deformation pattern. However, this does not invalidate the linear approach used for strength design, which conservatively ignores redistribution of peak forces (Sharei et al., 2017). Contrastingly, ignoring cracking in a buckling analysis is unconservative in this case due to the global stiffness reduction. Non-linear FE models of TRC are explored in Sections 4.4 and 6.2.

### 3.7.4 Variable shell thickness investigation

This investigation has shown that peak forces, stresses and section utilisations occur near the shell-column interface. Specifying the TRC section for this region might therefore cause the rest of the shell to be significantly over-designed, representing an inefficient use of materials. A shell of variable thickness might therefore be more efficient. This would be relatively simple to create in TRC due to the layered construction process and use of single-sided formwork.

An investigation was therefore carried out to explore whether thickening the shell near the corners might improve performance. The thickness was increased linearly from 60mm to 90mm over a distance of 500mm from the column edge. To ensure a realistic comparison, the parametric groin vault (Geometry 5) was then re-optimised using the same methodology described in Section 3.5.4. Optimal parameters of  $a = 0.448$ ,  $b = 0.354$  and  $\epsilon_{tie} = 0.605\text{mm/m}$  were found (compared with  $a = 0.439$ ,  $b = 0.363$  and  $\epsilon_{tie} = 0.577\text{mm/m}$  found in Section 3.5.4 for the uniform shell).

The utilisation distribution cannot be directly compared without a model for predicting the relationship between TRC strength and section thickness (which has not yet been introduced). Instead, the distribution of principal ULS moments are shown in Figure 3.19 for both the original and variable thickness shells, which can be considered a proxy for section utilisation.

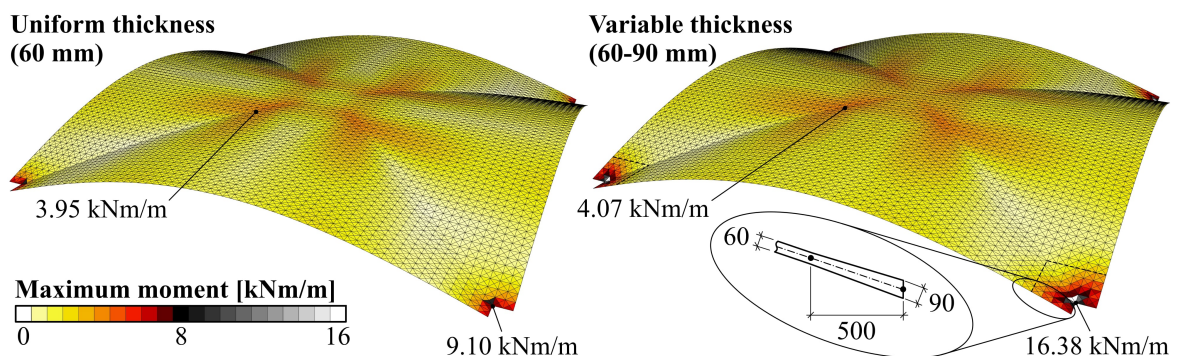


Figure 3.19: Envelopes of maximum principal ULS moments for the original optimised groin vault, with a uniform 60mm thickness, and a re-optimised groin vault with the thickness linearly increased to 90mm at the shell-column interface.

The higher corner thickness causes the moments in this region to increase considerably. In this case, the (mesh-dependent) peak value is 80% higher for a 50% increase in thickness, likely due to increased bending stiffness.

The moment capacity of a TRC section with top and bottom reinforcement would be expected to scale proportionally with the distance between the reinforcement and concrete compression zone, and therefore approximately with the section thickness. This analysis consequently suggests that any increase in bending strength would be offset by higher forces. Compressive strength would also increase with depth, although Figure 3.17 suggests that this would not significantly reduce utilisation.

Moments are also increased across the rest of the shell, despite no change in local thickness. Near the mid-span, the peak moment increased by 3.0% from 3.95kNm/m to 4.07kNm/m. Across the entire shell, the mean moment increased by 19% from 1.79kNm/m to 2.13kNm/m.

Based on a lower bound argument, adding material cannot possibly reduce the strength of the structure. However, this investigation indicates that an increase in thickness at the corners, which attempts to match the TRC strength to the force distribution, might not be an efficient means of improving material efficiency. The results also highlight the sensitivity of shell forces to small variations in thickness, with potential implications regarding construction accuracy.

### **3.8 Summary, findings and conclusions**

This chapter has introduced the thin-shell flooring system proposed in this dissertation. The basic behaviour was explored, allowing an approximate sizing of members for a typical application with 8m spans. A more detailed investigation was then carried out using linear FE analysis, enabling nine candidate shell geometries to be compared. This also revealed the structural behaviour in more detail, with implications for the selection of suitable materials, design methods and analysis approaches.

Key findings are summarised below:

- The low rise of the vault creates a large horizontal thrust, which must be resisted at the building's edge. Vertical deformation of the vault is sensitive to the stiffness of this horizontal restraint, and therefore a system of prestressed steel ties is proposed.
- Singly-curved groin vaults are a simple but effective means of defining a geometry with low self-weight and straightforward formwork construction.

- Only two dimensionless parameters are required to effectively optimise a groin vault defined by a Bézier curve. Setting these to minimise the bending strain energy creates a shell with good structural characteristics regarding vertical stiffness, vibration, force distribution and buckling resistance. Other shell geometries, including hypars and those found using dynamic relaxation, performed comparatively poorly. The parametrically optimised groin vault was therefore taken forward as a preferred design method.
- Preliminary results indicate that the vertical deflection, vibration and buckling resistance of a 60mm thick shell (featuring an optimised groin vault geometry) are adequate for a typical office application with 8m spans.
- Peak stresses are concentrated at the shell-column interface, and are mesh-dependent for the linear FE analysis model used in this instance. This presents a challenge for reliable specification of required TRC strength.
- Asymmetric live loads are critical for strength design across much of the shell, and must therefore be considered. Cracking is also expected under asymmetric loading at ULS.
- The 60mm thick TRC section described by Scholzen et al. (2015b) is at the limit of strength in this application, according to the design methodology set out in the same paper. However, greater material efficiency could be achieved by improving this model's accuracy under compressive forces, which dominate in this case, and by concentrating reinforcement near the shell surfaces.

### Conclusions: Chapter 3

Thin, shallow, groin-vaulted TRC shells of uniform thickness with prestressed steel ties are a feasible structural system for floors in multi-storey buildings, and show potential for high material efficiency. Whilst existing TRC design methods and materials could be applied in this context, these might be developed and refined to facilitate a more efficient design.





# Chapter 4

## Construction, modelling and design of suitable TRC materials

### 4.1 Introduction

In order to thoroughly assess the performance and suitability of the proposed system, both the ultimate strength and the deformation under service loadings must be predicted. A detailed understanding of material and structural behaviour is therefore required.

Flexibility of manufacturing methods, section geometries and materials leads to wide variations in the behaviour of TRC sections. Because of this, an analytical model developed for a particular application may not be suitable for another. The proposed vaulted floors are designed to act primarily in compression and with minimal embodied carbon, and therefore the expected reinforcement ratio is lower than for other, tension-critical, applications.

This chapter explores the characteristics of lightly-reinforced TRC through construction and physical testing of physical specimens. The results are then used to validate two analytical approaches: firstly a failure envelope for prediction of strength under combined axial and bending loads, and secondly a non-linear FE analysis model for prediction of load-deflection behaviour.

The following aims are addressed:

- To explore suitable materials for low-energy TRC construction.
- To gain an appreciation of manufacturing processes for TRC.
- To investigate the structural behaviour of lightly-reinforced TRC.
- To develop suitable methods for structural modelling and design of the proposed shells.

## 4.2 Experimental investigation

TRC specimens of 15mm and 30mm thickness were constructed and subject to three experimental testing methodologies: pure tension, four-point bending and eccentric compression. These experiments were carried out at the University of Cambridge. This section describes the materials used, specimen design and construction of the specimens, test methodologies and results.

### 4.2.1 Materials

#### Fine-grained concrete

A fine-grained concrete mix was developed with the composition shown in Table 4.1. Achieving a good workability for constructing thin TRC layers by hand was prioritised. The target 28 day compressive strength was 40MPa, intended to be representative of typical structural concrete.

Table 4.1: Fine-grained concrete composition

Material	Quantity [kg/m <sup>3</sup> ]
Portland cement	349
Fly ash	150
Aggregate (0 - 1mm)	747
Aggregate (1 - 2mm)	747
Water	199
Superplasticiser	5.13

The proportion of Portland cement was minimised to reduce both the embodied carbon of the mix and the alkalinity. The binder was made up of 70% Portland cement and 30% fly ash, the water to binder ratio was 0.4 and the aggregate to binder ratio was 3.0. This is significantly higher than usually found in fine-grained concretes for TRC, where ratios are typically below 1.8 (Brockmann, 2007; Du et al., 2017; Scholzen et al., 2015a). This further reduces the cement content and embodied carbon. Ten millilitres of polycarboxylate superplasticiser was added per kg of binder. In Table 4.1, this volume was converted to mass using the manufacturer's quoted density of 1030kg/m<sup>3</sup>.

A maximum aggregate size of 2mm was used to enable construction of thin cover layers. The aggregate particle size distribution was found to be of critical importance for achieving good strength. In preliminary testing, reducing the ratio of 0-1mm particles to 1-2mm

particles from the natural ratio of 3:1 to 1:1 increased the compressive strength by 43%, and this approach was therefore adopted.

The measured dry density of the material was  $2197\text{kg/m}^3$  (at 28 days). The total embodied carbon is  $0.155\text{kgCO}_2\text{e/kg}$ , or  $340\text{kgCO}_2\text{e/m}^3$ , based on the values given in Table 2.1.

Six fine-grained concrete prisms were constructed and tested in compression after curing in a water bath at room temperature for 28 days. Each was loaded along its long axis in a concrete compression testing rig to determine the strength and stress-strain characteristics, as shown in Figure 4.1. Strain was measured using a pair of mechanical extensometers on opposite sides of the specimen, measuring displacement over a gauge length of 80mm.

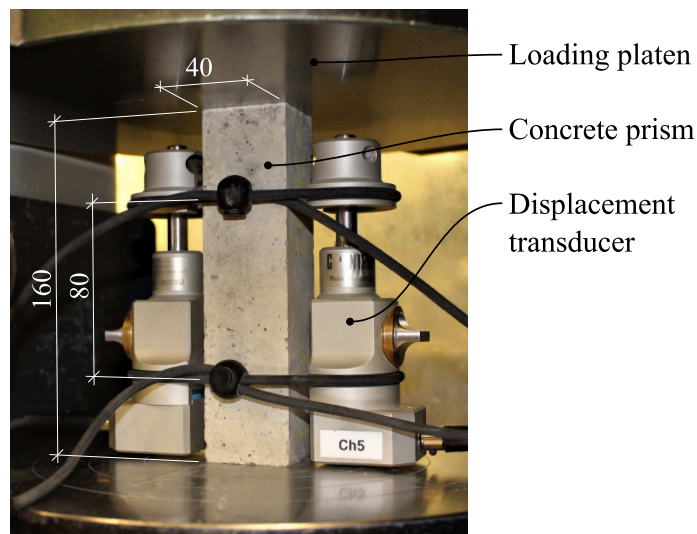


Figure 4.1: Concrete prism compression test arrangement (dimensions in mm).

The average stress-strain curves measured from four of the prism tests are plotted in Figure 4.2. The mean strength  $f_{cm}$  was  $47.2\text{MPa}$ , reached at an average peak strain of  $0.192\%$ . The data collected from the remaining two tests was unreliable, with the most likely cause being slipping of the extensometers at the concrete interface.

Also plotted in Figure 4.2 are two established theoretical models which relate concrete stress ( $\sigma_c$ ) and strain ( $\epsilon_c$ ) in compression. The first is a parabolic stress-strain model as proposed for non-linear structural analysis by Eurocode 2 (BSI, 2004a), as shown in Equation 4.1.

$$\sigma_c = f_{cm} \left( \frac{k\eta - \eta^2}{1 + \eta(k-2)} \right) \quad \text{for } 0 \leq \epsilon_c \leq \epsilon_{cu1} \quad (4.1)$$

where:

$$\eta = \varepsilon_c / \varepsilon_{c1}$$

$$k = 10.5 (E_{cm} \varepsilon_{c1} / f_{cm})$$

$$\varepsilon_{c1} = 0.07 f_{cm}^{0.31} \leq 0.28 \quad [\%]$$

$$\varepsilon_{cu1} = 0.35 \quad [\%]$$

$$E_{cm} = 22 (f_{cm} / 10)^{0.3} \quad [\text{GPa}]$$

$$\text{for } f_{cm} \leq 58 \quad [\text{MPa}]$$

This curve can be derived entirely from the mean concrete strength, with  $f_{cm} = 47.2 \text{MPa}$  corresponding to  $E_c = 35.0 \text{GPa}$  and  $\varepsilon_{c1} = 0.231\%$ .

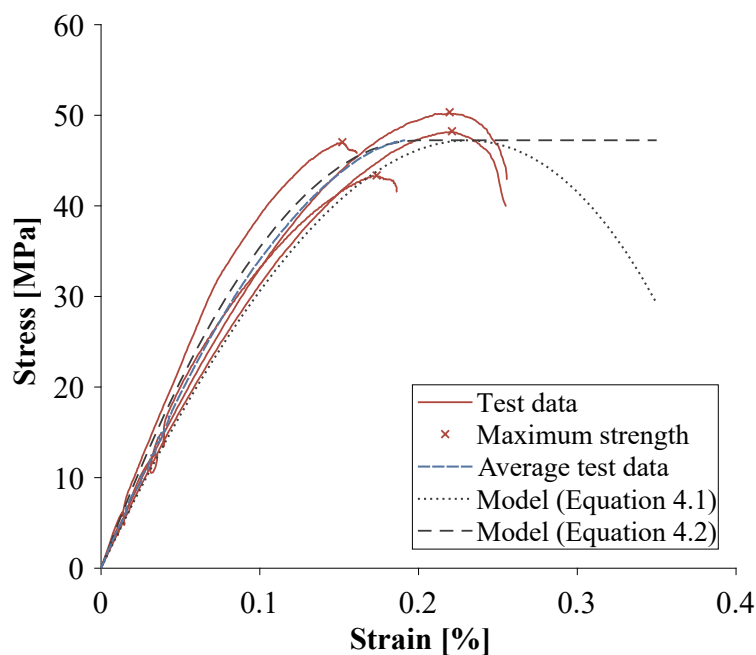


Figure 4.2: Fine-grained concrete prism compressive test results

The second theoretical curve is a parabola-rectangle approximation, as described in the FIB Model Code (FIB, 2012) and Eurocode 2 (BSI, 2004a). This model is not a reproduction of an experimentally determined stress-strain curve, but is a simplification of more complex behaviour under three-dimensional stress states in concrete beams (Kotsovos, 1982), and is used for ULS design of concrete sections in bending. The curve is defined by the compressive design strength ( $f_{cd}$ ) as well as three other parameters; the strain at peak strength ( $\varepsilon_{c2}$ ), the strain at failure ( $\varepsilon_{cu2}$ ) and the exponent ( $n$ ), as in Equation 4.2. In Figure 4.2, the curve has been plotted with  $f_{cd} = f_{cm}$  to allow comparison with the experimental data.

$$\begin{aligned}\sigma_c &= f_{cd} \left( 1 - \left( 1 - \frac{\varepsilon_c}{\varepsilon_{c2}} \right)^n \right) & \text{for } 0 \leq \varepsilon_c \leq \varepsilon_{c2} \\ &= f_{cd} & \text{for } \varepsilon_{c2} \leq \varepsilon_c \leq \varepsilon_{cu2}\end{aligned}\quad (4.2)$$

Where:

$$\begin{aligned}n &= 2 \\ \varepsilon_{c2} &= 0.2 \quad [\%] \\ \varepsilon_{cu2} &= 0.35 \quad [\%] \\ \text{for } f_{cm} &\leq 58 \quad [\text{MPa}]\end{aligned}$$

Comparing the two models shows that the parabola (Equation 4.1) predicts a lower stiffness than the parabola-rectangle (Equation 4.2), with the latter more closely matching the experimental curves. Beyond the peak strength, the experimental curves can be seen to descend more rapidly than predicted by Equation 4.1. However, since the descending part of the curve is highly dependent on test specimen geometry and friction with loading platens (Kotsovos, 1983), this is of limited significance.

Fine-grained concretes used for TRC are often less stiff than typical concrete of equivalent strength, due in part to a lower proportion of aggregates. Strains at peak strength of up to  $\varepsilon_{c1} = 0.5\%$  have been reported (Banholzer et al., 2006; Scholzen et al., 2015b; Verwimp et al., 2015). However, this does not appear to be the case here, possibly due to the relatively high proportion of aggregates used compared to many fine-grained concretes. The stress-strain models shown in Figure 4.2 were therefore adopted in Sections 4.3 and 4.4 for analysis of the TRC behaviour.

## Reinforcement

The reinforcement used was an AR-glass fibre textile with acrylic resin coating, chosen due to its wide availability, affordability and flexibility for the formation of curved shell structures. The embodied carbon of glass fibres is also significantly lower than carbon (2.1). The coating protects the outer fibres from damage during handling and acts as a barrier against the alkalinity of the cementitious matrix. It also adds some rigidity to the mesh through bonding together of the outer fibres, however the impregnation of the resin does not reach the centre of the yarns. Consequentially, the material might be considered as having characteristics between that of a non-impregnated and a fully impregnated fibre textile. Figure 4.3 shows the construction and geometry of the reinforcement. The yarns in the warp

direction consist of straight bundles of fibres, whilst those in the fill direction are in groups of three, woven between the warp yarns. Key properties of the material are shown in Table 4.2.

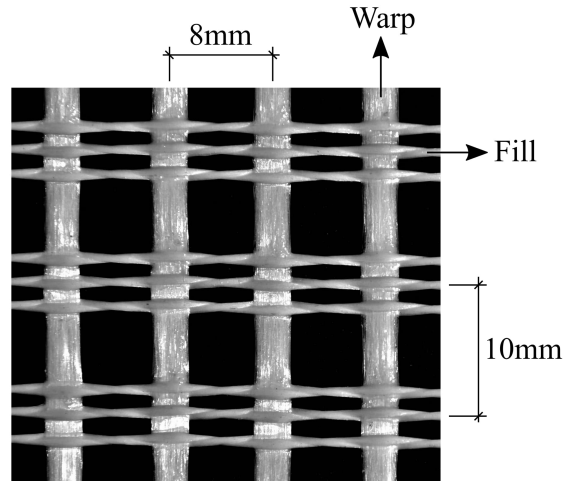


Figure 4.3: AR-glass reinforcement

Table 4.2: AR-glass fibre reinforcement properties

		Warp	Fill
Strength $f_t$	[MPa]	1192	1326
Stiffness $E_t$	[GPa]	64.0	55.7
Yarn weight	[g/m]	1.41	1.41
Yarn spacing	[mm]	8	10
Area $A_t$	[mm <sup>2</sup> /m]	65.3	52.2

The weights of the warp and fill yarns were determined by weighing samples of the reinforcement mesh with different aspect ratios, enabling each direction to be distinguished. The weight is made up of both the fibres and the epoxy coating, although the relative proportions were not provided by the manufacturer. This could have been determined through a burn-off test, however instead the material was treated as homogeneous in the calculation of its mechanical properties. An attempt was made to measure the density of the material through immersion in water, giving an average value of 1596kg/m<sup>3</sup>. This is considerably lower than the typical value of 2700kg/m<sup>3</sup> for glass, with the discrepancy likely to be caused by voids between the uncoated fibres and the lower density of the epoxy coating. Consequentially, if the measured value of density was used to convert the weight of the yarn to cross-sectional area, the result would be significantly higher than the true area. Instead, a glass fibre density of 2700kg/m<sup>3</sup> was assumed to calculate the yarn area, which is therefore

likely to be an over-estimate of the true fibre area due to the additional weight of resin. As a result, the values in Table 4.2 are not directly comparable with true glass fibre data.

Tensile tests on eight warp and eight fill yarns were carried out to determine the ultimate strength ( $f_t$ ) and stiffness ( $E_t$ ). Individual yarns were cut from the mesh and bonded between pairs of fibreboard plates using epoxy resin over a length of 80mm, which was sufficient to avoid fibre pull-out. The strain was measured using a laser extensometer, using the testing arrangement shown in Figure 4.4.

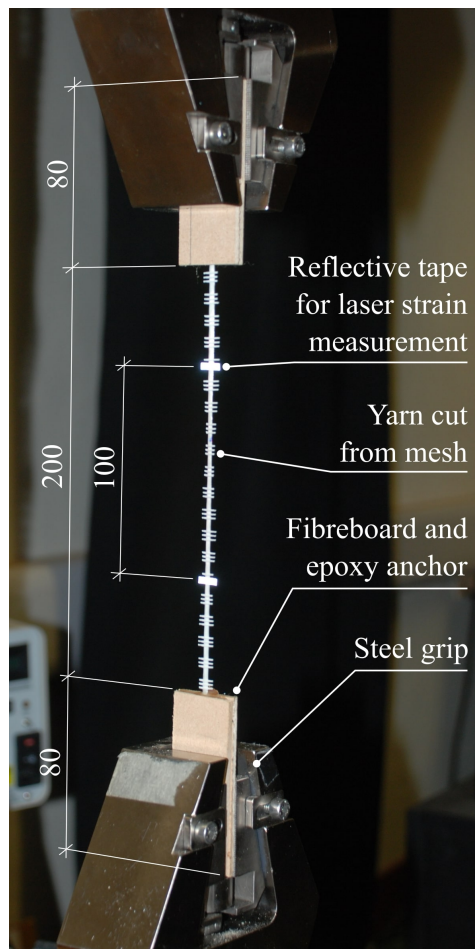


Figure 4.4: Reinforcement yarn testing arrangement (dimensions in mm).

Test results are shown in Figure 4.5, and indicate brittle-elastic behaviour. In each test, failure occurred at the interface between the yarn and anchor. Despite having the same weight, the fill yarns showed a consistently higher strength and a lower stiffness. Both differences are a result of variations in geometry; the warp fibres are straight and the fill fibres are woven between them, therefore having a wave-like curvature. The straightening of the twisted fill yarns upon loading manifests as a reduced stiffness. The lower strength of the warp yarns

may be due to a higher variation in stress across the fibres, since the load distribution through friction between the straighter warp fibres is likely to be smaller than in the more twisted fill fibres. The behaviour of the warp yarns is therefore closer to that of a fibre bundle with randomly variable strengths (Chudoba et al., 2006). The audible rupturing of a small number of fibres prior to failure, as heard in the warp yarn tests but not fill, supports this evaluation.

The strength of individual AR-glass fibres is typically 1800-3500MPa, and stiffness 70-76GPa (FIB, 2007). In both cases, the measured values in this case are smaller. This is because the strength of a fibre bundle is lower than that of an individual fibre, and the stiffness of the acrylic coating is lower than that of glass.

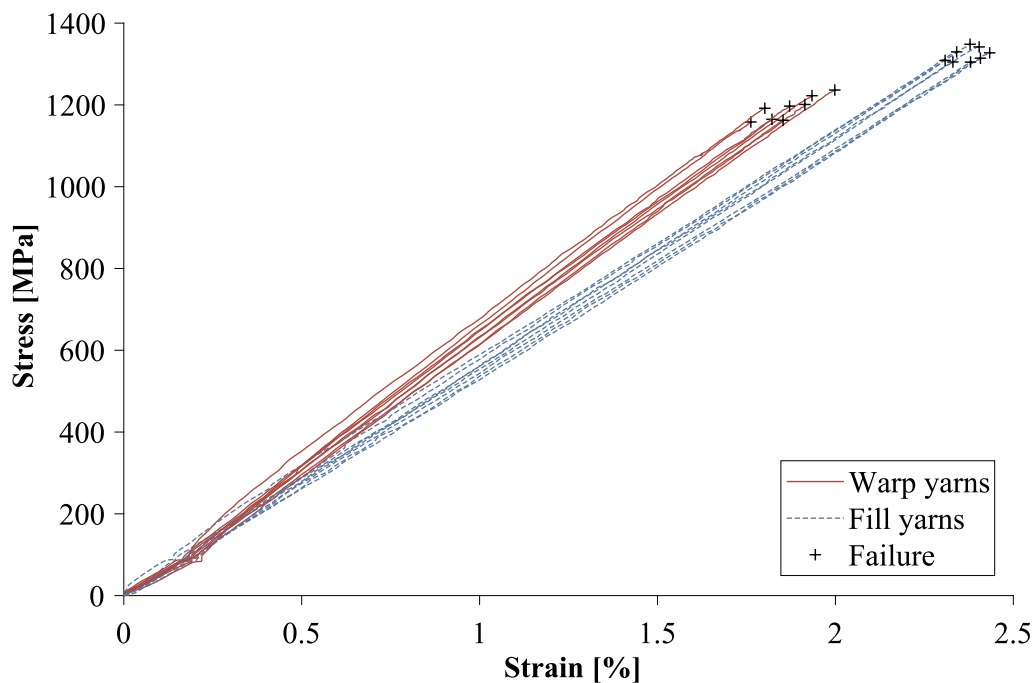


Figure 4.5: Results from tensile tests on individual reinforcement yarns, in both warp and fill directions.

As noted in Section 2.2.3, the tensile strength of textile reinforcement embedded in concrete ( $f_{tc}$ ) is less than that of individual yarns, due to non-uniform fibre stress distributions and, potentially, time-dependent phenomena. These effects are specific to each combination of textile reinforcement and concrete. Hegger and Voss (2008) therefore proposed that an effectiveness factor ( $k_1$ ) be applied to the ultimate reinforcement strength, defined in Equation 4.3. This value can be determined experimentally in tensile tests on TRC specimens. The value of  $k_1$  may be different in the warp and fill directions due to the differing yarn geometry.

$$k_1 = f_{tc}/f_t \quad (4.3)$$



### 4.2.2 Specimen construction

TRC specimens of 15mm and 30mm thickness were tested in tension, four-point bending, and eccentric compression. In each case, loading was aligned parallel to the warp reinforcement direction. Each specimen contained a single top and bottom layer of reinforcement with 3mm of cover. All specimens were 80mm wide, and therefore contained ten yarns per reinforcement layer. This resulted in reinforcement ratios of 0.871% and 0.435% for the 15mm and 30mm thick sections respectively (in the warp direction). These values are low compared to other existing TRC projects, even where stronger and stiffer carbon fibre is used instead (May et al., 2019; Scholzen et al., 2015b; Sharei et al., 2017).

According to European standard EN 206-1, a minimum of three samples per concrete batch are required to verify strength (CEN, 2000). In this case, four repeats were made of each test. It should be noted, however, that the accurate determination of characteristic strength values (95% exceedance probability) would require a much higher number of samples, as sufficient to represent a normal distribution.

Tensile and bending specimens were cast in flat panels of uniform thickness, 700mm long by 500mm wide, using the formwork shown in Figure 4.6a. These panels were cut into 80mm wide specimens after casting. The compression specimens were cast in strips in bespoke timber moulds (Figure 4.6c), which were also cut into 80mm wide specimens.

The manual construction techniques used in this instance would not be practical for full-scale shells, however the low number of reinforcement layers (compared to Scholzen et al. (2015a), for example) and uniform thickness of these TRC sections would enable fast automated fabrication using sprayed concrete and quick placement of reinforcement in sheets.

The fine grained mortar was mixed using a bell mixer. Each of the three concrete layers was spread by hand using trowels, with the thickness checked relative to the formwork tops using wooden guides. Pre-cut reinforcement pieces were placed by hand between each layer, and care was taken to ensure that the concrete was thoroughly worked-in around the reinforcement to minimise the presence of voids. The specimens were de-moulded within three days, cut into 80mm wide sections, placed in a water bath at room temperature for curing, and tested at ages between 27 and 33 days.

### 4.2.3 Tensile tests

#### Methodology

In testing, the ultimate tensile strength of TRC can be strongly influenced by the specimen geometry and load application method (Hartig et al., 2012). Brameshuber (2016) recommends



Figure 4.6: Construction of TRC test specimens, showing a) panel formwork for tensile and bending specimens, b) fine-grained concrete prior to trowelling, c) compression specimen formwork and d) de-moulded compression specimens prior to cutting.

clamping TRC strips between steel plates over a sufficiently large region to prevent debonding of reinforcement or slip of fibres. This was the approach taken in this case, as shown in Figure 4.7c.

Four TRC specimens of each thickness were tested in tension. The thickness of each specimen was measured, taking an average of four calliper readings across the central 300mm region. The average thicknesses of each group of four specimens were 15.30mm (standard deviation 0.44mm) and 31.39mm (standard deviation 0.26mm).

Steel clamping plates were used to apply the load, with 3mm thick rubber inserts assisting in gripping the specimen. The load was applied using displacement control at a rate of 4mm/min via pins through the clamping plates, which can therefore rotate freely.

The applied load and loading pin displacement were recorded at 0.1s intervals. This data is however insufficient to record an accurate stress-strain response of the material due to deformation of the clamping system, which arises from shearing of the rubber inserts, slip, and deformation of the TRC within the clamped region itself. Digital image correlation (DIC) was therefore used to measure displacement of the central, un-clamped region.

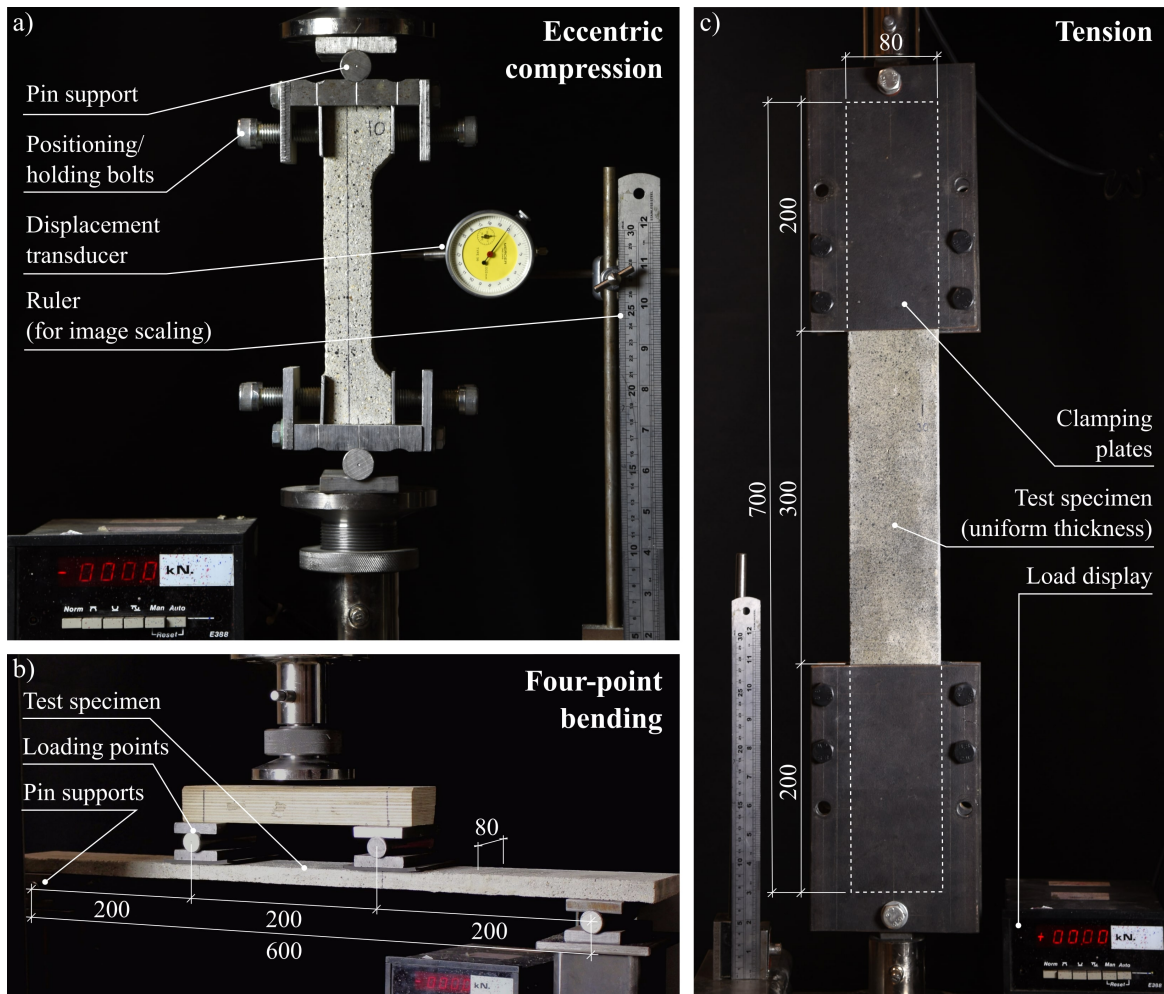


Figure 4.7: TRC testing arrangements showing a) eccentric compressions tests, b) four-point bending tests and c) tensile tests (dimensions in mm).

Photographs for DIC analysis were taken at four second intervals. A digital display was synchronised with the load cell so that each image displayed the applied load. A ruler was also positioned within the image (in the plane of the specimen surface) for scaling. The approximate size of a pixel was 0.15mm. The front face of each tensile specimen was flecked with black paint to create a random pattern with high-contrast, as favoured by the DIC algorithm.

The open-source software Ncorr (Blaber et al., 2015) was used to perform the DIC analysis, which runs through MATLAB. This software has been verified against commercial DIC software packages by Harilal and Ramji (2014). The main DIC algorithm used by Ncorr is based on the reliability-guided DIC framework developed by Pan (2009). The overall strategy of a DIC algorithm is to match small regions (subsets) of a reference (undeformed)

image to the same regions in a deformed image. The relative displacements of these subsets can then be found and used to determine the strain field. The size and spacing of the subsets affect the resolution and smoothing of the results. After some experimentation, a subset radius of 20 pixels and subset spacing of 5 pixels were chosen.

The output data for each image is a 2D array of displacement values, spaced at approximately 0.8mm in this instance. A bespoke MATLAB script was written to convert this data into a single value of average strain, which, combined with the load displayed in each image, enables the plotting of a stress-strain curve for each test. Firstly, the 2D array was converted to 1D by averaging the displacement across each row. The average strain was then taken as the gradient of a straight line of best fit found using the least-squares method. A limitation of this approach is that, by taking the average strain over the whole central region, the post-cracking results are potentially sensitive to the number of cracks.

An example of the DIC results and the calculation of average strain for a 15mm sample is shown in Figure 4.8. Individual cracks are shown clearly in the data, and these are smoothed out to calculate an average strain value from each image. The results highlight specimen slip, since displacement near the lower clamping plate is non-zero.

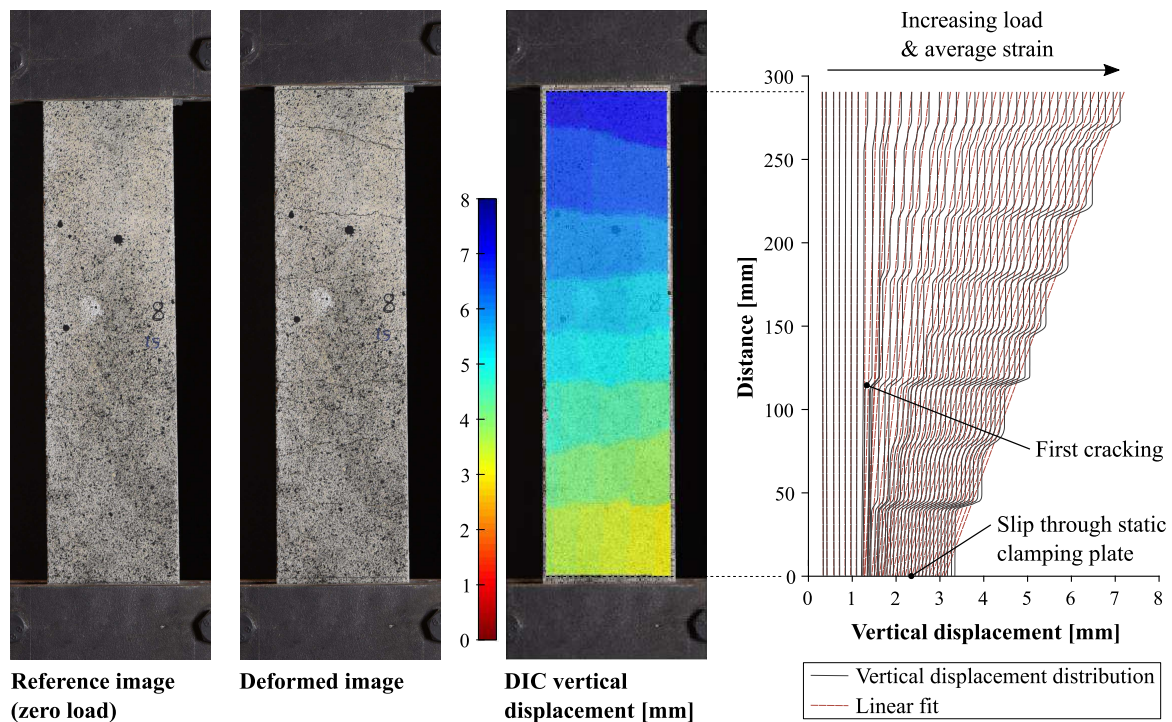


Figure 4.8: Example of DIC results and calculation of strain (15mm thick specimen).

## Results

Figure 4.9 shows the results from the tensile tests, including both the direct measurements of loading pin displacement and the strain results calculated using DIC. The load corresponds to the middle of the specimen, and therefore includes the self-weight of one pair of clamping plates plus half of the specimen itself.

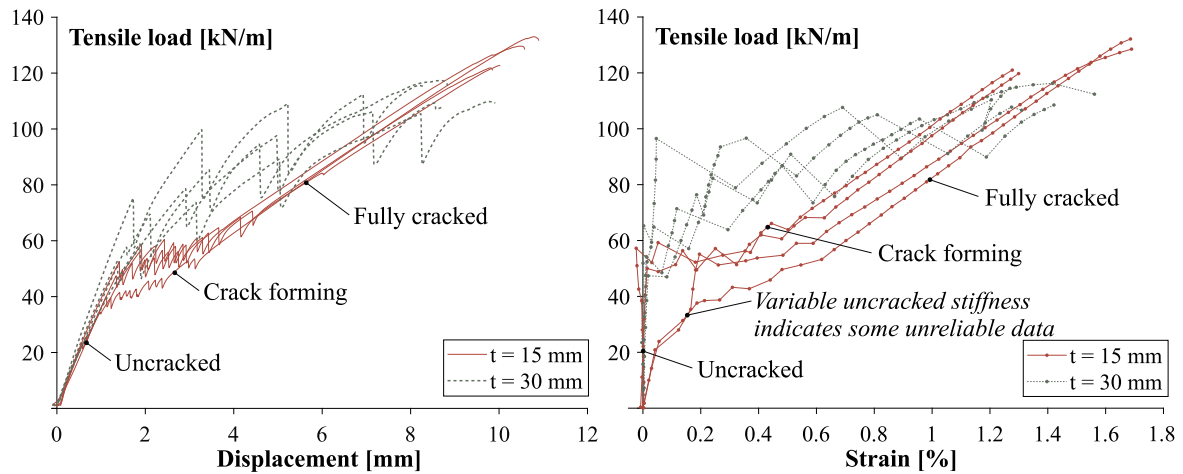


Figure 4.9: TRC tensile test results, showing both direct displacement measurements (left) and average strains calculated from DIC results (right).

The load-displacement results show clearly the initial uncracked linear behaviour and subsequent crack formation. For the 15mm specimens, fully cracked behaviour was then developed, which is again linear. However, for the 30mm specimens the reinforcement failed during the crack formation phase.

Linear-elastic behaviour is expected in the uncracked state, with stiffness dominated by the concrete and therefore proportional to the specimen thickness. However, Figure 4.9 (left) shows similar uncracked load-displacement gradients for the 15mm and 30mm specimens. This highlights the key limitation of this data, which is that a significant proportion of the measured displacement arises outside of the central 300mm region; from specimen slip, shearing of the rubber inserts and specimen deformation within the clamped region.

Figure 4.9 (right) shows the load-strain results from the DIC analysis, which aims to address this issue by measuring deformation over the central region only. The formation of individual cracks cannot be seen due to the low resolution of data points, each of which corresponds to a single image. However, the same uncracked, crack-forming and fully-cracked regions are visible in some of the results. The DIC results also show the large reduction in stiffness caused by cracking much more clearly and accurately than the load-displacement results.

The accuracy of the DIC data for small strains is also questionable, shown by the variation in uncracked stiffnesses. A typical concrete cracking strain is 0.01%, corresponding to an elongation of 0.03mm over the 300mm length investigated. This is significantly smaller than the approximate pixel size of 0.15mm. Although sub-pixel measurements are possible using DIC, high accuracy would not be expected in this case. A useful verification of the DIC results might have been made using the laser extensometer described previously in Section 4.2.1.

Figure 4.10 shows images taken from the tensile tests after, or near to, failure. For the 15mm specimens, an average of 7.5 cracks were observed across the central region, whilst this number was only 3.0 for the 30mm specimens. In all cases, ultimate failure occurred at the location of a crack in the concrete. This critical crack was located near or within the clamping plates for each of the 15mm specimens, but within the central region for all but one of the 30mm specimens.

Figure 4.10a shows the ruptured reinforcement. Only internal fibres are left exposed, which suggests a strong bond between the concrete and the outer fibres. The length of these exposed fibres was between 5mm and 15mm for both sets of specimens, giving some indication of the distance over which reinforcement force is transferred from the outer to the inner fibres.

Key results for each tensile test are summarised in Table 4.3. The average tensile strengths were 127kN/m and 113kN/m for the 15mm and 30mm sections respectively, corresponding to reinforcement stresses of 971MPa and 866MPa, and strength reduction factors ( $k_1$ ) of 0.814 and 0.726 (relative to 1192MPa for the reinforcement only). The strength of the textile is therefore reduced when embedded in concrete, and this effect is increased at lower reinforcement ratios (due to increasing crack width) as previously described by Hegger and Voss (2005).

The loads causing initial cracking were taken from the load-extension data. The locations of these first cracks were also noted and the local thickness recorded, thus enabling the tensile strength of the concrete to be calculated for each test. The average concrete tensile strength was 2.93MPa (standard deviation 0.34MPa) for the 15mm specimens and 2.27MPa (standard deviation 0.29MPa) for the 30mm specimens. In the majority of the tests, cracking initially occurred within or near to the clamping plates. This suggests that the effective tensile strength may have been reduced by the clamping pressure, which causes a tensile strain in the direction of loading due to Poisson's ratio effects.

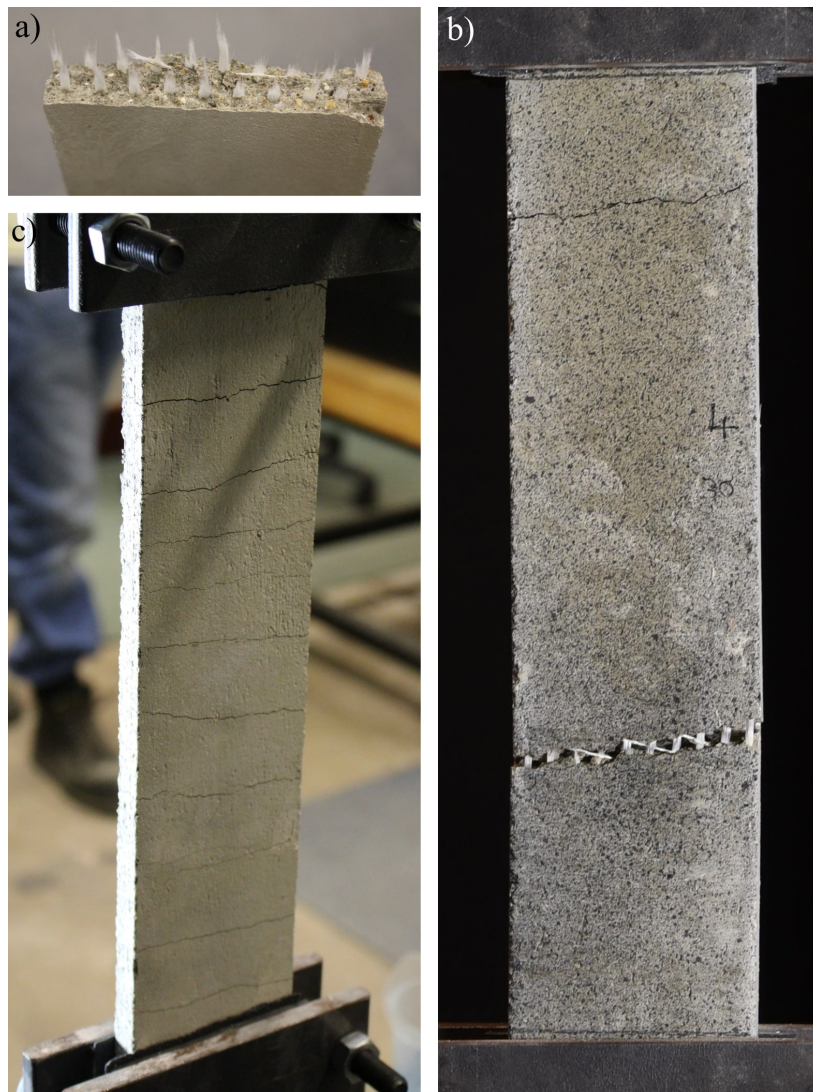


Figure 4.10: Images from tensile TRC tests, showing a) failed 15mm thick specimen, b) failed 30mm specimen and c) cracked 15mm specimen prior to failure.

#### 4.2.4 Four-point bending tests

##### Methodology

Four specimens of each thickness were tested in four-point bending using the test set-up shown in Figure 4.7b. Load was applied equally at two points in displacement-controlled tests, at rates of 10mm/min and 3.5mm/min for the 15mm and 30mm specimens respectively. Both the support and loading points were pinned to allow free rotation, with the supports also free to slide. Sheets of 3mm thick rubber were inserted beneath the loading points to reduce concentrated bearing forces.

Table 4.3: Tensile TRC test results summary.

Average thickness [mm]	First cracking load [kN/m]	Concrete tensile strength [MPa]	Ultimate load [kNm/m]	Reinforcement failure stress [MPa]
<i>15mm specimens</i>				
15.3	40.1	2.62	129.6	993
14.6	39.6	2.72	133.0	1019
15.7	47.5	3.02	122.7	940
15.6	52.4	3.37	121.9	933
<i>30mm specimens</i>				
31.1	75.3	2.42	115.6	885
31.2	57.7	1.85	117.4	899
31.7	78.6	2.48	109.3	837
31.6	73.7	2.33	109.9	842

The total applied load and the average displacement of the support points were recorded at 0.1s intervals. Unlike in the tensile tests, this displacement was assumed to represent the true deformation of the specimen due to the relatively large specimen displacements, the low applied forces in the spreader assembly and assumed low deformation of rubber inserts in compression. The moment in the central region was calculated assuming a constant lever arm of 200mm. At large curvatures, there is a possibility of this distance reducing as the specimen deforms, or increasing due to expansion caused by an eccentric neutral axis after cracking. The change in lever arm was measured by analysing images taken throughout the tests, showing a maximum change of 3% for the highest deformations recorded. This effect was therefore ignored.

## Results

Figure 4.11 shows the measured mid-span moment and loading point displacement from each four-point bending tests. Three distinct uncracked, crack forming and fully cracked regions are visible, showing a similar pattern to the tensile results. However, in this instance, both sets of specimens appear to have developed into a fully-cracked state prior to failure. The variation of uncracked stiffness between similar specimens is less than the fully cracked stiffness, since the latter is sensitive to crack distribution. Figure 4.12 shows examples of two specimens near failure, highlighting the greater curvature and number of cracks in the 15mm specimens.

For all specimens, failure was sudden and occurred due to tensile rupture of the reinforcement at the location of a large crack within the central region. Figure 4.13 shows typical



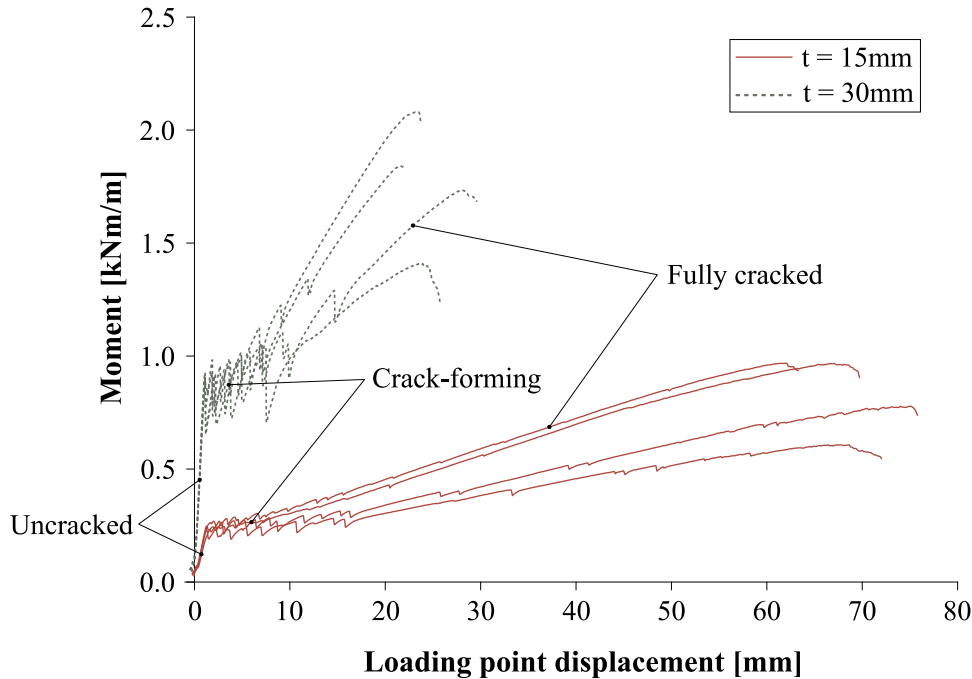


Figure 4.11: Results from four-point bending tests

examples of these locations after failure. Pull-out of reinforcement fibres is visible in both cases caused by breaking of the fibres near the crack. Crushing of the concrete is also visible in the compression zone, particularly for the 15mm thick specimen, however this was most likely initiated by the reinforcement failure.

Table 4.4 summarises key results from each test. The average ultimate moments were 0.832kNm/m (standard deviation 0.173Nm/m) and 1.768kNm/m (standard deviation 0.278kNm/m) for the 15mm and 30mm specimens respectively. The ratio of these average strengths might be expected to reflect the ratio of the distances between the bottom reinforcement layer and the centre of the concrete compression zone. Assuming a small compression zone, this ratio is 2.25, similar to the average strength ratio of 2.13. The large range of strengths recorded between similar specimens is likely a reflection of the sensitivity of the reinforcement failure to crack width. In practical design scenarios, this uncertainty would be dealt with through the use of characteristic values and partial factors.

The loading at first cracking was recorded for each test, allowing the flexural tensile strength of the concrete to be calculated based on the measured thickness of each specimen (included in Table 4.4). The average concrete flexural strengths were 6.43MPa (standard deviation 0.34MPa) and 5.96MPa (standard deviation 0.15MPa) for the 15mm and 30mm specimens respectively. These values are 119% and 163% larger than the concrete tensile strengths measured in pure tension. These discrepancies are in-line with the expected

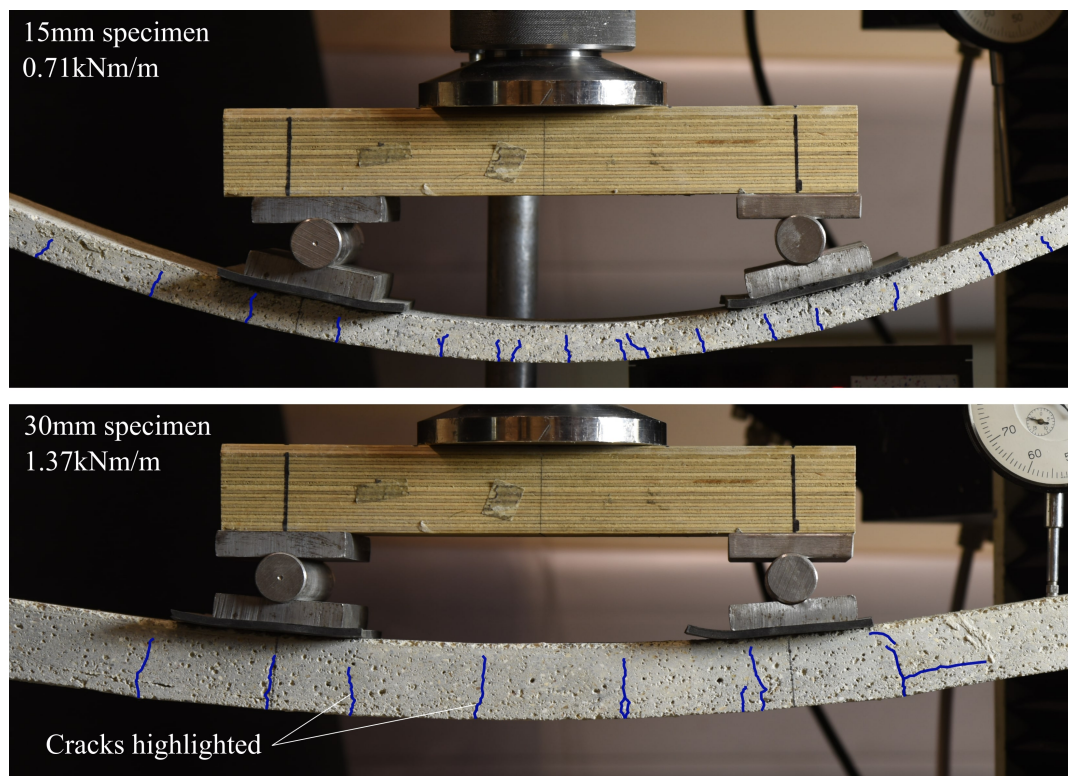


Figure 4.12: Typical 15mm (top) and 30mm (bottom) specimens at peak curvature with cracking patterns highlighted

size effect for brittle materials (Bazant and Planas, 1997; Bentz, 2019), discussed later in Section 4.4.5.

The tensile stress in the reinforcement at failure ( $f_{tc}$ ) is also included in Table 4.4, estimated by assuming a lever arm 3mm less than the measured specimen thickness. The results show considerable variation between specimens. The average stresses at failure were 1030MPa and 982MPa for the 15mm and 30mm specimens respectively, similar to the values calculated in the pure tensile tests (Table 4.3). This supports the observation that tensile rupture of reinforcement initiated failure. A greater number of tests would be required to determine whether there is a statistically significant difference in the reinforcement tensile strength in bending and tension.

## 4.2.5 Eccentric compression tests

### Methodology

Eccentric compression tests were carried out to determine the ultimate strength under combined axial compression and bending, using the test arrangement shown in Figure 4.7a.

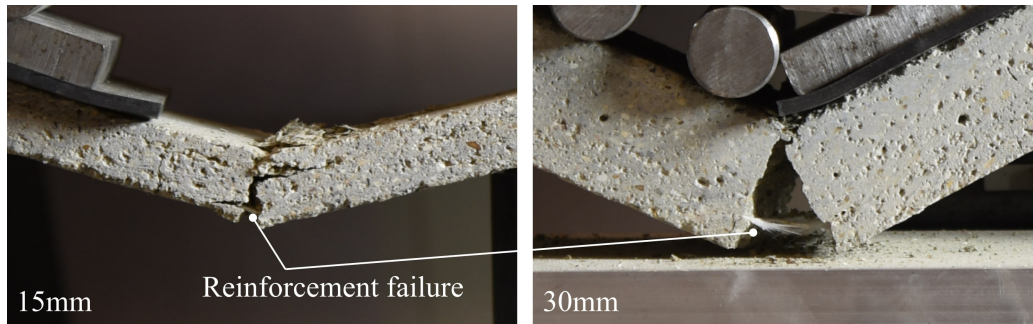


Figure 4.13: Failed regions TRC specimens after testing in four-point bending, showing tensile rupture and pull-out of reinforcement.

Table 4.4: Four-point bending tests on TRC specimens: result summary

Average thickness [mm]	First cracking moment [kNm/m]	Concrete tensile strength [MPa]	Ultimate moment [kNm/m]	Estimated reinforcement failure stress, $f_{tc}$ [MPa]
<i>15mm specimens</i>				
15.1	0.250	6.63	0.779	991
14.7	0.245	6.81	0.968	1267
14.9	0.228	6.20	0.609	787
15.6	0.247	6.08	0.887	1076
<i>30mm specimens</i>				
30.6	0.909	5.84	2.081	1157
30.3	0.904	5.90	1.353	759
30.4	0.913	5.92	1.842	1029
30.0	0.930	6.19	1.736	984

A total of 64 tests were performed; two specimen thicknesses tested at eight loading eccentricities, each repeated four times. The nominal eccentricities tested were 0mm, 2mm, 4mm, 6mm, 8mm, 12mm, 20mm and 45mm. Specimen geometry is shown in Figure 4.14, highlighting the increased end thickness used to ensure failure within the central region. The specimens were fixed in place using a pair of steel clamping plates at the top and bottom. Four bolts were used to securely fix the specimen at each end, preventing slipping, and to ensure precise setting of the loading eccentricity.

The applied load and the vertical displacement of the loading plate were measured at 0.1s intervals. A variable loading rate was used, ranging from 1mm/min to 4mm/min depending on the expected deformation.

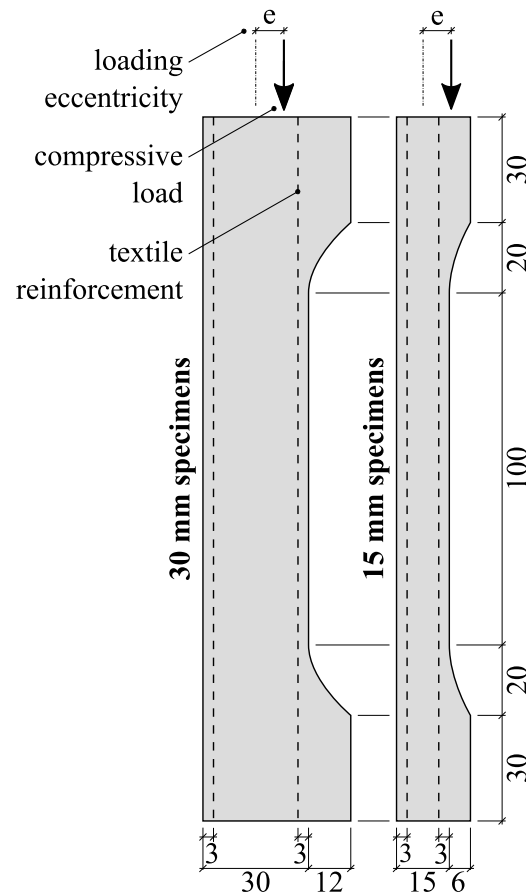


Figure 4.14: Eccentric compression test specimen geometry (dimensions in mm).

The applied moment is the product of the axial force and the eccentricity relative to the loading pins. This increases as the specimens deform, and was therefore measured to enable an accurate calculation of ultimate moment. Photographs were captured at four second intervals during the test by a fixed camera, and the maximum lateral displacement was scaled from the photograph taken prior to the maximum load. This measurement was verified through comparison with a dial gauge. This method also accounted for any initial misalignment of the specimen in the loading clamps. The estimated accuracy of these measurements is  $\pm 0.4$  mm, with errors arising primarily due to uncertainty in defining the specimen centrelines from the edges (which are not perfectly straight).

The thicknesses of each specimen were again averaged from four calliper readings taken over the central region.

## Results

Tables 4.5 and 4.6 show key results for each tested specimen including average thickness, maximum eccentricity prior to failure, ultimate axial and bending forces, and failure mode corresponding to Figure 4.15.

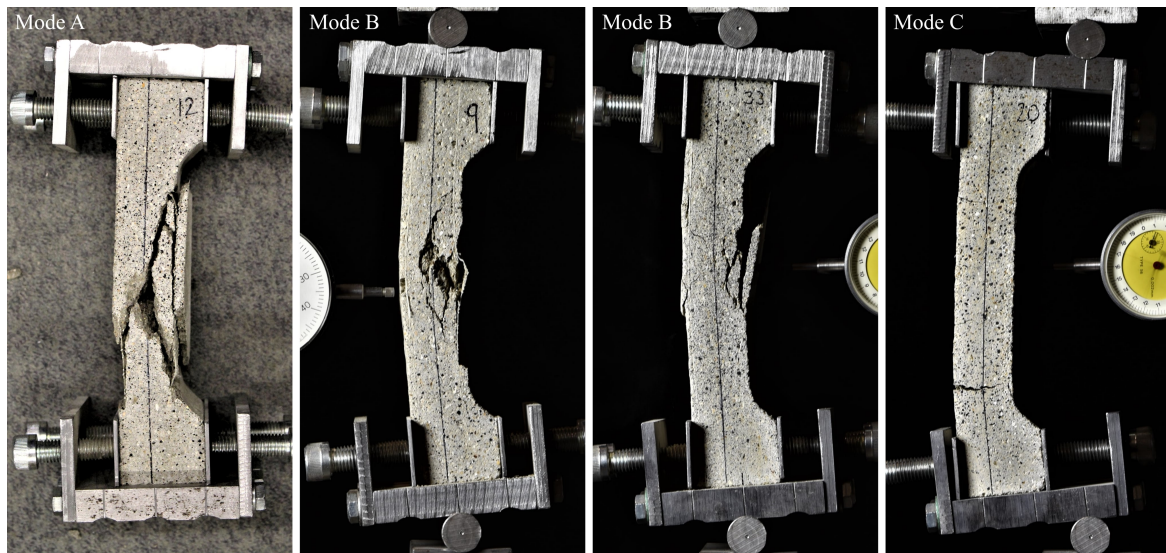


Figure 4.15: Failed 30mm specimens tested at 0, 4, 8 and 45mm loading eccentricities (left to right), showing explosive compression failure (mode A), partial concrete crushing (mode B) and reinforcement pull-out (Mode C).

A range of failure types were observed in the compression tests depending on the specimen thickness and loading eccentricity. Those for which  $e = 0-2\text{mm}$  failed explosively with cone shaped or inclined shear failure planes extending across the full width (Mode A), in a similar manner to the prism compression tests. At moderate eccentricities ( $e = 2-8\text{mm}$  or  $e = 2-12\text{mm}$  for the 15mm and 30mm specimens respectively), concrete was crushed only in the compression region of the section near the mid-span (Mode B). For the largest loading eccentricities, failure occurred prematurely via pull-out of the reinforcement due to insufficient anchorage (Mode C). This was characterised by the development of large cracks near the ends of the specimen and a steady reduction or plateau in the load-displacement results. For these specimens, the central fibres of the reinforcement yarns slipped despite the peripheral fibres remaining bonded to the concrete. The strength would have been higher had this not occurred, since the specimens would likely have gone on to fail either through concrete failure in the compression zone or tensile failure of the reinforcement. To avoid this issue, the test specimens would require re-designing with improved anchorage of the yarns beyond the region of maximum moment.

Table 4.5: Eccentric compression test results (15mm specimens).

<b>Thickness</b>	<b>Nominal eccentricity</b>	<b>Maximum measured eccentricity</b>	<b>N<sub>max</sub></b>	<b>M<sub>max</sub></b>	<b>Failure mode</b>
[mm]	[mm]	[mm]	[kN/m]	[kNm/m]	
14.10	0	0.62	809.5	0.50	A
14.00	0	0.23	782.2	0.18	A
15.27	0	0.83	622.6	0.52	A
15.03	0	0.61	732.7	0.45	A
14.23	2	3.31	594.3	1.97	A
13.93	2	2.64	563.7	1.49	A
15.47	2	3.11	578.7	1.80	A
15.00	2	2.66	566.9	1.51	A
13.80	4	4.69	414.5	1.94	B
14.37	4	5.07	480.6	2.44	B
15.47	4	4.03	383.2	1.54	B
14.93	4	5.39	413.5	2.23	B
14.90	6	6.43	237.2	1.53	B
13.73	6	6.91	188.9	1.31	B
14.40	6	7.39	172.3	1.27	B
15.47	6	7.82	223.7	1.75	B
14.47	8	8.30	101.7	0.84	C
13.67	8	8.99	72.4	0.65	C
14.77	8	9.37	97.3	0.91	C
15.97	8	9.01	117.2	1.06	C
13.33	12	18.84	34.6	0.65	C
14.67	12	17.72	41.2	0.73	C
14.50	12	16.64	44.4	0.74	C
16.03	12	17.73	42.3	0.75	C
13.10	20	30.92	23.5	0.73	C
14.53	20	28.73	24.9	0.72	C
14.80	20	28.86	27.4	0.79	C
16.07	20	28.27	28.4	0.80	C
13.07	45	55.07	9.8	0.54	C
14.63	45	54.01	11.0	0.59	C
14.53	45	53.26	11.1	0.59	C
16.27	45	54.05	11.5	0.62	C

Table 4.6: Eccentric compression test results (30mm specimens).

<b>Thickness</b>	<b>Nominal eccentricity</b>	<b>Maximum measured eccentricity</b>	<b>N<sub>max</sub></b>	<b>M<sub>max</sub></b>	<b>Failure mode</b>
[mm]	[mm]	[mm]	[kN/m]	[kNm/m]	
29.87	0	0.05	1524.6	0.08	A
31.03	0	0.32	1479.4	0.48	A
32.53	0	0.09	1580.5	0.14	A
29.87	0	0.69	1452.7	1.00	A
29.80	2	3.13	1458.7	4.56	A
29.90	2	2.51	1408.4	3.53	A
30.93	2	2.46	1269.2	3.13	A
31.13	2	2.02	1215.8	2.45	A
29.93	4	4.52	1189.9	5.38	B
29.70	4	4.66	1213.2	5.65	B
31.27	4	4.59	1251.3	5.75	B
30.83	4	6.13	1079.5	6.62	B
29.97	6	6.94	1090.5	7.56	B
29.67	6	7.34	1038.1	7.62	B
31.47	6	7.27	1109.7	8.06	B
30.73	6	7.41	920.7	6.82	B
29.60	8	9.94	816.2	8.11	B
30.70	8	8.66	900.0	7.80	B
31.53	8	8.83	819.6	7.24	B
30.13	8	10.23	710.1	7.27	B
30.70	12	13.53	465.0	6.29	B
31.70	12	13.97	495.7	6.93	B
29.50	12	13.02	487.7	6.35	B
30.00	12	13.81	444.0	6.13	B
30.17	20	24.42	143.2	3.50	B
31.97	20	24.41	159.3	3.89	B
30.50	20	23.88	151.7	3.62	B
29.43	20	23.89	138.1	3.30	B
32.60	45	49.16	39.8	1.96	C
29.27	45	49.06	36.5	1.79	C
30.40	45	50.76	44.2	2.25	C
30.47	45	49.22	31.0	1.52	C

Scatter in both the maximum load and eccentricity was observed between nominally similar tests. This is partially due to imperfect location of the specimens within the loading clamps: the average error in the starting eccentricity was 0.38mm. For the tests with a nominal loading eccentricity of 0mm, some bending was recorded because of small eccentricities arising from misalignment and lateral movement under loading. Further strength variation would be expected to arise due to inconsistent specimen geometry and the non-uniform distribution of material flaws.

Average compressive strengths of 50.3MPa and 48.5MPa were calculated for the 15mm and 30mm specimens respectively, from the tests with a nominal eccentricity of 0mm. In both cases this exceeds the value of 47.2MPa found from the tests on prisms (which were cast at the same time and tested at a similar age). This result is unexpected, since the presence of the reinforcement typically reduces compressive strength (Bochmann et al., 2017). It is possible that the process of producing the TRC by hand resulted in better compaction of the concrete compared to the prisms. Furthermore, the additional compliance in the pin supports of the TRC specimens compared with the rigid steel platens used for the prisms may have created a more even distribution of load, corresponding to increased load capacity.

#### **4.2.6 Experimental failure envelope**

Thin TRC sections fail under combinations of axial forces and bending moments, and their strength can therefore be described using a failure envelope. The strengths of each tested specimen are plotted in Figure 4.16, along with averages for each group of four similar repetitions. Linear interpolation between these points creates failure envelopes. Specimens which failed prematurely due to reinforcement pull-out (Mode C) give a lower-bound of the true strength, and are hence ignored unless their inclusion expands the failure envelope. For both specimen thicknesses, the peak bending capacity occurs in the presence of axial compression.

### **4.3 Analytical failure envelope**

The bi-linear failure envelope proposed by Scholzen et al. (2015b) has previously been discussed in Sections 2.2.3 and 3.4.5, and was shown in Figure 3.17. The bi-linear approximation under tensile loading has been verified experimentally (Scholzen et al., 2015c). However, Figure 4.16 shows that the same assumption in compression is highly conservative. Furthermore, since the bi-linear failure envelope relies on experimentally determined strength values (specific to a single TRC section), the extent to which the designer can quickly explore



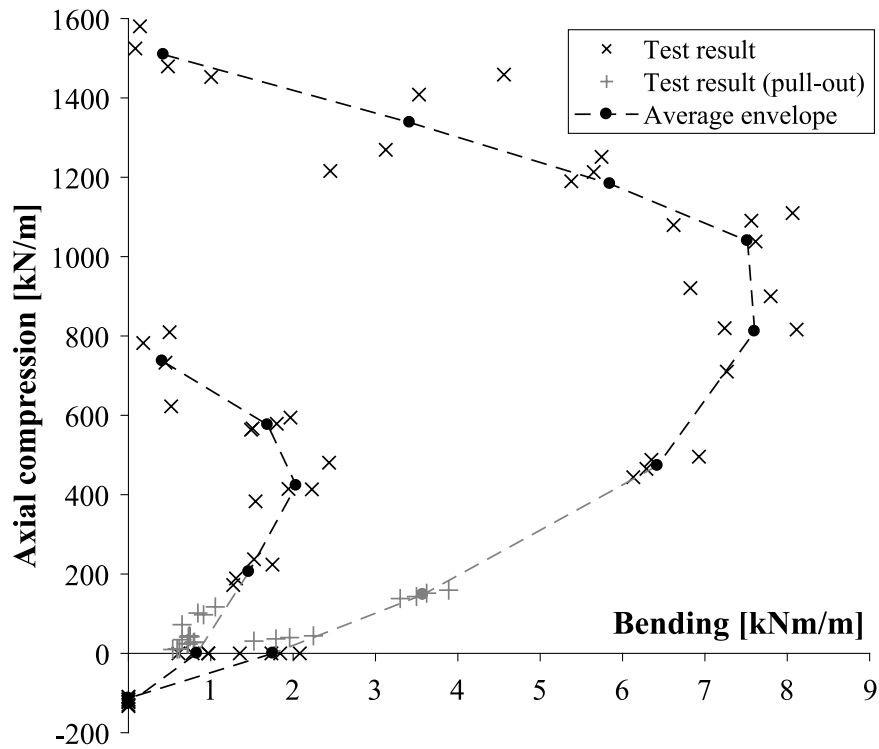


Figure 4.16: TRC failure envelopes based on experimental results.

possible variations in section thickness or reinforcement layout is limited. It is therefore proposed that a more realistic model be created to further improve design efficiency and describe the behaviour of TRC more accurately.

This section introduces an analytical model of TRC strength based on the stress-strain relationships of the constituent materials (Hawkins et al., 2018). This enables multiple sections to be analysed from a single set of tests, and captures the non-linear interaction between axial and bending forces causing failure.

### 4.3.1 Proposed theoretical model

Strength design of concrete beams or slabs with FRP reinforcement is based on the assumption that plane sections remain plane (FIB, 2007). An equivalent method is proposed for analysing TRC sections in bending by (Hegger and Will, 2016). The full failure envelope can therefore be described using stress-strain relationships for both the reinforcement and concrete, where failure is either caused by crushing of the concrete (at a compressive strain of  $\epsilon_{cu}$ ) or tensile rupture of reinforcement (at a tensile strain of  $\epsilon_{tu}$ ). The concrete is modelled using the parabola-rectangle model introduced in Section 4.2.1, and the reinforcement is assumed linear-elastic. Non-linearities arising from crack-bridging and de-bonding are

ignored. Examples of the resulting failure envelopes are shown in Figure 4.17 for a range of reinforcement ratios ( $\rho$ ).

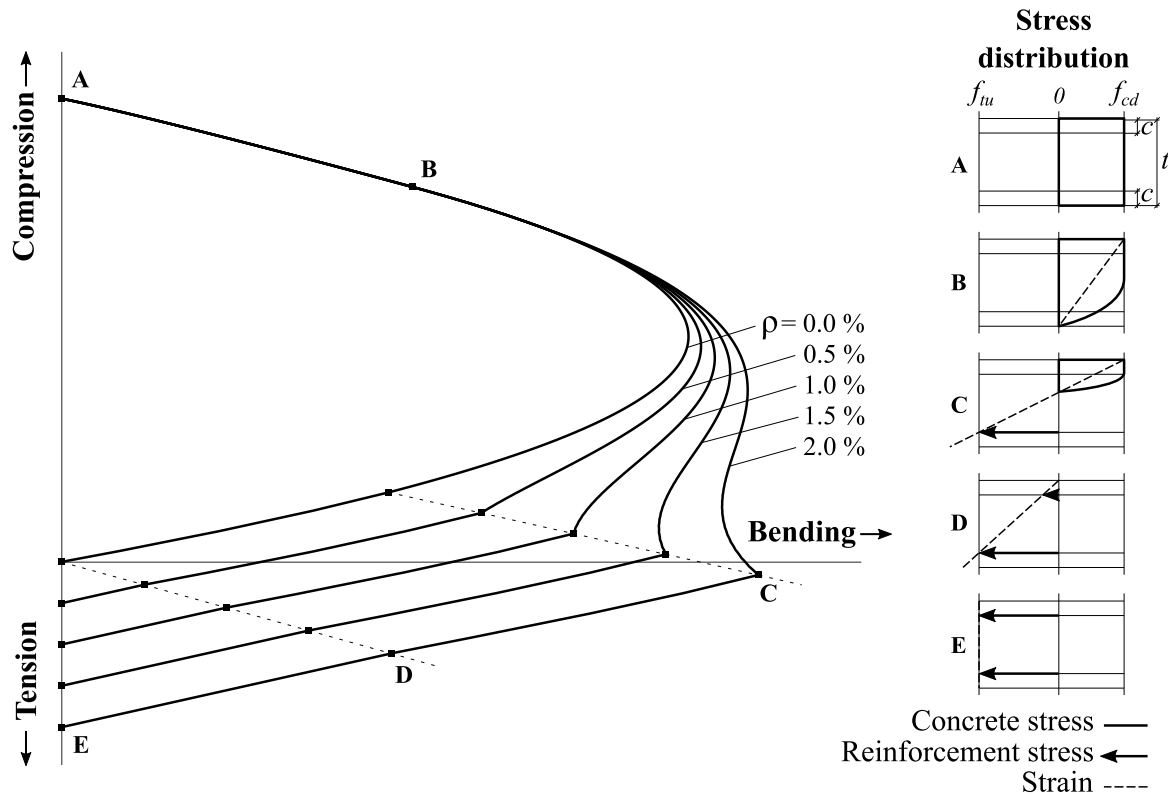


Figure 4.17: Proposed analytical failure envelopes with variable reinforcement ratio.

Each envelope is constructed by analysing the full range of linear strain distributions at failure. The forces are calculated using a numerical procedure, in which the TRC section is divided into layers each with a stress determined from the local strain. The contributions from each layer are summed to find the resultant axial force and bending moment. Five hundred layers were used in the calculation of force and moment (doubling this value was found to have a negligible effect on the calculated forces).

In order to verify this numerical model, analytical expressions were found for pairs of ultimate moment ( $M$ ) and axial force ( $N$ ) for each of the salient points A to E, highlighted in Figure 4.17. These are given in Equations 4.4 to 4.8.

$$\begin{aligned} N_A &= f_{cd}t \\ M_A &= 0 \end{aligned} \quad (4.4)$$

$$\begin{aligned}
N_B &= f_{cd}t \left( 1 - \frac{1}{3} \frac{\epsilon_{c2}}{\epsilon_{cu2}} \right) \\
M_B &= f_{cd}t^2 \left( \frac{1}{6} \frac{\epsilon_{c2}}{\epsilon_{cu2}} - \frac{1}{12} \left( \frac{\epsilon_{c2}}{\epsilon_{cu2}} \right)^2 \right)
\end{aligned} \tag{4.5}$$

$$\begin{aligned}
N_C &= f_{cd}(t-c) \left( \frac{\epsilon_{cu2}}{\epsilon_{cu2} + \epsilon_{tu}} \right) \left( 1 - \frac{1}{3} \frac{\epsilon_{c2}}{\epsilon_{cu2}} \right) \\
&\quad - E_t A_t \left( \epsilon_{tu} + \max \left( 0, c \left( \frac{\epsilon_{tu} + \epsilon_{cu2}}{t-c} \right) - \epsilon_{cu2} \right) \right) \\
M_C &= f_{cd}(t-c)^2 \left( \frac{\epsilon_{cu2}}{\epsilon_{cu2} + \epsilon_{tu}} \right)^2 \left( \frac{1}{2} \left( 1 - \frac{\epsilon_{c2}}{\epsilon_{cu2}} \right) \left( \frac{t}{t-c} \frac{\epsilon_{cu2} + \epsilon_{tu}}{\epsilon_{c2}} - \left( 1 - \frac{\epsilon_{c2}}{\epsilon_{cu2}} \right) \right) \right. \\
&\quad \left. + \frac{1}{3} \frac{\epsilon_{c2}}{\epsilon_{cu2}} \left( \frac{t}{t-c} \frac{\epsilon_{cu2} + \epsilon_{tu}}{\epsilon_{c2}} - 2 + \frac{15}{12} \frac{\epsilon_{c2}}{\epsilon_{cu2}} \right) \right) \\
&\quad + E_t A_t \left( \frac{t}{2} - c \right) \left( \epsilon_{tu} - \max \left( 0, c \left( \frac{\epsilon_{tu} + \epsilon_{cu2}}{t-c} \right) - \epsilon_{cu2} \right) \right)
\end{aligned} \tag{4.6}$$

$$\begin{aligned}
N_D &= -\epsilon_{tu} A_t E_t \left( 1 + \frac{c}{t-c} \right) \\
M_D &= \epsilon_{tu} A_t E_t \left( \frac{t}{2} - c \right) \left( 1 - \frac{c}{t-c} \right)
\end{aligned} \tag{4.7}$$

$$\begin{aligned}
N_E &= -2\epsilon_{tu} A_t E_t \\
M_E &= 0
\end{aligned} \tag{4.8}$$

The failure envelopes show both linear and non-linear regions. Both points A and B are independent of the reinforcement ratio since the section is entirely in compression. The points labelled C correspond to a ‘balanced failure’, at which the reinforcement and concrete are both theoretically at the point of failure. This point lies either on the compressive or tensile side, and therefore the failure mechanism in pure bending transitions from reinforcement tensile failure to concrete crushing with increasing reinforcement ratio. For larger reinforcement ratios, a point of inflection is observed where an increasing compressive force reduces, then increases, and then again reduces the ultimate moment capacity (between the points B and C). This behaviour is not usually present for steel reinforced sections, where the force in the steel is limited by the yield strength, but occurs because the textile stress increases all the way to failure. The moment capacity therefore increases even as the concrete compression zone becomes smaller. A similar result is shown in the failure envelopes proposed for the design of glass FRP reinforced columns by Zadeh and Nanni (2012). At point D, the strain is tensile

throughout the section and there is no strength contribution from the concrete. Between points D and E, the concrete is cracked throughout the total section depth and the failure envelope is linear, reflecting the elasticity of the reinforcement. The points at E are simply the strength of the reinforcement in tension ( $\rho t f_{td}$ ).

### 4.3.2 Comparison with experimental envelope

Figure 4.18 compares the experimental, proposed and bi-linear (Scholzen et al., 2015b) failure envelopes. The analytical failure envelopes are plotted using material and geometric parameters most closely corresponding to each specimen thickness, as summarised in Table 4.7, to enable a direct comparison.

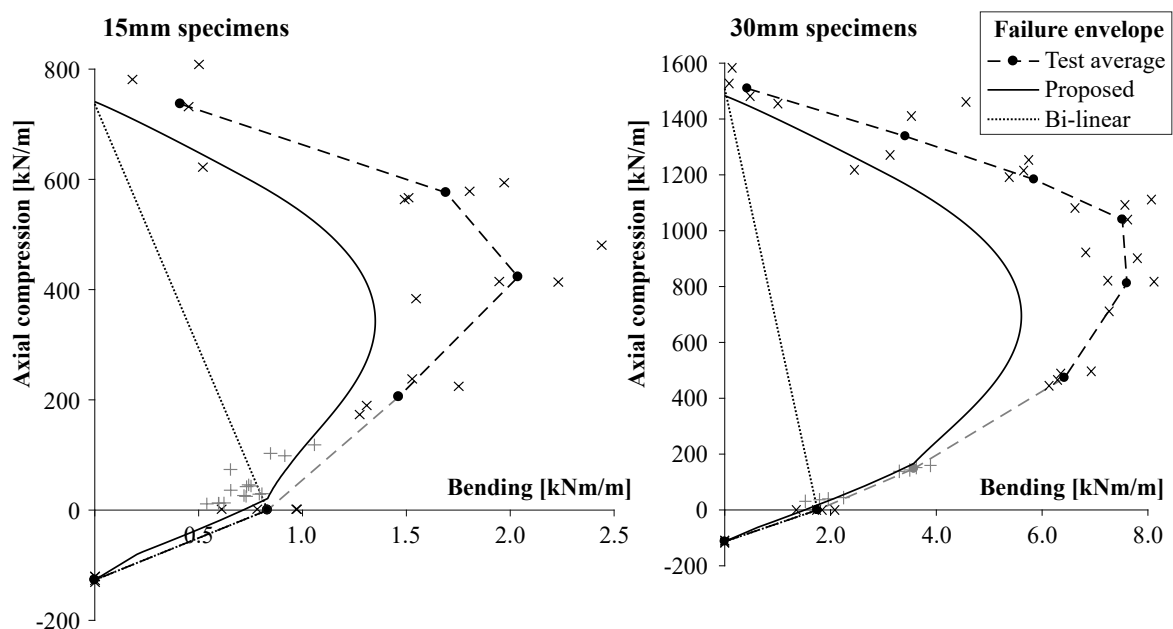


Figure 4.18: Comparison of experimental, proposed and bi-linear (Scholzen et al., 2015b) envelopes for the tested 15mm (left) and 30mm (right) thick specimens.

For both the 15mm and 30mm specimens, the proposed envelope lies within the average experimental envelope and therefore gives a consistently conservative strength prediction. Under pure compression or tension, the two envelopes would be expected to match since the theoretical envelope is defined by values from these tests. The slight discrepancies in pure compression strength are due to variation in specimen thickness. In pure bending, the theoretical model gives a close prediction of the true strength. Since failure under pure bending was initiated by the reinforcement, this suggests that the reinforcement strength values calculated from the tensile TRC tests are reliable.

Table 4.7: Summary of parameters used for plotting proposed failure envelopes in Figure 4.18

		15mm envelope	30mm envelope	Notes
<b>Section properties</b>				
$t$	[mm]	14.74	30.57	Measured average of all samples
$c$	[mm]	3	3	Design value
<b>Concrete properties</b>				
$f_{cd}$	[MPa]	50.3	48.5	TRC compression test average ( $e=0\text{mm}$ )
$\epsilon_{c2}$	[%]	0.2	0.2	Typical value
$\epsilon_{cu2}$	[%]	0.35	0.35	Typical value
$n$	-	2	2	Typical value
<b>Reinforcement properties</b>				
$f_t$	[MPa]	1192	1192	Average from reinforcement tests
$k_1$	-	0.814	0.726	Average from TRC tension tests
$E_t$	[GPa]	64	64	Average from reinforcement tests
$A_t$	[mm <sup>2</sup> /m]	65.3	65.3	Measured (includes weight of coating)

A larger disparity between the experimental and proposed envelopes is observed under combined compression and bending. Here the theoretical model is conservative, particularly around the region of maximum bending strength. The gradient of the proposed envelope at the largest compressive loads is steeper than the experimental envelope, showing a faster reduction in compressive strength with increasing applied moment. The failure in these regions is governed by the concrete properties alone, and therefore an investigation into the effect of the concrete model on the theoretical envelope was carried out.

### Sensitivity to concrete model

For a fixed maximum concrete strength, the ratio of bending to compressive force is influenced by the concrete stress-strain model, since the stress distribution in the compression zone dictates the effective lever arm. The bending moment at failure therefore increases as the stress-strain model approaches rigid-plastic.

The proposed failure envelopes for the tested specimens are re-plotted in Figure 4.19 using modified stress-strain models for the concrete. As well as the parabola-rectangle model, a rigid-plastic concrete model was used with strain limits of both 0.35% and 0.5%. This resulted in some increase in the predicted bending strength where failure is caused by concrete crushing (by up to 5.4% at the peak moment capacity). However, the changes are smaller than the discrepancies with the experimental strength shown in Figure 4.18.

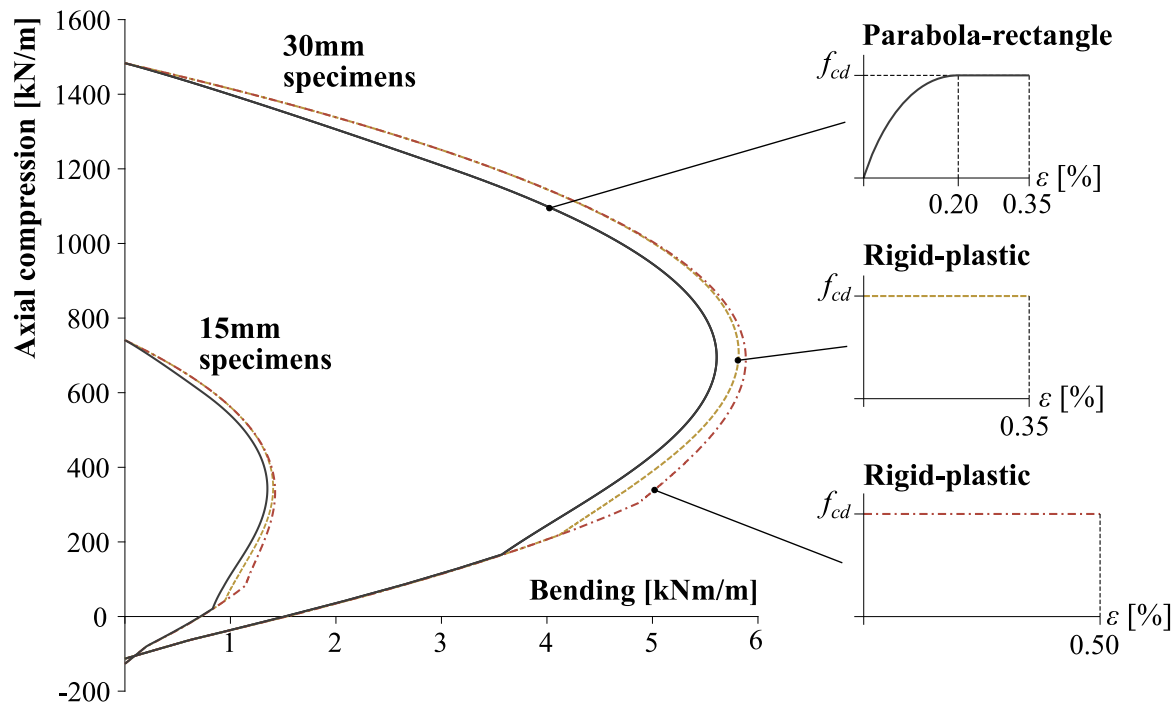


Figure 4.19: Influence of concrete stress-strain model on predicted failure envelope.

It can therefore be concluded that the failure envelope is not sensitive to the concrete model or strain limits. This means that, for design purposes, some uncertainty in the concrete model is allowable. The parabola-rectangle model can therefore be recommended as a conservative choice, which is also familiar to practising structural engineers. The tensile capacity of the concrete was found to have a negligible impact on the failure envelope.

### Size effects

The discrepancy between the predicted and measured strengths could instead be a result of an inverse relationship between the concrete strength and the size of the compression zone. Size dependent compressive strength is well documented in brittle materials such as concrete (Bazant and Planas, 1997). An increase in both ultimate strength and strain with reducing compression zone size was demonstrated by Kim and Yi (2002) in reinforced concrete beam-columns. Further work would be required to investigate and quantify the significance of this phenomenon for thin-walled structures with fine-grained concrete and textile reinforcement.

### 4.3.3 Comparison with bi-linear failure envelope

Scholzen et al. (2015b) acknowledge that a bi-linear failure envelope significantly underestimates the true bending strength in compression, and this is shown clearly in Figure 4.18. In this case, the proposed envelope predicts a section utilisation up to 2.1 and 3.7 times greater for the 15mm and 30mm sections respectively, compared to a bi-linear envelope. This potentially enables significant material savings in structures where combined bending and compressive forces dominate.

In the tensile region of the failure envelope, a linear approximation is approximately valid provided that the reinforcement ratio is sufficiently low to ensure that failure is always initiated by the reinforcement (see points C in Figure 4.17). For the results shown in Figure 4.18, a linear interpolation between test values would predict a slightly higher strength than the proposed envelope in this case. This is because the average experimental strength in pure bending was higher than that predicted by the proposed model. Interestingly, the non-linearity of the proposed envelope in the tensile region (a change in gradient at the points D in Figure 4.17) suggests that a linear interpolation may in fact be slightly unconservative. However, due to the lack of test results under combined tension and bending in this investigation, firm conclusions cannot be drawn here.

The amount of physical testing required to construct the failure envelope is greatly reduced by using the proposed method. Using material strength rather than section strength to determine the envelope enables a range of hypothetical sections to be analysed, thus allowing quicker exploration and optimisation of TRC section designs.

### 4.3.4 Practical application for shells

As discussed in Sections 2.2.3 and 3.4.5, the strength of textile reinforcement is reduced when bridging inclined cracks (Hegger et al., 2006b). The effective axial stiffness per unit length of the reinforcement is also a function of loading direction. These effects must therefore be accounted for in the application of the proposed failure envelope in shells, where forces are not necessarily aligned with the reinforcement. A method for determining the critical angle of loading ( $\alpha_\sigma$ ) in a shell was presented previously in Section 3.4.5. This section details the subsequent generation of direction-dependent failure envelopes.

An orthogonal textile reinforcement is defined by its cross-sectional areas ( $A_{t,0^\circ}$  and  $A_{t,90^\circ}$ ), stiffnesses ( $E_{t,0^\circ}$  and  $E_{t,90^\circ}$ ) and tensile strengths ( $f_{t,0^\circ}$  and  $f_{t,90^\circ}$ ) in each direction.

For stiffness calculation, shear resistance or interaction between orthogonal fibres is ignored. The direction-dependent stiffness  $(EA)_\alpha$  can therefore be expressed by Equation 4.9. This is derived by considering the deformation of an orthogonal reinforcement mesh

subject to uni-axial tension at an angle  $\alpha$  to the  $0^\circ$  direction. The result is consistent with typical modelling of composite structures (Jones, 1999).

$$(EA)_\alpha = (EA)_{t,0^\circ} \cos^4(\alpha) + (EA)_{t,90^\circ} \sin^4(\alpha) \quad (4.9)$$

The ultimate strength of the textile in tension is reduced by the factor  $k_\alpha$ , given previously in Equation 3.8. According to Scholzen et al. (2015b), the ultimate capacity under pure tensile loading is a combination of the strength in each reinforcement direction as follows:

$$F_{t,\alpha} = F_{t,0^\circ} \cos(\alpha) k_\alpha + F_{t,90^\circ} \sin(\alpha) (1 - k_\alpha) \quad (4.10)$$

Where:

$$F_{t,0^\circ} = k_{1,0^\circ} f_{t,0^\circ} A_{t,0^\circ}$$

$$F_{t,90^\circ} = k_{1,90^\circ} f_{t,90^\circ} A_{t,90^\circ}$$

The ultimate tensile strain can therefore be calculated using Equation 4.11:

$$\epsilon_{tu,\alpha} = \frac{F_{t,\alpha}}{(EA)_\alpha} \quad (4.11)$$

This then allows the analytical failure envelope to be plotted. To calculate a utilisation ratio, the local axial and bending forces are first plotted as a point on the interaction diagram. A straight line is then drawn from the origin passing through this point and intercepting the failure envelope, and the local utilisation is the ratio of the distances along this line to the loading point and the envelope intercept.

Where a shell is analysed through a finite element model, a separate failure envelope is required for each individual element due variations in critical loading direction. To save computation time, it is proposed to pre-calculate and store failure envelopes for a range of values of  $\alpha$ .

For the investigations described in this chapter, the loading is aligned with the reinforcement ( $\alpha = 0^\circ$ ), and therefore  $A_t = A_{t,0^\circ}$  and  $k_\alpha = 1$ .

### 4.3.5 Limitations and potential extensions

In the proposed method, the utilisation is calculated based on the forces acting in one direction only. However, the stress in the reinforcement is also influenced by the perpendicular forces, where these exist, except where the critical loading direction is aligned with the reinforcement (Voss and Hegger, 2006). A normal compressive stress would be favourable, since this both increases the effective strength of the concrete and reduces the tensile stress in the reinforcement. This might typically be expected in a compression shell. However, the



opposite is true for tensile forces. Further work is therefore required on this topic, to both improve the accuracy of the model and to ensure that it is consistently conservative. This would require the definition of a four-dimensional failure surface, where the strength of the section is governed by pairs of principal axial forces and bending moments.

This investigation has also indicated a variation of concrete compressive strength with the size of the compression zone. With further investigation, this could potentially be included within the analytical model to improve accuracy.

Finally, the reinforcement strength reduction factor ( $k_1$ ) is dependent on the crack width and therefore the reinforcement ratio. In this investigation, the value of  $k_1$  changed from 0.726 to 0.814 when the reinforcement ratio was doubled. Therefore, the reinforcement strength determined from tensile tests on a specific TRC section cannot strictly be used for a different section. A reliable solution would be to test specimens of more than one reinforcement ratio (encompassing the range expected in the final design) and interpolate  $k_1$  values between the results. Alternatively, an analytical method of determining the relationship between reinforcement ratio and textile reinforcement tensile strength would, if it were developed, reduce these additional physical testing requirements.

## 4.4 Non-linear finite element analysis

This section describes a computational modelling approach for TRC using non-linear FE analysis. The aim was to determine a material model suitable for analysing the proposed TRC shell structures. The experimental tensile and bending tests (for 15mm specimens) were used to assess the model.

### 4.4.1 Modelling methodology

The FE model was created in SOFiSTiK (2019). This software was chosen for its detailed concrete material models and built-in interface with Rhino.

The TRC was modelled using SOFiSTiK's QUAD elements. These 2D elements have four nodes and use discrete layers to model the composite behaviour of the concrete and reinforcement, including cracking and anisotropy. For each layer, the principal stresses are calculated using the defined concrete stress-strain curve. These stresses are then summed over all layers, and the reinforcement forces (including tension stiffening effects) are added to determine the total element forces. Twenty layers were used throughout the investigation of this section, as determined through a sensitivity study described in Section 4.4.2. This approach is potentially simpler than the non-linear micro-plane damage model proposed

for TRC by Chudoba et al. (2016), and relies less heavily on precise calibration against test curves.

Reinforcement was specified in discrete layers in orthogonal directions. To simplify the analysis, warp properties were specified in both directions, using the values given in Table 4.2. The composite tensile strength was  $f_{tc}=971\text{MPa}$ , as determined in the tensile TRC tests (Section 4.2.3). Compressive reinforcement strength was ignored.

The assumed concrete stress-strain model in compression was the parabolic model described in Equation 4.1 (shown previously in Figure 4.2), with a mean strength of  $f_{cm}=47.2\text{MPa}$  and Poisson's ratio of 0.2. In tension, the concrete was modelled as brittle-elastic with the mean tensile strength ( $f_{ctm}$ ) related to the mean compressive strength ( $f_{cm}$ ) according to Eurocode 2 (BSI, 2004a), as described in Equation 4.12. This gives an expected tensile strength of  $f_{ctm}=3.46\text{MPa}$  for the specimens tested.

$$f_{ctm} = 0.3(f_{cm} - 8)^{2/3} \quad [\text{MPa}] \quad (4.12)$$

Figure 4.20 shows the FE model used in the experiments, with a 15mm thickness and similar dimensions to the bending and tensile test specimens described in Section 4.2.4. It features an unstructured quadrilateral mesh of 989 elements, with a maximum element length of 10mm. The sensitivity of the model to mesh size is discussed in Section 4.4.2. An unstructured mesh was used to allow maximum flexibility in later simulations on thin-shell flooring systems with more complex geometry. The overhanging ends of the specimens were excluded in order to eliminate local Poisson's ratio effects, since these were not accounted for in the analytical models against which the FE results were compared.

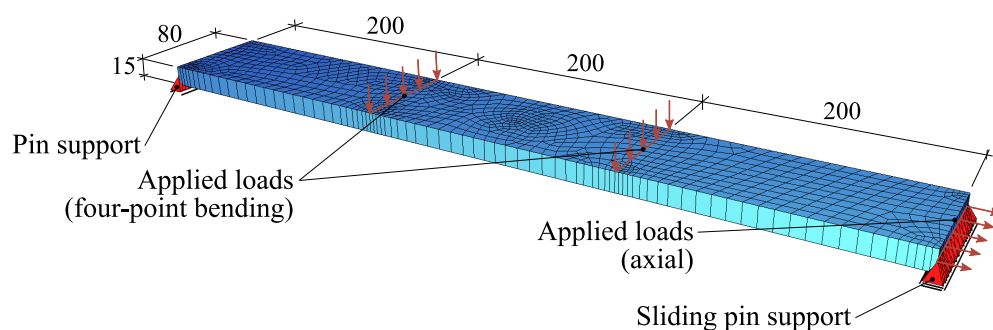


Figure 4.20: FE model used for comparison with experimental results.

### 4.4.2 Mesh density

A sensitivity study was carried out to determine the influence the maximum element size and the number of layers per element. A four-point bending test with a moment of 0.5kNm/m was modelled, similar to that described in Section 4.4.5. This structure and loading was chosen since the specimen contains both cracked and uncracked regions, increasing the potential mesh sensitivity. The results therefore indicate the maximum anticipated magnitude of inaccuracies caused by discretisation of the geometry and stress distribution.

The effect of the number of integration layers within each element was first investigated. The predicted deflection was found to reduce with increasing layers, tending asymptotically towards a minimum value. It was found that increasing the number of layers from 20 to 100 (the maximum permitted by the program) resulted in a 0.43% reduction in the measured deflection, at the cost of a 133% increase in computation time. Halving the number of layers to 10 increased the measured deflection by 1.00% with a 22% reduction in computation time. Twenty layers was therefore deemed to be an acceptable compromise between speed and accuracy.

Next, the mesh density was modified whilst keeping the number of layers constant at 20. The predicted deflection reduced with refinement of the mesh. Decreasing the maximum mesh size from 10mm to 1mm resulted in a mesh with 51913 elements, a 1.32% reduction in predicted deflection and computation time increase by a factor of 19. Conversely, doubling the maximum element size to 20mm increased the predicted deformation by 0.20% with a 45% reduction in computation time. A 10mm mesh size was therefore chosen, giving 989 total elements.

The following sections investigate the compressive, tensile and bending behaviour of the model in more detail. The results are compared to the experimental results from the 15mm thick TRC specimens. The 30mm specimen data was not used, due to the lack of post-cracking data obtained.

### 4.4.3 Compressive behaviour

A compressive load was applied in 20 steps up to a maximum load of 701.8kN/m, the predicted compressive strength of the section. This simulates a load-control test, and hence the descending part of the curve was not investigated. An identical match between the theoretical model and the FE results was observed, confirming the expected behaviour of the FE model.

#### 4.4.4 Tensile behaviour

The pure tensile tests were replicated to investigate the cracking and tension stiffening behaviour of the model.

In the uncracked state, the axial behaviour is linear-elastic with stiffness as the sum of the contributions from both concrete and reinforcement. Once the stress in the concrete reaches the tensile strength ( $f_{ctm}$ ), cracking occurs. A simplistic approach is to consider only the reinforcement stiffness post-cracking. However, due to bonding of the concrete and reinforcement between cracks, the concrete continues to make a stiffness contribution, and therefore the true stiffness of the cracked section lies between the uncracked and fully cracked values (Gilbert and Warner, 1978). This effect is known as tension stiffening.

The effects of tension stiffening were modelled according to Eurocode 2 (BSI, 2004a). In this model, the local tensile strain ( $\varepsilon$ ) is linearly interpolated between the uncracked ( $\varepsilon_{uncracked}$ ) and fully-cracked ( $\varepsilon_{cracked}$ ) values depending on the tensile stresses in the reinforcement at the applied loading ( $\sigma_s$ ) and at first cracking ( $\sigma_{sr}$ ), as shown in Equation 4.13.

$$\varepsilon = \zeta \varepsilon_{cracked} + (1 - \zeta) \varepsilon_{uncracked} \quad (4.13)$$

where:

$$\zeta = 1 - \beta \left( \frac{\sigma_{sr}}{\sigma_s} \right)^2$$

$$\beta = 1.0 \quad \text{for short-term loading}$$

$$\beta = 0.5 \quad \text{for long-term loading}$$

SOFiSTiK implements this model through a modification of the reinforcement tensile stress-strain curve, with an additional linear interpolation between the cracked and fully-cracked states, according to German standard DIN 1045-1 (DAfStb, 2003).

Again, 20 loading increments up to the ultimate strength of 126.8kN/m were analysed. Three separate sets of results were obtained with variable treatment of tension stiffening: using  $\beta=1.0$ ,  $\beta=0.5$  and with tension stiffening ignored. The results are shown in Figure 4.21, which also includes selected DIC data for comparison (shown previously in Figure 4.9).

#### Comparison of FE and theoretical models

There is generally good agreement between the theoretical model (Equation 4.13) and the FE results, indicating that the model works as expected. However with  $\beta=1.0$ , the strains

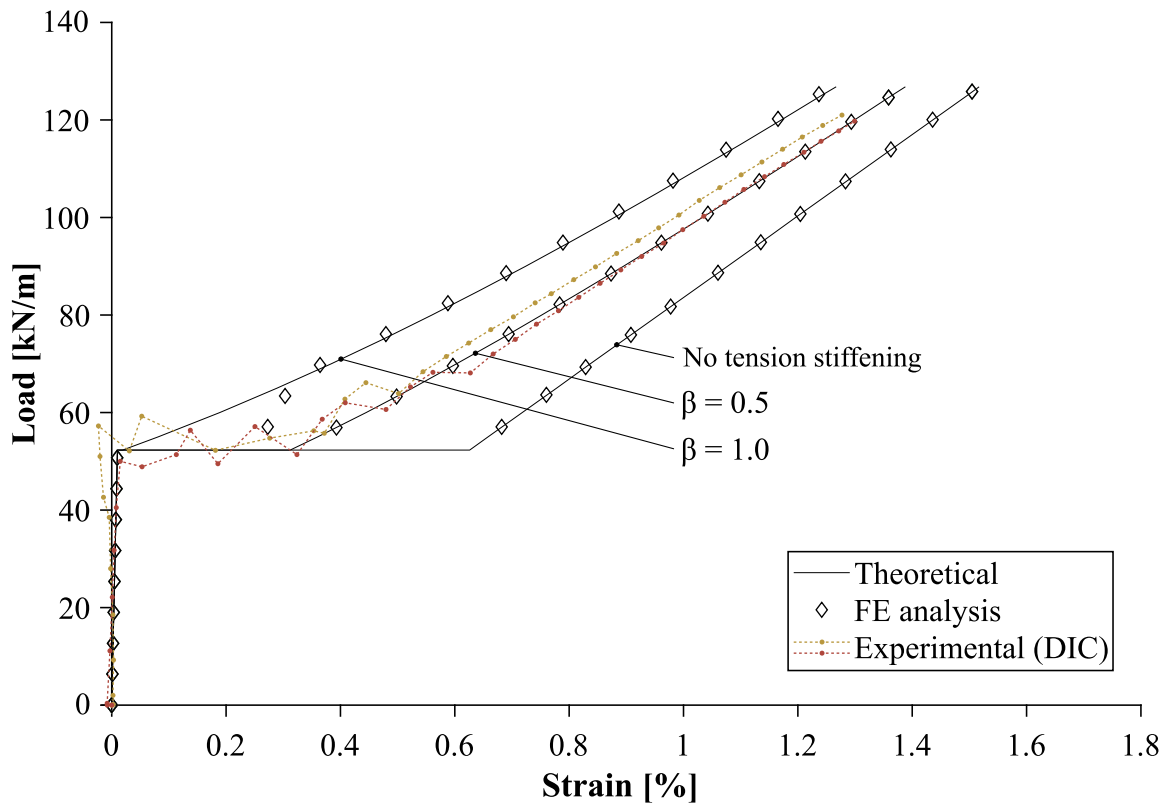


Figure 4.21: Non-linear FE analysis assessment: tension (15mm specimens).

predicted by the FE model at loads of 57.0kN/m and 63.4kN/m do not coincide with those predicted. This is due to the additional interpolation between the uncracked and cracked states assumed in the SOFiSTiK program, as described in German standard DIN 1045-1 (DAfStb, 2003), which was not included in the analytical model.

The average maximum load reached in the FE analysis was 125.2kN/m, slightly lower than the theoretical value. This is due to small variations in reinforcement stress caused by the irregular mesh.

### Comparison of FE and experimental data

Before cracking, the displacements were too small to be measured reliably using DIC. However, the post-cracking data matches the theoretical results well, particularly where tension stiffening is considered. The closest matching theoretical curve is that generated using  $\beta=0.5$  (as used for long-term loading in steel). It might be expected that the effect of tension stiffening is less for fibrous reinforcement than for steel, due to slip between bundled fibres (Banholzer et al., 2006), which is consistent with this result.

### Effect of loading direction

So far, the experiments described have all featured specimens or models with applied loading aligned with the warp direction. However, the post-cracking stiffness of a TRC section is direction-dependent. The relationship between loading direction and the stiffness of the reinforcement has been described already in Equation 4.9.

The FE model was re-run with the reinforcement oriented  $45^\circ$  to the direction of tensile loading. With the warp properties in both the  $0^\circ$  and  $90^\circ$  directions, a 50% reduction in post-cracking stiffness was observed in accordance with Equation 4.9. With tension stiffening included, the FE results again agreed with the theoretical model as outlined in Equation 4.13.

### 4.4.5 Bending behaviour

The behaviour and accuracy of the FE model was assessed in a final investigation of four-point bending behaviour. Loading was again aligned with the reinforcement.

#### Pure bending

In order to compare the behaviour of the FE model and the theoretical model, a 1D numerical model of TRC bending was created in MATLAB. The same stress-strain relationships for concrete and reinforcement were used. The primary assumption in the theoretical model is that of a linear strain distribution through the section, or plane sections remaining plane during deformation. For a given strain distribution, the net axial and bending forces on the section are calculated by summing the contributions from each layer as well as the reinforcement. This is a similar approach used by SOFiSTiK's QUAD finite element. Five hundred layers were used in this case, and it was found that doubling this value affected displacement results minimally (less than 0.001%).

Firstly, a moment curvature relationship for the 15mm thick TRC section was constructed by incrementally stepping the peak compressive strain in the concrete from zero to the maximum value of  $\epsilon_{cu1}=0.35\%$ . A total of 500 increments were used, again a sufficiently large number to avoid introducing measurable inaccuracies. For each strain increment, the neutral axis depth at which there is no net axial load in the section was found iteratively using the Newton-Raphson method. A check was also carried out to stop the generation of the moment-curvature diagram if the stress capacity of the reinforcement is reached. The predicted moment capacity was 0.721kNm/m, with failure initiated by rupture of the reinforcement.

Tension stiffening was again included according to Equations 4.13, except by interpolating curvature rather than axial strain values. The FE model was analysed under a pure bending load in order to compare the moment-curvature behaviour, with results shown in Figure 4.22.

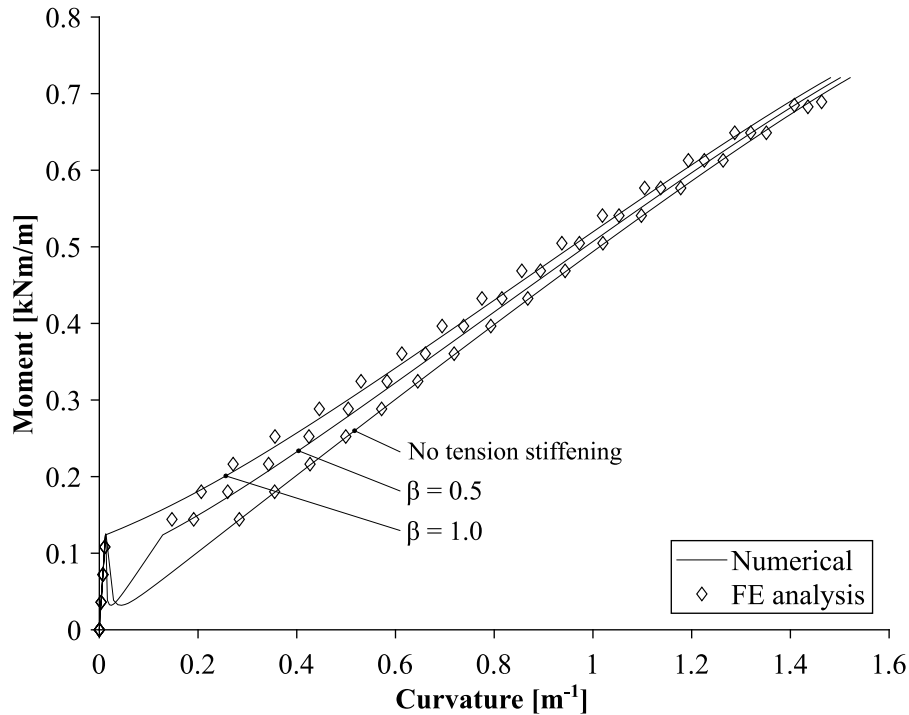


Figure 4.22: Moment-curvature relationships for a 15mm thick TRC section, comparing numerical and FE results with various treatment of tension stiffening.

The results show good agreement between the two approaches when tension stiffening is ignored, with some reduction of accuracy when included. A linear-interpolation between cracking and full tension-stiffening is again visible in the FE results for  $\beta = 1.0$ . In the FE model, the average maximum bending strength was 0.686kNm/m, 4.8% lower than predicted in the numerical model. This strength reduction is likely to be a result of local variations in reinforcement strength due to the irregular FE mesh. The numerical model effectively simulates a displacement-controlled test, whilst the FE analysis is load-controlled and therefore does not show a drop in load after cracking.

Compared to the tensile investigation, the predicted stiffness is less sensitive to the inclusion of tension-stiffening. This is expected, since the stiffness in bending is not purely governed by reinforcement.

The cracking moment predicted by the numerical model is 0.125kNm/m, which is based on a concrete tensile strength of  $f_{ctm} = 3.46\text{MPa}$  calculated from Equation 4.12. However, in the four experimental bending tests on 15mm specimens the average measured

cracking moment was 0.243kNm/m, corresponding to an estimated average tensile strength of 6.43MPa. This discrepancy is likely to be caused by size effects; a significantly smaller volume of concrete experiences higher tensile stresses under flexure than in pure tension. Bentz (2019) has demonstrated a consistent inverse relationship between tensile strength and the volume of concrete subject to maximum stress, consistent with the typical behaviour of brittle materials with random flaws according to Bazant and Planas (1997). Eurocode 2 (BSI, 2004a) acknowledges this phenomenon by specifying a greater mean concrete tensile strength in flexure ( $f_{ctm,fl}$ ) than in pure tension ( $f_{ctm}$ ). The strength increase is proportional to the section depth  $h$  in Equation 4.14.

$$f_{ctm,fl} = \max\{(1.6 - h) f_{ctm}; f_{ctm}\} \quad (4.14)$$

For a depth of  $h = 0.015\text{m}$ , this corresponds to an increase of 58.5% from  $f_{ctm} = 3.46\text{MPa}$  to  $f_{ctm,fl} = 5.48\text{MPa}$ . This is significantly closer to the measured value from the physical tests of 6.43MPa, albeit 14.8% smaller.

#### 4.4.6 Four-point bending

Both the 1D numerical and FE models were adapted to model the four-point bending tests, enabling a comparison with the experimental data. In the numerical model, the moment at each of 120 points along the beam was calculated and the curvature looked up from the previously stored values. The curvatures were then numerically integrated twice to find the complete deflected shape of the beam. This was done for a total of 200 loads from zero to failure.

The FE analysis was again run with 20 loading steps up to the predicted failure moment of 0.721MPa, incorporating the updated concrete tensile strength of  $f_{ctm,fl} = 5.48\text{MPa}$ . Figure 4.23 compares the 1D numerical, FE and experimental data.

Comparing the numerical and FE results first, a greater discrepancy can be observed after cracking than in the previous investigations. This is particularly visible where tension stiffening is ignored. The sensitivity to the mesh size and number of layers was discussed in Section 4.4.2 and found to be small. However, second-order effects might be influential, since these are included in the non-linear FE model, but not in the numerical model.



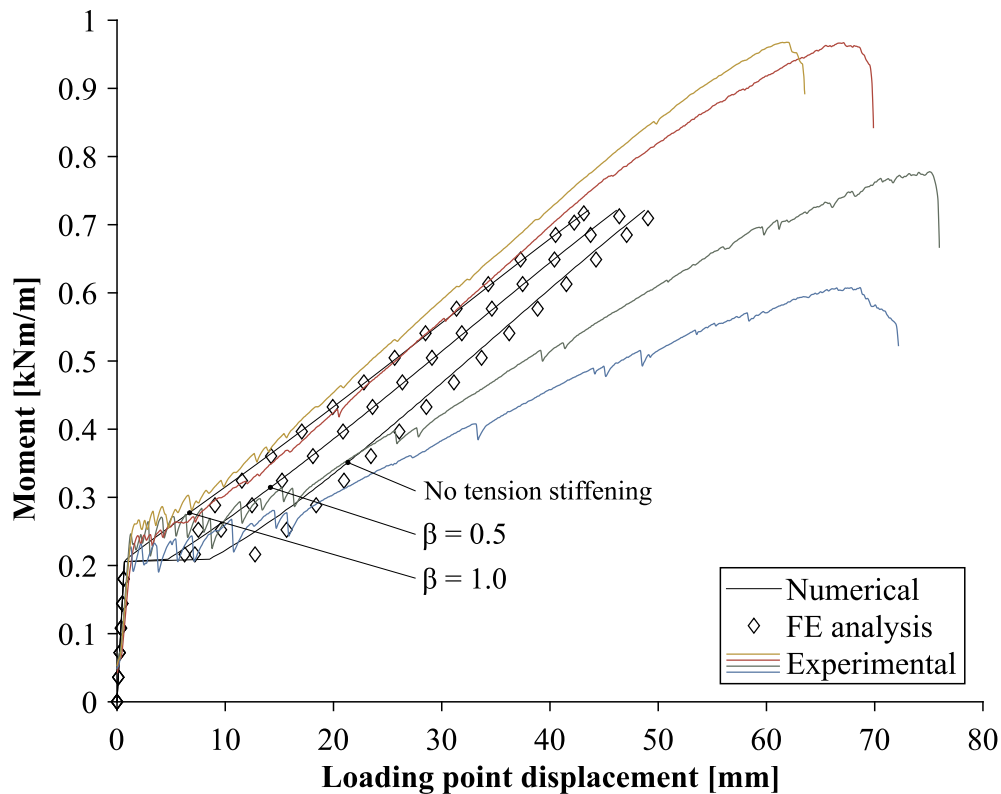


Figure 4.23: Non-linear FE analysis assessment: four-point bending (15mm specimens).

The FE analysis replicates the experimental data reasonably well. The cracking moment is underestimated due to the slightly lower prediction of tensile strength given by Equation 4.14. The cracked gradient is similar in the FE results regardless of the treatment of tension stiffening, although a horizontal offset between the three sets of results is visible. A similar offset exists between the experimental results, however including tension stiffening with  $\beta=0.5$  most closely represents the average experimental deflection.

## 4.5 Summary, findings and conclusions

In this chapter, a series of experimental tests were carried out on TRC specimens with low quantities of both reinforcement and cement. The structural behaviour in tension, bending, compression, and under combined loading was investigated. A novel analytical failure envelope for TRC was proposed, derived from the structural properties of its constituent materials. Finally, a non-linear finite element model of TRC was compared to theoretical models and experimental results.

Key findings are summarised below:

- The incorporation of two layers of AR-glass fibre textile reinforcement into thin concrete sections significantly increases the tensile strength and deformation capacity, even at low reinforcement ratios (0.871% and 0.435% in this case).
- The failure envelope for TRC under combined axial and bending loading is non-linear, and can be conservatively modelled using an analytical approach based on stress-strain models of concrete and reinforcement.
- This analytical failure envelope is significantly more accurate in compression than existing models, and predicts strengths up to 3.7 times greater in this instance. This can lead to considerable material savings. The reliance on experimental testing is also reduced, enabling simpler exploration and optimisation in the design of TRC shells.
- The non-linear structural behaviour of TRC can be approximated in an FE analysis using layered quadrilateral FE shell elements. In this case, the accuracy is within the experimental range.
- This FE model also indicates that tension stiffening effects are present in the material, which can therefore be included to improve accuracy.

#### **Conclusions: Chapter 4**

Vaulted floors are a novel application of TRC shells. Less reinforcement is required than for typical TRC sections due to the dominance of compressive forces. Despite this, accurate design and analysis methods can be formulated by combining established theoretical models for conventional steel-reinforced concrete with those used for TRC. The original techniques described in this chapter are used throughout the subsequent investigations of this dissertation, and underpin the eventual development of a complete design methodology.

# Chapter 5

## Experimental study of quarter-scale prototypes: Methodology and results

### 5.1 Introduction

The construction of prototypes is a vital step in demonstrating the practicality of a novel structural system. Questions of materials, casting and construction sequencing must all be addressed in detail, giving vital insight into how this might be achieved at a commercial scale. Furthermore, physical tests often reveal subtleties in structural behaviour which might be overlooked in a computational simulation, no matter how detailed. Crucially, physical testing also allows analysis methodologies to be implemented and verified.

A series of experimental investigations were therefore carried out with the following aims:

- To explore construction methods for thin TRC shells, highlighting potential issues and solutions for full-scale production.
- To investigate the structural behaviour of the proposed system, including the ultimate mode of failure.
- To test the effectiveness of the analysis methodologies developed in the previous chapter when extended to three-dimensional shell structures.

Initially, only two specimens were planned for construction: one with, and one without, foamed concrete fill. However, due to construction and testing issues with the first specimen, three were eventually built and tested. These are referred to as Shell 1, Shell 2 and Shell 3 hereafter, with only Shell 3 featuring the foamed concrete fill. Each shell had the same design

thickness, geometry and reinforcement, and the same formwork was re-used each time. The experiments described were carried out at the University of Bath.

This chapter firstly discusses specimen design, before describing the materials, construction process, measurement of geometry, load testing methodology and finally the results.

## 5.2 Specimen design

The specimen dimensions were limited by both the available laboratory space and the logistical need for the shells to be constructed by hand, without scaffolding. A maximum span of 2m was therefore chosen, which is a quarter-scale representation of a full-scale application with 8m spans as featured throughout Chapter 3.

This raises the question of whether this scaled-down specimen can represent similar structures at practical scales. In the idealised case of an arch in pure compression, as described in Section 3.3, the stresses in the shell remain constant if each of the length dimensions (span, height and thickness) are scaled in proportion to each other and the material properties and applied floor loading (per unit area) remain constant. This was the approach taken in the design of this experiment. At full scale, with additional loading applied to make up for the self-weight lost in the scaling process. It is therefore assumed that a larger reinforcement material could be used to give the same reinforcement ratio and similar overall structural characteristics. It should also be noted that scaling of concrete structures is also complicated by size effects for brittle materials, whereby smaller structures have a higher average strength due to the random distribution and severity of strength-governing flaws (Bazant, 2005).

In the simplest sense, the critical buckling load of the shell might also be considered to scale in a similar manner, based on analogy with an Euler column, which has the same critical stress if all dimensions are scaled proportionally. However, the stability of thin, shallow shells is also sensitive to initial imperfections (Verwimp et al., 2016), which might arise due to manufacturing errors. In this case, a small-scale specimen might give a conservative indication of performance, since these imperfections are proportionally larger.

### Design assumptions and methodology

Test specimen design was carried out prior to the work described in Chapter 4, and therefore features some differences in approach. The full design methodology is described in Hawkins et al. (2019), and not repeated here. The approach taken was to mirror the assumptions which might be made for a real project, including partial factors on loads and material strength. As a result, the design loadings do not represent a predicted failure load, but are simply used as a

means of generating a geometry. In Chapter 6, the experimental results are re-analysed using measured, unfactored material properties, to enable a reliable comparison between theory and experiment.

The same floor loadings as described in Section 3.4.3 were again used, along with an assumed self-weight at full scale of  $2.75\text{kN/m}^2$ , similar to that for the optimised groin vault in Table 3.2. This gave ULS design loadings of  $10.31\text{kN/m}^2$  (unfavourable) and  $3.75\text{kN/m}^2$  (favourable).

### Geometry

The specimen geometry is shown in Figure 5.1, and features a height of  $h = 200\text{mm}$  and corner support width of  $b_{col} = 125\text{mm}$ , each a quarter of the dimensions considered in the investigations of Chapter 3.

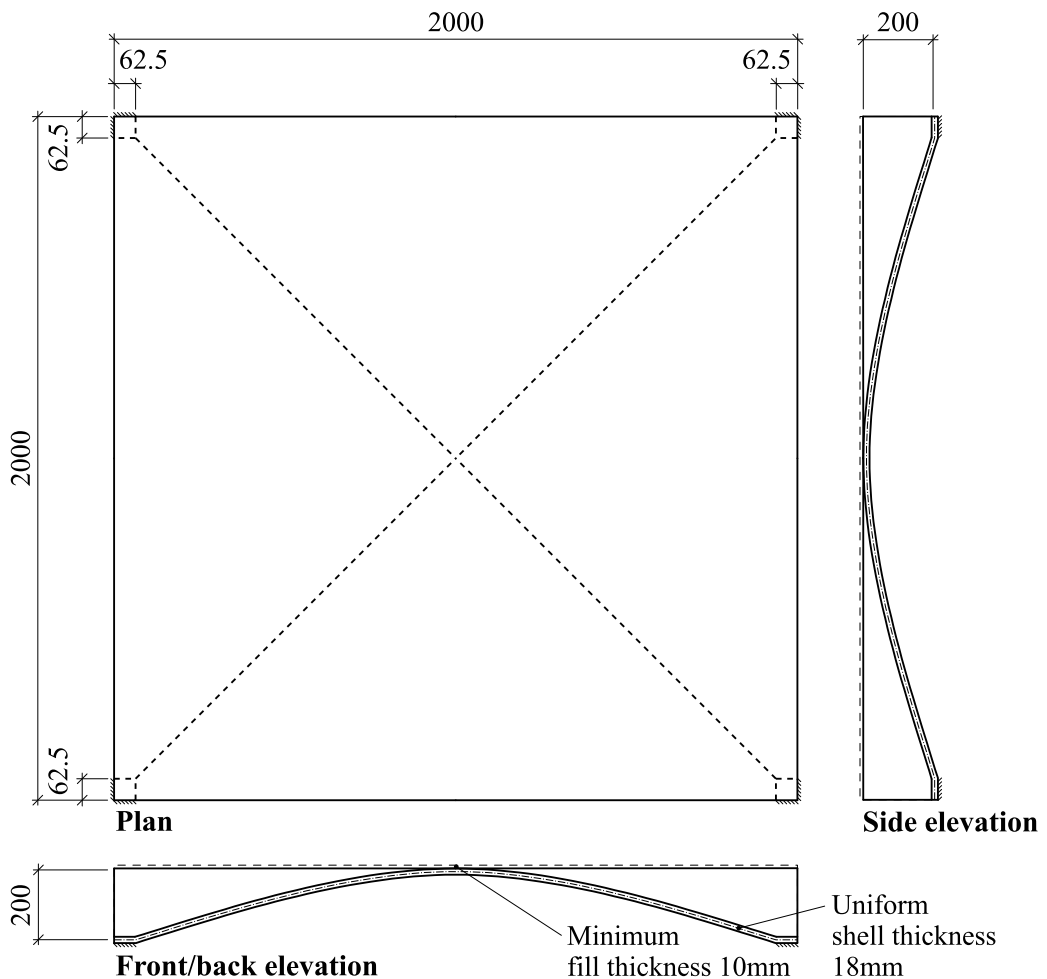


Figure 5.1: Test specimen design geometry.

The parametric optimised groin vault, introduced in Section 3.5.4, was adopted as the geometry of the test specimens. An iterative procedure, as detailed in Hawkins et al. (2019), was used to determine a shell thickness of  $t=18\text{mm}$ , corresponding to estimated compressive, tensile and bending strengths of  $384\text{kN/m}$ ,  $92.3\text{kN/m}$  and  $0.494\text{kNm/m}$  respectively for the TRC section. This gives a span to thickness ratio of 1:111, which is considerably thicker than most large-span concrete shells where 1:500 is common (Chilton and Isler, 2000). This might be expected, however, due to the shallow depth, relatively high live loading, small support area and non-rigid supports which characterise this application. This thickness is also low compared to Guastivino's tile-vaulted floors (1:24 to 1:48).

Tie rods of  $156\text{mm}^2$  cross-sectional area, equivalent to a 16mm outer diameter threaded rod, were chosen. The optimal geometric parameters were  $a = 0.385$ ,  $b = 0.326$  and  $\epsilon_{tie} = 0.56\text{mm/m}$ . With this optimised geometry, the total bending strain energy envelope was reduced by 9.8% compared to a parabolic profile.

### Critical live loading pattern

As described in Hawkins et al. (2019), a variety of live loads patterns were analysed to determine a critical loading arrangement for testing. The shell was split into four quadrants, with either the maximum ( $10.31\text{kN/m}^2$ ) or minimum ( $3.75\text{kN/m}^2$ ) ULS design loads applied in each, over the full set of possible permutations. Maximum loading over half of the shell only (Pattern 2 in Figure 3.6) gave the highest utilisation across the shell, and was therefore used to test the specimens to failure.

## 5.3 Materials

### 5.3.1 Textile reinforcement

AR-glass textile reinforcement, as described and tested in Section 4.2.1, was used to construct the shells. This was chosen for its low cost and embodied carbon (15% of that of carbon fibre according to Table 2.1), and to give an appropriate reinforcement ratio at the scale of the test specimens. Material properties were given previously in Table 4.2. The composite strength of the reinforcement was determined through tensile tests on TRC specimens cast alongside each shell, described later in Section 5.6.

### 5.3.2 Fine-grained concrete

#### Mix design

A bespoke fine-grained concrete mix was created for construction of the TRC shells. This material was similar to that described in Section 4.2.1, albeit with some small differences mostly arising from variations in the available materials between the laboratories in Cambridge and Bath.

For all shells, the binder consisted of 70% Portland cement and 30% fly ash, conforming to BS EN 450 N BSI (2012b). The Portland cement was strength rated at 42.5MPa, lower than the high-strength (52.5MPa) product used in the tests of Chapter 4. A lignin-based plasticiser, with a quoted density of 1100kg/m<sup>3</sup>, was included at 2ml per kg of binder. Compared to material described in Section 4.2.1, a lower aggregate/binder ratio of 2 was required to achieve the target strength. The maximum aggregate size was 2mm, and the particle size distribution was again modified to increase the final compressive strength. The proportion of 0-1mm particles was reduced from the natural value of 75% to 50%.

Table 5.1 shows the concrete composition for each specimen. Since the concrete was spread by hand trowelling onto an inclined surface, an appropriate workability was essential. Water was added to each mix until this was achieved, which resulted in a water/cement ratio of 0.45 for Shells 1 and 2 and 0.41 for Shell 3. This difference was likely a result of natural variations in the aggregate used and/or atmospheric conditions, and led to differences in density between the batches. Aside from this, similar concrete mix proportions were used for each shell.

Table 5.1: Fine-grained concrete composition and properties.

	Shell 1	Shell 2	Shell 3
<i>Composition</i>			
<b>Portland cement [kg/m<sup>3</sup>]</b>	424	422	446
<b>Fly ash [kg/m<sup>3</sup>]</b>	182	181	191
<b>Aggregate (0 - 1mm) [kg/m<sup>3</sup>]</b>	606	603	637
<b>Aggregate (1 - 2mm) [kg/m<sup>3</sup>]</b>	606	603	637
<b>Water [kg/m<sup>3</sup>]</b>	273	271	261
<b>Superplasticiser [kg/m<sup>3</sup>]</b>	1.33	1.33	1.40
<i>Material properties</i>			
<b>Dry density [kg/m<sup>3</sup>]</b>	2091	2081	2175
<b>Average cube strength [MPa]</b>	33.9	35.5	39.0
<b>Cube strength standard deviation [MPa]</b>	0.80	1.21	0.86

The embodied carbon of each mix was calculated using the material values given in Table 2.1, giving  $0.191\text{kgCO}_2\text{e/kg}$  ( $400\text{kgCO}_2\text{e/m}^3$ ) for Shells 1 and 2 and  $0.193\text{kgCO}_2\text{e/kg}$  for Shell 3 ( $421\text{kgCO}_2\text{e/m}^3$ ). These values are respectively 23% and 25% greater than that of the mix previously described in Section 4.2.1, due to the lower aggregate content and subsequent proportional increase in Portland cement.

### **Compressive strength**

Four 100mm cubes were cast and tested along with Shells 1 and 2, and six with Shell 3, at an age of 14 days. Average densities and strengths are included in Table 5.1, and show considerable variation between each shell. The higher strength of the concrete used for Shell 3 is likely a result of the lower water/cement ratio. For Shell 1, cubes were cast from a batch of concrete with poor workability (due to the use of an initially dry concrete mixer). The cubes were therefore poorly compacted, and may have had a reduced strength compared to the concrete used in Shell 1. TRC samples were also tested in compression for each of the shells, and the strength is compared to the cube tests in Section 5.6.3.

The measured compressive strengths were all considerably lower than that of the fine-grained concrete described in Section 4.2.1 ( $47.2\text{MPa}$ ). This is partly explained by age, since the concrete was 14 days old rather than 28. According to Eurocode 2, Equation 3.2 (BSI, 2004a), this should reduce strength by 18%. Other factors, such as lower cement strength and higher water/cement ratios are also likely to have contributed to the reduced strength. Despite this, the strengths achieved are more than adequate to represent typical concrete used in the construction industry.

### **Stress-strain response**

The stiffness of the concrete must be known for accurate FE modelling. Fine-grained concrete used for TRC has often been shown to have a considerably lower stiffness than would be expected of regular concrete with a similar strength (Scholzen et al., 2015b; Verwimp et al., 2015).

Six  $160\times 40\times 40\text{mm}$  prisms were tested in compression to failure. The prisms were cast separately to the shells, but featured the same materials and proportions as Shells 1 and 2 (with a water/cement ratio of 0.45). Testing was carried out after curing for 14 days. The experimental setup is shown in Figure 5.2. The apparatus differs from that described in Section 4.2.1; here the displacement was measured using a laser extensometer and digital image correlation (DIC) on opposite sides of the specimen. These alternative measurement techniques were used to avoid issues of poor data reliability which were



previously encountered using the mechanical extensometers. By averaging the two sets of results, any effects of bending are eliminated. The laser was oriented along the centreline of the specimen and measured over a gauge length of 80mm. Readings were taken at 0.1s intervals, synchronised with measurements from the load cell.

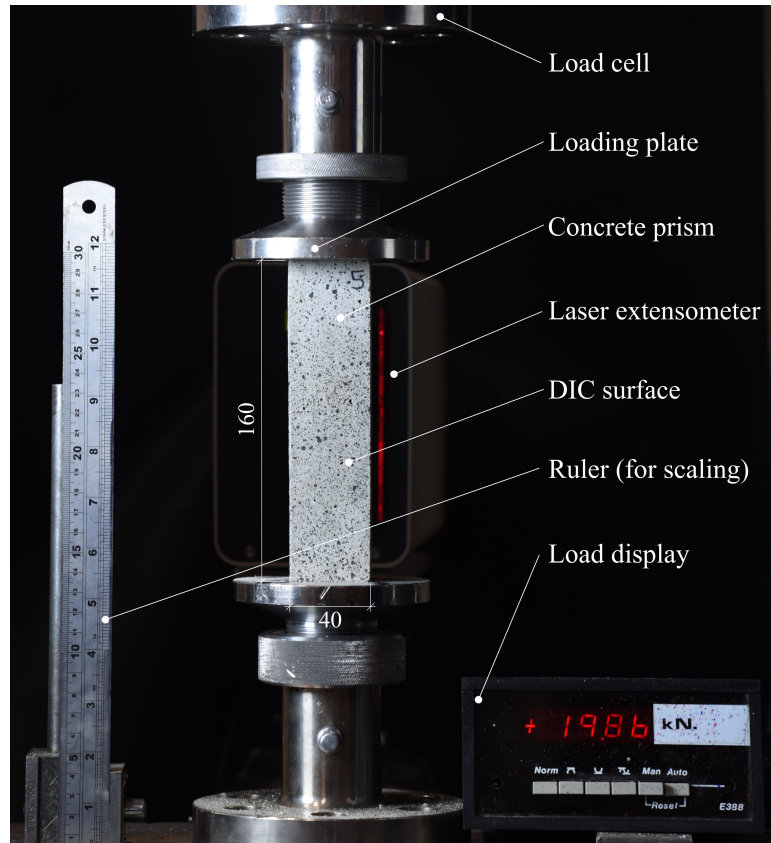


Figure 5.2: Compression testing of fine-grained concrete prisms.

The opposite face was flecked with black paint to assist the DIC analysis. Images were taken at four second intervals during the test using a digital camera, and the load corresponding to each image was captured from a digital display. The software Ncorr (Blaber et al., 2015) was used to calculate strains from these images using a similar procedure to that described in Section 4.2.3. A single value of strain was calculated for each image by taking the average over the middle 80mm region of the specimen, thereby eliminating end regions.

Results are shown in Figure 5.3, and include laser extensometer, DIC and averaged strain curves. At low stresses, some divergence between the two sets of measurements are visible. This may be caused by bending as the specimen beds in to the loading plates. The descending part of the curve is not shown in the DIC results, since this typically occurred too quickly to be captured. The right-hand graph compares the average strain values for each prism, and also plots the average across all tests.

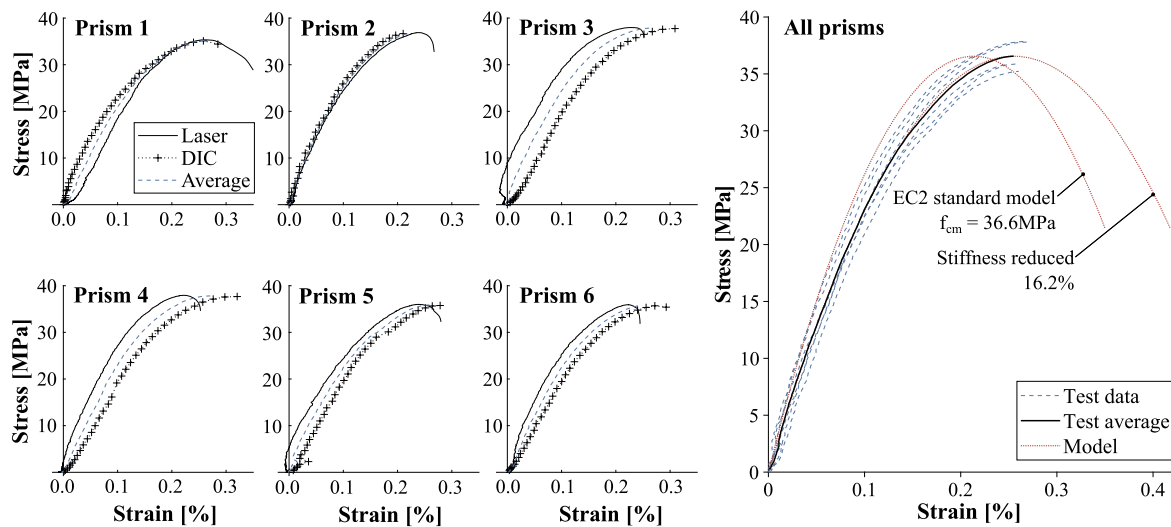


Figure 5.3: Stress-strain data measured from compression tests on fine-grained concrete prisms.

The average peak stress recorded was 36.6MPa, similar to the values from the cube tests given in Table 5.1. The right-hand graph on Figure 5.3 also includes curves plotted using the parabolic stress-strain model introduced in Equation 4.1. According to this model, the expected strain at peak stress  $\epsilon_{c1}$  for a mean strength of  $f_{cm}=36.6\text{MPa}$  would be 0.214%. However, the average measured value in this case was 0.255%, indicating a stiffness 16.2% lower. A modified theoretical curve is also plotted, which includes this stiffness reduction. This curve closely matches the average experimental results, and is the basis for the concrete model used in later FE analysis (Section 6.2).

### 5.3.3 Foamed concrete

Foam concrete was cast onto Shell 3 to create a level top surface. This section discusses the mix design and methodology, compressive testing and structural properties. The aim was to create a material with sufficient strength and robustness for the structural tests, whilst keeping density and embodied carbon low. A target compressive strength of 1.0MPa and dry density of  $800\text{kg/m}^3$  were established from preliminary experimental tests and estimated maximum test forces.

The foamed concrete was created by first mixing a mortar paste consisting of sand (with particle size below 1mm), binder (a CEMII/B blend of Portland cement and fly ash) and water. The sand/cement ratio was 1.0, water/cement ratio 0.5, and 2ml of lignin plasticiser was included per kg of binder. Foam was created separately and mixed into the mortar, thus

reducing the density to the target value. This was measured by casting and weighing cubes during mixing.

Precise details on the composition of the foaming agent (supplied by EAB Associates (2018)) are unavailable, apart from the density of  $1020\text{kg/m}^3$ . To create the foam, the agent was first diluted in water to 3% concentration by volume according to the manufacturer's specification. This mixture was then aerated using a power drill with a mixer attachment. The volume expansion of the diluted foaming agent using this method was approximately 10. This is significantly smaller than the quoted manufacturer's value of 22, which can be achieved using specialist foam generators.

Four 100mm cubes were cast simultaneously with the fill. The average wet and dry densities of these cubes were  $844\text{kg/m}^3$  and  $805\text{kg/m}^3$  respectively. Table 5.2 shows the material composition of the foamed concrete. These values were calculated using the average dry density, assuming a mortar density of  $2200\text{kg/m}^3$  and diluted foam volume expansion ratio of 10 (corresponding to a foam content of  $664\text{l/m}^3$ ). The additional water used to make the foam increases the water/cement content of the mixture from 0.50 (in the initial mortar) to 0.71. This was found to create a highly uniform and workable material.

Table 5.2: Foamed concrete composition.

Material	Quantity [ $\text{kg/m}^3$ ]
<i>Mortar</i>	
<b>Cement (CEMII/B)</b>	295
<b>Aggregate (0 - 1mm)</b>	295
<b>Water</b>	148
<b>Superplasticiser</b>	0.65
<i>Foam</i>	
<b>Foaming agent</b>	1.99
<b>Water</b>	64.4

### Embodied carbon

The embodied carbon of the foamed concrete was calculated using material values in Table 2.1. The CEMII/B cement was assumed to contain 28% fly ash in accordance with average UK values (Jones and Hammond, 2019), and the foaming agent was ignored. The resulting value of  $0.246\text{kgCO}_2\text{e/kg}$  is therefore a is greater than the fine grained concrete of Shell 3, but due to its low density the volumetric embodied carbon is less than half, at

198kgCO<sub>2</sub>e/m<sup>3</sup>. If the foaming agent is assumed to have a similar embodied energy to a superplasticiser, these values would increase by 2%.

### Structural characteristics

The four foamed concrete cubes were subject to compression tests to determine strength and deformation characteristics. Since the foam was cast five days after the construction of Shell 3, and tested alongside it, the cubes were only nine days old at the time of testing.

The experimental set-up is shown in Figure 5.4. Each cube was loaded between steel plates at a rate of 1mm/min. Load and displacement were recorded at 0.1s intervals, and the strain was calculated by dividing the measured displacement by the gauge length of 100mm. Any deformation of the loading plates was therefore ignored.

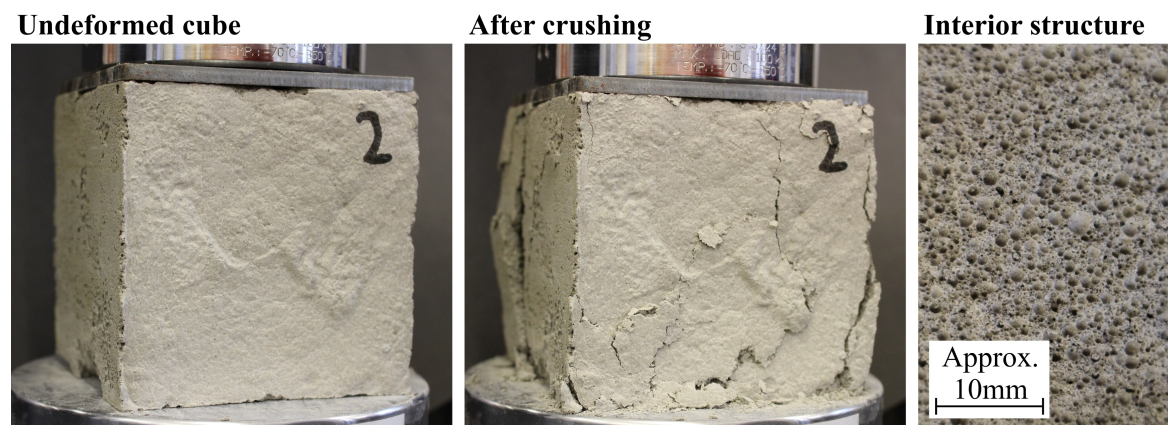


Figure 5.4: Foamed concrete compressions tests, showing a 100mm cube before (left) and after (middle) crushing. The interior structure of the foam is also shown (right).

Results are given in Figure 5.5. Note that the strain values have been shifted to align each data set, compensating for variable bedding-in of the specimens.

The experimental curves show initially linear-elastic behaviour followed by a crushing plateau. The average stiffness prior to crushing was 0.238GPa. Two of the cubes reached their maximum strength at the end of the elastic region, whereas two developed a greater load capacity after crushing had begun. The average peak stress was 0.91MPa, compared to 0.83MPa at first crushing. At a strain of 3%, the average stress had dropped to 0.62MPa, a value which remained approximately constant at higher strains. Due to the young age of the specimens, the measured strength and stiffness are likely to under-estimate the long-term values.

A theoretical stress-strain curve was also developed for later use in FE modelling, and is included in Figure 5.5. The compressive stress-strain curves of brittle-elastic foams

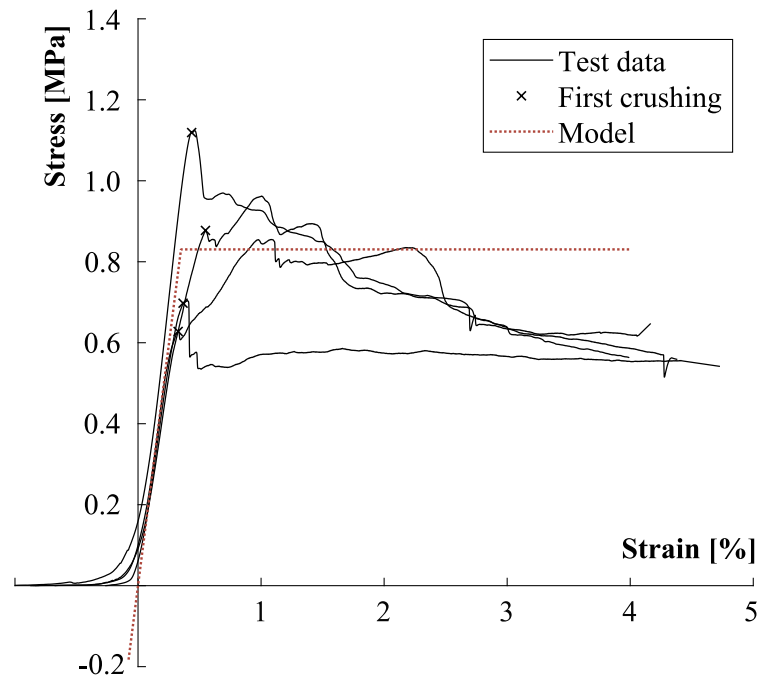


Figure 5.5: Measured stress-strain response of foamed concrete cubes.

typically exhibit three distinct regions: a linear elastic stage, a crushing plateau and, finally, densification (Gibson and Ashby, 1999). The material was assumed linear-elastic until crushing at 0.83MPa, with a fully-plastic plateau beyond. In tension, the behaviour is brittle-elastic and the tensile strength was taken as 22% of that in compression in accordance with the European Standard for aerated concrete, DIN EN 12602 (DIN, 2016). This is a conservative ratio according to Valore (1954). A Poisson's ratio of 0.33 was assumed, as is typical for closed-cell foams (Gibson and Ashby, 1999).

## 5.4 Construction

### 5.4.1 Formwork

Figure 5.6 shows the timber formwork used in the construction of all three shells. Four identical sections, triangular in plan, were fabricated separately and bolted together. This approach simplified construction and transportation, and ensured that the formwork could be removed without damaging the shells.

The single curvature of the groin vault allowed the forming surface to be constructed from initially flat sheets of 4mm thick plywood. These were fixed to a rigid frame of 18mm thick plywood and timber stiffeners. The plywood across the diagonals was cut to the vault

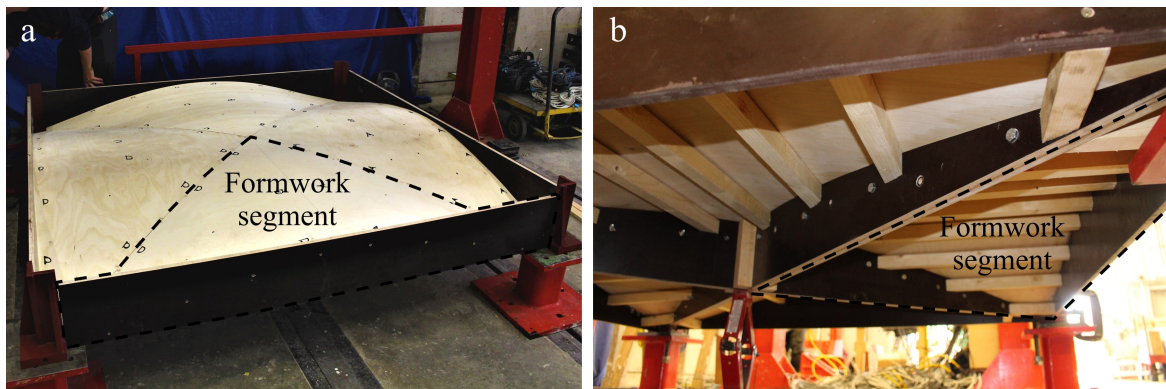


Figure 5.6: Shell formwork constructed from four identical triangular segments bolted together.

profile, with minor adjustments made to allow for the thickness of the shell and plywood. An assessment of the geometry and construction accuracy of the formwork is given in Section 5.5.

#### 5.4.2 Tie rods and corner supports

The shell was cast onto steel supports at each corner, with dimensions shown in Figure 5.7. These were set upon 300mm tall steel plinths bolted securely to a strong-floor. As shown in Figure 5.8, ETFE sheets were used to allow free horizontal sliding whilst restraining rotation about the horizontal axes.

The support was extended to the full height of the filled shell and stiffened with 15mm thick gusset plates to maximise rigidity. This is only an approximation of the support conditions of the full-scale, multi-storey system. However, the aim was to create a well-defined boundary system which could be reproduced in FE modelling.

The four ties were threaded steel rods (grade 8.8) of 16mm outer diameter with a quoted tensile strength of 70.3kN. Each was threaded into the baseplate at one end but free to slide at the other. The free end was secured with a nut, as shown in Figure 5.8. Pre-strain could therefore be applied through tightening of this nut, with the angle of rotation proportional to the applied pre-strain. Each consisted of two lengths of threaded rod connected with a steel coupler (allowing installation). The stiffness of the tie rods was determined through tensile tests described in Section 5.9.1.

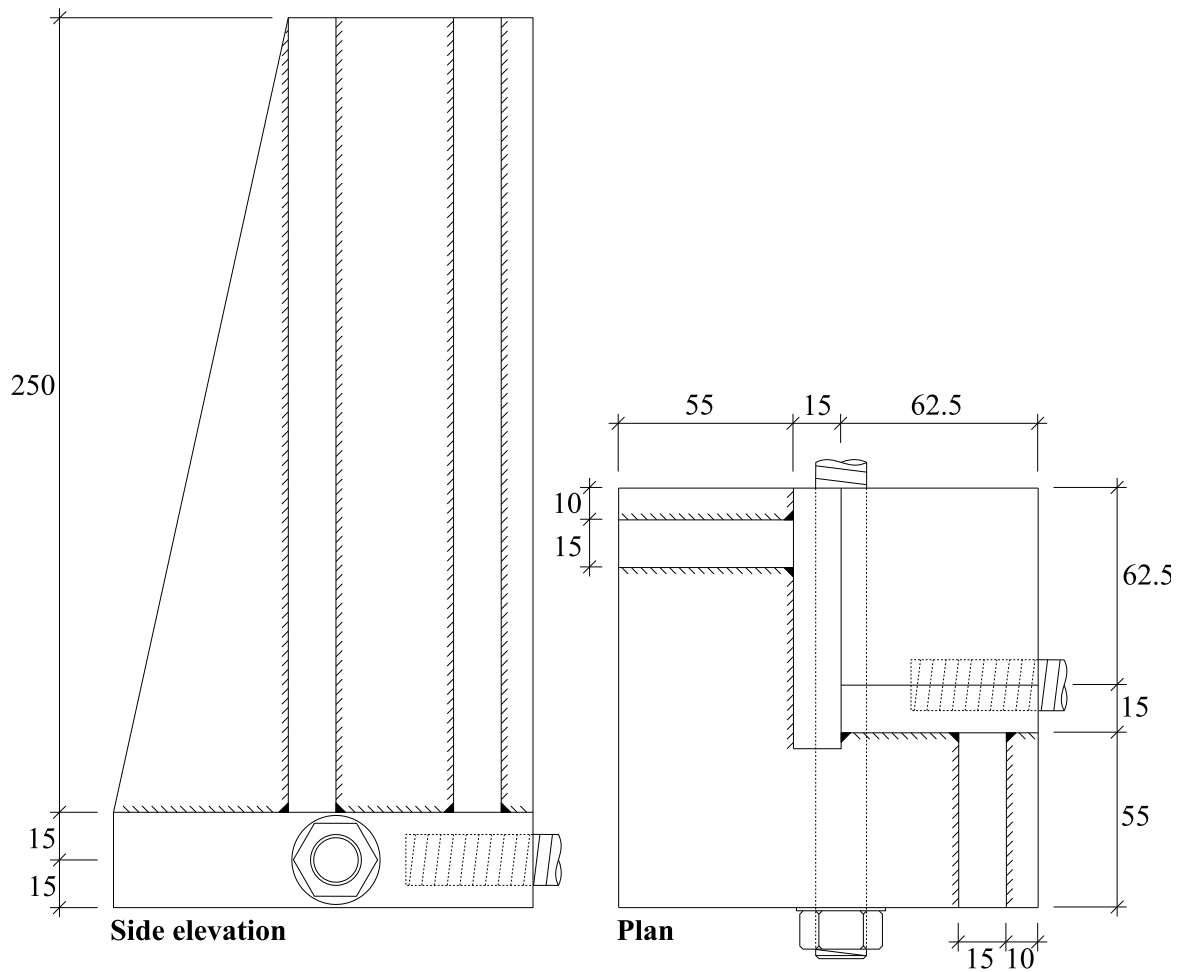


Figure 5.7: Corner support constructed from steel plates (all dimensions in mm).

### 5.4.3 Casting the textile reinforced concrete shells

Prior to casting of each shell, the forming surface was levelled using screw jacks and coated with an oil-based release agent to assist removal. The steel corner supports were then positioned, using the tie rods for alignment, and clamped in place.

Three layers of fine-grained concrete were formed by hand using steel trowels, with reinforcement placed in between, as shown in Figure 5.9c. Each of the two reinforcement layers consisted of four triangular segments, each overlapping by 50mm to ensure transfer of load, as shown in Figure 5.9a. The warp direction was aligned parallel to the formwork edges.

The total construction time for each shell ranged from three to five hours. Although the concrete workability was good, some force was required to spread the concrete evenly

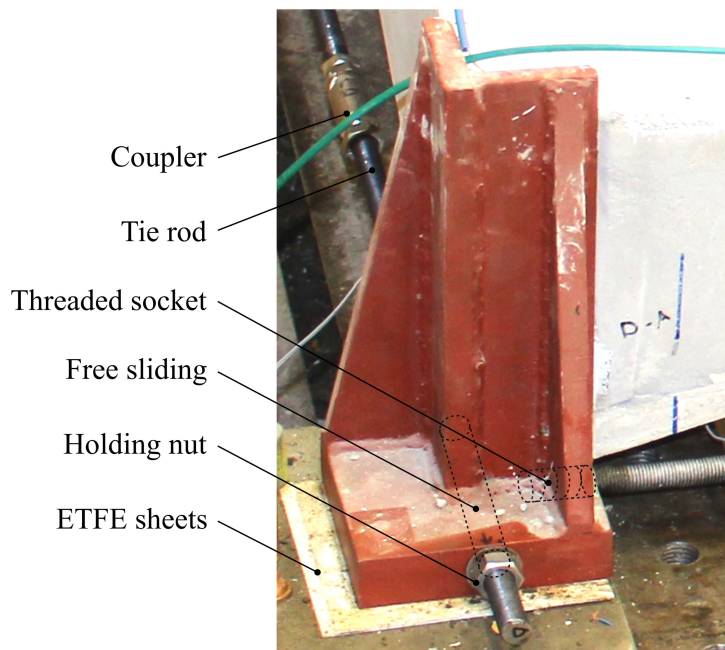


Figure 5.8: Corner support and tie details.

by hand, particularly for the thin cover layers. The rigidity of the formwork was therefore essential; this construction method would not have been possible using flexible formwork.

The deformation of the plywood forming surface was checked during the construction using a dial gauge. A location of low stiffness was chosen at the mid-point between two stiffeners near the highest point of the shell, showing 0.6mm movement after casting Shell 1. This was most likely caused by pressure from trowelling, rather than the self-weight of the concrete.

For each shell, four batches of concrete were mixed: one for each cover layer and two for the middle layer. This minimised drying out of the concrete and reduced the risk of premature setting. The target layer thicknesses of 3mm, 12mm and 3mm (totalling 18mm) were monitored during construction using guides on the formwork, spirit levels and spot checks. The concrete was also weighed out across each segment to achieve the desired average thickness. After construction of each shell, the total thickness was measured in detail using a digital 3D scanner (detailed in Section 5.5).

Although the manual construction process was time consuming, and thickness control was challenging, it is presumed that these issues could be overcome easily in future using concrete spraying equipment. The low number of reinforcement layers, its ease of application and uniformity, and the use of single-sided formwork would permit fast batch-construction at full-scale.



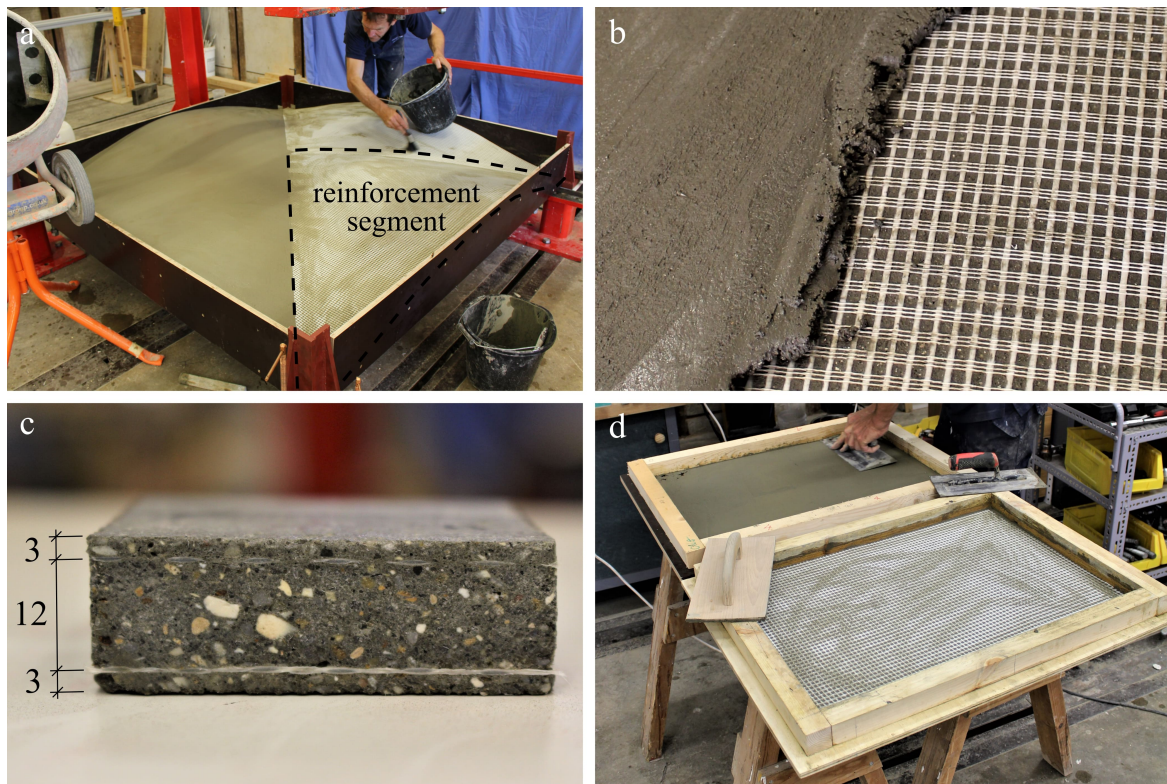


Figure 5.9: Construction of the TRC concrete shell, showing a) the application of a reinforcement layer, b) detail of the reinforcement and fine-grained concrete, c) TRC cross-section and d) construction of flat TRC panels for strength testing.

Each shell was constructed and tested in-situ, one after the other. The manufacturing process was therefore continuously refined, leading to notable differences between the three shells, as outlined below:

- The first batch of concrete mixed for Shell 1 (bottom cover layer) was dry and difficult to form. This possibly led to the lower cube strengths recorded for Shell 1. This was easily solved for Shells 2 and 3 by pre-wetting the concrete mixer.
- Detailing issues at the corner supports were deemed to have caused the premature failure of Shell 1, described in detail in Section 5.8.1. For Shells 2 and 3, this issue was resolved by setting the formwork a few millimetres above the casting surface of the corner supports and offsetting the height difference with concrete, thus avoiding a corner intrusion of steel into concrete.
- Delamination of the bottom cover layer was observed during testing of Shells 1 and 2. This was resolved in Shell 3 by applying more pressure during forming of the middle concrete layer in order to minimise voids around the reinforcement.

- For Shell 3, the water/cement ratio was reduced to achieve the correct workability (noted previously in Section 5.3.2).

Two flat TRC panels were also constructed simultaneously with each shell using the same materials and construction techniques. These are shown in Figure 5.10d. These panels were later cut into samples for testing in tension, bending and compression, as described in Section 5.6.

### Shell 3: casting of foamed concrete

Foamed concrete was cast onto Shell 3 with the formwork still in place, five days after shell construction. The formwork was struck two days later. Side panels were removed first to avoid damage to the fill, revealing the interior structure of the foamed concrete as illustrated in Figure 5.10.

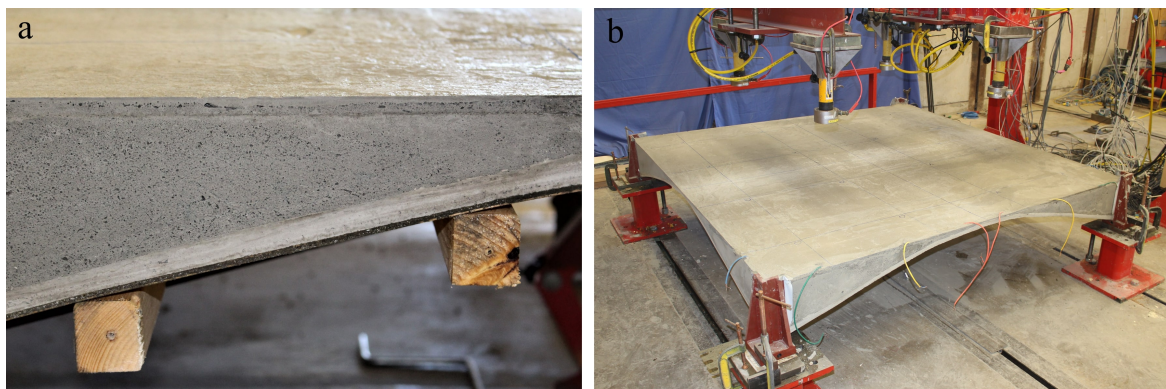


Figure 5.10: Shell 3 construction showing a) detail of formwork, shell and fill after removal of side-panel and b) the completed structure with formwork removed.

## 5.5 Measurement of geometry

Shell structures derive strength from geometry, and their performance can therefore be sensitive to manufacturing errors. Whilst efforts were made to construct the formwork and shells accurately, some deviation from the design was inevitable since both were constructed by hand. It is important to isolate the effect of these errors on the behaviour of the shells to enable a reliable assessment of the analysis methodologies. The first part of this process is the measurement of the shells themselves, which this section describes.

### 5.5.1 Methodology

The geometry of each surface was measured using an Artec 3D Eva digital scanner (Artec, 2015), shown in Figure 5.11. Digital scanning technologies collect high-resolution geometric data without the need for physical contact. However, scanning the shell underside after formwork removal was not possible due to space restrictions. Instead, the formwork was measured before casting and assumed as the bottom shell surface. The top surface was also scanned, prior to formwork removal, and compared with the formwork scan to determine the complete shell geometry. This technique assumes that the formwork remains static during construction, and therefore the 0.6mm previously measured indicates one source of error. For Shell 3, the top surface of the foam was also measured.

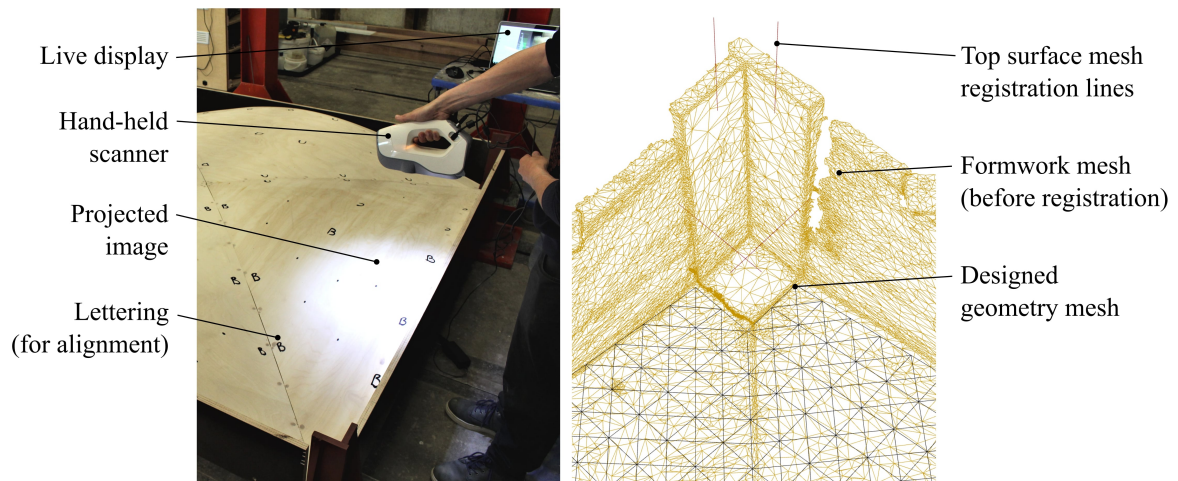


Figure 5.11: Measurement of shell geometry using a hand-held digital scanner. The left-hand image shows the scanner in use, while the right-hand shows the output mesh imported into Rhino, along with the 'as-designed' shell geometry and lines used for registration of the top and bottom shell surface scans.

Four overlapping scans of each surface were made, which were then processed in order to create a single surface mesh for later analysis. This was completed using the software Artec Studio. The meshes for each shell were imported into Rhino and positioned using a bespoke and repeatable registration process. Six transformation variables (three translations and rotations in the  $x$ ,  $y$  and  $z$  axes) define the precise location of each scan. These were set using a genetic algorithm in Grasshopper using the Galapagos component, to accuracies of 0.1mm (translations) and  $0.01^\circ$  (rotations), using a multi-stage process:

1. Each mesh was firstly positioned approximately by eye.
2. The formwork mesh was then registered to the designed formwork geometry. This was a three-stage process. Firstly, the vertical side panels of the formwork were removed by deleting mesh faces with a normal greater than  $30^\circ$  to the  $z$ -axis.
3. The formwork mesh was then located on plan ( $x$  and  $y$  translation,  $z$  rotation), by minimising the number of nodes which lie outside of the vertical projection of the design geometry.
4. The elevation of the formwork mesh ( $z$  translation,  $x$  and  $y$  rotation) was then set by minimising the average error between the nodes of the designed geometry mesh and the closest point on the scanned mesh. This sets the formwork scan as closely to the designed geometry as possible.
5. The top surface mesh was then registered to the bottom (formwork) surface. The corner supports, which remained clamped during construction, were used to align the scans. In each corner, four lines were positioned intersecting flat surfaces; two in the  $z$  direction and one in the  $z$  and  $y$  directions (Figure 5.11). The distance between the intersection points of each line (through both scans) was used to quantify the level of alignment. All six transformations were optimised simultaneously, and the fitness value minimised was the sum of the squares of the distances between the sixteen pair of intersection points. The distances were squared in order to ensure a central alignment in the case of a mismatch in size.
6. For Shell 3, the scan of the foam surface was registered in a similar manner to the top surface of the shell.

The scanner has a quoted accuracy of 0.1mm for the location of points in 3D space. However, errors also accumulate over distance. Table 5.3 shows the average and maximum distances between corresponding pairs of intersection points for each shell, after completion of the final registration phase.

The results give an indication of the level of accuracy of the scans, although are likely to represent upper bounds due to the location of the corner supports at the far edges of each mesh. This significantly larger errors for Shell 1 suggests a possible movement of the supports between scans.

Table 5.3: Misalignment of the scanned top (shell) and bottom (formwork) scanned meshes after registration. The results refer to the distances between intersection points through the corner supports.

	Shell 1	Shell 2	Shell 3
<i>Vertical</i>			
<b>Average [mm]</b>	2.69	0.73	1.53
<b>Maximum [mm]</b>	4.92	0.95	2.06
<i>Horizontal</i>			
<b>Average [mm]</b>	0.72	1.12	0.54
<b>Maximum [mm]</b>	2.42	2.05	1.10

## 5.5.2 Results

Figures 5.12, 5.13 and 5.14 show the measured geometry of each shell, including the formwork error, mid-surface error, thickness and sections through the centrelines of the four corner support surfaces. For Shell 1, the steel support surfaces of the corner supports are missing from the formwork scan. This resulted in some erroneous results in the corners and incomplete sections.

A comparison of key results is given in Table 5.4. Formwork geometry errors accumulated with the construction of each shell, as shown by the steady increase in standard deviation. This permanent deformation of the forming surface is likely caused by mechanical pressure and moisture from the casting process. For Shell 3, the maximum formwork error was 7.8mm, near corner A.

Table 5.4: Comparison of key results from the scanned geometry of each shell.

	Shell 1	Shell 2	Shell 3
<b>Formwork error (standard deviation) [mm]</b>	2.71	2.83	3.44
<b>Mid-surface error (standard deviation) [mm]</b>	2.71	3.27	3.89
<b>Thickness (standard deviation) [mm]</b>	3.05	2.89	2.69
<b>Thickness (average) [mm]</b>	19.88	20.41	18.64

The three shells show some similarities in thickness distribution. For example, thicker regions are typically seen along the creases between formwork sections, and near the corners. This is a result of smoothing over the creases in the formwork surface. For Shells 2 and 3, large thicknesses in the corner support surfaces are also shown, due to the deliberately high setting of the formwork. All shells had an average thickness higher than the design value of 18mm, and Shells 1 and 2 were considerably thicker on average than Shell 3. Since a similar

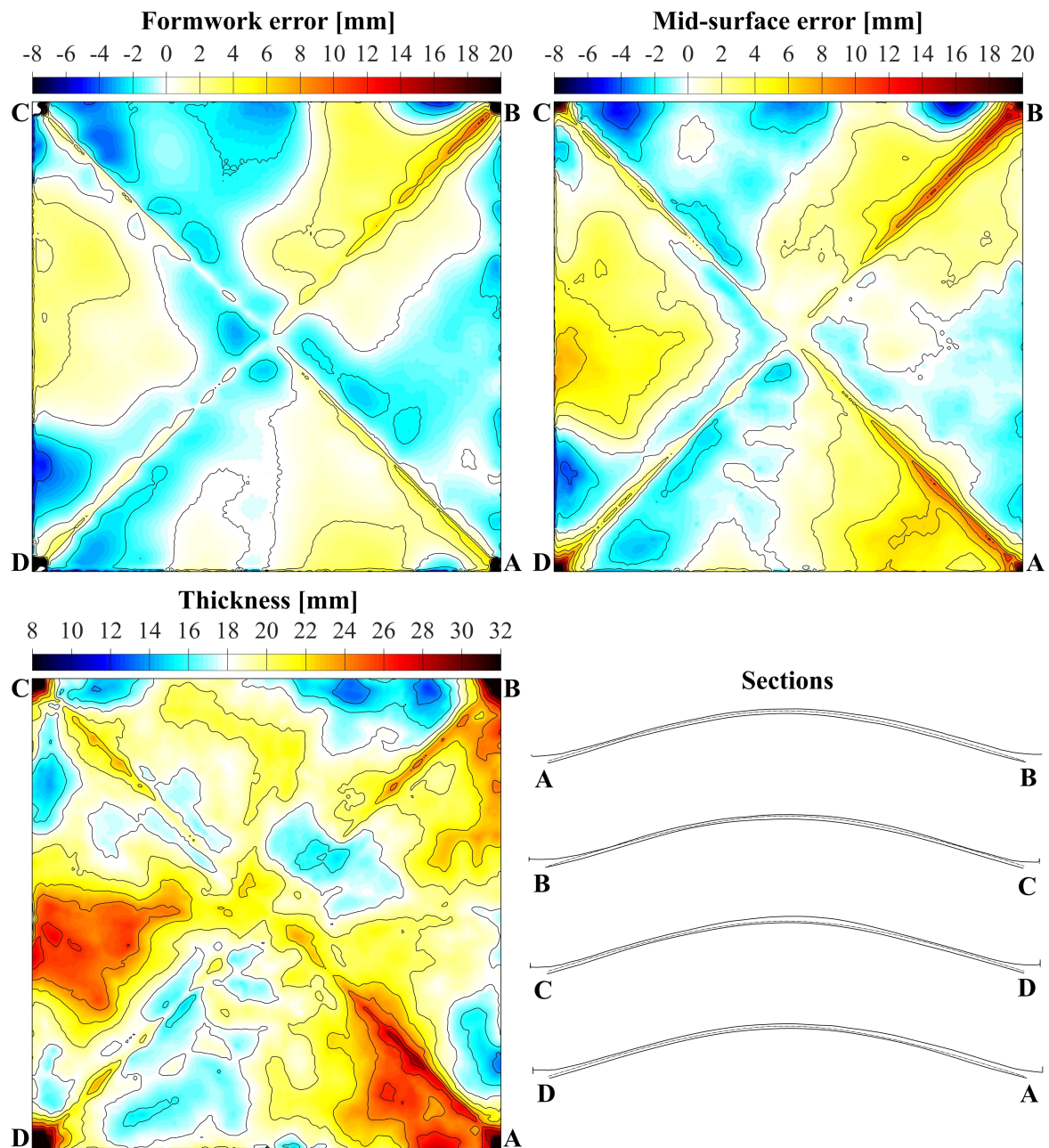


Figure 5.12: Shell 1 measured geometry and comparison with intended design.

mass of concrete was added for each casting, this may be explained by the higher density of the concrete used for Shell 3 (see Table 5.1). The standard deviation of thickness decreases with each successive shell, possibly indicating refinement of the construction technique.

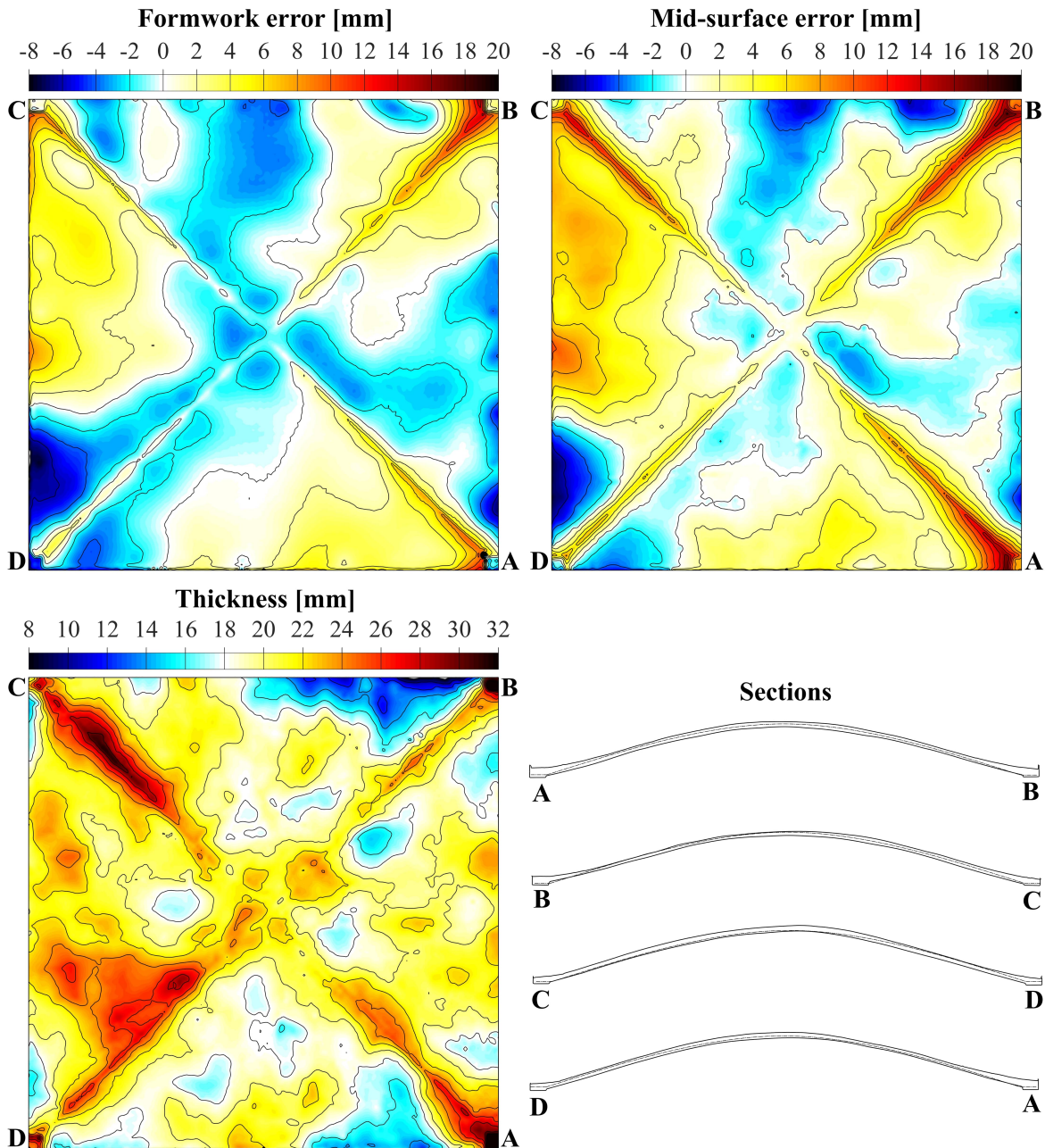


Figure 5.13: Shell 2 measured geometry and comparison with intended design.

### 5.5.3 Discussion

The scanning gives a high level of detail, however the accuracy of the measurements is not guaranteed. The accumulations of error over the large scanned surfaces are unknown. This could potentially be assessed in future work by scanning a similarly sized structure of known thickness, such as a plywood panel, and quantifying the measured variation. The assumption

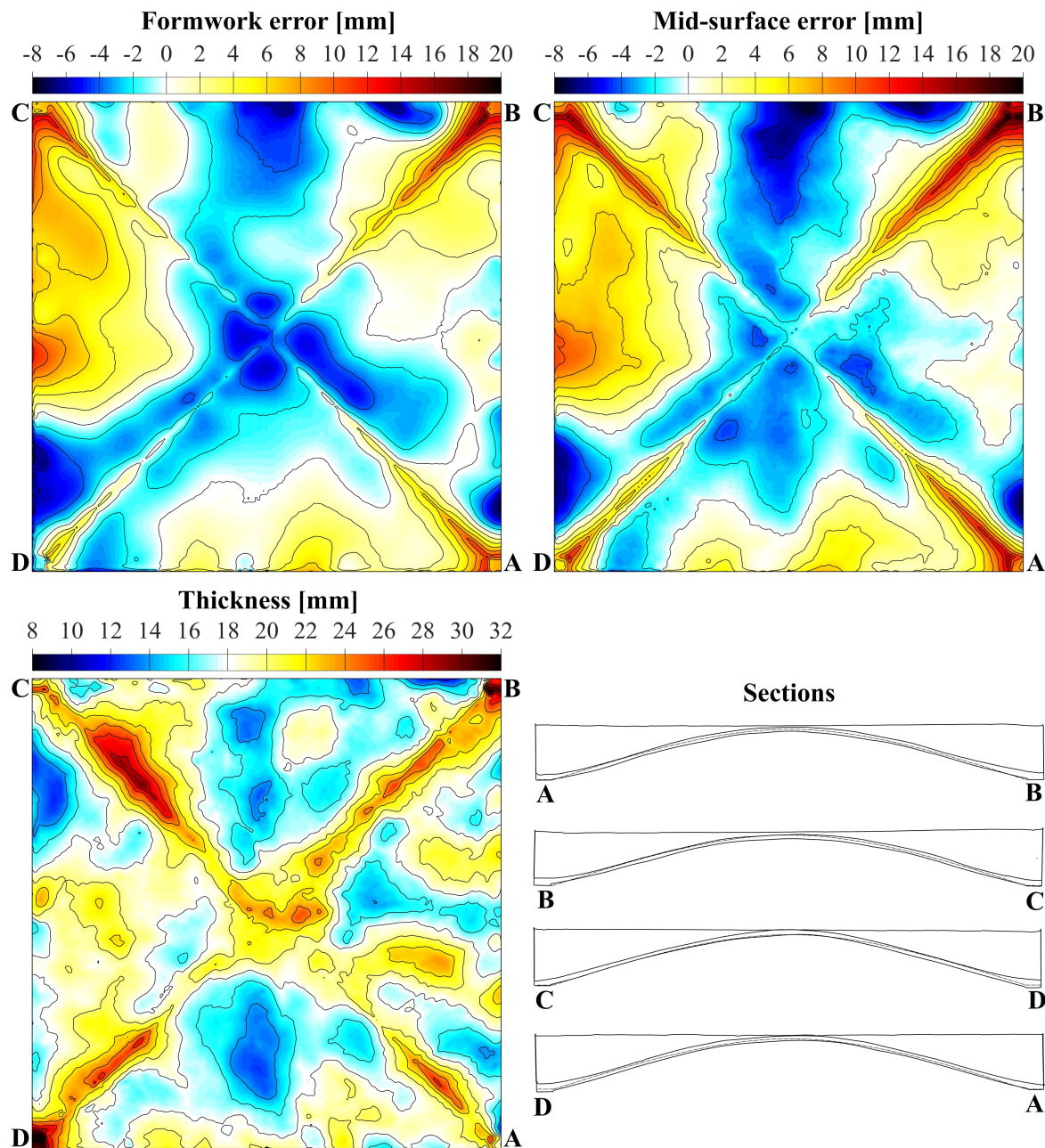


Figure 5.14: Shell 3 measured geometry and comparison with intended design.

that the formwork does not deform during casting was also shown to be untrue, shown by the measured 0.6mm movement (at one point only).

An attempt was made to directly measure the accuracy of the thickness plots. Calliper measurements were taken at eight points around the edge of the shell, to be used in the analysis of strain gauge data. These were compared with similar locations in the scanned data. The magnitude of the resulting discrepancies can be described by their standard deviations,



which were 2.38mm, 1.12mm and 1.06mm for Shells 1, 2 and 3 respectively. The larger errors present in Shell 1 are consistent with the greater misalignment between the two scans (Table 5.3).

Despite the variable accuracy of the measurements, the data collected still provides a valuable representation of the magnitude and pattern of construction errors. The data is also in sufficient detail to be incorporated into finite element analysis models, thus enabling the effect of construction inaccuracy to be later isolated and quantified (Section 6.3).

Formwork inaccuracy, which increased with each successive shell, could potentially be reduced through a re-design. The largest errors occurred at the formwork's edge, where only the straight stiffening elements support the 4mm plywood. Including a continuous support, cut to the profile of the shell edge, would have significantly reduced these errors. Orientating the stiffeners perpendicular to the current configuration (following the arch profile) would have also created a stiffer and more accurate forming surface.

## 5.6 Textile reinforced concrete specimen tests

Panels of 18mm thick TRC were cast alongside each shell, using the same batches of concrete, identical construction methods and in similar environmental conditions (Figure 5.9d). These were cut into specimens and tested in tension, four-point bending and compression. Both the warp and fill reinforcement directions were investigated, and tests were performed within one day of the corresponding shell test.

These tests were carried out to study the quality of shell materials and manufacturing, and quantify any variation between shells. In addition, they provide the data required to plot failure envelopes which, through comparison with the experimental shell test results, were used to assess the TRC strength design methodology (in Section 6.5). Tensile, bending and compressive strengths are required to plot bi-linear TRC failure envelopes (proposed by Scholzen et al. (2015b)), and the composite reinforcement tensile strength is required to plot analytical TRC failure envelopes (as detailed in Section 4.3).

### 5.6.1 Tensile

For each shell, four 100mm wide TRC strips were tested in tension; two along each of the warp and fill reinforcement directions. The specimens were clamped between steel plates with rubber inserts to provide grip and protection, using an identical test arrangement as described in Section 4.2.3. This is shown in Figure 5.15a.

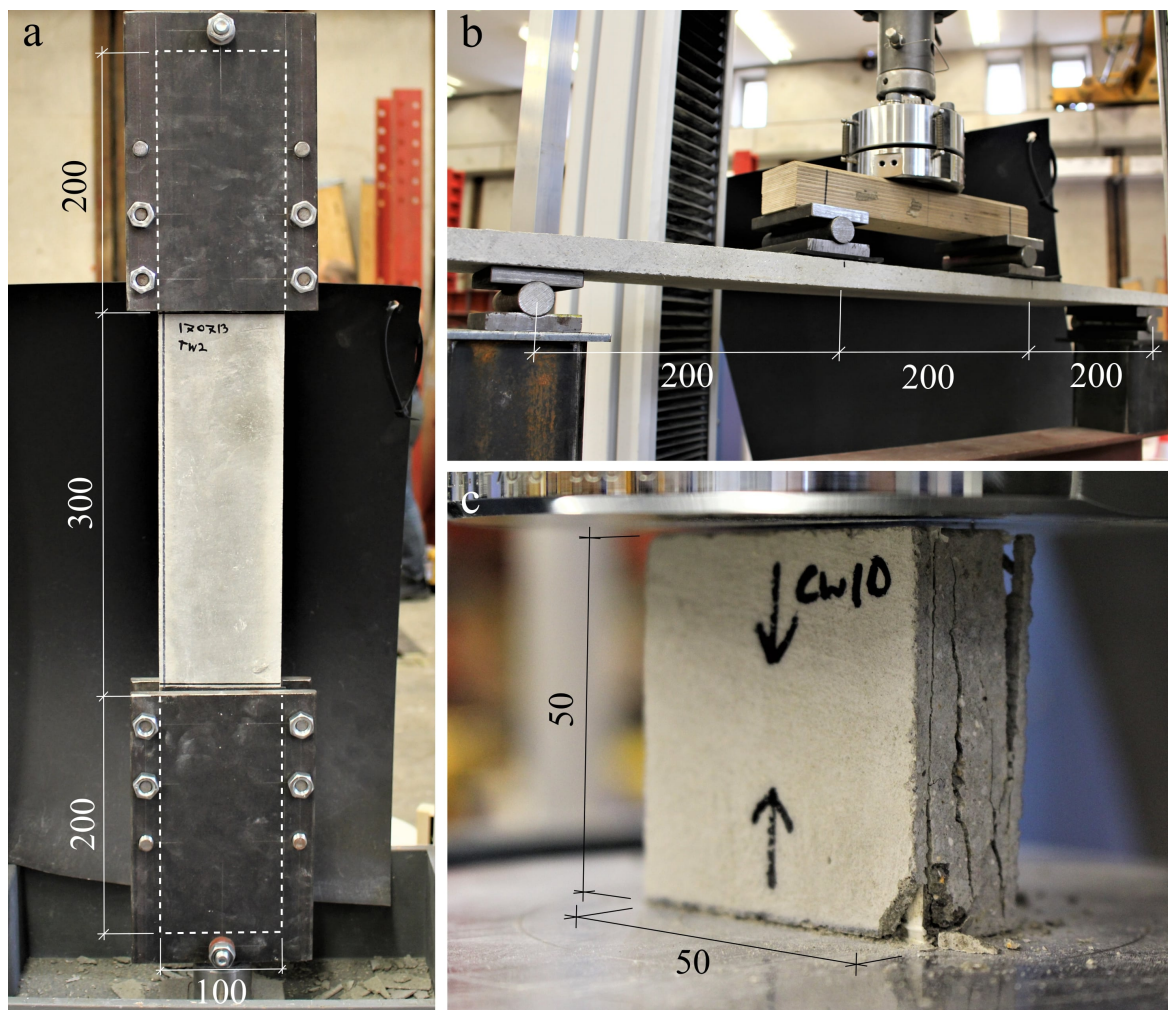


Figure 5.15: Testing arrangements for TRC specimens, including a) tensile tests, b) four-point bending tests and c) compressive tests.

Load-extension results are shown in Figure 5.16, and show distinct uncracked, cracking and fully-cracked regions similar to those observed in Section 4.2.3. Due to slip and deformation at the clamping plates, the results do not accurately indicate the change in stiffness of the specimen upon cracking. The first warp specimen for Shell 1 was tested cracked prior to the test due to an earlier experimental error.

For Shells 1 and 2, some delamination of the bottom concrete cover layer occurred at or near the failure load due to poor bonding around the reinforcement. This is highlighted in Figure 5.17a, along with the wide spacing between cracks. In all tests, failure occurred due to tensile rupture of reinforcement at the location of a large crack. As example of the fibre pull-out of the fill reinforcement is shown in Figure 5.17b.

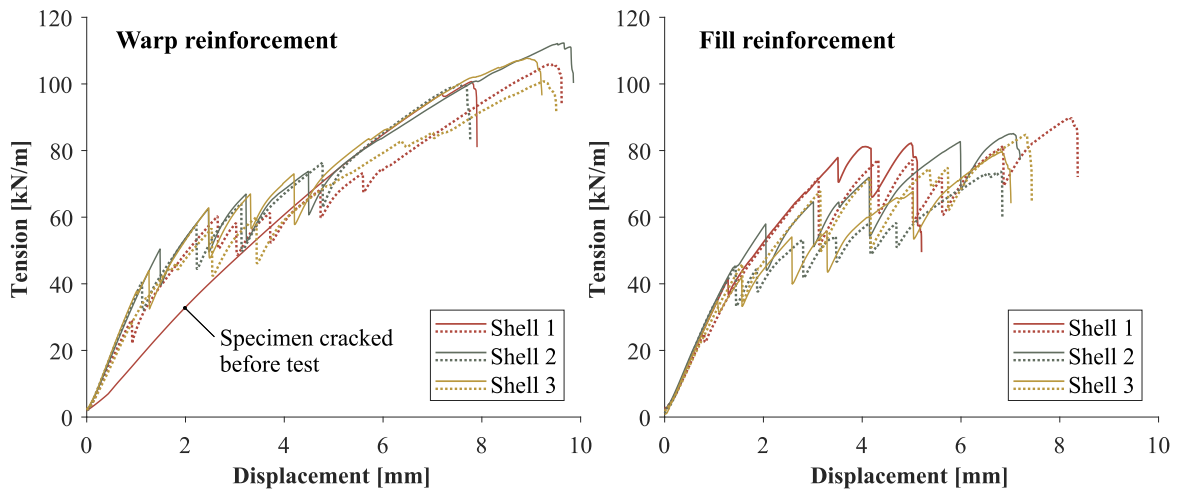


Figure 5.16: Tensile TRC test results for warp (left) and fill (right) reinforced specimens.

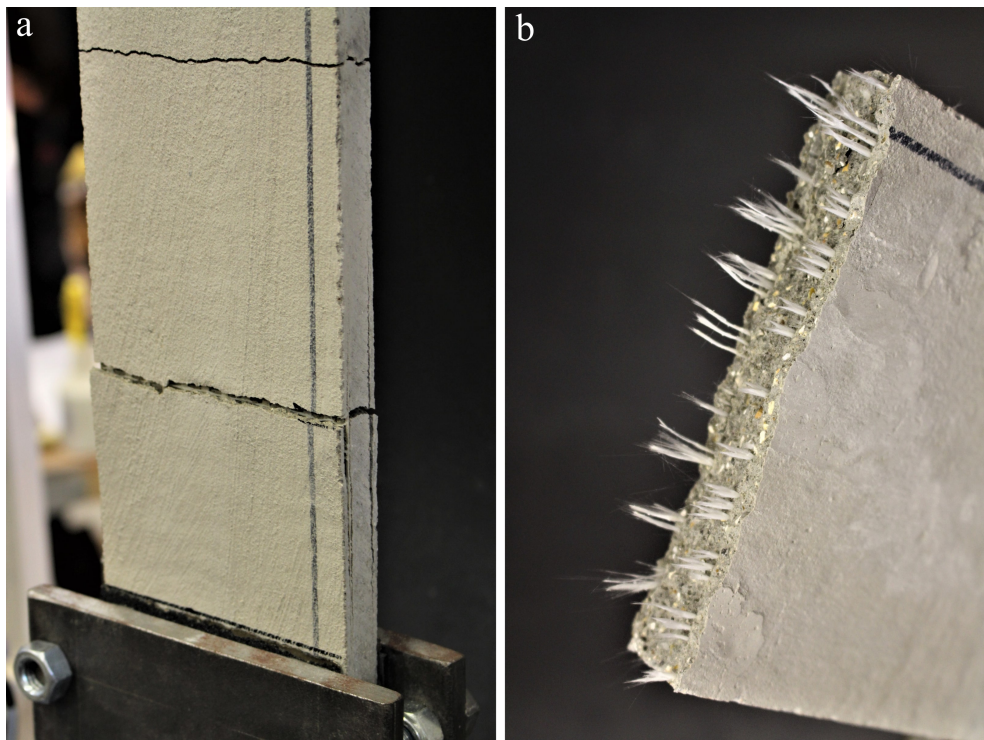


Figure 5.17: Tensile testing of TRC specimens, showing a) cracking and delamination of cover layers and b) fibre rupture and pull-out (fill direction).

Table 5.5 gives key results from each of the tensile tests. The strength of the concrete was calculated from the load at first cracking and the local thickness. The average across all specimens was 2.19MPa, although significant variation was noted.

Table 5.5: Tensile tests on TRC specimens: result summary

Measured average thickness [mm]	First cracking load [kN/m]	Concrete tensile strength [MPa]	Ultimate load [kNm/m]	Reinforcement failure stress [MPa]
<b>Shell 1: Warp direction</b>				
17.0	31.7	1.87	100.7	804
16.7	29.1	1.75	105.9	845
<b>Shell 2: Warp direction</b>				
18.2	50.4	2.77	112.3	827
18.2	40.5	2.22	99.8	796
<b>Shell 3: Warp direction</b>				
17.3	37.8	2.00	107.7	825
16.3	46.2	2.86	100.8	804
<b>Shell 1: Fill direction</b>				
18.8	41.4	2.20	82.2	788
19.1	25.0	1.31	89.8	861
<b>Shell 2: Fill direction</b>				
18.3	45.0	2.45	85.1	815
18.2	45.3	2.50	73.6	705
<b>Shell 3: Fill direction</b>				
18.9	34.9	1.85	79.7	763
19.5	45.9	2.45	84.7	811

The ultimate tensile strengths were higher in the warp direction, corresponding to the larger reinforcement area. Variation between Shells 1, 2 and 3 was low. The average reinforcement strengths over all tests were 817MPa and 791MPa in the warp and fill directions respectively, corresponding to tensile strengths of 106.7kN/m and 82.6kN/m for the TRC section. This gives composite reduction factors ( $k_1$ ) of 0.685 and 0.597 respectively, relative to the tensile strengths given in Table 4.2.

The composite strength in the warp direction is lower than that observed in Section 4.2.3, by 6-16%. It has been previously hypothesised that the strength is influenced by the crack width. The smaller number of cracks observed in the shell specimens suggest larger crack widths, which may lead to greater local stress concentrations in the reinforcement. The weaker concrete used, and younger age at testing, could have reduced the bond strength, leading to fewer and larger cracks. The discrepancy highlights the sensitivity of the composite reinforcement strength to the matrix material, and supports the argument that this value should be determined through physical testing.

The tensile tests highlight the structural contribution of the reinforcement. Compared to an unreinforced section (first cracking), the tensile strength is increased by factors of 2.7 and 2.1 in the warp and fill directions respectively. The gain in strain capacity is considerably larger, although not measured accurately in this case.

### 5.6.2 Four-point bending

Specimens of similar dimensions were also tested in four-point bending, using the testing arrangement shown in Figure 5.15b. As for the tensile tests, two warp and fill specimens were tested along with each shell. Of each pair, one was loaded in sagging and one in hogging (relative to the shell orientation). The bottom cover layer, constructed first, is in tension under sagging and vice versa.

Results are shown in Figure 5.18, and a summary of key values is given in Table 5.6. In each test, initially linear behaviour was observed, followed by cracking and a corresponding reduction in stiffness. In some cases, a fully-cracked linear region is reached. The uncracked stiffness was similar for all specimens, but the cracked stiffness was higher in the fill direction, reflecting the larger reinforcement area. A typical crack distribution is shown in Figure 5.19a.

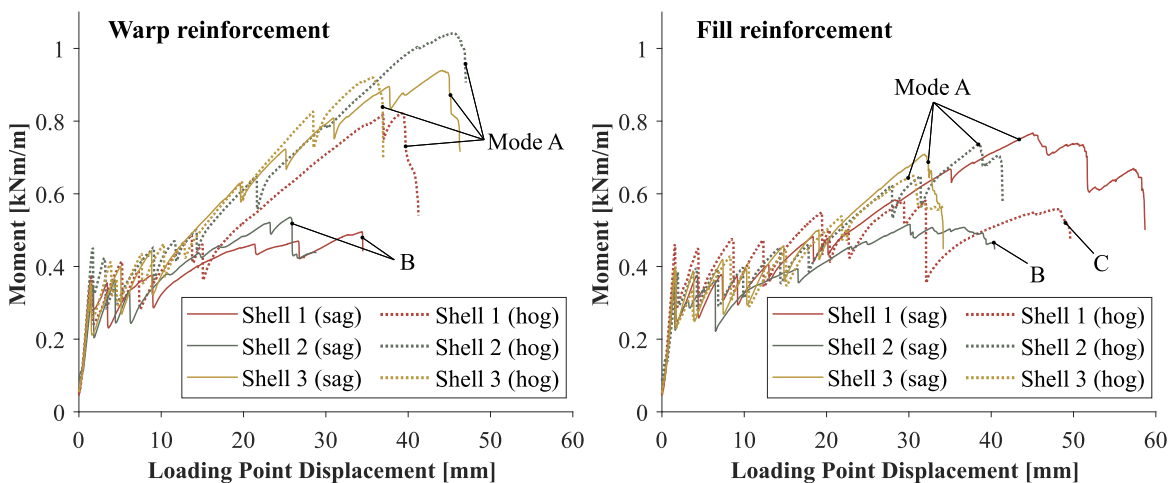


Figure 5.18: Relationship between mid-span moment and loading point displacement for warp (left) and fill (right) TRC specimens tested in four-point bending.

Three different modes of failure were observed in the bending tests, referred to as A, B and C in Figure 5.18 and Table 5.6. The highest strengths were recorded for failure mode A, where tensile rupture of the reinforcement occurred. In Mode B, this was prevented by premature delamination of the bottom (tensile) reinforcement. This occurred in sagging for Shells 1 and 2, and was caused by poor bonding of the cover layer as shown in Figure 5.18b.

Table 5.6: Four-point bending tests on TRC specimens: result summary

<b>Orienta- tion</b>	<b>Failure mode*</b>	<b>Measured average thickness</b> [mm]	<b>First cracking moment</b> [kN/m]	<b>Concrete flexural strength</b> [MPa]	<b>Ultimate moment</b> [kNm/m]	<b>Reinf. stress at failure</b> [MPa]
<b><i>Shell 1: Warp direction</i></b>						
Sagging	B	17.9	0.362	7.25	0.496	530
Hogging	A	17.6	0.377	7.35	0.821	900
<b><i>Shell 2: Warp direction</i></b>						
Sagging	B	17.8	0.347	6.39	0.536	577
Hogging	A	17.9	0.451	8.24	1.042	1030
<b><i>Shell 3: Warp direction</i></b>						
Sagging	A	18.8	0.288	4.96	0.939	948
Hogging	A	18.4	0.356	6.94	0.920	954
<b><i>Shell 1: Fill direction</i></b>						
Sagging	A	17.9	0.349	6.64	0.767	984
Hogging	C	18.9	0.460	7.54	0.582	702
<b><i>Shell 2: Fill direction</i></b>						
Sagging	B	18.2	0.368	6.40	0.516	651
Hogging	A	18.2	0.384	6.95	0.736	929
<b><i>Shell 3: Fill direction</i></b>						
Sagging	A	18.4	0.394	6.67	0.709	881
Hogging	A	18.1	0.389	6.99	0.650	824

\*Mode A: Tensile reinforcement rupture.

Mode B: Delamination of cover and reinforcement on tension side.

Mode C: Delamination of cover on compression side.

It is likely that, for this failure mode, the strength was influenced by the anchorage length of the reinforcement. It is thus unclear how the weak bond might affect the strength of the shells themselves, where the anchorage length typically higher. Mode C was also caused by delamination of the same cover layer, this time occurring at the top (in compression). The issue of poor bond was resolved in Shell 3, as demonstrated by the consistent Mode A failure.

The stress in the reinforcement at failure was estimated in a similar manner to Section 4.2.4. Using the specimens which failed through Mode A only, the average estimated reinforcement stresses were 958MPa and 905MPa in the warp and fill directions respectively. These values are 17% and 14% greater than those measured in pure tension.

Flexural concrete strengths were calculated from the moments at first cracking and local section thicknesses, and are included in Table 5.6. Considerable variation between samples

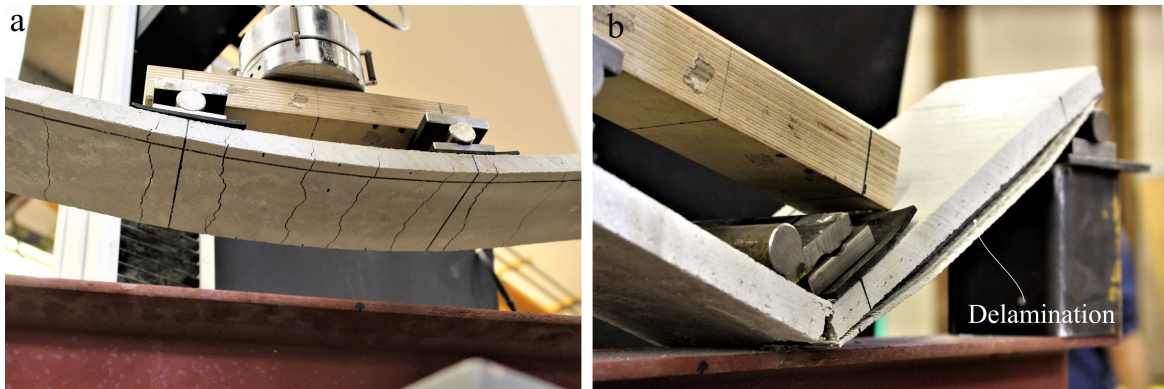


Figure 5.19: Testing of TRC specimens in four-point bending, showing a) high curvature and distribution of cracks (Shell 2, fill direction, hogging) and b) premature failure in due to delamination of reinforcement (Shell 2, warp direction, sagging).

was observed, however there is no significant difference between the shells. The average flexural strength of 6.86MPa is 3.13 times greater than the average tensile strength measured in the tensile tests, showing a similar pattern to the tests of Section 4.2.

The average moment at first cracking was 0.377kNm/m. This means that the presence of the reinforcement resulted in an increase in strength by factors of 2.47 and 1.90 in the warp and fill directions respectively (considering failure Mode A only). By comparison, the ratios of average displacements at peak load and first cracking were 26.9 (warp) and 23.9 (fill), an order of magnitude higher. This highlights important properties of this glass-fibre reinforced TRC section; a significant drop in rotational stiffness upon cracking and large curvature at failure.

### 5.6.3 Compression

The compressive strength of the fine-grained concrete was previously determined through cube tests (Section 5.3.2). However, the TRC differs from the cubes in thickness, construction method and by the presence of reinforcement. Each of these factors potentially affects compressive strength. Typically, TRC has lower strength than unreinforced concrete, since the layering process and presence of reinforcement create planes of weakness for crack initiation (Bochmann et al., 2017), and compressive tests were therefore performed on the TRC itself.

Square specimens (50x50mm) were cut from the TRC panels (18mm thick) cast alongside each shell. This size was limited by the 50kN maximum capacity of the loading rig used. Each specimen was placed between steel plates and compressed at a displacement rate of 0.5mm/minute. Twelve warp and twelve fill specimens were tested for Shells 2 and 3. Due to

accidental damage, only eleven warp and ten fill specimens were tested for Shell 1. In order to minimise bending of the specimen, the top and bottom surfaces were made parallel to a tolerance of 0.1mm by sanding.

Failure of the specimens was typically sudden and explosive. Cracks always occurred in the plane of the reinforcement, as shown in Figure 5.20a. Delamination of the reinforcement and cover layer was also commonly observed (Figs. 5.20b and 5.20c), indicating a plane of weakness.



Figure 5.20: TRC samples tested in compression, showing a) typical crack pattern after failure (Shell 3), b) splitting in the reinforcement plane (Shell 1) and c) spalling of the cover layer before failure (Shell 2).

Figure 5.21 compares the compressive strengths of the 100mm cubes and 50mm TRC squares. Firstly, it is clear that the variation between the TRC specimens is much higher than the cubes. This might be expected due to their smaller size, since the distribution of flaws is statistically more variable. The presence of the reinforcement, as well as the layered construction method, might also increase variation. For Shells 2 and 3, the average strength of the TRC sections was lower than the cubes. The fill direction is also weaker, possibly reflecting the greater reinforcement area. This suggests that using the cube strengths might be unconservative for design.

For Shell 1 however, the opposite pattern of strength is observed. As discussed in Section 5.3.2, the cubes cast with Shell 1 used a batch of concrete with workability issues, possibly reducing the cube strength. However, this does not explain why the TRC specimens are significantly stronger than Shell 2 (despite the similarities in concrete mix) and hence calls into question the reliability of the TRC results.

Testing the specimens between flat steel plates will cause bending where the top and bottom surfaces are not close to parallel. It is therefore possible that more careful cutting and sanding of the Shell 1 specimens resulted in a more uniform load distribution. If the strain at failure is assumed to be 0.255%, as measured in the prism tests described in Section 5.3.2,



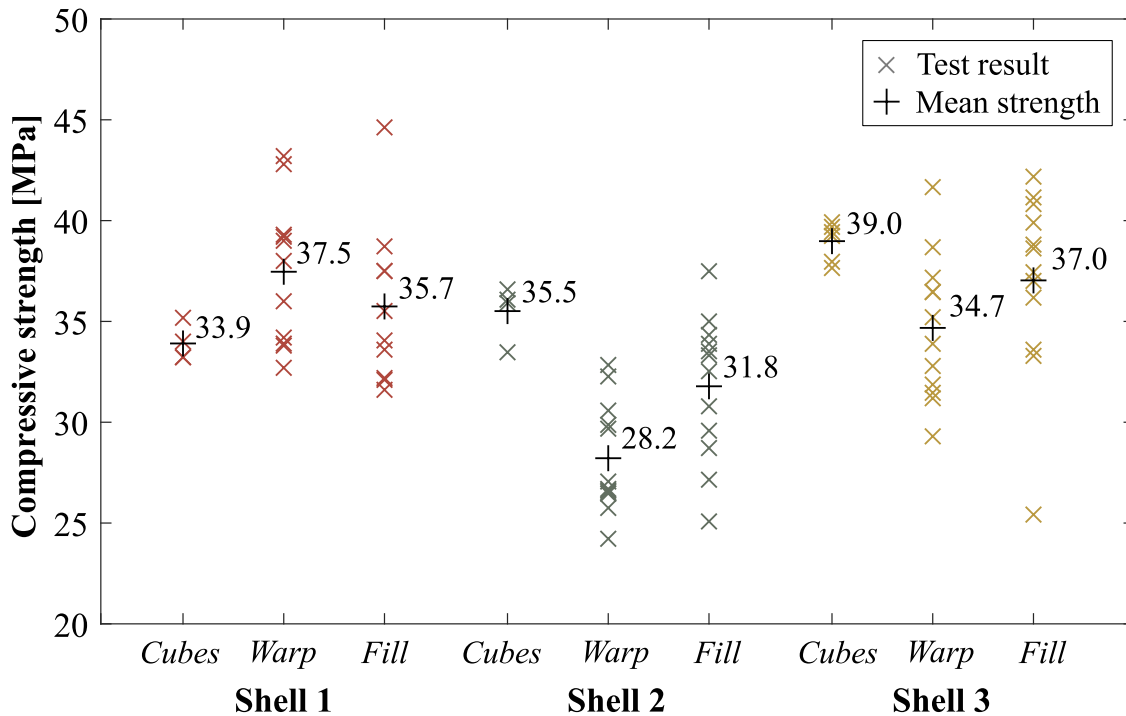


Figure 5.21: Comparison of compressive strengths recorded in cube and TRC tests for each shell.

then the corresponding shortening of a 50mm tall specimen would be just 0.13mm. This is comparable to the tolerance of 0.1mm achieved through sanding, suggesting that even this small variation in height could cause a high non-uniformity of stress. The test methodology might therefore be improved by using pin-jointed loading plates to eliminate bending (as in Section 4.2.5).

To conclude, these results do not conclusively show that the TRC is significantly weaker in compression than the unreinforced prisms and cubes. The prism strength of 36.6MPa was therefore assumed as a baseline value for the TRC shells in later analysis.

## 5.7 Shell test methodology

This section describes the methodology of the main shell tests. Shells 2 and 3 were tested 14 days after casting, and Shell 1 at 18 days.

### 5.7.1 Loading

Loading was applied using four hydraulic jacks. Each was distributed to four points on the shell via a load-spreader assembly, creating a grid of sixteen 200mm square loading patches at 500mm centres, intended to approximate a uniformly distributed load (Figure 5.22). The loading patches consisted of 150mm square steel plates, levelled using dental plaster to a minimum depth of 30mm.

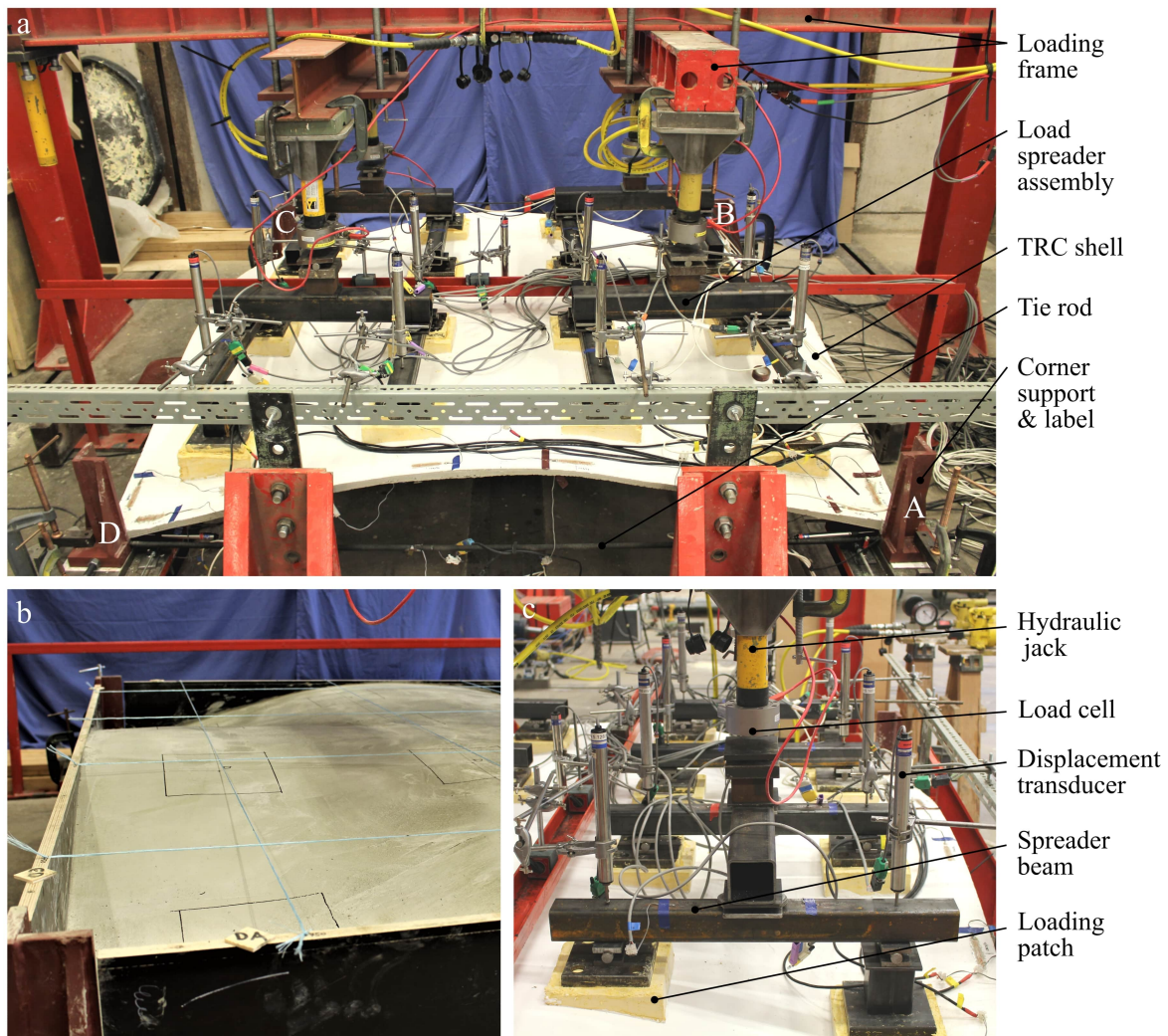


Figure 5.22: Test arrangement and loading of shell specimens, showing a) an overview of the test set-up b) setting out of loading points and c) load-spreader assembly with instrumentation.

The load-spreader assemblies were fully articulated using a system of pins and ball joints to create even load distribution during deformation. Separate tests were performed on each of the four assemblies to verify this assumption, which are detailed in Section 5.9.2.

The four specimen corners and corresponding jacks were labelled A, B, C and D as shown in Figure 5.23. Jacks A and B were controlled independently of C and D, thus allowing application of an asymmetric load.

Other loading options considered included water-filled bags or sand bags, however these require large volumes of material and restrict access to the top surface of the shell for instrumentation. Loading using an inflatable membrane was also considered, although in this case the applied pressure would be normal to the surface, resulting in different loading for the unfilled and filled shells. Hydraulic jacks were eventually chosen for their speed, control and ease of data logging using load cells. They also approximately simulate a displacement controlled test, which allows post-peak structural behaviour to be explored.

### 5.7.2 Instrumentation

The tests were monitored using load cells, displacement transducers and strain gauges at the locations shown in Figure 5.23. All data was logged at one second intervals.

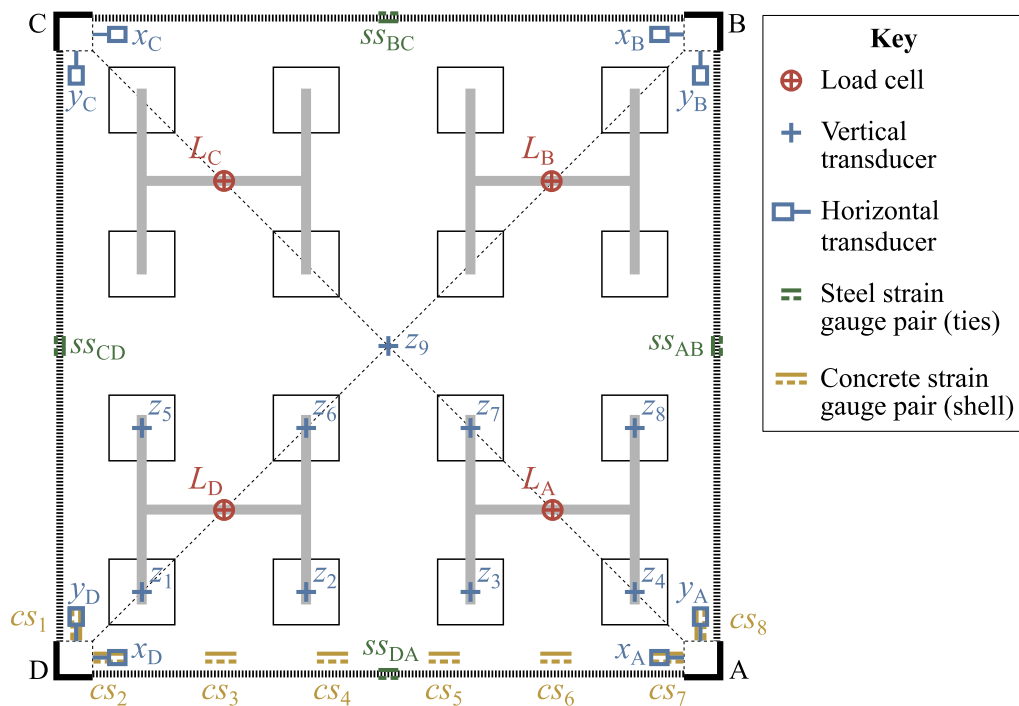


Figure 5.23: Instrumentation set-up showing locations and labelling of load cells, transducers and strain gauges (similar for all specimens).

Load cells were placed beneath each hydraulic jack and used to control the tests. Nine displacement transducers were located above the shell to measure the vertical deformation.

Due to the limited number of transducers available, only one half of the shell was measured, with the other half assumed to behave symmetrically. Eight vertical transducers were centred above loading patches (Figure 5.22c) and one at the centre, directly on the shell surface.

Eight further transducers measured horizontal displacements, placed in orthogonal pairs at the bases of each corner support, as shown in Figure 5.24b. The extension of each tie could therefore be calculated as the difference of the readings at each end to eliminate rigid-body movements.

Strain gauges were attached in opposite pairs onto each tie rod. Separate tensile tests on each were conducted to calibrate the tie force to the average strain (as described in Section 5.9.1).

Finally, a total of sixteen concrete strain gauges (of 60mm length) were fixed to the shell surface in top and bottom pairs, as shown in Figure 5.24a. Pairs were spaced at 355mm centres at a distance of 30mm from the shell's edge. DIC was not considered practical at the time of instrumentation set-up, due to the danger of equipment damage below the shell and congestion above.

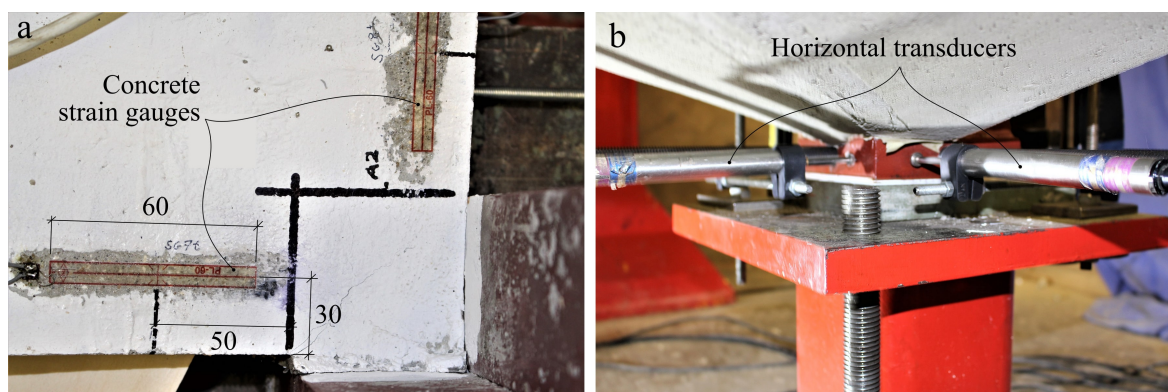


Figure 5.24: Instrumentation details including a) concrete strain gauges near a corner support and b) transducers monitoring horizontal displacement of corner supports.

### 5.7.3 Test sequence

Each shell was subject to five test phases, summarised in Figure 5.25. These were intended to approximately simulate a real-world sequence of construction and use, and also to maximise the amount of information collected from each specimen. In the first phase, a uniform load was applied up to the minimum design load ( $3.75\text{kN/m}^2$ ). The pre-strain was then applied in the second phase by tightening the tie bolts. The third and fourth phases involved a uniform loading and unloading, peaking at the maximum design load ( $10.31\text{kN/m}^2$ ). In the fifth and

final phase, the load was increased over jacks C and D (to failure) whilst being held constant in jacks A and B, thus simulating an asymmetric live load.

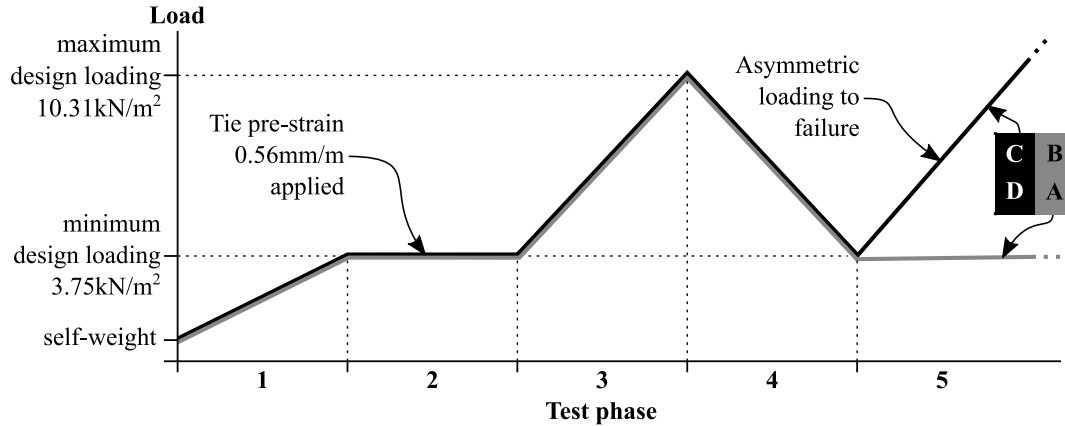


Figure 5.25: Load testing phases.

Before loading the hydraulic jacks, the shells support their own self-weight plus that of the load-spreader assemblies ( $0.405\text{kN/m}^2$ ). This was taken into account when calculating the jack force required to reach the target loads. The self-weight of each test specimen is summarised in Table 5.7, which also compares the as-designed geometry with that measured in Section 5.5. The same load increments were applied in each test (based on the as-designed self-weight of  $0.376\text{kN/m}^2$ ), and therefore the total loads, including self-weight, are slightly different. This is accounted for in the results given throughout the following section.

Table 5.7: Assumed self-weight of each test specimen, based on the as-design shell geometry. These values were used to calculate the total supported load.

	Density [ $\text{kg/m}^3$ ]	Plan area [ $\text{m}^2$ ]	<i>As designed</i>		<i>As measured</i>	
			Average thickness [mm]	Self- weight [ $\text{kN/m}^2$ ]	Average thickness [mm]	Self- weight [ $\text{kN/m}^2$ ]
<b>Shell 1</b>	2091	4.072	18.00	0.376	19.88	0.415
<b>Shell 2</b>	2081	4.072	18.00	0.374	20.41	0.424
<b>Shell 3</b>	2175	4.072	18.00	0.391	18.64	0.405
<b>Fill</b>	805	4.000	55.56	0.439	52.23	0.412

## 5.8 Shell test results

This section firstly describes the testing of each shell individually (Sections 5.8.1, 5.8.2 and 5.8.3), before making a separate comparison between the three sets of data (Section 5.8.4).

The loads given throughout this section are total loads including the self-weight of each specimen (calculated using the measured geometry as given in Table 5.7). This results in an initial offset along the load axis. All other measurements are shown relative to the start of the test.

### 5.8.1 Shell 1

Figure 5.26 shows the test sequence and key events for Shell 1. The first phase of uniform loading was carried out successfully. Phase 2 was then begun, with the tie rod holding nuts being tightened sequentially in steps. Tie D-A then unexpectedly failed at a load of approximately 9.2kN due to the bar not being fully threaded into the coupler. This occurred before the total tie pre-strain had been applied, at an average load of  $4.58\text{kN/m}^2$ . The total loss of a tie caused an instantaneous spreading of supports D and A (by 6.0mm) and a downwards vertical displacement (by up to 9.6mm). This also caused a drop in load to an average value of  $1.55\text{kN/m}^2$  due to extension of the jacks. The structure did not fail, however hogging cracks were noted at supports D and A (Figure 5.28b), as well as sagging cracks near mid-span (Figure 5.28a). Several strain gauges were damaged in the incident, possibly due to cracking, resulting in incomplete and unreliable data in the remainder of the test. Some of the the horizontal transducer data was also lost due to slipping of the holding clamps.

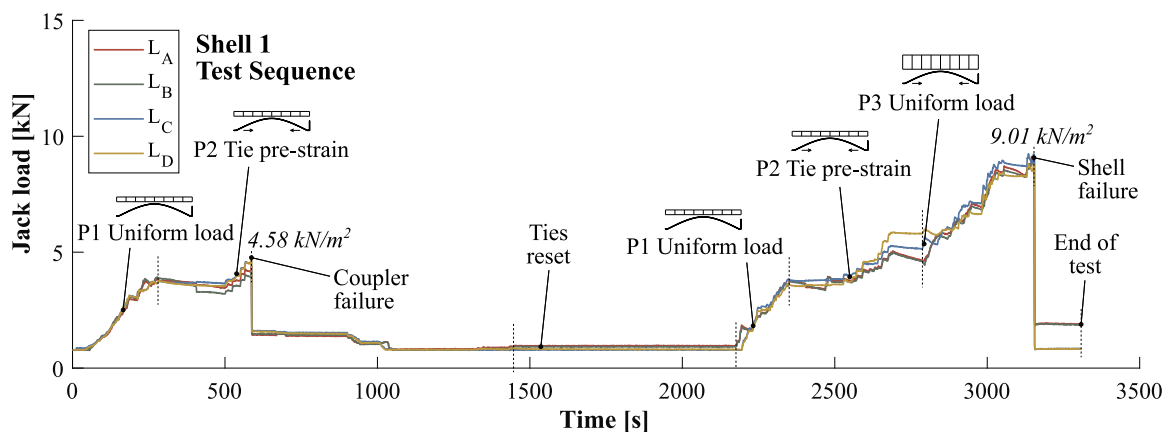


Figure 5.26: Shell 1 test sequence. The variation of jack loads (including self-weight) over time is plotted with test phases, key events and peak average loads highlighted.

The tie was threaded back into the coupler, and the fixing bolt tightened until the strain in tie C-D read a similar value to the three others. The test was then re-started from Phase 1. According to the transducers at  $x_A$  and  $x_D$ , the supports D and A were spread by 4.9mm at the restart relative to their original positions. The mid-span transducer ( $z_9$ ) also read a vertical displacement of 8.3mm at the re-start. These represent 'locked-in' deformations, with associated cracks and stresses.

Figure 5.27 shows the variation of vertical displacement with the average applied jack load after the re-start. Test Phase 1 was successfully completed up to an average load of  $3.75\text{kN/m}^2$ . The response from the vertical transducers is approximately linear, with the largest displacements recorded at mid-span ( $z_9$ ). By symmetry, the transducer pairs ( $z_1, z_4$ ), ( $z_2, z_3$ ), ( $z_5, z_8$ ) and ( $z_6, z_7$ ) should be similar, and this is approximately observed in the results.

The pre-strain was then applied in Phase 2. This resulted in uplift of the shell, corresponding to an increase in jack loads to an average of  $5.34\text{kN/m}^2$ . In subsequent tests, this effect was countered by releasing pressure in the jacks to maintain a constant load.

Phase 3 was then begun. The vertical stiffness was similar to Phase 1. Some delamination of the bottom cover layer was observed, particularly in corner B (shown in Figure 5.28c). This was a result of poor bond of the concrete around the bottom reinforcement layer. Failure of the shell occurred suddenly during Phase 3 due to collapse at corner C, at an average load of  $9.01\text{kN/m}^2$ . Figure 5.28d shows the failure region, indicating a compressive or shear failure.

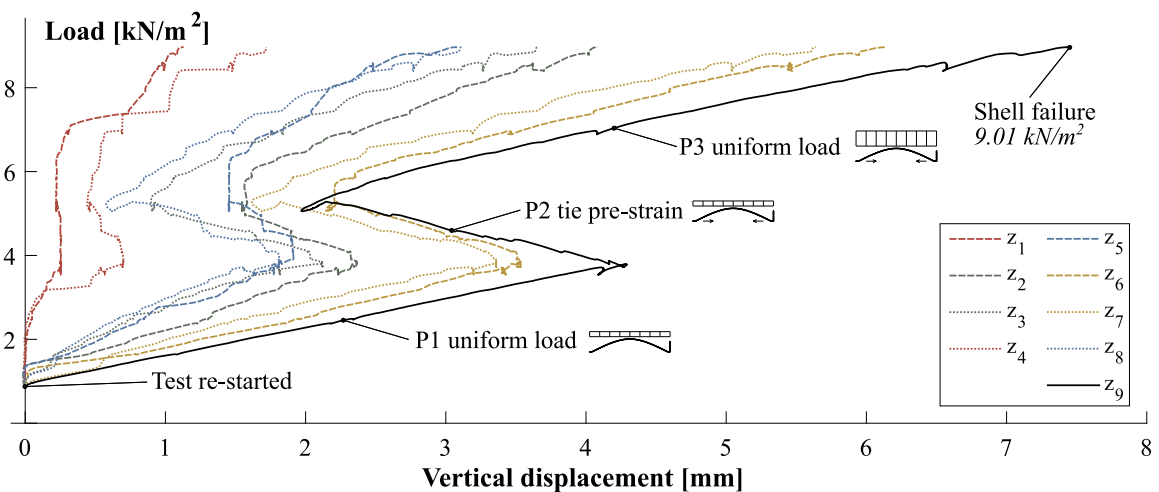


Figure 5.27: Measured vertical displacement against average loading for Shell 1, after restarting the test following accidental failure of tie C-D.

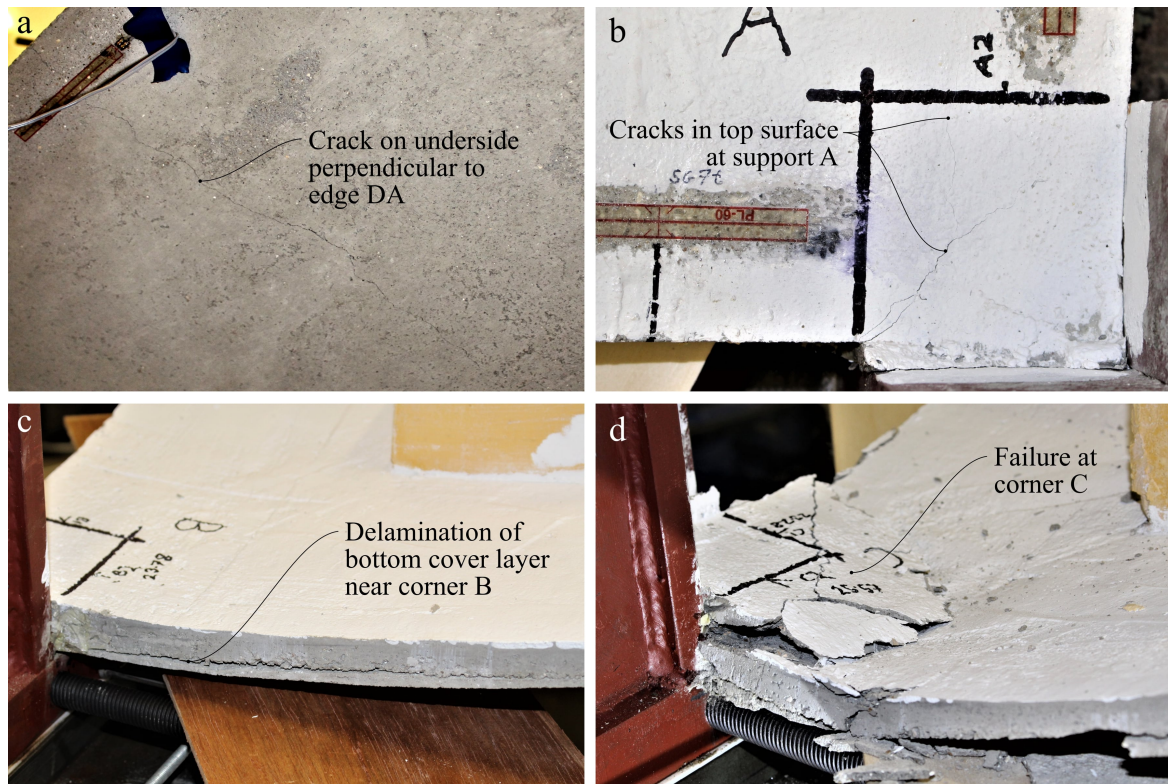


Figure 5.28: Images from the testing of Shell 1, showing sagging a) and hogging b) cracks caused by premature failure of the tie C-D, c) delamination of the bottom cover layer and d) failure of the structure near the support at C.

Inspection of the failure region at corner C revealed defects which were the assumed causes of collapse. These are illustrated in Figure 5.29. Firstly, it was found that the shell was significantly under-thickness near the corner support, with a measured minimum of approximately 12mm. The steel support was also protruding into the shell, due to the formwork being set too low relative to the corner supports. It is hypothesised that this led to a large concentration of stress and subsequent crack initiation. Poor bonding of the concrete around the lower reinforcement, as previously mentioned, is likely to have further weakened the TRC. These issues were therefore addressed in the construction of Shell 2, as highlighted in Figure 5.29.



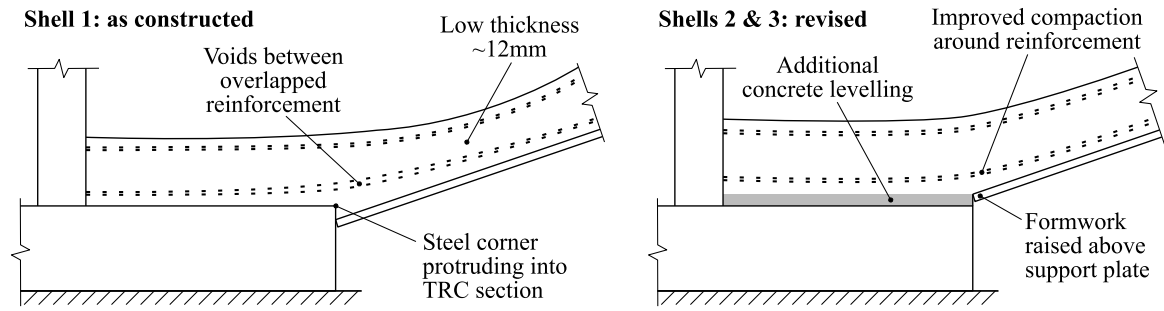


Figure 5.29: Construction defects leading to premature failure at corner C for Shell 1 (left), and the subsequent improvements made to the formwork positioning and manufacturing method for shells 2 and 3 (right).

### 5.8.2 Shell 2

Figure 5.30 shows the test sequence for the second shell. Graphs of vertical displacement, horizontal displacement and tie force against average load for each test phase are given in Figure 5.31.

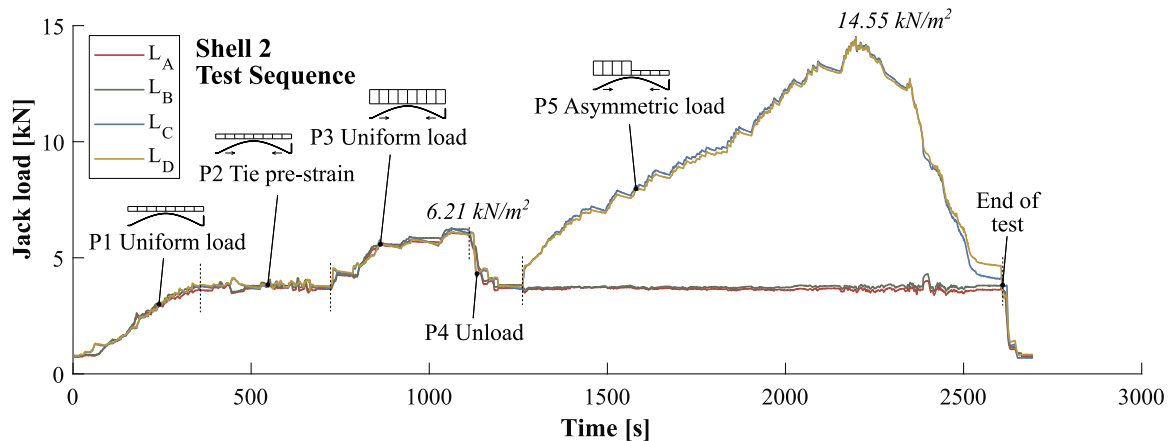


Figure 5.30: Shell 2 test sequence. The variation of jack loads (including self-weight) over time is plotted with test phases, key events and peak average loads highlighted.

In Phase 1, the load was increased uniformly by  $2.97\text{kN/m}^2$  to a total value (including self-weight) of  $3.80\text{kN/m}^2$ . The displacement response was linear, reaching  $3.73\text{mm}$  at mid-span (corresponding to a vertical stiffness of  $0.80\text{MN/m}^3$ ). The average tie extension at the end of Phase 1 was  $0.57\text{mm}$ , and the change in tie force was  $7.02\text{kN}$  (giving a tie stiffness of  $12.32\text{kN/mm}$ ).

Pre-strain was applied during Phase 2, with the load held approximately constant by a controlled release of pressure in the jacks. The uplift at mid-span was  $4.08\text{mm}$ . The average shortening of the ties was  $0.80\text{mm}$ , corresponding to a strain of  $0.40\text{mm/m}$ . However, this

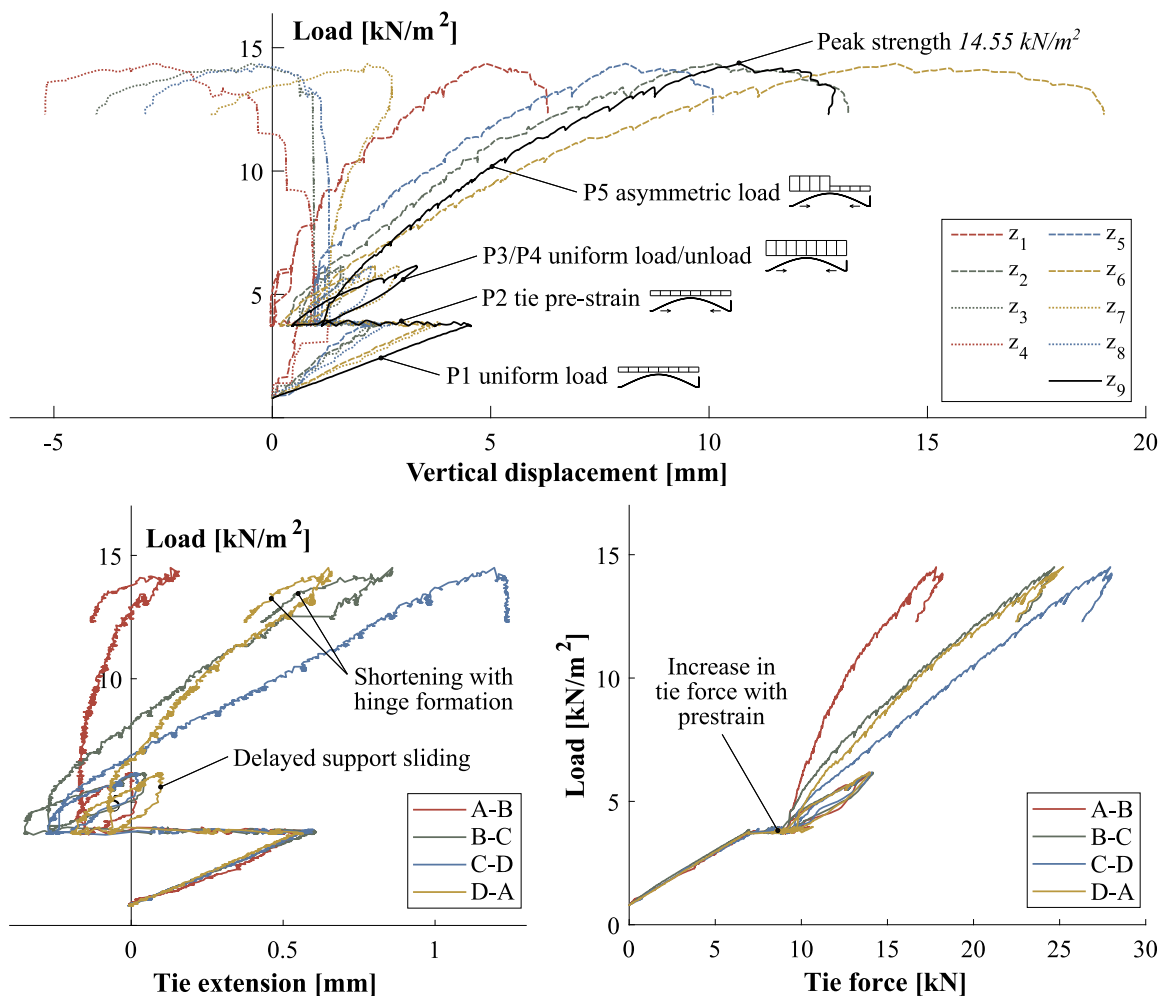


Figure 5.31: Shell 2 test results, showing the variation of vertical displacement, tie extension and tie force with average load. In Phase 5, the load is calculated as the average of  $L_C$  and  $L_D$ .

ignores elongation of the tie due to additional tension, which increased by 1.97kN. Based on the tie stiffness calculated in Phase 1 (12.32kN/mm), this corresponds to an additional elongation of 0.16mm, and therefore a total pre-strain of 0.48mm/m over the full tie length. This is smaller than the design value of 0.56mm/m, although it is possible that the measured tie shortening underestimates the pre-strain applied due to 'sticking' of the supports, whereby a certain frictional force must be overcome before the corner supports begin to slide. This effect is visible in the tie extension results, as highlighted in Figure 5.31.

In Phase 3 (uniform loading), spalling of the bottom cover layer began to occur near the corner supports. This is illustrated in Figure 5.32a and, similarly to Shell 1, was likely caused by poor bonding between the first and second concrete layers. Because of this, it was decided

to begin Phase 4 (unloading) early, at  $6.21\text{kN/m}^2$ , to ensure the completion of all test phases. A permanent increase in mid-span deflection during Phases 3 and 4 of  $0.68\text{mm}$  was measured. This potentially indicates settling of the supports or damage to the shell. Hysteresis can also be seen in the tie extension data during these loading phases, possibly caused by friction preventing free horizontal sliding of the supports.

In Phase 5, the loading was increased in jacks C and D only. The vertical displacement results show the corresponding loss of symmetry, with transducer  $z_6$  measuring the greatest downwards movement. Uplift was recorded in transducers  $z_4$  and  $z_8$ . Similarly, the distribution of tie extension and load was asymmetric, with tie C-D showing the greatest increase in load.

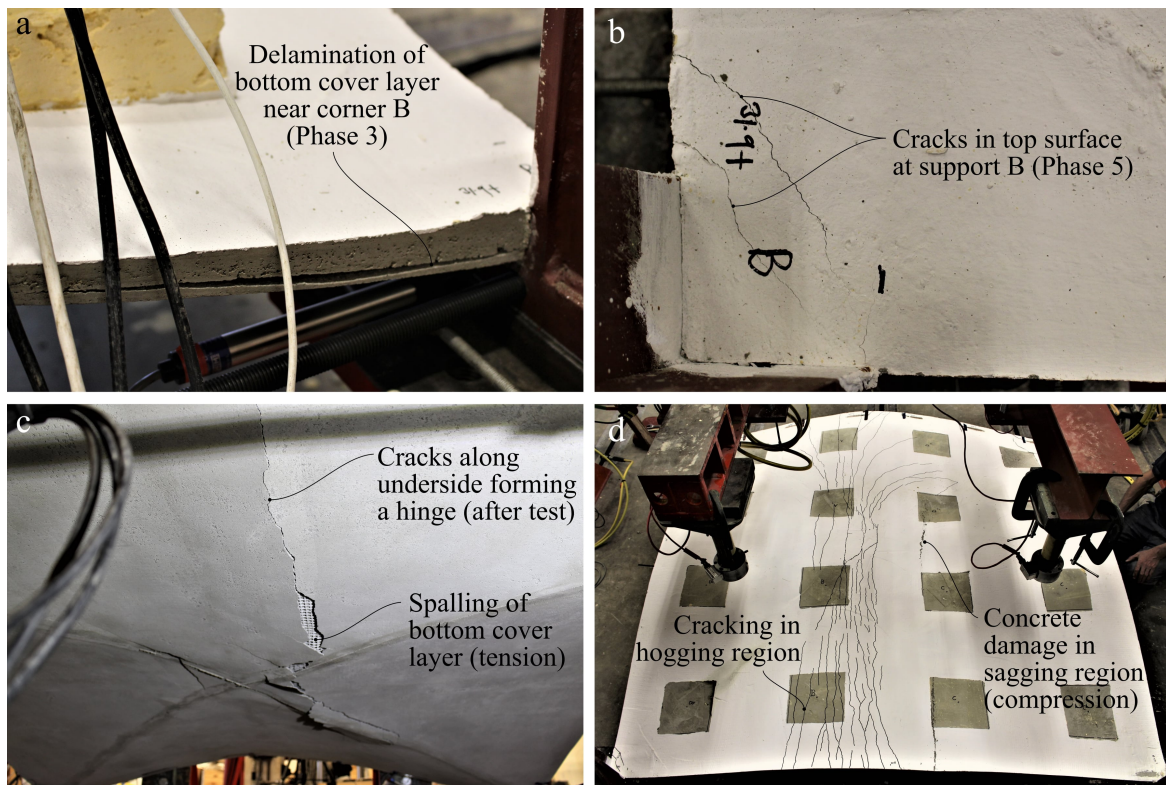


Figure 5.32: Images from the testing of Shell 2, showing a) separation of bottom cover layer during uniform loading, b) hogging cracks at support B during asymmetric loading, c) a sagging hinge formed at large asymmetric loads and d) hogging cracks highlighted on the specimen after the test.

A loss of linearity in the vertical displacements can also be observed in Phase 5. The vertical stiffness reduces at higher loads. Cracks on the shell underside first appeared at a load of  $6.6\text{kN/m}^2$ . These later developed into a well-defined hinge, with some delamination of the bottom cover layer, as shown in Figure 5.32c. A neighbouring hogging region of

distributed cracking also emerged (Figure 5.32d). There was also evidence of cracking near the corners at higher loads (Figure 5.32b). This is strongly suggestive of the formation of a hinged collapse mechanism, with approximately linear regions of sagging and hogging along the centre of the shell combined with localised rotation at the corners creating a four-hinged mechanism. The shortening of ties B-C and C-D is also consistent with this deformation behaviour.

Jack extension was continued beyond the peak load, resulting in large vertical deformations of up to 42mm (downwards) and 15mm (upwards) when the test was stopped. These results are excluded from Figure 5.31 to improve clarity. Despite extensive cracking and deformation, the structure did not fail catastrophically and retained a load of approximately 5kN/m<sup>2</sup>. The large rotations, extensive cracking and lack of sudden failure each suggest that the primary action is bending rather than compression, since the latter would be expected to exhibit a more sudden, explosive failure.

The maximum asymmetric loading reached, including the self-weight, was 14.55kN/m<sup>2</sup>. This indicates that, had the uniform loading applied in Phase 3 been increased to the intended value, the shell would likely have not failed locally at the corners. Modifications to the construction method outlined in Figure 5.29 were therefore deemed successful. The issue of delamination did however persist, but was addressed in the construction of Shell 3.

### Strain gauge results

Figure 5.33 shows the results from the shell strain gauges, at the locations shown previously in Figure 5.23. For each top and bottom pair, the average axial strain  $\epsilon_a$  was calculated as well as the bending strain  $\epsilon_b$  (as defined in the figure). The measured thicknesses at each location are also shown for reference. The raw data featured considerable noise due to the small strains being measured, and the data has therefore been smoothed in the plot (using a moving average over five results) to aid clarity. During the test, some strain gauge readings became suddenly very large, either due to cracking or a malfunction of the instrumentation, and these results have been removed from Figure 5.33 where indicated.

The strain gauge data highlights the structural behaviour of the shell in several ways. In Phase 1, the compressive strains were greatest at the supports, as expected. The bending strains indicate hogging at the corners ( $cs_1$ ,  $cs_2$ ,  $cs_7$  and  $cs_8$ ) and sagging towards the mid-span ( $cs_3$ ,  $cs_4$ ,  $cs_5$  and  $cs_6$ ). This is the expected deformation for a shell spreading outwards with supports fixed against rotation. In Phase 2, the situation was reversed, as the supports were pushed back together. The compression at the corners also increased. Phases 3 and 4 showed similar behaviour to Phase 1. In Phase 5, the bending strains indicate the sudden formation of a crack at approximately 6.6kN/m<sup>2</sup>. As the asymmetric load increased,

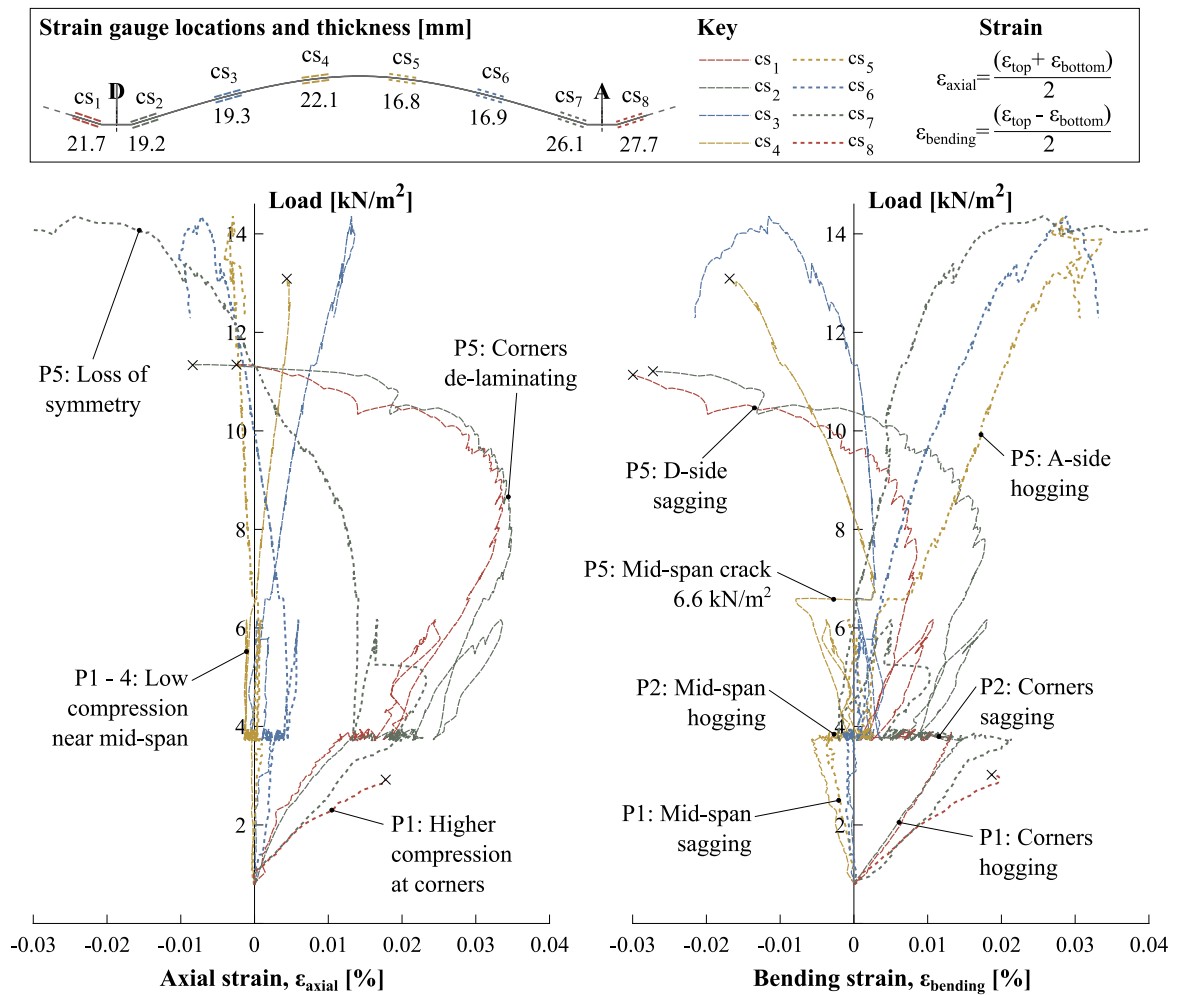


Figure 5.33: Average compressive strain (left) and curvature (right) collected using concrete strain gauges during the testing of Shell 2. Hogging curvature is positive.

the symmetry in curvatures was correspondingly lost. Gauge pairs near the more heavily loaded corner D ( $cs_1$  to  $cs_4$ ) show sagging whilst the remaining pairs show hogging. The compressive strain at the corners unexpectedly reduced during Phase 5, which may be a result of delamination of the bottom cover layer.

A key result from the strain gauge data is that the bending strains are comparable to, or larger than, the axial strains. This is particularly visible near to the mid-span (gauges  $cs_4$  to  $cs_6$ ) where compressive forces are small throughout. This does not necessarily indicate that bending is the dominant mechanism of load resistance, but arises because the low thickness of the shell means that even small bending forces create comparatively large strains.

The maximum compressive strain recorded throughout the test was 0.081%, which occurred at the peak asymmetric load on the top surface at gauge location  $cs_1$ . This is

significantly lower than the peak strain of 0.255% recorded in the prism tests, suggesting that crushing was not imminent. Higher compressive stresses would, however, be expected closer to the corner supports. Maximum compressive stresses could have been determined using local DIC measurements at corner supports.

### 5.8.3 Shell 3

#### Accidental damage

The formwork of Shell 3 was removed seven days after casting, requiring removal of the tie rods. The corner supports were therefore clamped in place to prevent slippage. However, the day afterwards, the corner supports accidentally slipped due to an insufficient clamping force. Precise displacement data was not available, since no instrumentation was set up at the time, however it was estimated that the supports slipped horizontally by up to 8mm. Visible damage to the structure included sagging cracks in the shell and separation of the shell and fill, as illustrated in Figure 5.34. Significant vertical displacement of approximately 30mm was measured at mid-span, and gaps of 3mm to 4mm had also opened up between the top of the foamed concrete fill and the corner supports.

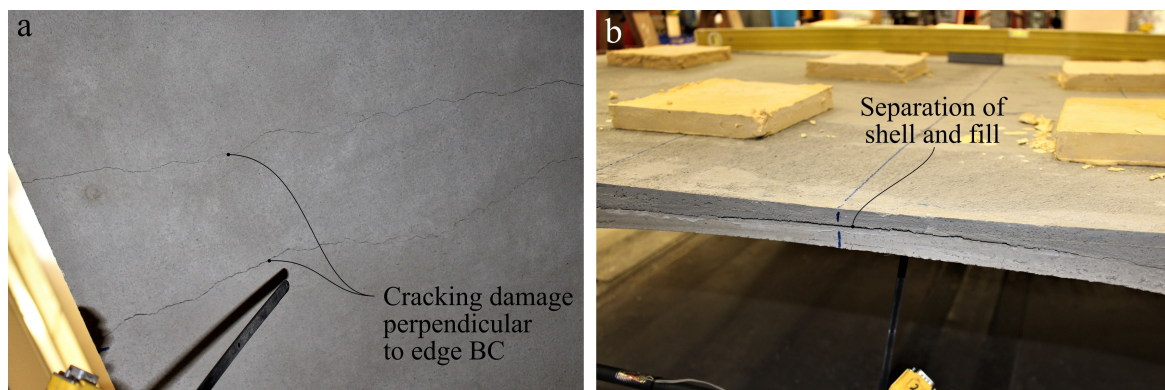


Figure 5.34: Damage to Shell 3 caused by accidental slip of the corner supports after formwork removal. Image a) shows cracking on the underside of the shell and image b) shows separation of the foam and TRC.

Despite the deformation and damage, it was decided that the shell was still fit to be tested. The ties were re-inserted and stressed in order to reposition the corner supports, causing uplift of the shell and closing of the cracks. This was continued until the gaps between the top of the foam and the corner supports were no longer visible. The geometry was then measured using the digital scanner, and this was compared to the scan taken immediately after formwork removal. Registration of the two scans was carried out using the same methodology as

described in Section 5.5, despite the known horizontal movement of the supports. The results indicated a residual downward vertical displacement of up to 8mm in the middle of the shell, and horizontal support displacements of between 1.2mm and 2.5mm.

### Test results

The test sequence for the third shell is shown in Figure 5.35. Graphs of vertical displacement, horizontal displacement and tie force are given in Figure 5.36.

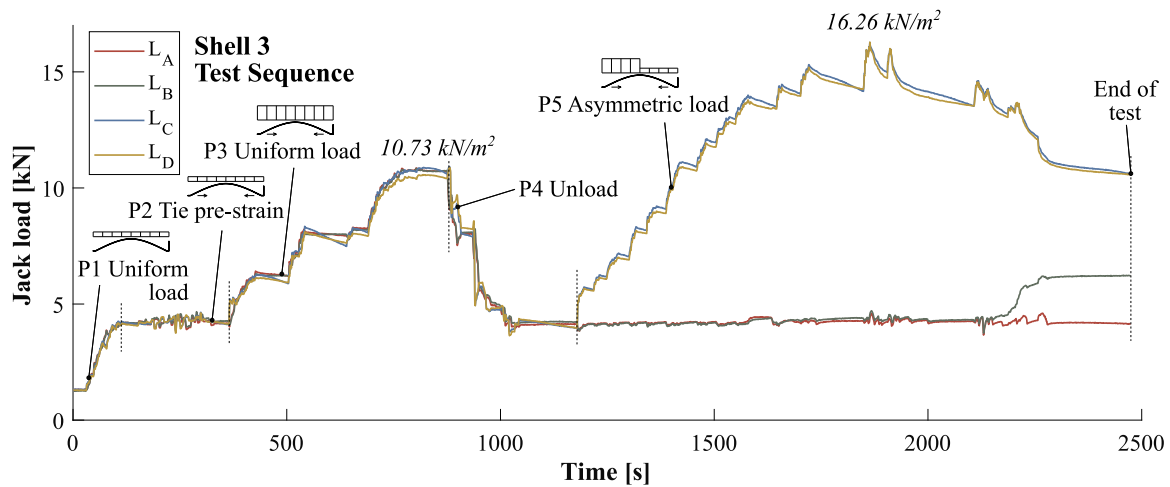


Figure 5.35: Shell 3 test sequence. The variation of jack loads (including self-weight) over time is plotted with test phases, key events and peak average loads highlighted.

In Phase 1, the jack loads were increased by an average of  $2.96\text{kN/m}^2$  (a total load of  $4.18\text{kN/m}^2$ , with self-weight included). The increase in vertical deflection was  $3.21\text{mm}$ , giving a stiffness of  $0.92\text{MN/m}^3$ . The average change in tie extension and load were  $0.51\text{mm}$  and  $6.70\text{kN}$  respectively (a tie stiffness of  $13.14\text{kN/mm}$ ).

In Phase 2, the mid-span uplift was  $3.85\text{mm}$ . The average shortening of the ties was  $0.80\text{mm}$ , with a tension increase of  $1.75\text{kN}$ . The corresponding pre-strain, again accounting for elastic elongation, was calculated as  $0.46\text{mm/m}$ . This value is similar to Shell 2.

Phase 3 was completed up to an average uniform load of  $10.73\text{kN/m}^2$  without any visible signs of cracking or delamination of the shell. All three sets of results given in Figure 5.36 show linear behaviour during loading, albeit with some hysteresis on unloading. This is particularly evident in the tie extension data, which is hypothesised to be a result of friction at the supports.

In the final asymmetric loading phase, the structural response was linear until the first cracks began to appear, visible in the foamed concrete fill at approximately  $13.4\text{kN/m}^2$  (Figure 5.37a). It should be noted that some cracks were already present in the structure

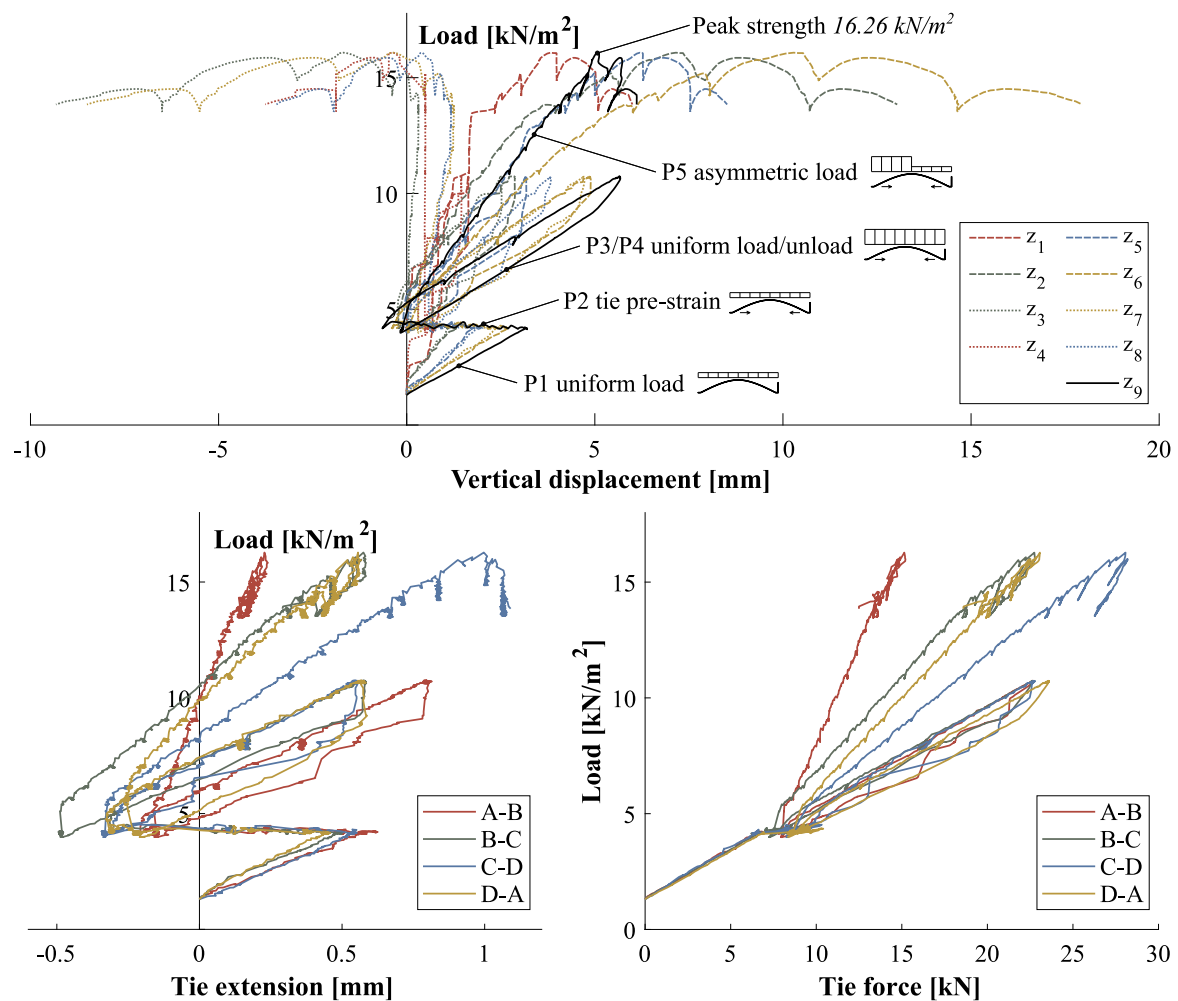


Figure 5.36: Shell 3 test results, showing variation of vertical displacement, tie extension and tie force with average load. In Phase 5, the load is calculated as the average of  $L_C$  and  $L_D$ .

due to the initial damage. As the deformation increased, the TRC and foamed concrete began to separate at the interface (Figure 5.37b). A similar pattern of cracking to Shell 2 was eventually observed, with the formation of distinct sagging and hogging hinges across the centre of the shell (Figure 5.37c and 5.37d). Some crushing of the concrete can be seen in Figure 5.37c in the hogging region, potentially indicating that the ultimate section strength had been reached locally. The maximum applied load was  $16.26 \text{ kN/m}^2$ , however the structure continued to deform and support load beyond this peak. The test was stopped when the uplift beneath loading jack B reached its physical limit, with extreme vertical displacements of 25mm (downward) and 13mm (upward) measured. Again, catastrophic failure did not occur, nor did rupture of the reinforcement, and a load of approximately  $10 \text{ kN/m}^2$  was retained despite the large deformations.



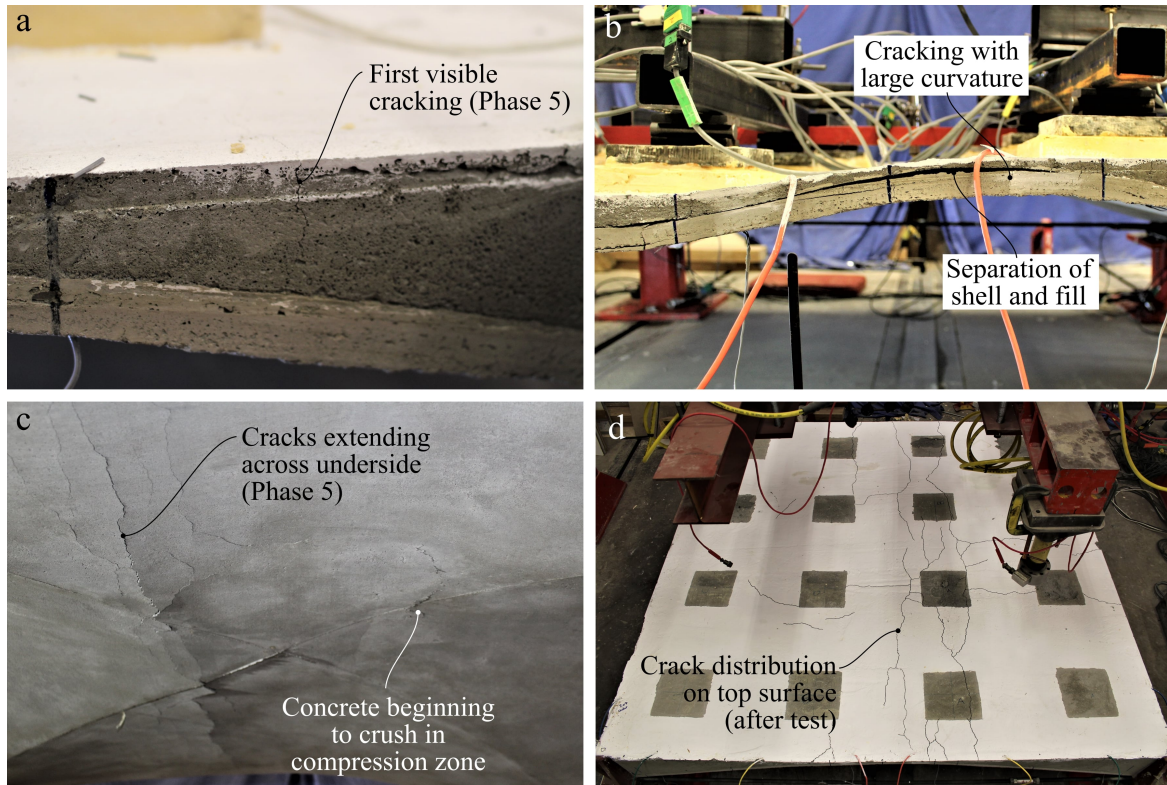


Figure 5.37: Images from the testing of Shell 3. Photographs include a) the first visible cracking caused by hogging in the foam; b) large curvatures, cracking and separation of the shell and fill after the peak asymmetric load; c) cracks in the sagging region of the shell; d) cracks observed in the top surface of the foamed concrete fill after the test.

### Strain gauge results

Figure 5.38 shows the strain gauge results for Shell 3. These plots were produced in a similar manner to those of Shell 2 (Figure 5.33).

In Phase 1, high compression and hogging curvature at the supports can be seen, and low compression and sagging curvature near the mid-span. This pattern is similar to Shell 2, however the strains are smaller in magnitude. Phases 3 and 4 are similar to Phase 1. The high compressive strain in gauge pair  $cs_8$  may be a result of the lower shell thickness compared to the other corner gauges.

In Phase 5, sagging and hogging curvature can be clearly seen in gauge pairs  $cs_3$  and  $cs_4$  respectively. The strains remain approximately linear until first cracking at  $13.4\text{kN/m}^2$ , where the same two mid-span gauge pairs quickly begin reading very high tensile strains (indicating cracks).

The bending strains are comparable, or larger, than the axial strains, as for Shell 2. The maximum compressive strain measured throughout the test was 0.109%, recorded at the top

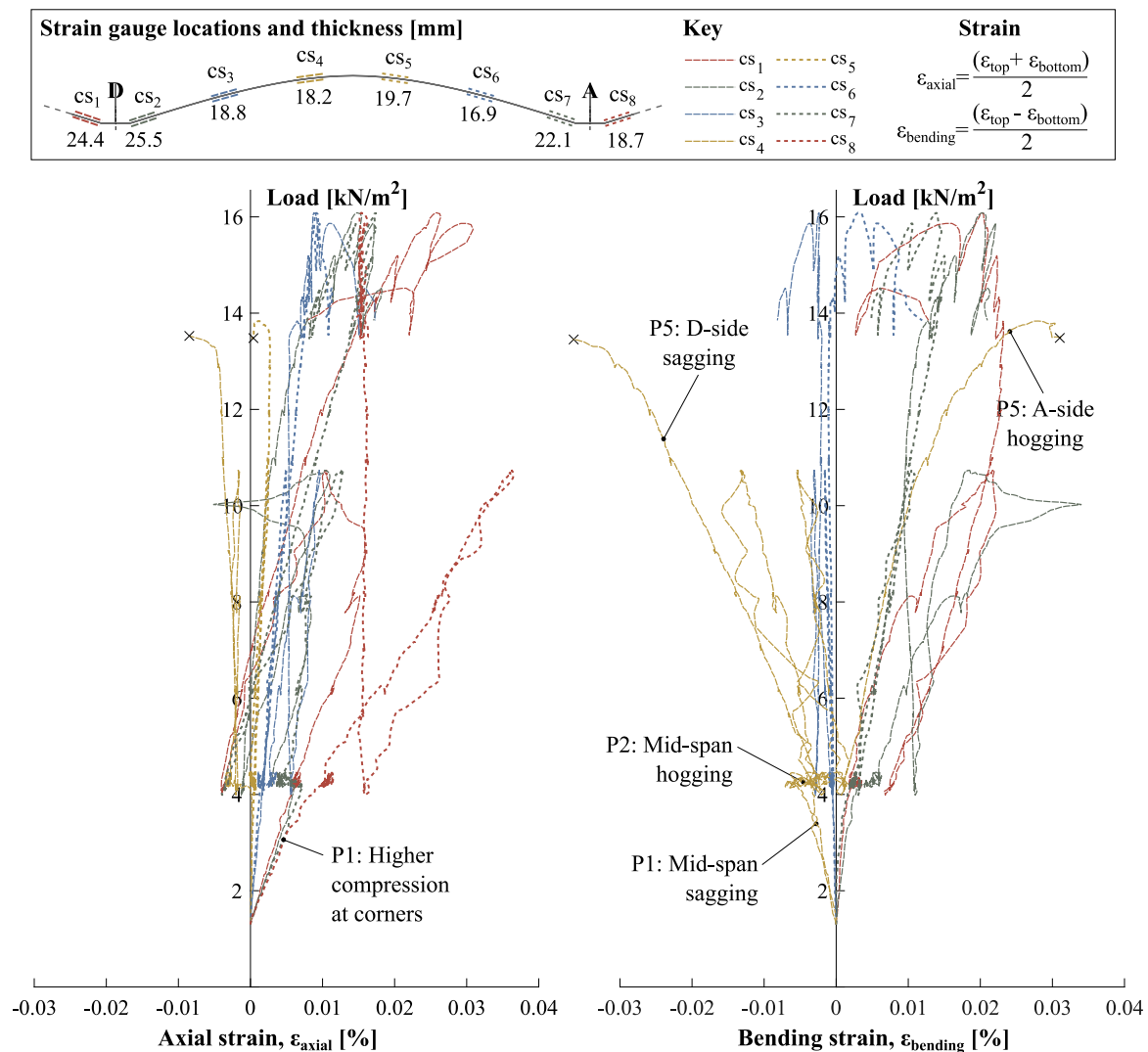


Figure 5.38: Average compressive strain (left) and curvature (right) collected using concrete strain gauges during the testing of Shell 3.

surface at  $cs_4$  at the peak asymmetric load. Again, this suggests concrete stresses well below the peak strength (although absolute maximum values are not known).

## 5.8.4 Comparison between shells

### Vertical displacement

Figure 5.39 compares the mid-span displacement (transducer  $z_9$ ) against the average maximum applied load for each shell. The initial vertical offset is a result of the difference in self-weight between the specimens.

The results highlight differences in vertical stiffness. Shells 1 and 2 are similar, whilst that of Shell 3 is noticeably higher. In Phase 1, vertical mid-span stiffnesses of 0.68MN/m, 0.66MN/m and 0.90MN/m were calculated for Shells 1, 2 and 3 respectively using a linear line of best fit. This suggests that the foamed concrete fill had a stiffening effect, although the influences of concrete stiffness and shell geometry variations are unclear at this stage (these effects are later isolated in the FE analysis described in Section 6.2). The observed de-bonding of the TRC and foam would also have diminished its structural contribution, although the significance of this is not yet known.

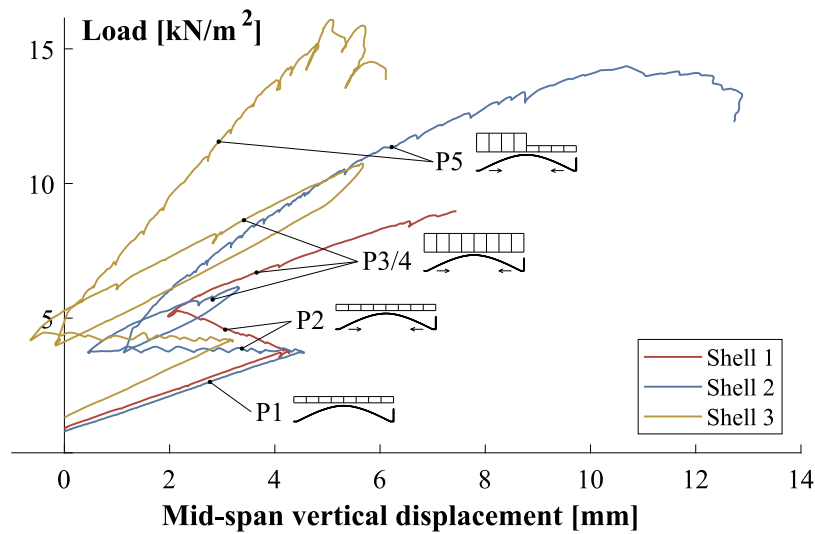


Figure 5.39: Comparison of mid-span vertical displacement with average load between the three shell tests. The five test phases are labelled P1 to P5. The results indicate a higher stiffness in Shell 3.

### Horizontal displacement and tie force

Figure 5.40 compares average tie extension and jack load for Shells 2 and 3. The data collected for Shell 1 is not shown, since the accidental failure of the tie coupler affected the reliability of the transducer data. Compared to the vertical displacements (Figure 5.39), the behaviour is much more similar between the two shells. This suggests that the foamed concrete does not significantly affect the thrust in the tie, which is an indicator of the amount of arching action.

Figure 5.41 plots the average tie extension and tie force for Shells 2 and 3, showing similar results for each.

Phase 2 shows the shortening of the ties due to the application of pre-strain. In all other phases, gradients are approximately similar and indicate the average stiffness of the ties

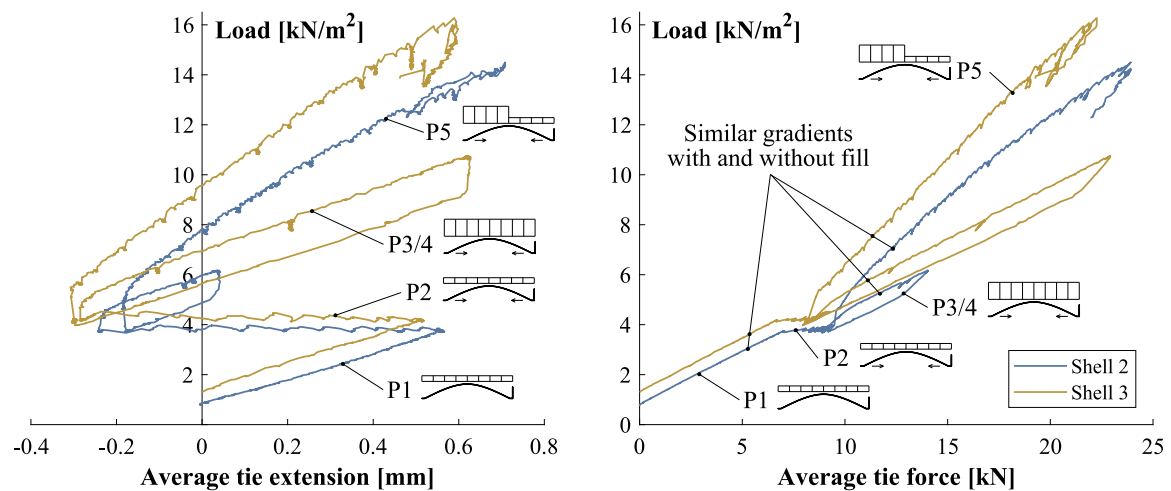


Figure 5.40: Average tie extension (measured using horizontal transducers) and the tie force (measured using strain gauge pairs) for Shells 2 and 3.

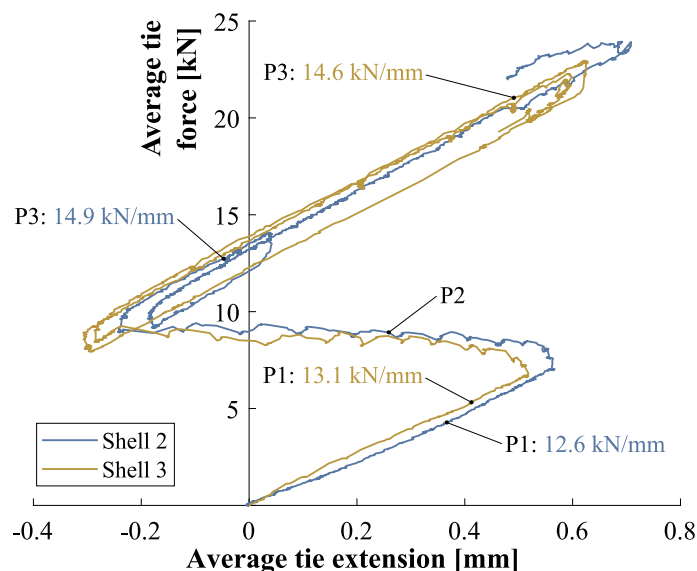


Figure 5.41: Graph of average tie extension and force for Shells 2 and 3 (all test phases). The gradient indicates the tie stiffness, which is highlighted for uniform loading Phases 1 and 3.

in units of  $\text{kN/mm}$ . These are marked on the figure for Phases 1 and 3. In both cases, the stiffness is greater in Phase 3 (after the pre-strain is applied). The reason for this is unclear, but might be a result of greater friction at the supports at higher loads. Since a reliable value of tie stiffness is required for analysis, an additional experiment was carried out to measure the tie stiffness directly (described in Section 5.9.1).

## Concrete strain

The concrete strain gauge results were simplified to enable comparison between the shells. The average axial and bending strains were calculated, with the latter including both sagging and hogging as positive values. Strain gauges  $cs_1$  and  $cs_8$  were not included in order to eliminate the unreliable results collected for  $cs_8$  in Shell 2, whilst maintaining symmetry. Results are shown in Figure 5.42.

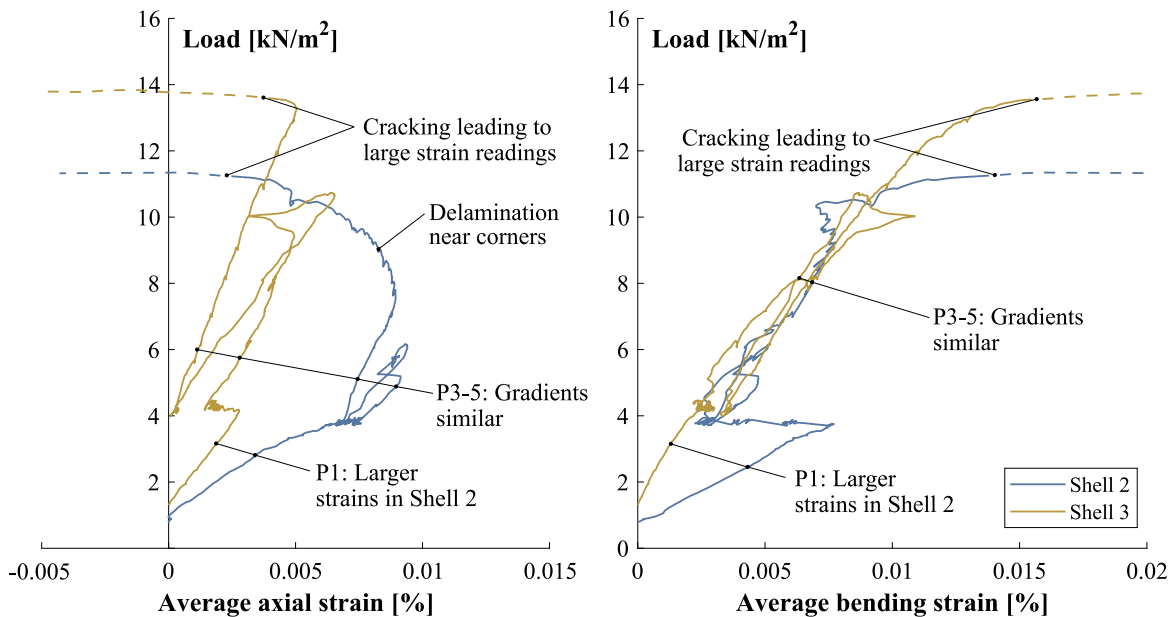


Figure 5.42: Comparison of average axial (left) and bending (right) strains at gauge locations  $cs_2$  to  $cs_7$  for Shells 2 and 3.

In Phase 1, the increase in both axial and bending strains are significantly greater per unit load for Shell 2 than Shell 3. This suggests that the foamed concrete fill might have a significant stiffening effect. However, in Phases 3 to 5 the differences in gradient are not as obvious. Combined with the high level of noise in the data and delamination issues in Shell 2, this makes definitive conclusions difficult to draw. The effect of the fill is investigated through FE analysis in Section 6.3.4.

## 5.9 Supplementary tests

### 5.9.1 Tie rod tests

The axial stiffness of the tie assembly is required for FE modelling, however this cannot be easily determined due to the geometric complexity of both the bar and coupler. The stiffness

has already been calculated directly from the shell test results, as shown in Figure 5.41, however the accuracy of these values is uncertain due to the large variation between test phases and potential influence of friction at the supports. Tensile tests were therefore performed on the bar assemblies in order to gain an accurate measure of stiffness. These tests were also used to calibrate the strain gauges on the tie rods, enabling conversion from strain to force.

Each tie rod was loaded to 50kN and unloaded three times, using the testing arrangement shown in Figure 5.43. Cyclic loading was performed to eliminate bedding-in effects. Load, displacement and strain were measured at one second intervals. The initial length of the tie rods was 2007.5mm, matching the shell test.

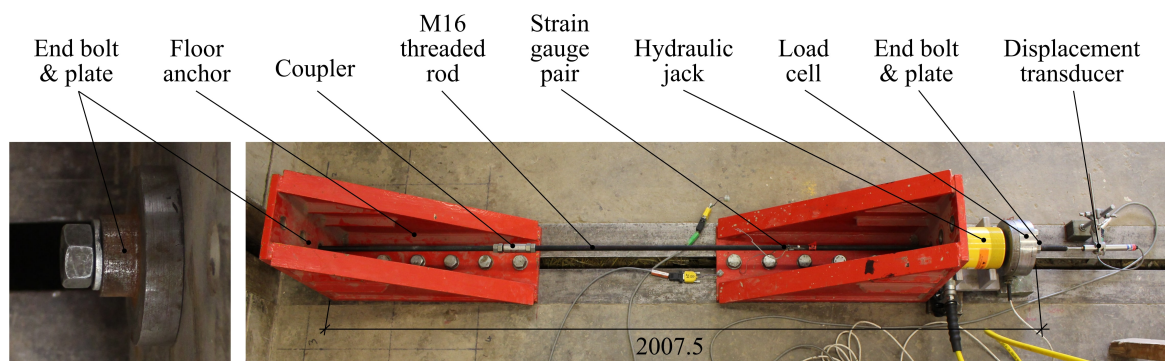


Figure 5.43: Tensile testing arrangement for tie rod assemblies.

The measured load-extension curves are shown in Figure 5.44. For the most part the relationship is linear, as expected. However, a reducing stiffness can be seen at loads lower than around 2kN. This was observed for each loading cycle, and was therefore not an initial bedding-in effect. The coupler and holding bolts are the likely cause of this behaviour, since full contact between components is only achieved above a certain load. The stiffness of each tie was calculated as the average gradient of the load extension curves, using a straight line approximation. Values below 5kN were ignored to exclude the non-linear region. This stiffness was then converted to an equivalent diameter for a steel cylindrical rod (assuming a Young's Modulus of 210GPa). Results are given in Table 5.8.

The calculated average axial stiffness is 13.70kN/mm, which sits in the mid-range of the values calculated directly from the shell tests (Figure 5.41), and is equivalent to a steel tie of diameter 12.91mm. This is significantly smaller than the outer diameter of 16mm, although this would be expected for a threaded bar. It is also possible that elastic deformation of the testing rig may have influenced the results, in which case the true stiffness of the tie rod assembly would be higher than that measured.

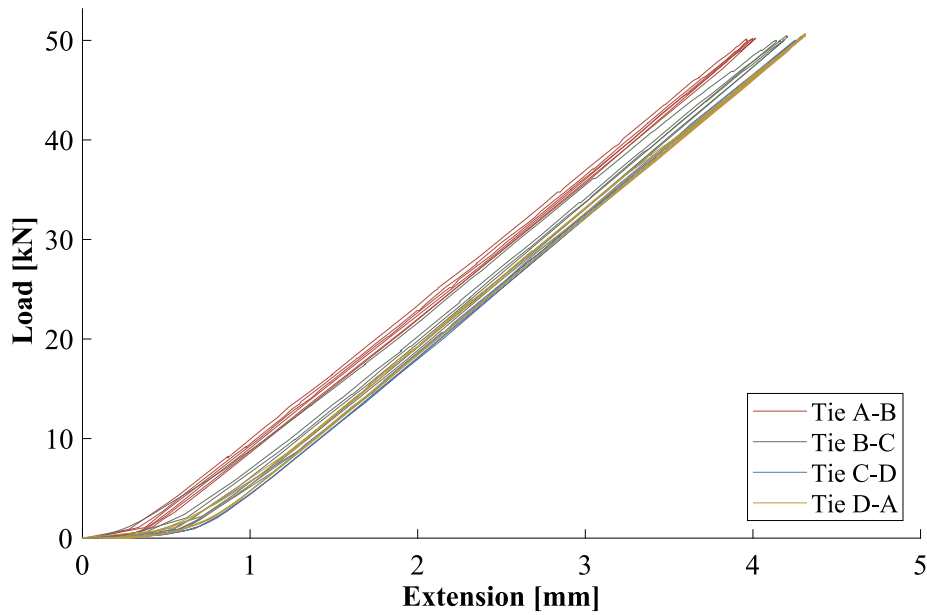


Figure 5.44: Tie rod tensile testing results.

Table 5.8: Summary of results from tensile tests on tie rod assemblies.

Tie	Axial stiffness [kN/mm]	Equivalent steel diameter [mm]	Strain gauge calibration [N/ $\mu\epsilon$ ]
<b>A-B</b>	13.63	12.88	28.28
<b>B-C</b>	13.59	12.86	29.53
<b>C-D</b>	13.95	13.03	28.78
<b>D-E</b>	13.63	12.88	28.68
<b>Average</b>	13.70	12.91	28.82

For each test, the average strain (from each strain gauge pair) was plotted against the load, showing a linear relationship at all loads. Calibration factors were then calculated as the gradient of a straight line approximation of these plots, and are also included in Table 5.8. Some variation between calibration factors is to be expected, since the local cross-section area at the strain gauge location is dependant on the amount of thread removed. Individual factors for each tie were therefore used in the calculation of tie force.

### 5.9.2 Load-spreader assembly tests

The load-spreader assemblies were designed to distribute each jack load to evenly four points as the shell deforms. To achieve this, the design included pin joints at each loading point

and ball joints between the beams. An experimental investigation was carried out to validate assumption of even load distribution.

An example of a load-spreader assembly and the test set-up is shown in Figure 5.45. This is similar to the arrangement used during the shell tests, with the addition of four load cells at the support points. A load of 12kN, cycled three times, was applied to each of the four load-spreader assemblies. The test was repeated six times, with one of the supports incrementally raised by 10mm to a maximum of 50mm. In this way, the effect of vertical deformation on the load distribution was investigated.

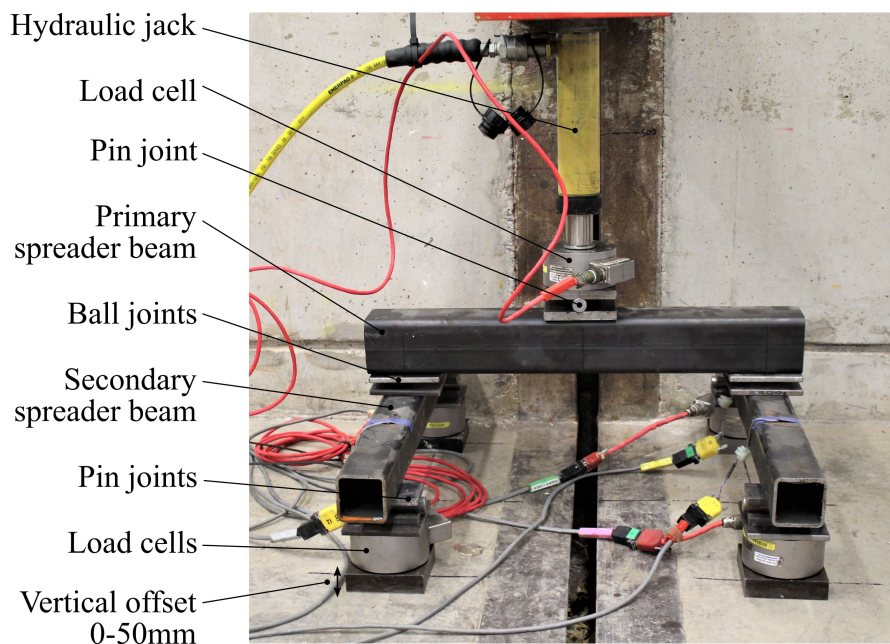


Figure 5.45: Load-spreader testing arrangement.

Using the load cell data, a single value of load distribution was calculated for each of the four supports using the gradient of a linear line of best fit. Figure 5.46 shows the percentage deviation from a perfectly uniform (quarter) load distribution for each test. The results for each assembly are included, with vertical offsets of 0-50mm.

With all supports level, the standard deviation between loads was 2.4%, with a maximum of 4.2%. At a 50mm offset, these values rose to 6.2% and 11.4% respectively. An approximately linear relationship between the support offset and load distribution error was noted. In the shell tests, the differential vertical displacement between adjacent loading points was consistently lower than 5mm, and thus an expected maximum load deviation of 5% might be reasonably assumed. The most likely cause of uneven distribution is geometric errors in the assemblies due to inaccurate placement of hinges and supports.



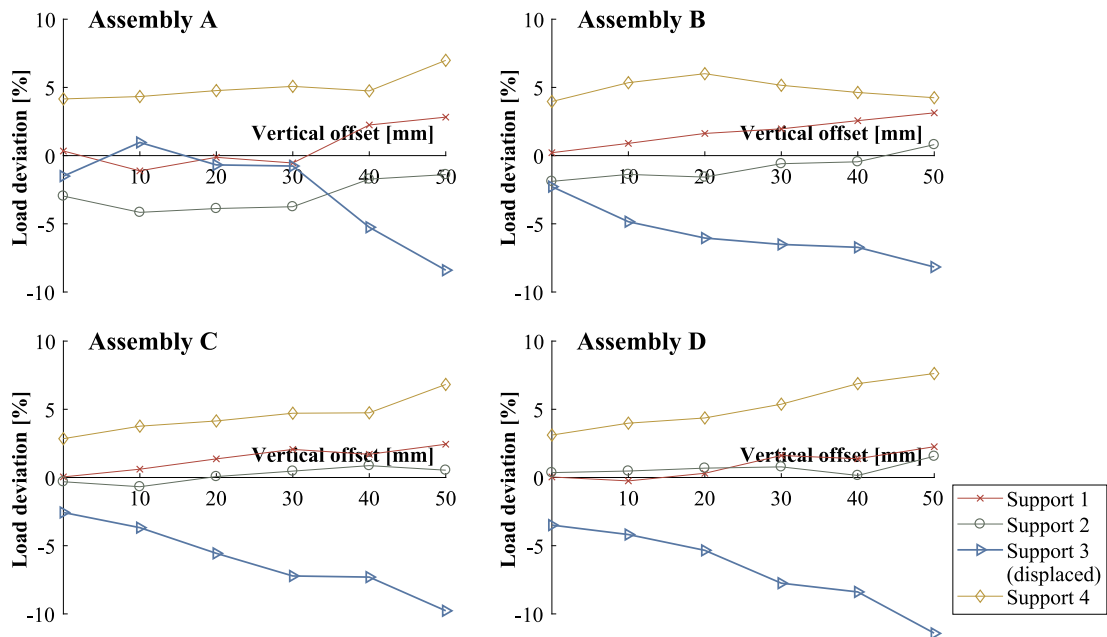


Figure 5.46: Result from the load-spreader tests, showing the percentage deviation from a perfectly even distribution at each loading point (measured from the load cells).

## 5.10 Summary, findings and conclusions

This chapter has described the design, construction and testing of three 18mm thick prototype shell floors. Challenges concerning practical construction, testing, instrumentation and results interpretation have been addressed and detailed. Three prototypes were constructed; Shell 1 (no fill), Shell 2 (no fill) and Shell 3 (with fill). The first of these failed prematurely due to manufacturing defects, however these were identified and addressed in later shells which were successfully loaded through five test phases and failed under an asymmetric load higher than the design strength.

The experiments have given valuable insight into the feasibility of the proposed system as well as the structural behaviour. Key findings are summarised below:

- A rigid timber formwork system is a practical solution for the construction, by hand, of singly curved TRC groin vaults.
- Foamed concrete with a low density, strength and stiffness can successfully create a level top surface and transfer loads to the shell.
- With or without the fill included, the shells resist load primarily through arching action, as indicated by the large axial forces in the ties.

- The inclusion of the foamed concrete fill increases the stiffness and strength of the shells under an asymmetric load.
- A TRC shell with 2m span, a span to height ratio of 10, and span to thickness ratio of 111, is capable of resisting floor loads greater than those typically required for ULS building design.
- The shells are able to perform effectively despite the presence of considerable manufacturing errors in both thickness and centreline geometry, although the corner regions can fail prematurely unless detailed correctly.
- Under an asymmetric load, close to the ultimate strength, distinct regions of cracking form leading to large deformations. The presence of the foamed concrete fill does not alter this failure mechanism.
- The shells are robust enough to avoid catastrophic failure caused by accidental loss of a horizontal support.

### **Conclusions: Chapter 5**

Physical prototyping and load testing has confirmed that the proposed system is viable, in terms of structural performance, robustness and manufacturing simplicity.

# Chapter 6

## Experimental study of quarter-scale prototypes: Analysis

### 6.1 Introduction

The experimental investigations described in the previous chapter were replicated in an FE analysis, with the aim of simulating the tests as closely as possible. This model was then used in several investigations, exploring:

- The validity of the experimental data.
- The sources of variation between the shells.
- The accuracy of the non-linear modelling methodology, described in Section 4.4, and comparison with a linear FE approach.
- Verification of the failure mode, and factors affecting the ultimate strength.
- The effect of the foamed concrete fill on the strength and stiffness.
- The significance of the measured geometric construction errors on the strength and stiffness of the shells.
- The validity of the strength design methodology using an analytical failure envelope, described in Section 4.3.

This chapter firstly describes the FE modelling methodology. Preliminary investigations are then discussed, which were used to characterise and refine the model. A number of sensitivity studies are then carried out to isolate the effects of individual variables on the

behaviour of the model, with the results then compared to the experimental data. Finally, the utilisation-based strength design methodology is implemented and its validity assessed through comparison with experimental behaviour.

## 6.2 Modelling methodology

Figure 6.1 shows the finite element model used in the investigations, which was created and analysed in SOFiSTiK (2019). The TRC was modelled using quadrilateral shell elements, matching those used in Section 4.4, and the foamed concrete with solid tetrahedral elements (where included).

Each tie rod was modelled with a two-noded beam element representing a steel cylinder with a Young's modulus of 210GPa and diameter of 12.91mm. This gives an axial stiffness matching the average value determined in the tests described in Section 5.9.1. The ties were connected at corner nodes, each of which were restrained against translation in the  $z$  direction and rotation about the  $x$  and  $y$  axes. The shell nodes within each corner support area were constrained in the  $z$  direction only. The edge nodes within these regions were rigidly coupled with the tie connection node below, as shown in Figure 6.1, to simulate a rigid corner support.

The node at the shell centre was restrained against translation in the  $x$  and  $y$  axes, and rotation about the  $z$  axis, to prevent rigid-body movements.

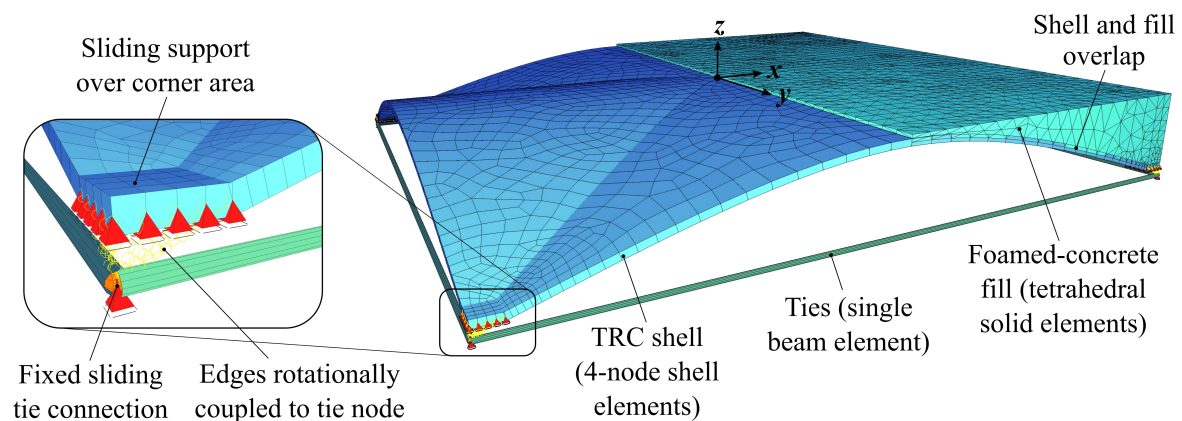


Figure 6.1: Overview of FE model, including meshing and boundary conditions.

The vertical plates of the corner supports (against which the foamed concrete was cast) were not modelled. This is consistent with the observed lack of bond between the two materials, indicated by the gaps which opened up during loading.

Loads were applied as uniform pressures over sixteen 200mm square patches. The stiffness of the steel plates and plaster at the loading patches was therefore ignored. Self-

weight was also included in the model to realistically replicate the physical tests, the applied jack load was the same in each test phase regardless of the self-weight of the model (consistent with the physical tests).

### 6.2.1 Importing measured geometry

The shell geometry measured through digital scanning, presented previously in Section 5.5, was imported into the model. This was achieved by modifying a mesh previously generated from the as-designed shell geometry, using a custom script in Grasshopper. Each node was relocated to be mid-way between the top and bottom scan surfaces. An individual thickness for each quadrilateral shell element was also calculated as the average at the four corner nodes, creating a shell of continually varying thickness. A uniform cover of 3mm was assumed throughout, since the true cover was not measured. This modified mesh was then exported from Rhino back into SOFiSTiK for analysis, enabling exploration of the effects of imperfections in Section 6.3.5.

### 6.2.2 Materials

A summary of the material parameters assumed in the model is given in Table 6.1. Both linear and non-linear analyses were performed.

#### Concrete modelling

For non-linear analysis, the TRC was modelled in a similar way to that described in Section 4.4.1, using SOFiSTiK's QUAD element with 20 integration layers. Using the results from the prism tests, a mean compressive strength of  $f_{cm}=36.6\text{MPa}$  was assumed. As in Section 4.2.1 (Equation 4.1), this value was used to define the stress-strain curve according to the standard concrete models given in Eurocode 2 (BSI, 2004a). The stiffness was modified to match the prism data, as shown in Figure 5.3, corresponding to a reduction in stiffness of 16.2% applied to the variables  $E_{cm}$ ,  $\epsilon_{c1}$  and  $\epsilon_{cu1}$ .

Variation in compressive strength was noted between each shell in the cube and TRC compression tests, described previously in Section 5.6.3. The influence of the mean strength on the structural behaviour is therefore investigated using the FE model in Section 6.3. The flexural strength of the concrete was assumed as the average value from the TRC four-point bending tests. Again, the sensitivity of the shell's maximum load capacity to this value was investigated using the model.

## Reinforcement

Unlike Chapter 4, the differences between the reinforcement properties in the warp and fill directions were included in the model. SOFiSTiK only permits a single reinforcement material per element, and therefore some modification of parameters was required to properly represent the measured differences in strength and stiffness. The fill Young's modulus (Table 4.2) was specified in both directions, however the reinforcement area in the fill direction was reduced from its measured value of  $52.2\text{mm}^2/\text{m}$  to  $45.4\text{mm}^2/\text{m}$  to account for the lower stiffness in this direction. Consequentially, the stresses calculated in the fill reinforcement will be larger than their true values by the same proportion (15.0%). The ultimate tensile strength was taken as the average in the warp direction from the TRC tensile tests (Section 5.6.1).

Tension stiffening was included according to Eurocode 2 (BSI, 2004a) with a coefficient of  $\beta=0.5$ , which was previously found to best reproduce the tensile and bending behaviour of similar TRC specimens (Section 4.4.4).

## Foamed concrete

The foamed concrete was assumed brittle-elastic in tension and elastic-plastic in compression, using the model described in Section 5.3.3. SOFiSTiK's BRIC tetrahedral solid elements, each with four nodes, were used to model the foam. An unstructured mesh was used to avoid irregularly shaped elements. A perfect bond between the TRC shell and foamed concrete was assumed, although this contrasts with the de-bonding observed in the testing of Shell 3.

### 6.2.3 Behaviour and refinement of the model

#### Orientation of shell elements

The quadrilateral shell elements of the TRC shell are surfaces. Their thickness is not explicitly modelled, but dictates the stiffness and stresses within the element. In most applications, the thickness is orientated centrally about the element surface, since this means that support and interface forces are aligned with the centroid of the (uncracked) shell section. However, for the model as shown in Figure 6.1, this leads to an issue whereby the half of the shell thickness overlaps the solid foamed concrete elements. Where the fill is included, this creates an artificial increase in stiffness and self-weight.

This could be overcome by modelling both the shell and fill with solid elements, however it was desired to maintain shell elements in order to utilise SOFiSTiK's non-linear reinforced concrete modelling capabilities. Another potential solution is to relocate the elements to

Table 6.1: Material parameters used in FE model.

<b><i>Fine-grained concrete</i></b>		
<b>Density (Shell 2), <math>\rho_c</math> [kg/m<sup>3</sup>]</b>	2081	Measured from cubes (Shell 2)
<b>Young's modulus [GPa]</b>	27.2*	Equation 4.1
<b>Poisson's ratio</b>	0.20	
<b>Compressive strength, <math>f_{cm}</math> [MPa]</b>	36.6	Prism tests
<b>Flexural strength, <math>f_{ctm}</math> [MPa]</b>	6.86	TRC bending tests
<b>Tension stiffening coefficient, <math>\beta</math></b>	0.5	
$\epsilon_{c1}$ [%]	0.255	Prism tests
$\epsilon_{cu1}$ [%]	0.418*	Equation 4.1
<b><i>Reinforcement</i></b>		
<b>Density, <math>\rho_f</math> [kg/m<sup>3</sup>]</b>	2700	
<b>Young's modulus [GPa]</b>	64.0	Table 4.2 (warp direction)
<b>Poisson's ratio</b>	0.20	
<b>Tensile strength (composite), <math>f_{tc}</math> [MPa]</b>	817	TRC tensile tests (warp)
<b>Area (warp) [mm<sup>2</sup>/m]</b>	65.3	Table 4.2 (warp direction)
<b>Area (fill) [mm<sup>2</sup>/m]</b>	45.4†	Table 4.2 (fill direction)
<b><i>Foamed concrete</i></b>		
<b>Density, <math>\rho_{fc}</math> [kg/m<sup>3</sup>]</b>	805	Measured from cubes
<b>Young's modulus [MPa]</b>	0.24	Cube tests (Figure 5.5)
<b>Poisson's ratio</b>	0.33	Gibson and Ashby (1999)
<b>Compressive strength [MPa]</b>	0.83	Cube tests (Figure 5.5)
<b>Flexural strength [MPa]</b>	0.18	$0.22f_{fill,c}$ Dini (2006)
<b>Compressive strain limit [%]</b>	4.0	Cube tests (Figure 5.5)

\*Stiffness reduction factor of 0.84 applied, based on prism tests.

†modified to account for use of Young's modulus in fill direction.

the top surface (at the interface with the fill) and orientate them downwards, away from the fill. Whilst this solves the problems of overlap, it creates an eccentricity between the shell centroid and supporting nodes.

An investigation was carried out to identify the differences in behaviour between these two approaches, which is shown in Figure 6.2. A uniform 1kN/m<sup>2</sup> load was modelled using a linear analysis. The self-weight was not included, enabling a direct comparison of structural behaviour. Four models were analysed; featuring each approach, with and without the fill. In each case, the 'as-designed' shell geometry was used, with a maximum mesh size of 50mm.

The key difference between the force distributions occurs at the inner corner of the support area. This node experiences a large vertical reaction force in all models. Whilst a local concentration of force is likely to exist in the real structure at this location, a large peak reaction is undesirable due to possible stability issues for non-linear analysis, and

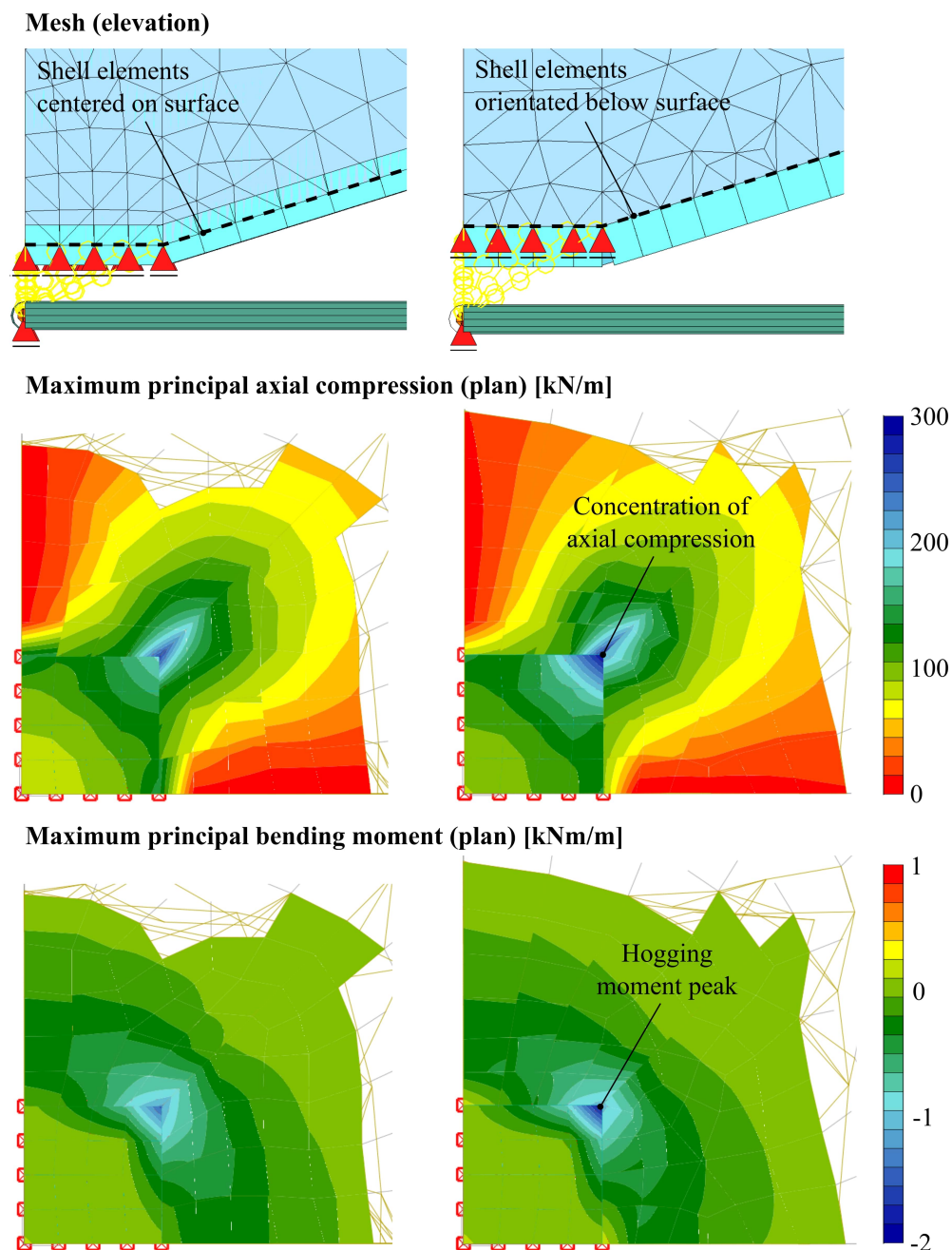


Figure 6.2: Alternative modelling approaches at the shell and fill interface, including centred shell elements with overlap (left) and projecting of shell elements below the plane (right). The differences in axial and bending forces at the corner supports are highlighted, using results from the models with fill included.

increased mesh sensitivity (as noted previously in Section 3.4.2). Where the shell elements are orientated below the surface, the offset of this force creates an increased local spike in hogging moment and compressive force (Figure 6.2).



Table 6.2 shows key results from each of the four analysis models. These show that orientating the shell elements below the surface results in an increase in mid-span deflection. This is likely caused by increased rotation of the shell at the inside corner of each support area, caused by the eccentricity of the vertical support. A larger total strain energy was also noted in the models with eccentric shell elements, presumably another consequence of the increased peak support forces.

In this model, the correct self-weight is 1.61kN (fill omitted) and 3.39kN (fill included). The different self-weights calculated in the two models without fill reflect variations in the shell surface area, with a slightly larger surface area required when shell elements are orientated below. With the fill included, the greater volume of solid elements gives creates an over-estimate of 0.3kN.

Table 6.2: Key results from the investigation into the orientation of shell elements in the finite element model.

<b>Fill Shell elements</b>	Omitted Centred	Omitted Below	Included Centred	Included Below
<b>Mid-span deflection [mm]</b>	2.68	2.72	2.50	2.54
<b>Total strain energy [N/m<sup>2</sup>]</b>	8.39	8.49	7.28	7.30
<b>Total self-weight [kN]</b>	1.61	1.62	3.69	3.39

The centred approach was chosen due to the improved behaviour at the corner supports. However, this does lead to large errors in self-weight calculation. A solution was devised whereby an equivalent density of the shell  $\rho_{c,eq}$  was calculated in order to compensate for the overlap, according to Equation 6.1:

$$\rho_{c,eq} = \rho_c - 0.5\rho_{fc} \quad (6.1)$$

With this modification, the calculated total self-weight of the specimen was equal to the theoretical value.

### Linear vs Non-linear Analysis

In order to correctly model the influence of cracking observed in the tests, a non-linear analysis is required. The ultimate load capacity of the structure can also be predicted using a non-linear analysis, as indicated by non-convergence of the model. This might be a result of local concrete crushing, tensile reinforcement rupture or global instability.

Each loading phase was modelled sequentially in the non-linear model, with any cracks carried over from one phase to the next. Test Phases 1, 3 and 5 were run in multiple stages in

order to capture intermediate data points. In the final phase, a repeatable procedure was used to determine the maximum stable load. The asymmetric load (jacks C and D) was increased in  $1.0\text{kN/m}^2$  increments until instability occurred. The load was then reduced by  $0.5\text{kN/m}^2$  and the analysis re-run (using the last stable load as the initial state). If stable, the load was increased by  $0.25\text{kN/m}^2$ , and so on. By halving half the load increment each time, the largest stable load was converged upon (to a final accuracy of  $0.125\text{kN/m}^2$ ).

Two similar FEA models were compared, one linear and one non-linear, using the parameters given in Table 6.1. A mesh with a maximum element size of  $50\text{mm}$  was used in both cases, with a total of 1916 quadrilateral elements (the influence of mesh density is investigated in the next section). The key differences between these models are the non-linearity of concrete, including cracking, and the inclusion of geometric non-linearity.

Figure 6.3 compares the vertical displacement corresponding to transducers  $z_2$ ,  $z_3$  and  $z_9$ . Only minor differences between the linear (blue) and non-linear (yellow) models can be seen in the results, suggesting that cracking either does not occur, or that its effect on the overall stiffness is small.

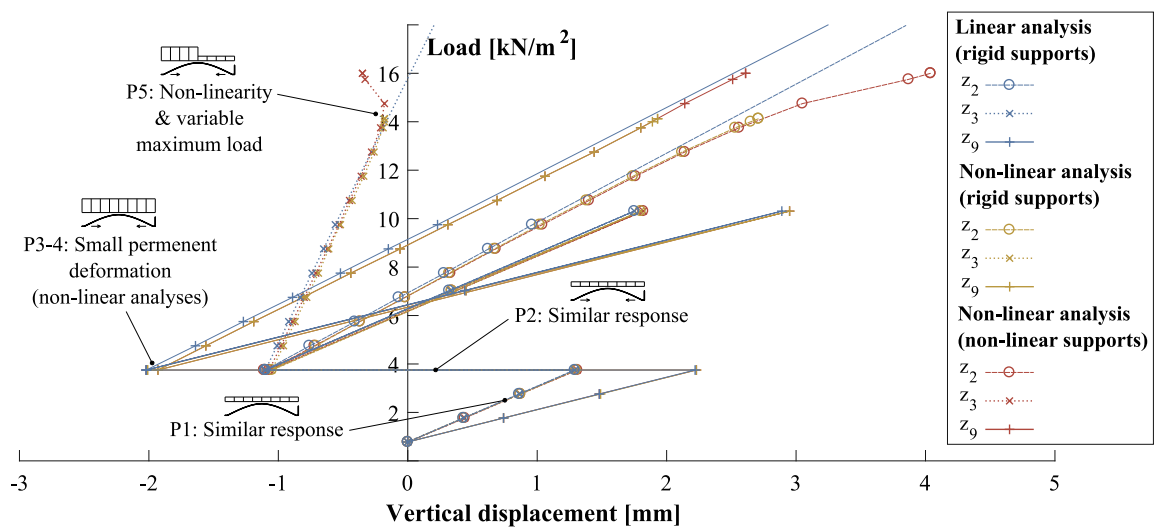


Figure 6.3: Comparison of predicted vertical displacements using linear and non-linear finite element analyses. In the latter case, rigid vertical corner supports are also compared with non-linear compression only rigid springs.

In the non-linear model, the tensile strength of the concrete is first exceeded at the end of Phase 4, at the inner points of the corner support area on the underside of the shell, caused by a sagging moment. This is the likely cause of the small permanent deformation visible in the non-linear results after the Phase 3-4 load-unload cycle. In Phase 5 (asymmetric load), cracking is first observed at a load of  $9.75\text{kN/m}^2$ , however no significant reduction in stiffness

is observed in Figure 6.3. Non-linearity begins to emerge at loads above  $14\text{kN/m}^2$  when further cracking develops.

The stresses in the reinforcement can be used to identify the locations of cracked regions. Figure 6.4 shows the reinforcement stress near to the maximum asymmetric load in the non-linear FE model, as well as deformations (amplified by 50 times). Cracked regions in hogging and sagging can be seen across the middle of the shell, as well as around the corner supports, closely resembling those observed in the physical tests on Shells 2 and 3. This indicates that a similar four-hinged mechanism is forming in the non-linear FE model.

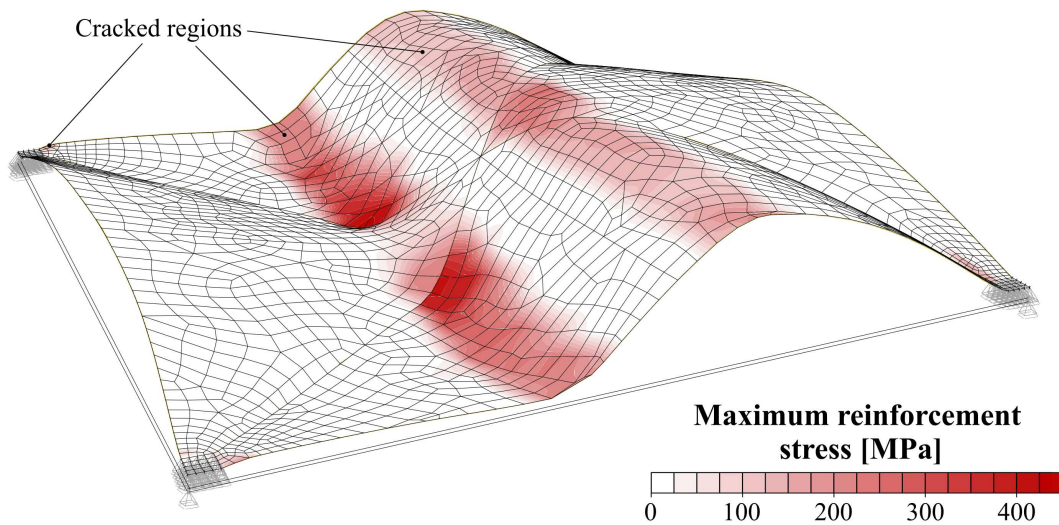


Figure 6.4: Maximum reinforcement stress (top or bottom) in the non-linear FE model, at the maximum stable asymmetric load (Phase 5). The deformation is also shown, amplified by a factor of 50.

The maximum stable asymmetric load supported in the non-linear analysis is  $14.13\text{kN/m}^2$ , slightly lower than the measured strength of Shell 2 ( $14.55\text{kN/m}^2$ ). At this load, the concrete reaches its maximum compressive stress ( $36.6\text{MPa}$ ) at the inner point of the corner supports C and D. At this location, a large vertical reaction force causes a high stress in the adjacent elements. The smaller these elements are, the greater the stress within them, and hence this peak stress is dependent on the mesh geometry in this region (noted previously in Section 3.4.2). With a linear material model, this stress concentration can simply be ignored when interpreting the results. However, with a non-linear material, the peak stress leads to model instability, limiting the maximum loading which can be applied and, consequentially, the usefulness of the model (since concrete crushing was not observed in the physical tests).

### Refinement of Corner Supports and Meshing Sensitivity

The support conditions at the corners were modified with the aim of reducing stress concentrations and mesh sensitivity.

In the two models compared in the previous section, all the nodes within the corner supports are fully fixed in the vertical direction. Each corner therefore effectively acts as a rigid moment support. It has been previously noted that large vertical reactions are concentrated at the inner corner. Immediately behind these nodes, tensile reaction forces occur due to the bending stiffness of the shell elements. In the real structure however, the concrete was cast against a painted steel surface and it is therefore unlikely that this interface has tensile capacity. It was hypothesised that eliminating the tensile reaction forces would correspondingly reduce the peak compressive force at the corners, potentially mitigating the problematic stress concentrations.

The rigid vertical supports within the corner regions were replaced with non-linear springs with zero tensile capacity. In compression, a spring stiffness of  $3000\text{GN/m}^3$  was adopted, based on concrete with a stiffness of  $27\text{GPa}$  being compressed over a depth of  $9\text{mm}$  (half the shell depth). A compressive yield stress equal to the mean strength of the concrete ( $f_{cm}$ ) was also defined. This means that, for very large loads, some plastic redistribution of bedding stress can occur. Again, this potentially reduces the magnitude of the point load at the inner corner.

An experiment was undertaken to assess the effect of the corner modelling strategy on the peak compressive corner stresses, as well as that of mesh density. Three strategies were analysed; linear (rigid supports), non-linear (rigid supports) and non-linear (with the non-linear supports as described above). Three meshes with increasing element density were also used. These had maximum element edge lengths of  $70\text{mm}$ ,  $50\text{mm}$  and  $30\text{mm}$  giving the total number of elements to be  $900$ ,  $1916$  and  $4716$  respectively.

Figure 6.5 compares the peak concrete compressive stresses at the corner support at the end of test Phase 3 (a uniform total load of  $10.31\text{kN/m}^2$ ). The magnitudes and directions of vertical reactions are also shown for each node in the support area. The linear analysis gives the largest peak stresses and reaction forces. This indicates that cracking and/or softening of the concrete evens out the load distribution. Comparing the two non-linear analyses isolates the effect of re-modelling the corner supports. Using the non-linear springs, the tensile reaction forces are eliminated, and the compressive forces are more uniform. This creates a small reduction in peak stresses. Regardless of the modelling strategy, the peak stress increases as the mesh is refined.

Table 6.3 compares key results from the nine analysis models. The influence on deformation was investigated by comparing the vertical and horizontal stiffness in Phase 1.

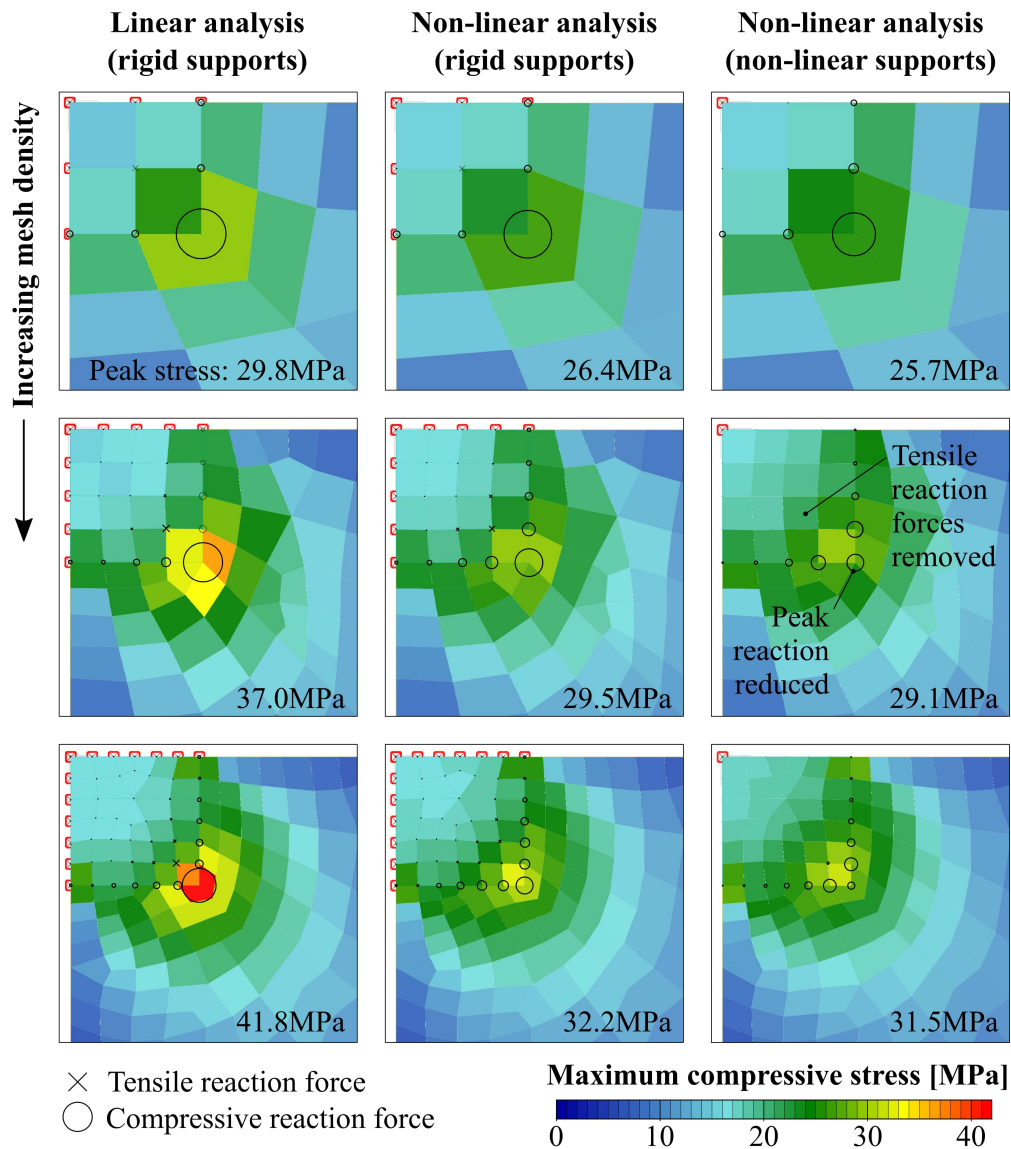


Figure 6.5: Maximum principal concrete compressive stresses and support node reaction forces, at corners, under a uniform total load of  $10.31\text{kN/m}^2$  for nine analysis models.

The results show that the vertical stiffness is not significantly affected by either the mesh density or the modelling strategy. This is also shown in Figure 6.3, and is consistent with St Venant's principle that the support reactions have local influence only. However, the horizontal stiffness is slightly lower (greater tie extension and thrust) with the tensile support reactions eliminated, and for finer meshes. This indicates higher thrust in the ties, perhaps due to a reduction in bending stiffness at the corners.

The maximum stable asymmetric load, at which the peak concrete stress first reaches  $f_{cd}$ , was determined in each case. As expected, this was influenced by the both modelling strategy

and mesh density. The largest maximum loads were reached in the non-linear model with non-linear supports, although the mesh sensitivity in the results was similar to that of other models. Further attempts to reduce the mesh sensitivity were also made, by reducing the compressive stiffness of the bedding support or levelling the descending part of the concrete stress-strain curve (hoping to increase stress redistribution through plasticity). Whilst these did slightly increase the ultimate asymmetric load, mesh sensitivity could not be eliminated.

Table 6.3: Comparison of finite element modelling approaches.

<b>Mesh density</b>	<b>Linear analysis (rigid supports)</b>	<b>Non-linear analysis (rigid supports)</b>	<b>Non-linear analysis (non-linear supports)</b>
<b><i>Vertical stiffness (Phase 1) [MN/m<sup>3</sup>]</i></b>			
Coarse	1.34	1.34	1.34
Medium	1.34	1.33	1.33
Fine	1.34	1.33	1.34
<b><i>Horizontal stiffness (Phase 1) [MN/m<sup>3</sup>]</i></b>			
Coarse	6.54	6.52	6.50
Medium	6.53	6.52	6.45
Fine	6.52	6.51	6.43
<b><i>Maximum load (Phase 5) at concrete crushing [kN/m<sup>2</sup>]</i></b>			
Coarse	12.50	16.03	18.37
Medium	10.50	14.13	16.00
Fine	9.63	12.25	14.65

The peak asymmetric load is dictated in the non-linear models by crushing of the concrete at a point of stress concentration. It is therefore mesh-sensitive, and hence cannot be treated as a meaningful prediction of the true strength. However, it is still desirable to minimise the magnitude of the stress concentrations, since the greater stability allows more insight into the behaviour of the shells at higher loads. For this reason, the model with non-linear supports was used in subsequent investigations of this section. The intermediate mesh density was chosen throughout to balance stress concentration with detail of results.

## 6.3 Sensitivity studies

This section explores the influence of several variables on the behaviour of the FE model by modifying each in isolation. These changes are all made relative to a base model, which features the as-designed shell geometry, uniform thickness, non-linear supports and the material properties given in Table 6.1. A summary of the parameters investigated, and their influence they are shown to have, is shown in Table 6.4.

Table 6.4: Variables investigated in the non-linear FE model and their influence on structural behaviour.

Section	Variable	Influence on structural behaviour
6.3.1	Concrete flexural strength	Low sensitivity within expected range, but cannot be ignored completely.
6.3.2	Concrete compressive strength	Low influence on maximum stable asymmetric load.
6.3.1	Concrete stiffness	Small influence on overall stiffness.
6.3.3	Tie rod stiffness	Influences both vertical and horizontal stiffness.
6.3.4	Inclusion of concrete fill	Small stiffness increase. Reduction of bending moments.
6.3.4	Stiffness of foamed concrete fill	Very small influence on overall stiffness.
6.3.5	Shell thickness	Small influence on overall stiffness.
6.3.5	Geometric errors (as measured)	Increased bending throughout the shell leading to reduced stiffness and increased stresses.

### 6.3.1 Concrete flexural strength

The first investigation concerns the tensile strength of the fine-grained concrete ( $f_{ctm}$ ). Although the shells are designed primarily as compressive structures, tensile stresses and cracking were observed in the tests, due to flexure, particularly under an asymmetric load. As a result, the tensile strength of the concrete might be expected to influence the strength and stiffness of the shells. This is also a parameter which can vary depending on the concrete mix, specimen dimensions and local shell forces.

The assumed tensile strength in previous investigations has been 6.86MPa, derived from the TRC bending tests (Section 5.6.2). Three additional models were analysed using wide-ranging values of 0.00MPa, 3.43MPa (50% reduction) and 10.29MPa (50% increase). The results are shown in Figure 6.6, which compares the mid-span deflection predicted by the four models.

In test Phases 1 to 4, where loading is uniform and tensile stresses are small, modifying the strength had very little effect, with only a small reduction in stiffness occurring when the tensile strength is ignored entirely. In Phase 5 however, the influence of tensile strength is much more noticeable. At zero, the deformation response was immediately non-linear and the reduced bending stiffness led to large rotations, small concrete compression zones and increased peak compressive stresses. The maximum stable load was  $8.94\text{kN/m}^2$ , at which point the peak compressive strength of the concrete was reached at the corners. The three models with a finite tensile strength showed identical behaviour up to the onset of cracking in the central region of the shell, at which a small divergence in the results was noted. In each case, instability was again caused by crushing at the corners. The peak stable load increased with the tensile strength, albeit with a lower sensitivity at higher values.

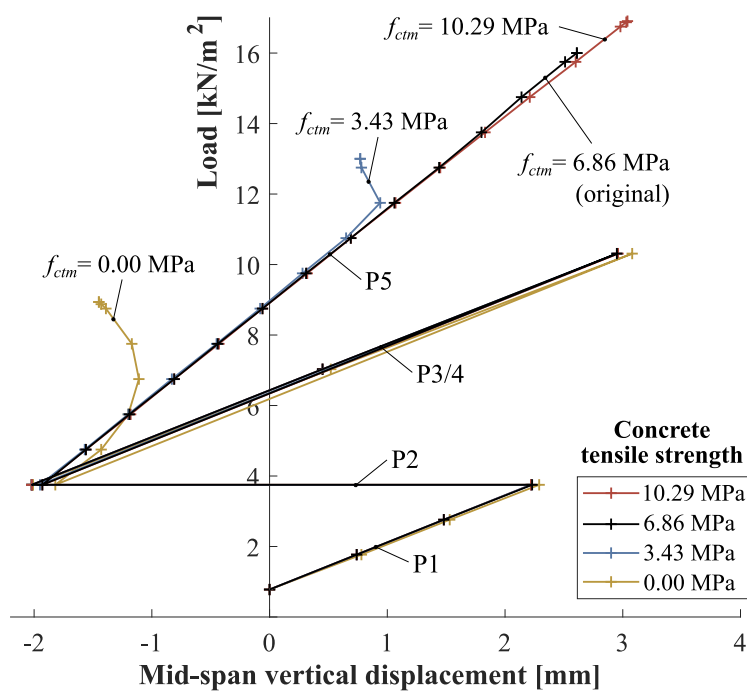


Figure 6.6: Effect of modifying the concrete tensile strength ( $f_{ctm}$ ) on the mid-span displacement predicted by the FE model.

The results suggest that the additional rotational stiffness provided by concrete in tension is vital for successful operation of the shells under asymmetric, but not uniform, loading. However, only a small tensile strength is required for a dramatic change in behaviour. The sensitivity is therefore likely to be low within the range of values measured in TRC flexural tests (4.96 to 8.24MPa in Section 5.6.2).



### 6.3.2 Concrete stiffness and compressive strength

Another variable is the compressive strength of the concrete ( $f_{cm}$ ). The measured average cube strength was higher for Shell 3 (39.0MPa) than for Shell 2 (35.5MPa), and it is therefore important to understand the influence this might have had on shell performance.

The assumed concrete stress-strain curve is the parabolic model first described in Section 4.2.1. In this model, increasing the compressive strength ( $f_{cm}$ ) also affects the Young's modulus  $E_{cm}$  and the strain at maximum load  $\epsilon_{c1}$ , consistent with the behaviour of concrete of different strengths according to Eurocode 2 (BSI, 2004a).

In this investigation, four stress-strain curves were modelled in addition to that of the base case (given in Table 6.1). These are shown in Figure 6.7, along with key parameters for each. Curves 1 and 2 were created by modifying  $f_{cm}$  by  $\pm 20\%$ , with the changes to stiffness consistent with Equation 4.1. For curves 3 and 4, the stiffness was modified independently of strength by scaling the curve along the strain axis, again by  $\pm 20\%$ .

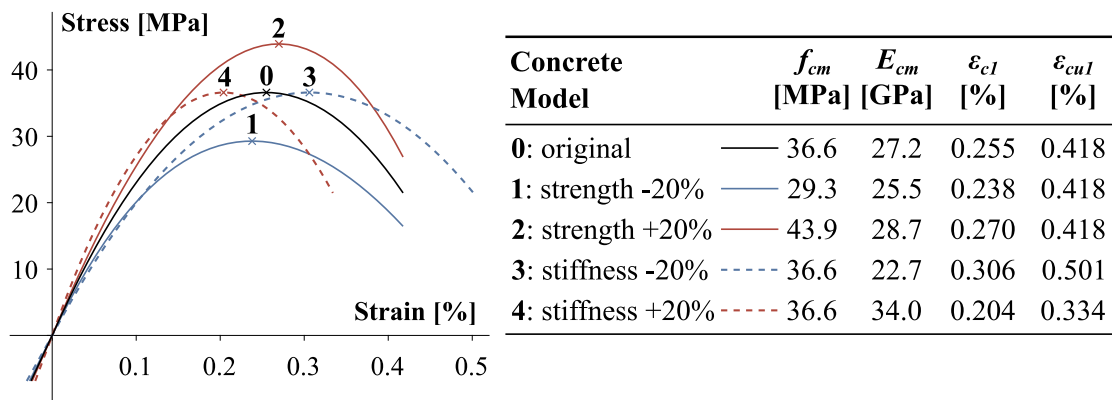


Figure 6.7: Summary of the modified concrete stress-strain curves investigated in the non-linear FE model. Curves 1 and 2 vary  $f_{cm}$ , while curves 3 and 4 modify the stiffness only.

Varying  $f_{cm}$  in curves 1 and 2 led to small corresponding changes in the maximum stable asymmetric loads in Phase 5 (by  $-6.6\%$  and  $+5.5\%$ ). These are smaller than the  $\pm 20\%$  change in strength, which suggests that the peak corner stresses increase rapidly near the maximum stable loads. This was confirmed through interrogation of the analysis results, and may be a result of the formation of a similar cracking mechanism as observed in the physical tests (shown previously in Figure 6.4).

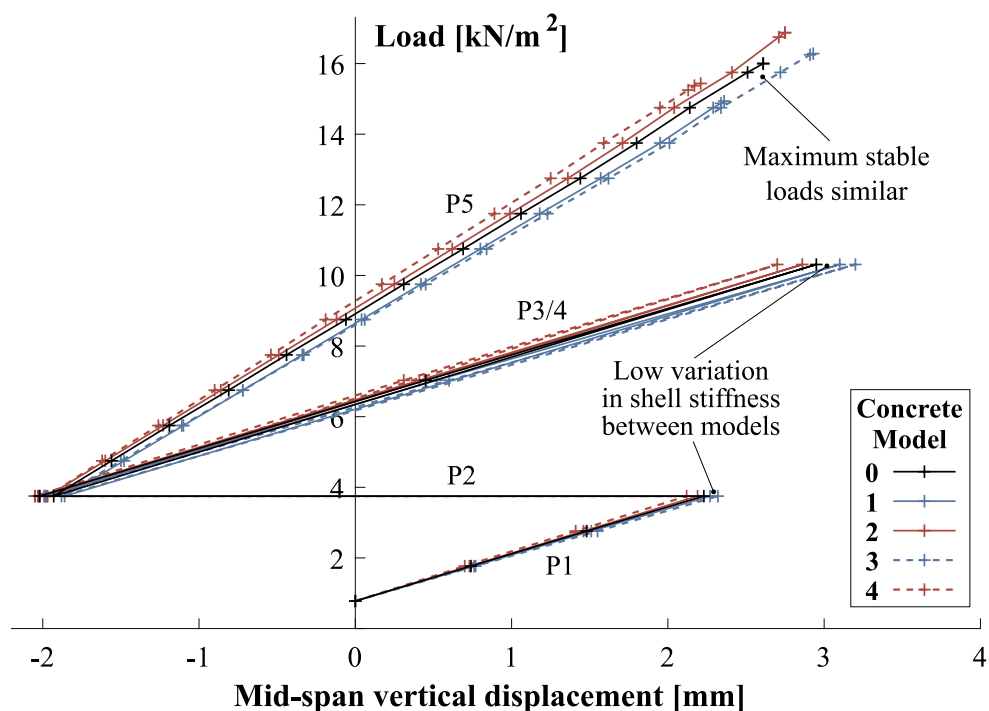


Figure 6.8: Effect of modifying the concrete compressive strength and stiffness on the mid-span displacement predicted by the FE model.

A comparison between the mid-span displacement predicted by each model is given in Figure 6.8. Considering test Phase 1, decreasing (curve 3) and increasing (curve 4) the concrete stiffness by 20% affected the vertical stiffness by only  $-3.9\%$  and  $+5.2\%$  respectively, indicating a low sensitivity. The horizontal stiffness (tie extension) was even less affected by the 20% change in stiffness ( $<1.5\%$ ). This indicates that the shell deformation is not sensitive to the stiffness of the concrete itself.

This investigation has demonstrated a low sensitivity of both strength and stiffness to variations in concrete properties, indicating that this was not the reason behind the differences between Shells 2 and 3 noted previously.

### 6.3.3 Tie rod stiffness

The tie stiffness measured by tensile testing (Section 5.9.1) was  $13.70\text{kN/mm}$ , and this is the value assumed in the base model. To investigate the sensitivity, this was both decreased and increased by 20%. The same tie pre-strain of  $0.56\text{mm/m}$  was applied each time in Phase 2.

Figure 6.9 shows the effect on both the mid-span displacement and average tie extension. It is clear that, compared to the concrete stiffness, the influence on shell deformation is more significant. In Phase 1, the 20% reduction and increase in tie stiffness modified the

vertical stiffness by  $-15.8\%$  and  $+15.5\%$  respectively compared to the original model. This trend is also repeated throughout later loading stages, and suggests that the most important mechanism causing vertical displacement is spreading of the supports rather than shortening of the shell itself. As expected, the influence on the horizontal stiffness was even greater, with a  $-18.8\%$  and  $+18.7\%$  changes measured. These are less than  $20\%$  because the tie force also increases with stiffness.

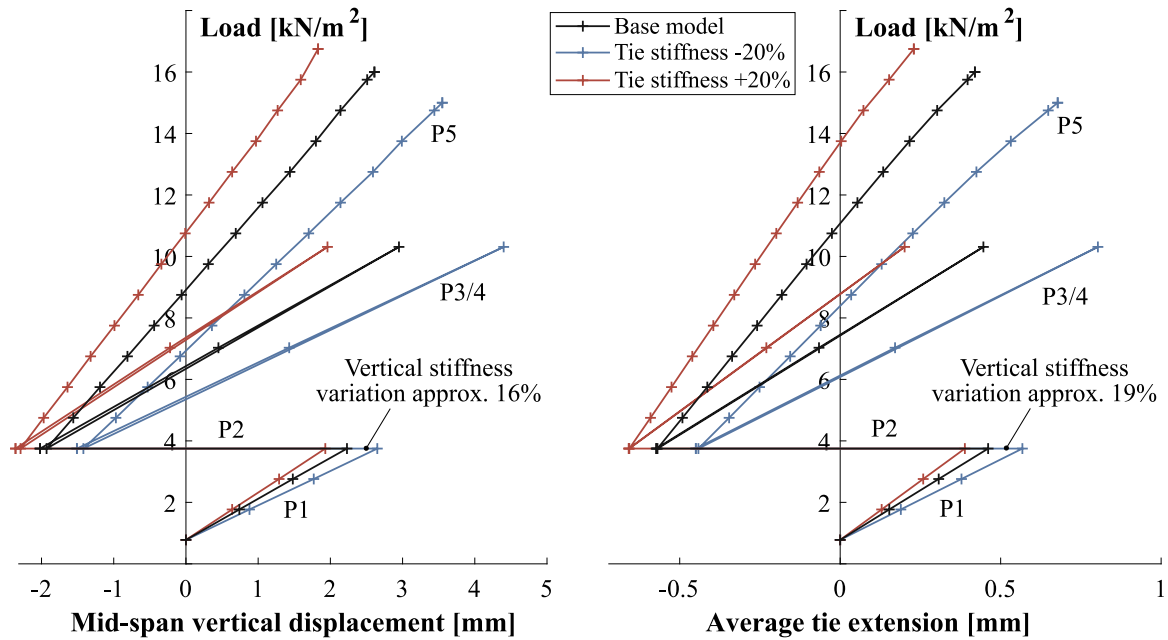


Figure 6.9: Influence of tie stiffness on the mid-span displacement and average tie extension in the non-linear FE model.

A higher tie stiffness reduces the amount of bending in the shell. This has a corresponding effect on the peak concrete stresses and therefore the maximum stable asymmetric loads, which were  $15.0\text{kN/m}^2$ ,  $16.0\text{kN/m}^2$  and  $16.8\text{kN/m}^2$  for the three models in order of increasing tie stiffness.

The results show that tie stiffness has a significant effect on the deformation of the shells. However, this cannot account for the measured differences between the three physical specimens, since the same ties were used each time.

### 6.3.4 Foamed concrete fill

The only difference, by design, between the test specimens was the presence of the foamed concrete fill. This investigation aims to isolate its effect on strength and stiffness, and

therefore determine whether this could have accounted for the differences between Shells 2 and 3.

Along with the base model, two additional analyses were performed with the fill included; the first with the foamed concrete properties as-measured (Table 6.1) and the second with both the stiffness and strength (tensile and compressive) of the fill doubled. The load was again applied only in the regions of the sixteen loading patches, but to the top surface of the fill rather than the shell itself, consistent with the physical testing of Shell 3.

In both cases, the stresses in the foam remained largely within the strength limits, with the exception of small localised areas of crushing near supports C and D. As a result, it can be assumed that the strength of the fill has little influence.

Figure 6.10 compares the vertical mid-span displacement and the average horizontal tie extension over the test phases. The inclusion of the fill adds a self-weight of  $0.439\text{kN/m}^2$  (Table 5.7) with a corresponding shift in the vertical axis. In both sets of results, the inclusion of the fill caused a similar stiffness increase both vertically and horizontally, by 7% in the first model and 9% in the second (Phase 1). This corresponds to a reduction in tie force by similar proportions, indicating lower thrust due to the increased bending stiffness of the structure.

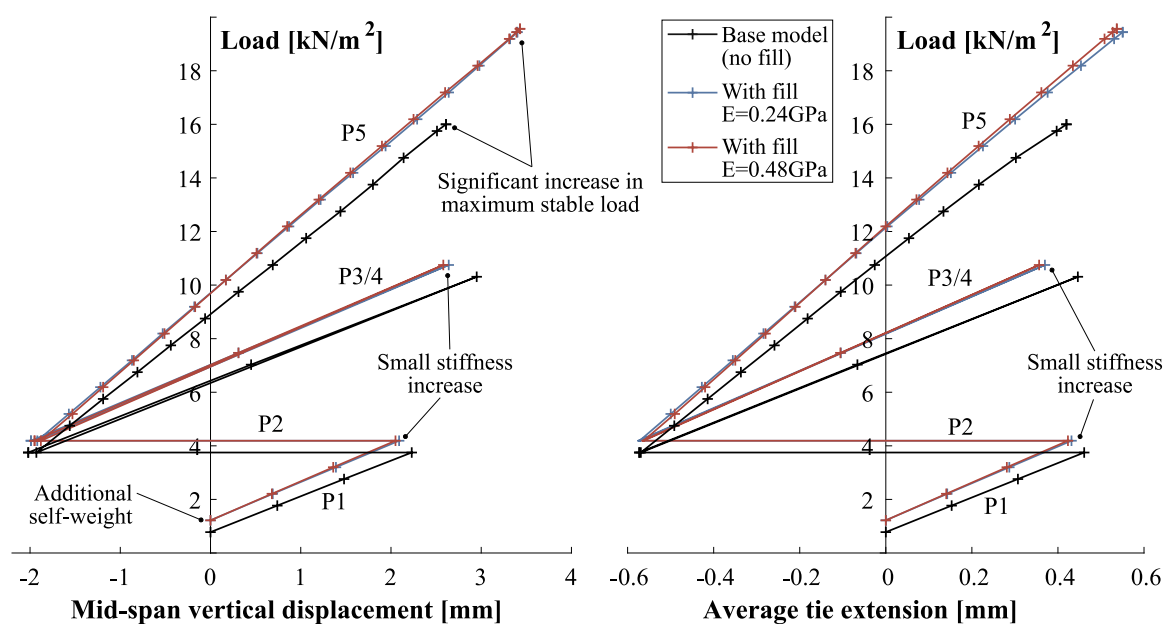


Figure 6.10: Effect of the inclusion of the foamed concrete fill in the FE model, with one and two times the measured stiffness of 0.24GPa.

The maximum stable load increased dramatically with the inclusion of the fill, from  $16.0\text{kN/m}^2$  with no fill to  $19.4\text{kN/m}^2$  and  $19.6\text{kN/m}^2$  for the first and second models respectively. The stiffness of the fill itself therefore had only a marginal influence.

The fill might be expected to affect the behaviour in two ways; firstly by increasing the stiffness of the structure and secondly by spreading the load from the jacks onto the shell more evenly. The former would be strongly influenced by the stiffness of the fill material, whilst the latter would not. The effect of doubling the fill stiffness was small, suggesting that load spreading was more significant than the increased stiffness of the structure. This may have been intensified by the use of loading patches rather than a fully uniform load.

It was previously established (from the strain gauge results of Section 5.8) that bending moments contribute significantly to shell stresses. Figure 6.11 shows how the fill significantly reduces bending moments, in this case at an asymmetric load of  $16.00\text{kN/m}^2$ . In both sets of results, the locations of the loading patches can be inferred on the more heavily loaded half. Large hogging moments are also visible at supports C and D. Although the patterns of bending are similar, their magnitudes are reduced by an average of 41% with the inclusion of the fill. This also explains the significantly higher stable loads achieved, since the smaller bending forces at the support reduce peak concrete stresses.

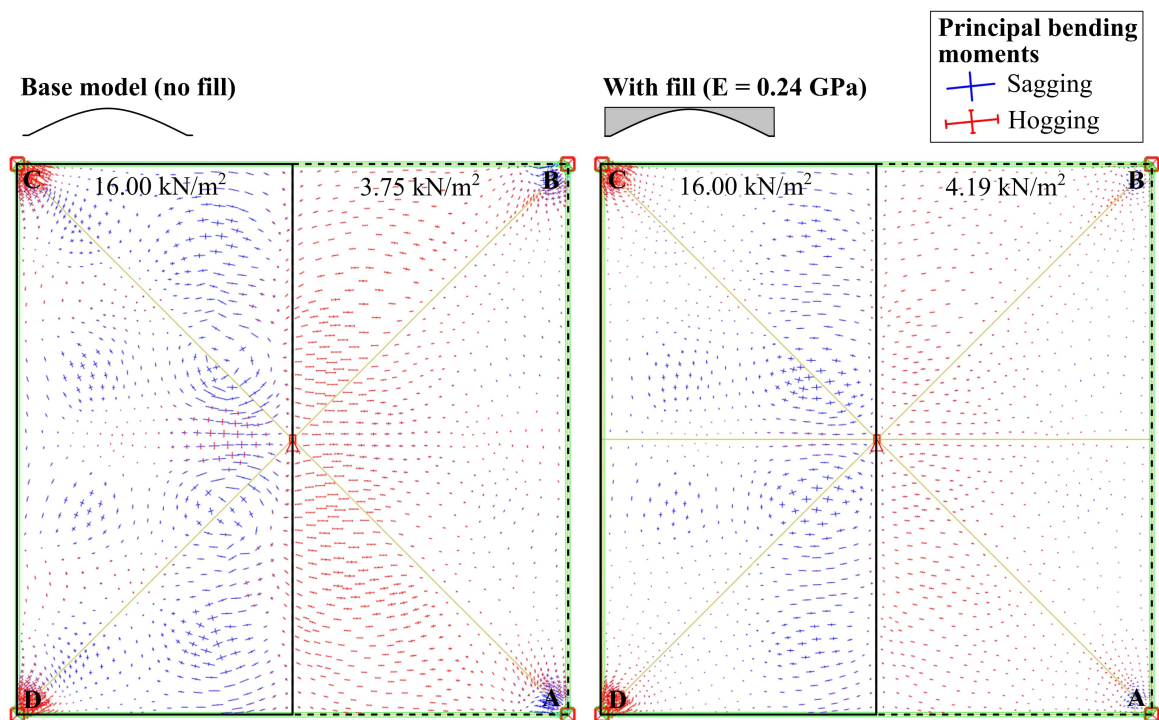


Figure 6.11: Comparison of principal bending moments with and without the foamed concrete fill in the analysis model at similar asymmetric loads.

The significant effect of the fill on bending forces has potential implications for design efficiency, since ignoring the fill could lead to over-estimation of bending forces, although the effect is likely to be exaggerated by the modelling of loading patches in this case.

### 6.3.5 Shell geometry and thickness

The measurement of the shells indicated variations in both average and local thicknesses, as well as errors in the centreline geometry (Section 5.5). Six models were therefore compared in an investigation into shell geometry and thickness, as summarised in Table 6.5. The average measured thicknesses for each shell deviated from the design value of 18mm, and this might be expected to affect the strength and stiffness of the structures. To isolate this effect, two separate comparisons were made: one with the thickness increased uniformly to the average measured value, and another with the complete measured geometry (including errors). The same approach was taken for Shell 2 and Shell 3, with the latter models including the foamed concrete fill. Shell 1 was not investigated due to the limited amount of data gathered in the test. Figure 6.12 compares the designed and measured (Shell 2) geometries. Key differences include a significant increase in thickness near the corners and a less pronounced crease along the diagonal boundary between formwork segments.

Table 6.5: Summary of shell geometries analysed in the FE model.

Model	Fill	Shell thickness	Shell geometry
2A	No	Uniform 18.00mm	Designed
2B	No	Uniform 20.41mm	Designed
2C	No	Measured Shell 2 (Figure 5.13)	Measured Shell 2 (Figure 5.13)
3A	Yes	Uniform 18.00mm	Designed
3B	Yes	Uniform 18.64mm	Designed
3C	Yes	Measured Shell 3 (Figure 5.14)	Measured Shell 3 (Figure 5.14)

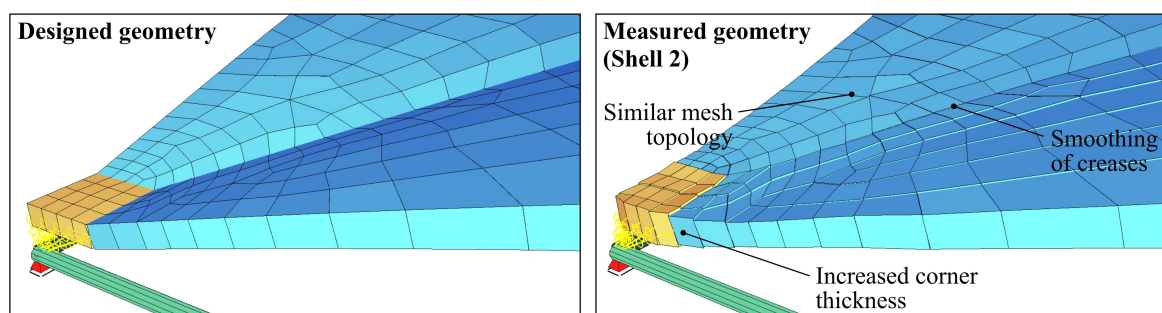


Figure 6.12: Comparison between designed and measured meshes for Shell 2.

Key results are shown in Figure 6.13. In the unfilled (Shell 2) results, a uniform increase in thickness of 11.9% (model 2B) resulted in Phase 1 stiffness increases of +5.2% (vertical) and +2.6% (horizontal). This was likely caused by an increased bending stiffness throughout the shell. A similar pattern is observed with the fill included (model 3B), albeit with lower variation corresponding to a smaller thickness increase.

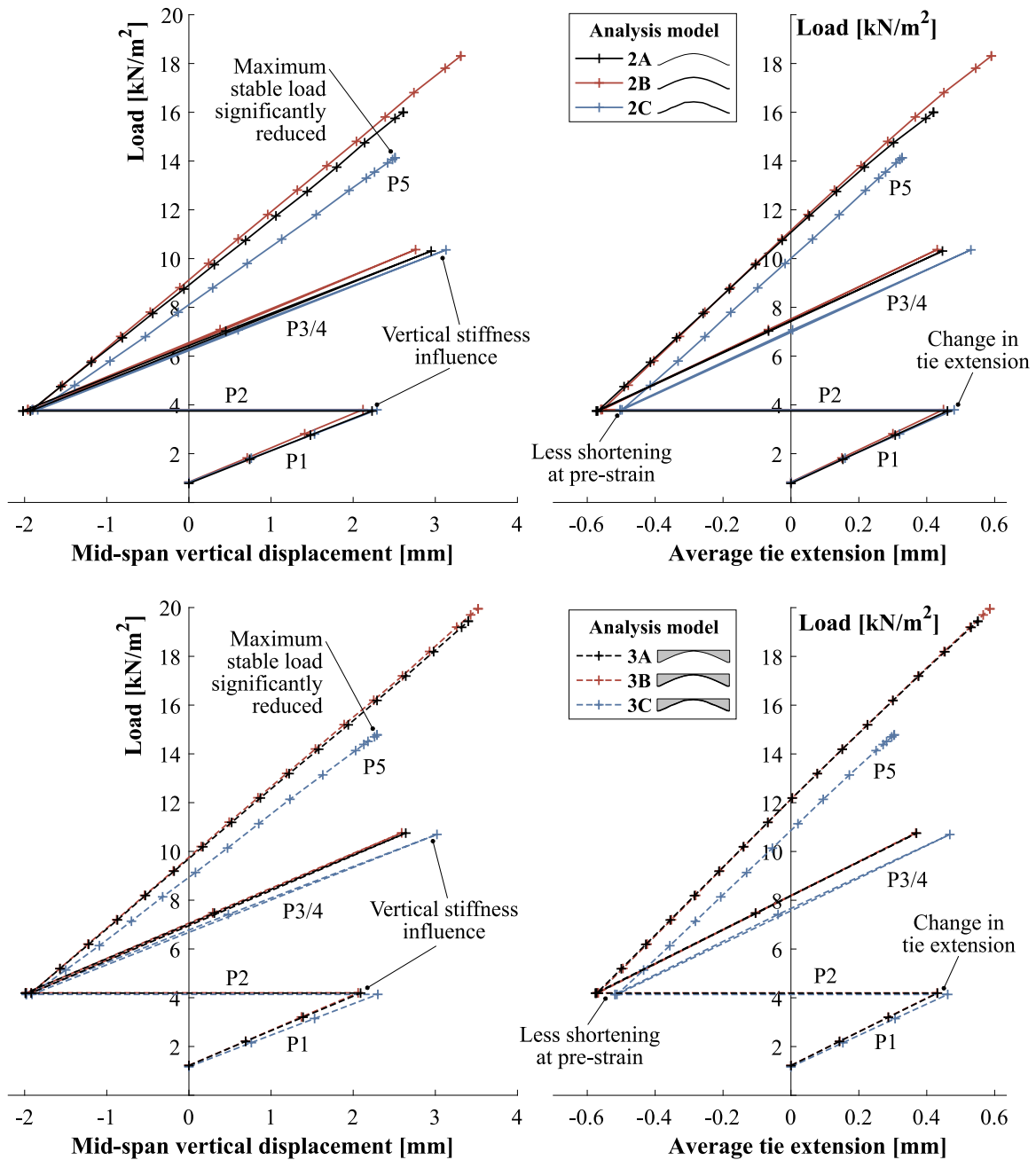


Figure 6.13: Influence of shell thickness and geometric construction errors on mid-span deflection and average tie extension, according to non-linear FE analysis.

Comparing these results to the measured geometry for Shell 2 (model 2C), we notice a considerable drop in both vertical (-7.4%) and horizontal (-6.6%) stiffness. With the fill included (model 3C), even greater changes in stiffness, -10.4% vertically and -6.8% horizontally) are observed. In both cases, the larger horizontal displacements imply a corresponding increase in tie force (thrust). This may be a result of the shallower overall height of the shell, as visible in the sections of Figures 5.13 and 5.14. Another effect of the geometric errors can also be seen in Phase 2, where the shortening of the ties is reduced despite application of the same pre-strain. Interrogation of the bending forces suggests that this is caused by increased stiffness of the shell at the thicker supports.

The maximum stable load was also considerably reduced using the measured geometry (models 2C and 3C). This again results from local behaviour at the corner supports, where significant increases in peak stress were observed. Figure 6.14 compares the distribution of principal moments for the designed and measured shell geometries at the maximum symmetric load (Phase 3), and shows increases at the corner supports by up to 6.5 times. These are caused partly by local irregularities in node location, but also by the locally increased thickness of the shell, since the higher stiffness attracts more bending as the shell deforms. This is consistent the observations of the previous investigation into variable thickness shells (Section 3.7.4).

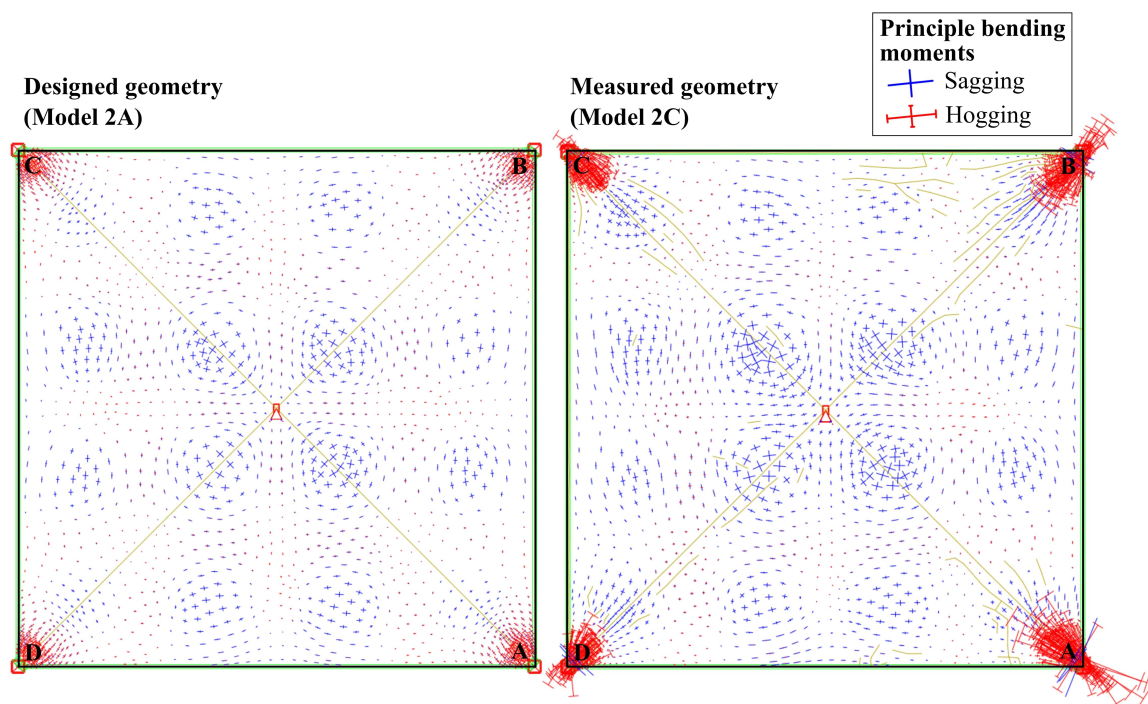


Figure 6.14: Comparison of principal bending moments using the designed (left) and measured (right) shell geometry under a uniform load (Phase 3).



Figure 6.14 also shows a general trend for increased bending moments throughout the central parts of the shell. These might be expected to arise at locations of increased stiffness, or because deviations from the designed geometry create local eccentricities relative to a smooth line of thrust.

The results suggest that the shells would have been stiffer and stronger had they been constructed precisely with the designed geometry. This indicates that modifications to the manufacturing process that could improve accuracy would increase structural efficiency. It also implies that it is unconservative to assume a perfect geometry in design, unless the required manufacturing tolerances can be assured.

## 6.4 Comparison with experimental results

This section compares the finite element model with the experimental data, with the aim of providing insight into the behaviour observed in the tests.

The FE models compared are those labelled 2C and 3C in Figure 6.13. These both feature material properties given in Table 6.1. Model 2C includes the scanned geometry of Shell 2, and similarly omits the fill, whilst model 3C replicates the geometry of Shell 3, including the fill. These should therefore enable a direct comparison with the experimental data. Figure 6.15 compares the vertical displacements, tie extensions and tie forces of Shells 2 and 3 and the FE models.

The most striking discrepancy between the FE models and the experimental results occur for vertical deflections. Here, the stiffness predicted by both FE models are similar, since the stiffening effect of the fill (model 3C) is largely cancelled out by the increased thickness of model 2C. In both cases, the predicted deflections at the end of Phase 1 are much smaller than measured in the tests, by 50% and 28% for Shells 2 and 3 respectively. The discrepancies are smaller in later phases, but still persist.

Based on the findings of Section 6.3, variations in material properties are unlikely to have caused this disparity. It was shown in Section 6.3.3 that vertical deflection is sensitive to tie stiffness. The FE models also underestimate tie extensions over Phase 1, but by only 15% and 11% for Shells 2 and 3 respectively, and therefore this can only account for part of the underestimate of vertical deflection.

It is possible that additional deformation of the support structure was measured in the tests, potentially due to compression of the ETFE sheets or flex in the steel supporting columns. This could have been measured by using vertical transducers on the shell at the corners, and eliminated by subtracting these displacements from the measurements on the shell itself.

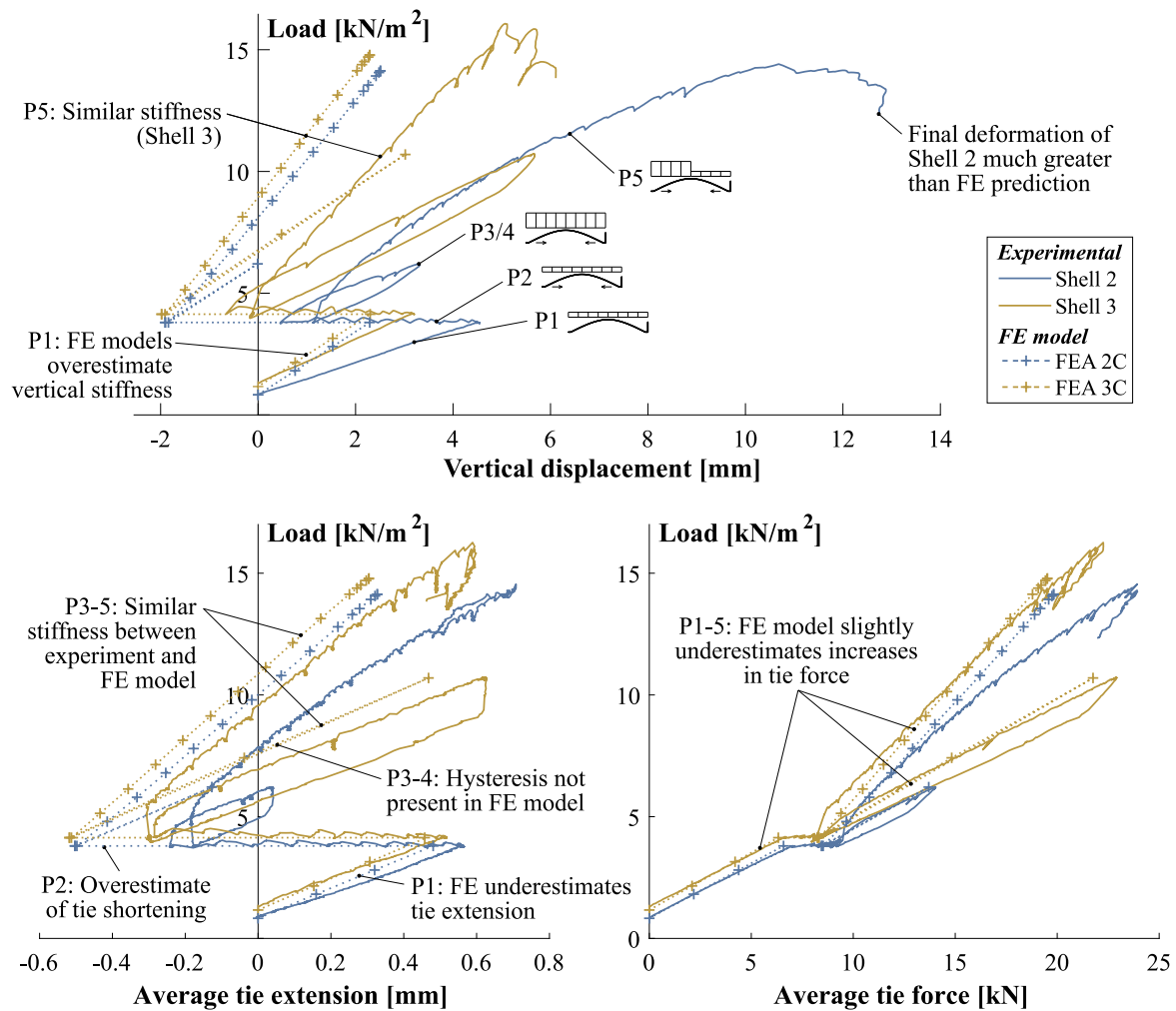


Figure 6.15: Comparison between FE models and experimental results for Shells 2 and 3.

The FE models also fail to capture the differences in vertical stiffness measured between the shells, and therefore appear to underestimate the influence of the fill. This is unexpected, since the de-bonding between the shell and fill observed for Shell 3 would be expected to reduce its stiffening effect, and this was not replicated in the FE model. In Section 6.3.4, the influence of the fill stiffness was shown to be low, but the effect of distributing the applied load was identified as important. This effect may have been greater in the physical specimens than the FE models, since in the latter case the applied pressure was assumed uniform over each loading patch. In reality, the stiffness of the loading plate and plaster would have created uneven stress distribution, with load concentration at the edges. For Shells 1 and 2, this may have significantly increased bending moments and deflection. If this was the case, then the experimental results might over-estimate the stiffening effect of the fill for real applications,

since this was a result of the load application method. This might be explored in future tests by using an alternative loading method.

The average tie forces are also compared in Figure 6.15, and show that the FE model only marginally underestimates the rate of increase in tie force, for both shells. The shells have the ability to resist load through both axial force, which generates thrust, and through bending, which does not. The slightly higher thrusts measured in the tests suggest that the former mechanism is more prevalent than in the FE model. This could be a result of an over-estimate of the shell's bending stiffness, which might also account for the discrepancy in vertical displacements.

In Phase 5, the distribution of cracks predicted by the FE model was similar to that observed in the tests, as shown previously in Figure 6.4. The maximum reinforcement stress in the FE models was approximately 400MPa. This indicates that the reinforcement was not close to failure at the maximum load, and is consistent with the lack of reinforcement rupture observed in the tests.

For the FE models of Shell 2, the first cracks near the mid-span (Phase 5) occurred at a load between 10kN/m<sup>2</sup> and 11kN/m<sup>2</sup>. This compares to 6.6kN/m<sup>2</sup> the real shell. Assuming that first cracking is governed by the tensile stress of the concrete, this suggests that the value in the model (based on the TRC bending tests) is too large. This might be expected due to the larger size of the shells than the test specimens. However, the earlier onset of cracking may also have been caused by the uneven distribution of applied pressure beneath the loading patches, as noted previously.

The large vertical displacement of Shell 2 during Phase 5 was not replicated in the FE model. This is because the deformation capacity of the model is limited by the peak stresses at corners, which lead to stability issues. For this reason, the stability of the non-linear FE model can not be reliably used to predict the ultimate load of the shells. This justifies the use of a utilisation based approach, which the next section explores.

## 6.5 Strength utilisation analysis

In Section 4.3, an analytical failure envelope was proposed for the prediction of TRC strength under combined axial and bending forces. This is a development of a bi-linear envelope detailed by Scholzen et al. (2015b). In both cases, the approach is to determine the strength utilisation across a TRC structure using local axial and bending forces, which can be calculated using a finite element model. The results from the shell tests provide an opportunity to apply and assess this methodology.

This section firstly introduces the finite element model used to calculate the forces in the shells. The failure envelopes are then calculated and examined, using material parameters matching the shells. These are then combined to predict the utilisation at key loads from the physical tests. The influences of geometry errors and the fill are also investigated.

### 6.5.1 Methodology

#### Analysis model

The FE model used to determine the forces was similar to that described in Section 6.2, albeit using a linear analysis. An earlier comparison of linear and non-linear models (Section 6.2.3) showed that these yield similar force distributions, except locally at the corner supports or where the non-linear model is close to instability. Values of density, Young's modulus and Poisson's ratio were taken from Table 6.1. All models also featured rigid vertical supports at the corners.

#### Failure envelopes

Each failure envelope was plotted using material parameters matching those of the shells, enabling direct comparison with experimental data.

Table 6.6 summarises the input variables used to create the analytical failure envelope, which was carried out according to the methodology described in Section 4.3. The variable properties of the reinforcement in each direction were fully accounted for in the model. The concrete stress-strain curve assumed was the parabola-rectangle described previously in Equation 4.2. The stress-strain curve was not modified despite the low stiffness of the fine-grained concrete measured in the prism tests, because the concrete stiffness has previously been shown not to significantly affect the failure envelope (Section 4.3.2).

The bi-linear envelope is based on experimental values of strength measured in the TRC tests (Section 5.6), which are summarised in Table 6.7. Averages across all shells were used, although specimens suffering from de-lamination were ignored. In compression, the prism value of strength was chosen for consistency with the analytical envelope, despite the variation in between the shells noted previously (see Section 5.6.3). The two envelopes are therefore coincident in both pure tension and compression.

Figure 6.16 compares the three envelopes, and also shows the variation of strength with direction (relative to the warp reinforcement). This is particularly significant at angles near  $45^\circ$  due to the reduction factor  $k_\alpha$  (Equation 3.8).

As noted in Chapter 4, Section 4.3.2, the analytical envelope predicts considerably higher strengths in combined compression and bending. However, in this instance, the analytical

Table 6.6: Material properties used in the calculation of analytical failure envelopes for utilisation calculation.

		Warp	Fill	Origin
<b>Concrete properties</b>				
$f_{cd}$	[MPa]	36.6	36.6	Prism tests (Section 5.3.2)
$\varepsilon_{c2}$	[%]	0.20	0.20	Typical value (Equation 4.2)
$\varepsilon_{cu2}$	[mm]	0.35	0.35	Typical value (Equation 4.2)
$n$	-	2	2	Typical value (Equation 4.2)
<b>Reinforcement properties</b>				
$f_t$	[MPa]	1192	1326	Reinforcement tests (Section 4.2.1)
$k_1$	-	0.685	0.597	TRC tensile tests (Section 5.6.1)
$E_t$	[GPa]	64.0	55.7	Reinforcement tests (Section 4.2.1)
$A_t$	[mm <sup>2</sup> /m]	65.3	52.2	Reinforcement tests (Section 4.2.1)

Table 6.7: Summary of tensile, bending and compressive strengths used to create bi-linear failure envelopes for analysis of the shell tests.

		Warp	Fill	Origin
Tension	[kN/m]	106.7	82.6	TRC tensile tests (Section 5.6.1)
Bending	[kNm/m]	0.931	0.712	TRC tensile tests (Section 5.6.2)
Compression	[kN/m]	658.1	658.1	Prism tests (Section 5.3.2)

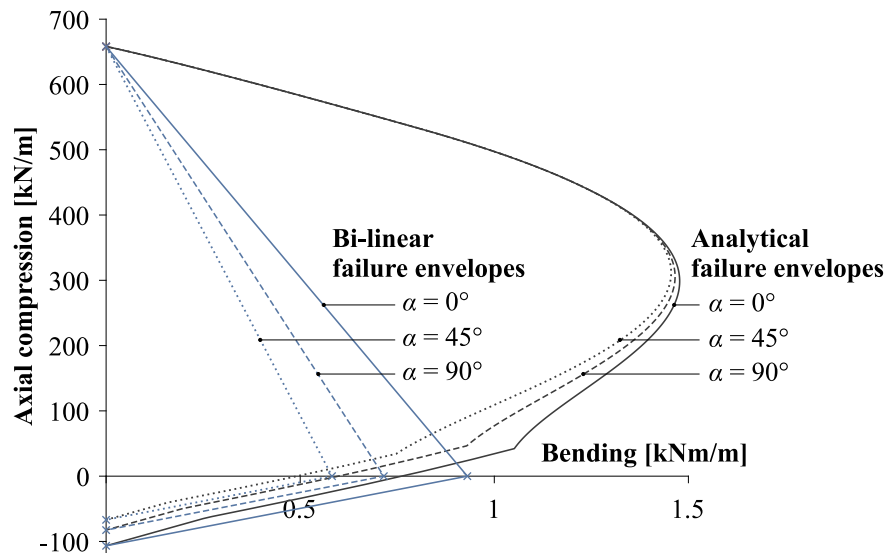


Figure 6.16: Comparison of analytical and bi-linear strength envelopes, highlighting the effect of loading angle relative to the warp direction.

model under-estimates the experimental bending strength. This is linked with the lower reinforcement strengths found in the tensile tests (used for the analytical model) than in bending. The discrepancy may also be partly because the specimens tested in bending were, on average, thicker than 18mm (see Table 5.6). The result is that the analytical envelope predicts consistently lower strengths on the tensile side of the envelope.

## 6.5.2 Results and discussion

Two states of loading were used to evaluate the utilisation analysis. The first was the uniform design load at the end of Phase 3 ( $10.31\text{kN/m}^2$ ), which was carried by Shell 3 without failure. The second was the maximum asymmetric load at which Shell 2 failed ( $14.55\text{kN/m}^2$ ).

Figure 6.17 shows the corresponding strength utilisation distributions, based on the analytical failure envelope. In both cases, increased utilisation caused by bending beneath the loading patches is visible. For the uniform load, the whole of the shell is utilised at below 1.0, indicating no failure. This is consistent with the results of the physical testing of Shell 3 as well as the non-linear analysis of the previous section.

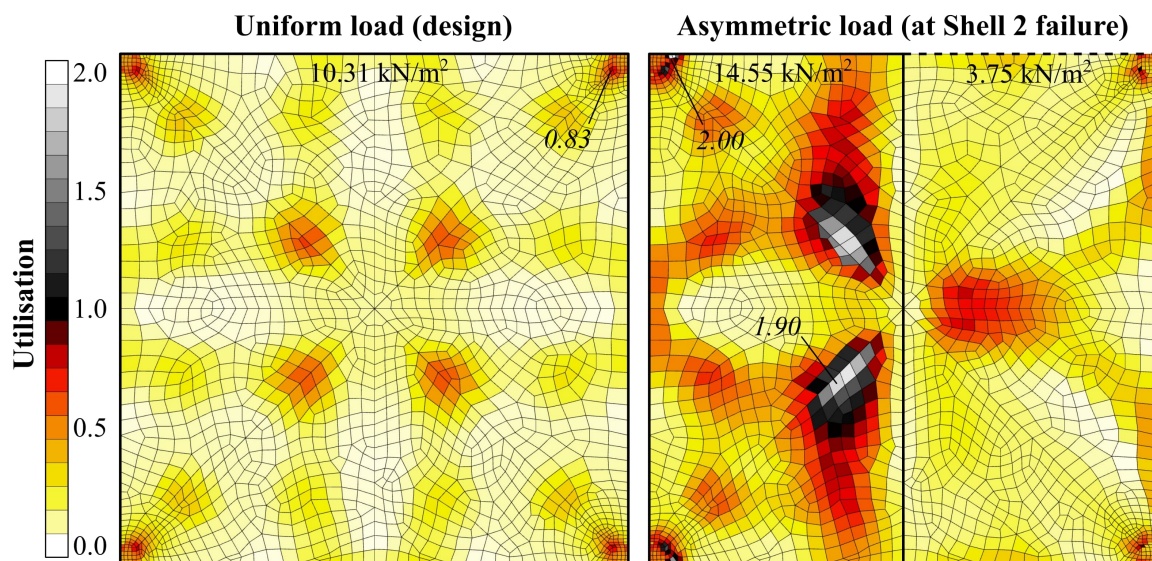


Figure 6.17: Calculated maximum utilisations per element for uniform (left) and asymmetric (right) loads, using the analytical failure envelope. Peak values are highlighted.

The asymmetric load, by contrast, shows some over-utilised elements. These exist at the supports, where concrete crushing is predicted, however local stress concentrations at the corners are a likely influence at this location. Near the shell centre, some elements predict tensile failure of reinforcement. This contrasts with the low reinforcement stresses

encountered in non-linear modelling, and the lack of reinforcement failure observed in the Shell 2 test. A number of factors could however explain this under-estimate of strength:

- An under-estimate of bending strength in the analytical model due to the higher reinforcement strength measured in bending than in tension, as highlighted in Figure 6.16.
- The principal stresses in this region are aligned at nearly  $45^\circ$  to the reinforcement, and thus the reduction factor  $k_\alpha$  (Equation 3.8) is approximately 0.5. It is possible that this strength reduction factor, an approximation proposed by Scholzen et al. (2015b), is conservative for this particular reinforcement and concrete combination. This could be investigated in future through tests with inclined reinforcement.
- As noted previously in Chapter 4 (Section 4.3.5), the utilisation calculation method considers only the forces in the directions of principal stress on each surface of the shell, and ignores the normal forces. Where these are compressive, this leads to an over-estimate of reinforcement stress.
- The true thickness of Shell 2 is greater than 18mm in these regions, shown by the results of Figure 5.13, leading to a higher bending strength.
- Local stiffening of Shell 2 caused by the plaster loading patches, which were not featured in the FE model.
- The inability of the linear analysis model to redistribute stress (through cracking) leads to larger peak bending forces.

This approach only includes the possibility of two types of failure; either local crushing of the concrete or rupture of the reinforcement. However, the hinged collapse mechanism observed for Shells 2 and 3 does not necessarily require either, being instead governed by global geometry and stiffness. Despite this, the utilisation methodology gives a broadly accurate representation of the loads and locations of failure, particularly where the conservatism in the model and influence of local stress concentrations are taken into account.

### **Failure envelope comparison**

In Figure 6.18, left, the critical pairs of axial and bending forces for each element are plotted for both loading scenarios. Both failure envelopes are included to highlight the critical force combinations. The utilisation distribution is also compared between the envelopes using a histogram (Figure 6.18, right).

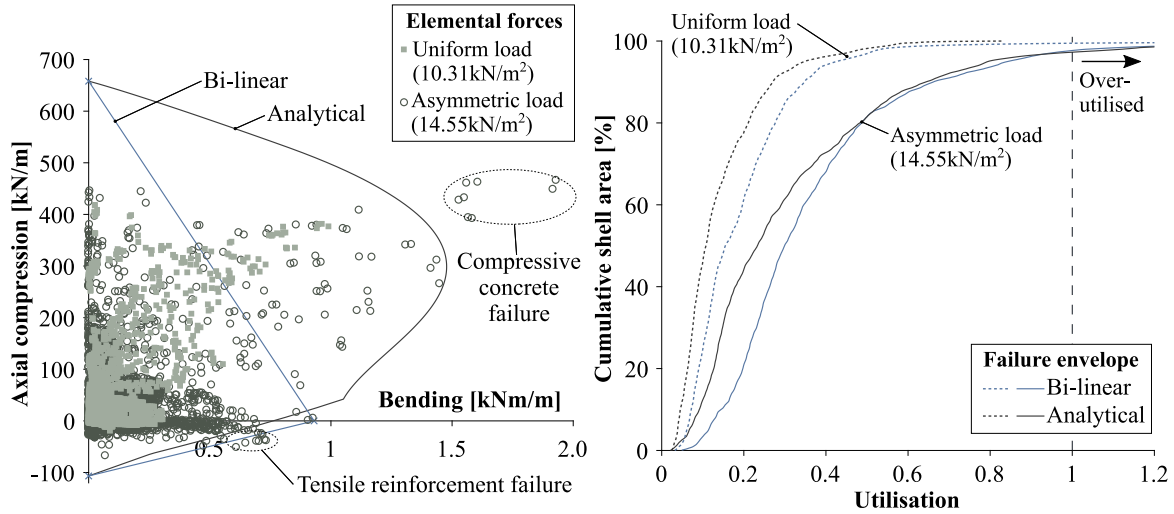


Figure 6.18: Comparison of failure envelopes for utilisation prediction. The left graph plots the elemental forces for both the uniform and asymmetric loads, calculated from the FE analysis, and compares these to each envelope. On the right, histograms are used to compare the utilisation distributions over both load scenarios.

The results reveal the distribution of forces throughout the shell, showing a skew towards compression, albeit with significant bending and some tension. The analytical envelope captures the spread of forces well, suggesting efficient section design in terms of reinforcement ratio. Elements for which concrete compressive failure is predicted are highlighted in Figure 6.18. These occur near the corner supports, and hence their magnitudes are mesh-dependent. However, they are also located where the biggest discrepancy between failure envelopes exists. The result is that the bi-linear envelope predicts unrealistically high utilisations, indicating failure for the uniform load where the analytical does not.

In the asymmetric load, other over-utilised elements can be seen for combined tension and bending. These are located near the shell centre, as highlighted in Figure 6.17. Here, the bi-linear envelope is less conservative, as previously noted from Figure 6.16. Since these cross the tensile region of the failure envelope, the utilisation could be reduced by providing more reinforcement.

In all cases, the axial forces are comfortably lower than the strength in pure compression or tension. The bending forces are therefore critical in determining the utilisation. This is consistent with the large bending stresses found throughout the shells in both the experimental strain gauge data and non-linear FE analysis.



### **Influence of fill**

In the non-linear FE analysis of Section 6.3, the inclusion of the fill was shown to have a considerable influence on predicted bending moments, and this might also affect the utilisation distribution.

Figure 6.19 shows the utilisation distribution both with (top left) and without (bottom left) the fill, at the asymmetric load. In both cases, the analytical failure envelope was used for utilisation calculation.

Considerable reductions can be seen throughout the shell due to the lower bending forces, caused by increased stiffness and load spreading. Figure 6.20 compares the histogram of utilisation in each case. The average falls from 0.32 to 0.21 with inclusion of the fill. This suggests that excluding the fill in the model is conservative, but may lead to over-design.

### **Influence of geometry errors**

Figure 6.19 also includes utilisation distributions using the measured geometry, both without the fill (Shell 2) and with it (Shell 3). Geometric errors would be expected to influence the utilisation results in two ways, firstly by changing the predicted forces and secondly by variations in the local strength, which is a function of thickness. The latter was accounted for in the model by defining failure envelopes individually for each element based on the local thickness, assuming a constant cover to reinforcement of 3mm.

For the unfilled shell, the results in Figure 6.20 shows a general reduction in utilisation across the shell area, from an average of 0.31 to 0.28. This is largely because of the higher average thickness measured for Shell 2 (20.41mm). However, Figure 6.19 shows some regions of increased utilisation which arise due to higher bending forces. With the fill included, the average utilisation is increased when geometry errors (Shell 3) are taken into account, since the average measured thickness (18.64mm) is insufficient to counter the increased bending moments.

Both without and with the shell, the measured geometry gives higher utilisations near the corner supports, despite the thicknesses in these regions significantly exceeding 18mm. This suggests that the higher strength is not enough to overcome the greater bending forces. This is consistent with the findings from the non-linear FE analysis (Section 6.3.5), again suggesting that increasing the thickness near the corners does not increase the shell's strength. It should be noted, however, that the behaviour in these locations is sensitive to the local mesh as well as the support conditions.

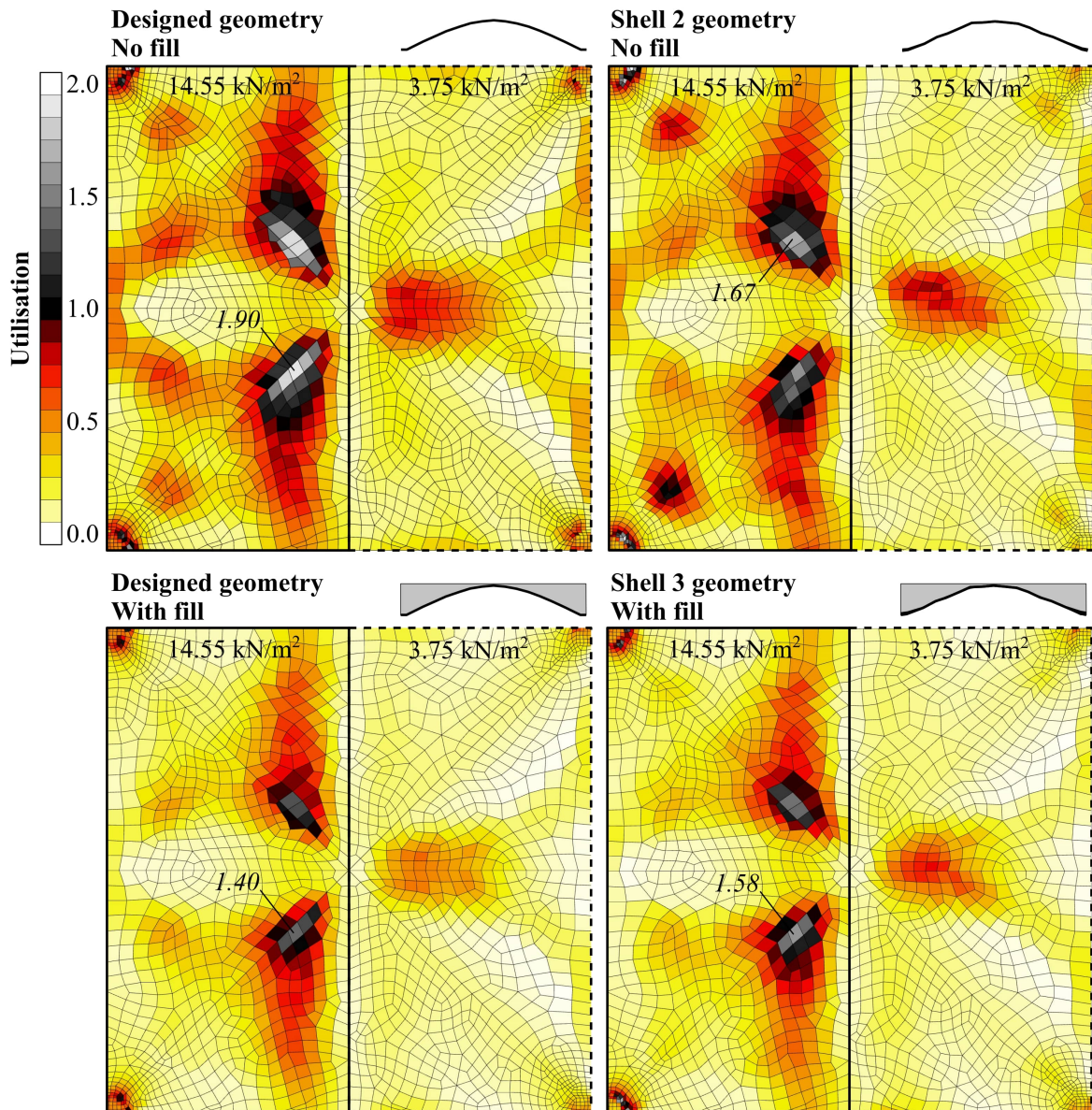


Figure 6.19: Utilisation distribution at the asymmetric load at which Shell 2 failed, calculated using the analytical failure envelope. Four models are compared, with and without both the fill and geometry errors. In the latter cases, elemental utilisation envelopes are modified according to the local thickness.

## 6.6 Summary, findings and conclusions

This chapter has described the structural analysis of the quarter-scale prototypes, the construction and testing of which was detailed in Chapter 5. A non-linear FE model was used to replicate the tests and to assess the influence of a range of variables on the structural behaviour.

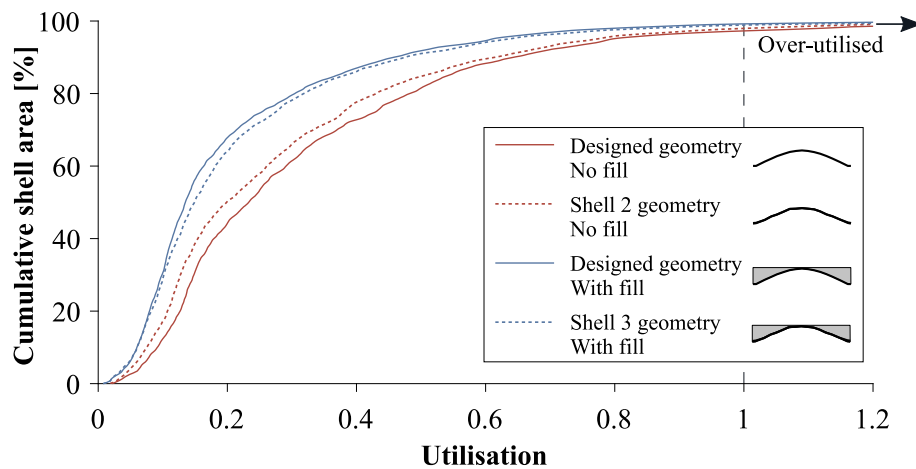


Figure 6.20: Histogram comparing the distribution of utilisation over the shell area for the four models featured in Figure 6.19.

The strength design methodology, which uses a novel analytical failure envelope described in Section 4.3, was also implemented and the results compared with the experimental data.

The main findings are summarised as follows:

- The non-linear material model for TRC, developed in Chapter 4 (Section 4.4) successfully replicates the deformations and cracking behaviour observed in the tests when incorporated as part of a 3D model.
- Stress concentrations near the corner supports are problematic for FE modelling, dictating the maximum stable load in non-linear analysis.
- Bending forces have a significant influence on the peak shell stresses, local strength utilisation and the predicted ultimate load. As such, factors which affect the bending moment distribution, such as the inclusion of the foam concrete fill, geometric errors or tie stiffness, have a correspondingly significant influence.
- The stiffening influence of the foamed concrete fill may have been exaggerated in the physical tests by the use of discreet loading patches, compared to a shell with uniformly distributed loads.
- The successful operation of the shell under an asymmetric load is reliant on the tensile strength of the concrete, albeit with a low sensitivity within the range of values expected.
- The overall deformation of the structure is more sensitive to the tie stiffness than that of the TRC.

- In this case, the measured manufacturing errors have a negative impact on the stiffness and strength of the shell, largely due to the introduction of additional bending forces.
- Analysis of strength utilisation, using the methodology developed in Section 4.3, successfully indicates the failure location and gives a conservative estimate of strength. Although this analysis can not replicate the subsequent formation of a hinged collapse mechanism, it remains a reliable tool for the designing the shell section.

**Conclusions: Chapter 6**

The structural behaviour of the proposed system can be replicated successfully using FE analysis, which can therefore provide insight into how it might most effectively be designed and built. FE analysis can therefore be incorporated into a complete design methodology which, in combination with the theoretical models developed in Chapter 4, enables investigation of behaviour and performance at full-scale.

# Chapter 7

## Design refinement and comparative case study

### 7.1 Introduction

In previous chapters, design and analysis methodologies for the proposed flooring system have been developed and verified through computational modelling and physical testing. This now allows the principal aim of the project, to create a practical means of minimising embodied CO<sub>2</sub> in buildings, to be addressed. This chapter introduces further practical design refinements and assesses the performance of the proposed system in detail, aiming to:

- Extend the design methodology such that the required concrete strength and reinforcement area can be specified using a linear FE analysis.
- Explore design parameters in more detail, leading to a repeatable strategy for determining an efficient shell thickness, tie diameter, column size and total depth for a given span and performance specification.
- Consider additional structural requirements for floors in buildings, such as lateral stability and robustness.
- Compare the weight, depth and embodied CO<sub>2</sub> with common alternative floor construction typologies using a realistic case study.

### 7.2 Methodology

This section describes the approaches and assumptions which are common throughout the investigations of this chapter.

### 7.2.1 Analysis and Design

In Section 6.2.3, it was shown that non-linear effects, such as cracking and softening of concrete, have a minimal influence on structural behaviour, with two exceptions: the peak corner support stresses, and the predicted deformations at asymmetric loads very close to the experimentally-determined ultimate capacity. A linear finite element model using Karamba (Preisinger, 2013), similar to that described in Section 3.4.1, was therefore used to calculate both forces and deformations throughout this chapter. This lower-bound approach is conservative; the structure is designed to resist a system of forces in equilibrium with applied loads, with redistribution of forces ignored.

The TRC section was designed according to the strength design methodology presented in Section 4.3, and in Hawkins et al. (2018). The use of an analytical failure envelope, based only on section geometry and constituent material parameters, allows exploration and optimisation of the TRC section without the need for each possible section design to be tested individually. The reinforcement requirements are typically dictated by critical regions near the middle of the shell, which experience large bending forces with low compression, and the required concrete strength is determined by the large compressive forces at the shell-column interface. In the latter case, further consideration is required to ensure that the results, and therefore the design, is not dependent on the FE mesh used.

Buckling was not found to occur in the prototype tests, or the non-linear FE models of Sections 3.6.6 and 6.2, and is therefore not considered in the design methodology used in this chapter. However, a buckling check (including initial imperfections) should be made as part of a detailed design in practice.

#### **TRC utilisation at corner supports**

The shell-column interface has been identified in previous investigations as a critical region for determining the required strength of the shell (Sections 3.4.2 and 6.2.3). However, the peak forces predicted by FE analysis do not converge with increasing mesh refinement, indicating a stress singularity at the column corner caused by the sharp re-entrant geometry and a large nodal reaction, both common causes of stress singularities (Williams, 1952). In real structures however, these peaks are redistributed due to non-rigid supports and softening of materials caused by localised cracking, crushing or yielding. In the physical tests, this is why Shells 2 and 3 did not fail at the corner supports despite FE predictions indicating several over-utilised elements (Figure 6.17).

A methodology for determining the section utilisation at the shell-column interface was therefore devised, aiming to be reliable, repeatable and independent of mesh size. The model is shown in Figure 7.1.

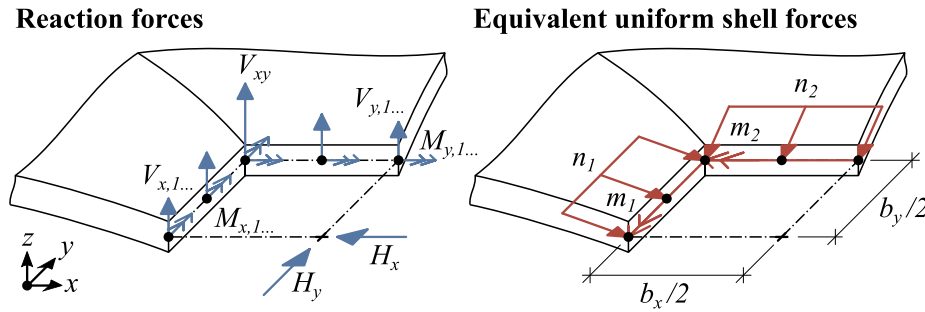


Figure 7.1: Reaction forces and corresponding uniformly distributed forces at the shell-column interface.

In the proposed model, nodal reactions are converted to equivalent uniformly distributed loads. The uniform axial forces per unit length ( $n_1$  and  $n_2$ ) are the vector sums of the corresponding tie forces ( $H_x$  and  $H_y$ ) and the vertical nodal reactions ( $V_x$  and  $V_y$ ), distributed over the column edge widths ( $b_x$  and  $b_y$ ), as shown in Equation 7.1. The reaction at the inner corner ( $V_{xy}$ ) is shared equally between the two faces.

$$n_1 = \frac{2}{b_y} \sqrt{\left(\sum V_x + \frac{V_{xy}}{2}\right)^2 + H_x^2}$$

$$n_2 = \frac{2}{b_x} \sqrt{\left(\sum V_y + \frac{V_{xy}}{2}\right)^2 + H_y^2}$$
(7.1)

Similarly, the moments per unit length ( $m_1$  and  $m_2$ ) are the sum of corresponding nodal values ( $M_x$  and  $M_y$ ):

$$m_1 = \frac{2}{b_y} \sum M_x$$

$$m_2 = \frac{2}{b_x} \sum M_y$$
(7.2)

This is a lower-bound approach, and as such it relies on the assumption that the material is able to redistribute stress in a ductile manner. Similar methods are commonly applied to crushing of concrete, such as the use of a rectangular stress block for bending failure (Kotsovos, 1982). Ibell and Burgoyne (1994) also used a similar approach for predicting the capacity of anchorage zones for prestressing tendons, whereby stresses calculated using a linear elastic FE analysis are averaged before a failure criterion is applied.

The reliability (and mesh sensitivity) of this approach was tested using a model of Shell 2 at the experimentally determined failure loads of  $14.55\text{kN/m}^2$  and  $3.75\text{kN/m}^2$ , applied uniformly over each half of the shell. The methodology was implemented in Grasshopper as a modification to the FE model described in Section 3.4.1. The utilisation calculation featured the analytical failure envelope and the TRC material parameters corresponding to the test specimen (as given in Table 6.6). Three different mesh densities were modelled, each with four times as many elements as the previous.

Figure 7.2 compares the peak elemental utilisation values with those calculated using the proposed model. The latter gives approximate averages of the local elemental utilisation values, and mesh sensitivity is significantly reduced.

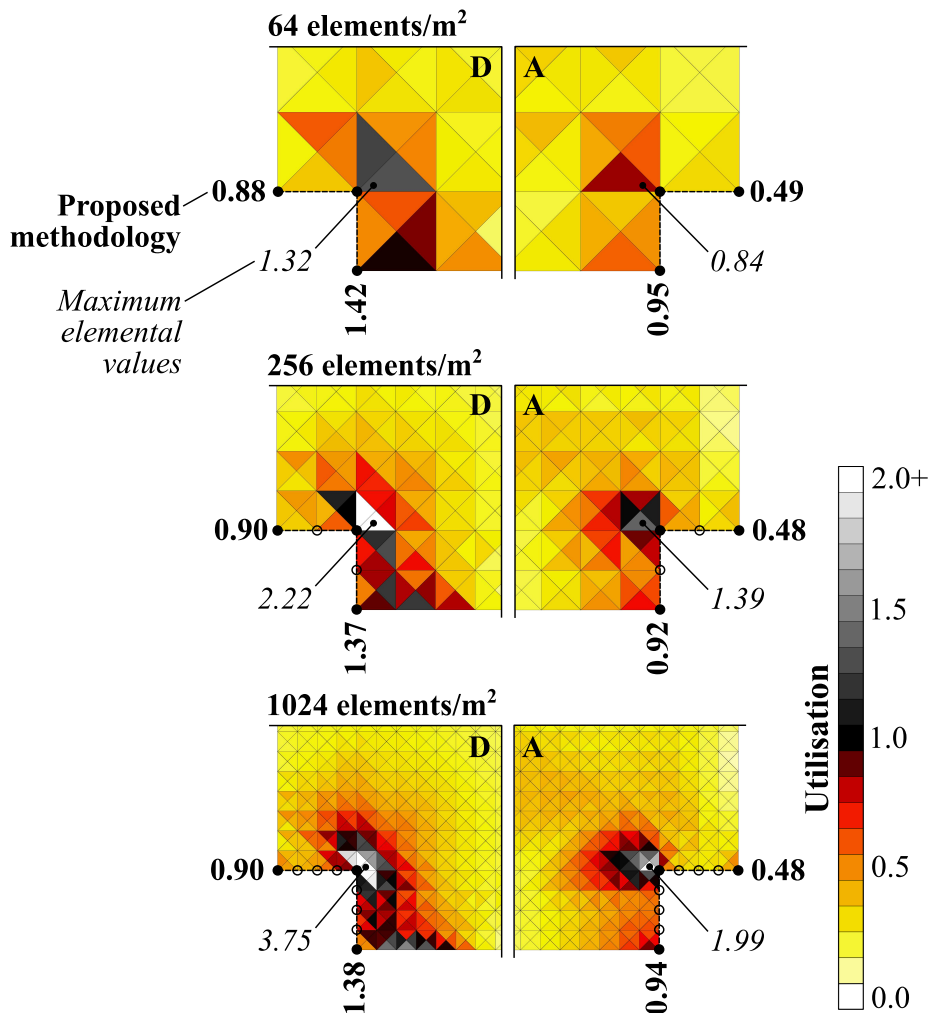


Figure 7.2: Comparison of elemental strength utilisation values and those calculated using the proposed method at the shell-column interface. The loading, geometry and material parameters are those corresponding to Shell 2 at the maximum asymmetric load.



In this case, the critical region is at corner D. The predicted utilisation is 1.38 (at the highest mesh-density). The asymmetric load at which this critical value is equal to 1.00 is  $12.14\text{kN/m}^2$ , and this is therefore the predicted strength of the structure using the proposed methodology. This is smaller than the measured failure load of  $14.55\text{kN/m}^2$ , indicating that the approach is conservative, in this example. It was therefore incorporated into the TRC strength design methodology and is used throughout this chapter. Elemental utilisation values are still used for regions away from the corner supports, where mesh-sensitivity is significantly smaller.

### 7.2.2 Loading and deflection criteria

The floor loadings assumed throughout Chapter 3 (Section 3.4.3), typical for an office in the UK, were again assumed in the investigations of this chapter.

Serviceability checks were also undertaken, based on maximum vertical deflections under uniform loads. Two serviceability requirements are considered; firstly the total deflection  $\delta_{tot}$  (less than  $\text{span}/200$ ) and, secondly, that due to the live load only  $\delta_{live}$  ( $\text{span}/360$ ). The proposed deflection limits apply to internal spans with brittle partitions (e.g. plasterboard) and are typical recommended values for composite floors (Couchman et al., 2000).

The effects of creep are also considered using a simplified approach suitable for linear analysis, whereby the Young's modulus of the concrete is reduced for long-term loadings by a factor of  $(1 + \varphi)$ , where  $\varphi$  is the creep coefficient. This variable depends on the relative humidity, thickness of the concrete element, type of cement, age of loading (e.g. removal of formwork), aggregate type and concrete strength. In this investigation, a simplified approach is taken assuming a creep coefficient of  $\varphi = 2.5$  in all cases. This is the long-term value for a 50mm thick shell of C32/40 concrete exposed on one side to an indoor environment of 50% relative humidity, loaded 28 days after casting, and was calculated according to Eurocode 2 (BSI, 2004a). In a real project, a more specific evaluation would be required if long-term deflections are of concern.

Only the quasi-permanent proportion of the total load, which in this case includes dead and live loads with factors of 1.0 and 0.3 respectively, are assumed to be influenced by creep. The remaining proportion of the live load is short-term and hence the full Young's modulus is used. Total deflections are calculated by summing values found from separate analyses, as summarised in Table 7.1. The total ( $\delta_{tot}$ ) and live ( $\delta_{live}$ ) load deflections are hence calculated according to Equations 7.3 and 7.4 respectively:

$$\delta_{tot} = \delta_1 + \delta_2 + \delta_3 \leq l/200 \quad (7.3)$$

$$\delta_{live} = \delta_2 + \delta_3 \leq l/360 \quad (7.4)$$

Table 7.1: Long-term and short-term vertical deflections calculated for serviceability criteria.

Deflection	Creep coefficient, $\varphi$ [-]	Tie pre-strain	Load factors	
			Dead	Live
Long-term dead, $\delta_1$	2.5	Yes	1.0	0.0
Long-term live, $\delta_2$	2.5	No	0.0	0.3
Short-term live, $\delta_3$	0.0	No	0.0	0.7

### 7.2.3 Materials and embodied carbon

This section details the material properties assumed throughout this chapter. They are based on data collected in the experimental investigations of Chapters 4 and 5, or literature where indicated. For all materials, strength reduction factors are included to emulate a practical ULS design scenario.

Embodied CO<sub>2</sub> values are also required for each material, firstly to inform the design refinement (Section 7.3) and secondly for comparison with alternative flooring systems (Section 7.5). Estimations of embodied carbon can vary considerably for similar materials, owing to variations in transportation, energy sources, manufacturing methods and local recycling practices, as well as differences in accounting methodologies between studies. However, since the total embodied carbon is used only as a means of comparison between equivalent floor designs in this instance, some uncertainty in the values is acceptable. All figures given consider production only (cradle-to-gate), and are given as a carbon dioxide equivalent (CO<sub>2</sub>e).

#### Fine-grained concrete

In accordance with Eurocode 2 (BSI, 2004a), the design concrete strength  $f_{cd}$  is the characteristic cylinder strength  $f_{ck}$  with a partial factor of  $\gamma_c=1.5$ . The maximum and minimum strength range considered is  $12\text{MPa} \leq f_{ck} \leq 90\text{MPa}$ . Eurocode relationships between strength, Young's modulus (for FE analysis) and strain curves (for creating analytical failure envelopes) are also assumed. A dry concrete density of  $2200\text{kg/m}^3$  is used in all self-weight calculations.

The embodied carbon of concrete is approximately proportional to cement clinker content, and therefore varies with strength and mix design, as detailed previously in Section 2.3.1. Figure 7.3 compares the embodied carbon and 28 day cylinder strength values found in six published studies from various geographical regions. Where required, cube strengths have been converted to cylinder strengths using a factor of 0.8.

An investigation by Purnell and Black (2012) compares the embodied carbon of a range of mixes with cube strengths from 17MPa to 120MPa, using the BRE mix design method described by Teychenné et al. (1997). A considerable reduction in CO<sub>2</sub> is achieved by replacing 40% OPC with fly ash. The role of plasticiser in reducing water-cement ratio, thus increasing strength, is also demonstrated. Two sets of values are also included from the ICE database (Jones and Hammond, 2019), the first using 100% OPC and the second with 35% OPC replacement. The values derived by McGrath et al. (2012), based on average ready-mix concretes in Ireland, are similar. Kim et al. (2016) calculated the embodied carbon for concrete used in 10 high-rise building projects under construction in South Korea. The embodied carbon is higher in the superstructure than substructure, due to the inclusion of GGBS to reduce heat of hydration in the latter case. In Australia, Flower and Sanjayan (2007) give the embodied carbon of concretes of various strengths for a medium-rise housing project in Melbourne, whilst Nath et al. (2018) looked at high-strength concretes with varying levels of fly ash for marine applications. The mix used for the specimens of Chapter 4, described in Section 4.2.1, is also included, although it should be noted that this is an average rather than a characteristic strength value.

The results show a positive correlation between strength and embodied carbon, albeit with considerable scatter, driven partly by variable levels of OPC replacement.

A consistent relationship between strength and embodied CO<sub>2</sub> is required for the investigations of this chapter. The curve given by Purnell and Black (2012) for 100% OPC was therefore chosen, as highlighted in Figure 7.3, since this provides continuous data over a large strength range and sits approximately within the other values found in literature. It should be acknowledged that, with high levels of OPC replacement and plasticiser use, the embodied carbon could be reduced relative to this curve.

### **Textile reinforcement**

The TRC section is assumed to be reinforced with matching top and bottom AR-glass reinforcement meshes, with a cover of 5mm (similar to 4.6mm used in the pavilion at the University of Aachen, as described by Scholzen et al. (2015a)). The cross-sectional area of the textile reinforcement mesh ( $A_t$ ) is a variable parameter adjusted to give the required strength according to the ULS design methodology.

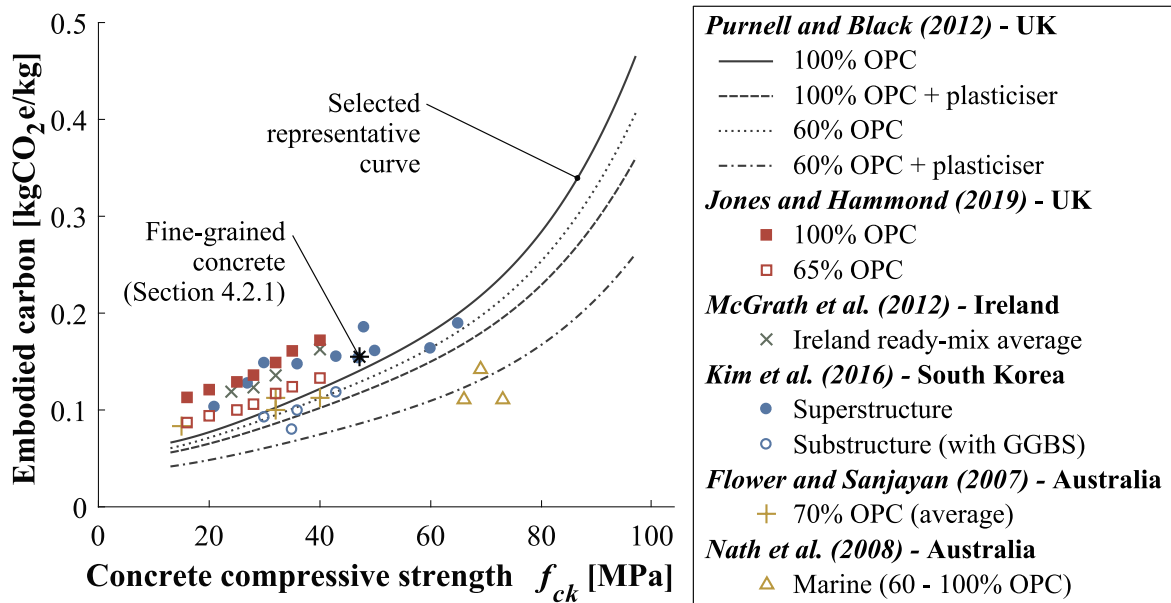


Figure 7.3: Variation of embodied carbon with concrete strength in literature. The relationship assumed in this chapter is highlighted.

A Young's modulus of 64.0GPa, as determined for the AR-glass mesh in Section 4.2.1, is assumed in both orthogonal directions. Although this is an average value, rather than characteristic, the sensitivity of the predicted strength to material stiffness is low (see Section 4.3.2). The composite tensile strength of the textile depends on the reinforcement ratio, with more strength expected at higher volumes of reinforcement (as demonstrated in Section 4.2.3). The lowest measured composite strength of  $f_{tc}=866\text{MPa}$  is assumed throughout this investigation, which was found for the 30mm thick specimens with a reinforcement ratio of 0.435% (Section 4.2.3). This should be a conservative value for higher reinforcement ratios. An additional strength reduction factor of 1.5 was also applied, matching that used by Scholzen et al. (2015b), resulting in a design value of 577MPa (in both directions).

A life cycle analysis carried out by PwC (2016) gives the cradle-to-gate embodied carbon for a variety of glass fibre products, including chopped strands, mats and rovings, with values ranging from 1.23-2.03kgCO<sub>2</sub>e/kg. It is likely that textile reinforcement would be at the upper end of this range due to the two-stage manufacturing process (assembly into yarns followed by textile weaving). A higher value of 2.63kgCO<sub>2</sub>e/kg is given in the EcoInvent database (V2.2) (Frischknecht et al., 2005), whilst Kemna et al. (2011) quotes 3.36kgCO<sub>2</sub>e/kg for raw glass fibres.

The product used for the experiments of this dissertation also included an acrylic coating, although the proportion was not measured. According to the CES database (Granta Design Ltd., 2018), acrylic has an embodied carbon of 4.64-5.11kgCO<sub>2</sub>e/kg. Since this is higher than

that of glass fibres, the coating would therefore create a small increase in the total embodied carbon of the reinforcement.

The chosen value for in this chapter is  $3.0\text{kgCO}_2\text{e/kg}$ . This is the average for glass fibres given by the CES database (Granta Design Ltd., 2018), previously included in Table 2.1, and sits at the upper intermediate of the range of values discussed. A density of  $2700\text{kg/m}^3$  is also assumed throughout. It should be noted that switching from glass to carbon fibres, which might improve fire resistance (Bisby, 2016; Krüger and Reinhardt, 2006), would lead to a significant increase in embodied carbon.

### **Foamed concrete**

The strength and stiffness contributions of the foamed concrete are ignored in the FE model. The key design requirements for this material are therefore to minimise weight and embodied carbon per unit volume.

Table 7.2 shows several examples of low density foamed concrete mixes were found in literature. The total embodied carbon of each was calculated using the constituent material quantities, and the embodied carbon values as given previously in Table 2.1 (along with calcium sulfo-aluminate cement at  $0.822\text{kgCO}_2\text{e/kg}$ , from Jones et al. (2017)). The material used for the construction of Shell 3, as described in Section 5.3.3, is also included for comparison.

The embodied carbon per unit volume is wide-ranging for the materials considered, but is approximately proportional to the Portland cement content. Reducing the overall density of the material (increasing the proportion of voids) reduces embodied carbon per unit volume, albeit with a corresponding strength decrease.

Kearsley and Wainwright (2002), Tikalsky et al. (2004) and Jones et al. (2017) all demonstrated that replacing OPC with fly ash can give significant carbon reductions without loss of strength. It is also possible to eliminate Portland cement entirely by using a geopolymer foam (Zhang et al., 2014). Experiments by Kargin et al. (2017) and Zhang et al. (2015) have created geopolymer foams with densities of  $420\text{-}870\text{kg/m}^3$  and compressive strengths of  $1.3\text{-}4.6\text{MPa}$  using only fly ash, GGBS and small quantities of alkali-activators (sodium hydroxide and sodium silicate). As noted in Section 2.3.1, this potentially leads to significant reductions in embodied carbon.

Another method of levelling the surface above the shell would be to use a granular fill material. Aggregate or recycled (crushed) concrete each have a very low embodied carbon, although the self-weight would be higher than a foam.

A compressive strength of  $0.83\text{MPa}$  was found to be sufficient to avoid crushing in the load testing of Shell 3. A lower strength (and therefore density) might well be adequate,

Table 7.2: Summary of foamed concrete constituents, strengths and calculated embodied carbon values.

C	Constituents* [kg/m <sup>3</sup> ]				Density [kg/m <sup>3</sup> ]		Strength [MPa] [MPa] (age [days])	Embodied carbon [kgCO <sub>2</sub> ] per m <sup>3</sup> per kg	
	FA	CSA	W	S	Wet	Dry			
<b>Section 5.3.3 and Hawkins et al. (2019)</b>									
214	81	-	212	285	844	805	0.83 (9)	198	0.246
<b>Kearsley and Wainwright (2002)</b>									
215	645	0	251	0	1111	810	7.1 (365)	201	0.249
276	552	0	237	0	1065	821	8.6 (365)	256	0.312
415	415	0	249	0	1079	833	8.6 (365)	382	0.459
<b>Tikalsky et al. (2004)</b>									
149	302	0	226	0	678	660	0.71 (28)	138	0.210
311	0	0	185	0	497	490	1.09 (28)	284	0.579
<b>Jones et al. (2017)</b>									
335	0	0	165	0	500	-	0.31 (28)	306	0.611
165	135	35	165	0	500	-	0.42 (28)	180	0.361
200	0	0	100	0	300	-	0.18 (28)	182	0.608
100	80	20	100	0	300	-	0.25 (28)	108	0.361

\*C=cement; FA=fly ash; CSA=calcium sulfo-aluminate cement; W=water; S=sand.

although this would require verification and is likely to depend on the floor finish used. As a conservative upper estimate, a dry density of 800kg/m<sup>3</sup> (similar to that used in testing) is assumed for self-weight. To reflect the potential variability of the fill material and its embodied carbon, three values are considered throughout this chapter: 0kgCO<sub>2</sub>e/m<sup>3</sup>, 100kgCO<sub>2</sub>e/m<sup>3</sup> and 200kgCO<sub>2</sub>e/m<sup>3</sup>.

## Steel

The steel tie was modelled with a Young's modulus of 210GPa. Since the tie diameter is governed by stiffness rather than strength requirements, it is assumed that steel with a suitable yield strength could be specified and no explicit strength checks are therefore carried out.

The steel properties assumed in the design of flat slabs and composite floors are detailed in Sections 7.5.2 and 7.5.3 respectively. A density of 7840kg/m<sup>3</sup> is used in all calculations.

Embodied carbon values for steel were taken from the ICE (Jones and Hammond, 2019), as shown in Table 2.1, and vary depending on the specific product. The steel ties were assumed to have a similar embodied carbon to reinforcing bars, whilst a higher value (that of a galvanised steel sheet) was used for the profile deck of the composite floors (described in Section 7.5.3).

## 7.3 Minimising embodied carbon

The section explores how parameters such as shell thickness, tie diameter, column size, span and rise affect the total embodied carbon of the proposed structural system, based on the design methodology which has now been established, and thus how this can be minimised by the engineer. In all cases, the carbon contribution of the columns is ignored.

### 7.3.1 Optimising shell thickness and tie diameter

The first investigation explores the influence of shell thickness ( $t$ ) and tie diameter ( $d$ ). These variables do not significantly affect the overall size of the structure or influence other building components and architecture. They are therefore likely to be purely within the remit of the engineer to specify. The aim is then to devise a repeatable methodology to optimise these parameters to minimise embodied carbon for any given span, height and column size.

#### Method

In this investigation, a constant span of 8m in each direction and a rise of 800mm was assumed for the shell geometry. Individual designs were generated for ranges of  $50 \leq t \leq 90$  mm and  $30 \leq d \leq 70$ , each in 10mm steps. For each design, the geometric parameters  $a$  and  $b$  (which define the Bézier curve control points, as shown in Figure 3.10) and the pre-strain ( $\epsilon_{tie}$ ) were optimised using the methodology described in Section 3.5.4. The required area of reinforcement and concrete strength were then defined using the ULS design methodology; the former is dictated by bending near the mid-span, and the latter at the column-interface (using the approach described in Section 7.2.1). The total self-weight and embodied carbon were then calculated for each design.

#### Results

Table 7.3 shows the optimised geometry, required material strengths, embodied carbon and self-weight for each combination of  $t$  and  $d$ . It should be repeated that the embodied carbon values given do not reflect an accurate indication of environmental impact, but are used as a simplified cradle-to-gate comparison between designs.

Some variation in the optimal groin vault profile (parameters  $a$  and  $b$ ) occurs between the various designs. However, the greatest physical distance between any two Bézier curves is only 12mm, indicating that the optimal geometry does not vary significantly. However, due to the geometric sensitivity of the structures, these small variations in geometry can have appreciable effects on the magnitudes of bending forces, particularly near the shell-column

interface. The self-weight of the fill is therefore approximately uniform across all designs, making an average contribution of  $1.28\text{kN/m}^2$ .

The optimal tie pre-strain ( $\epsilon_{tie}$ ) is inversely correlated with the tie diameter, as expected, but also increases steadily with shell thickness. This is most likely due to the small additional self-weight.

Table 7.3: Summary of shell designs for various combinations of thickness  $t$  and tie diameter  $d$ , including embodied carbon totals, for a constant span of 8m and depth of  $h=800\text{mm}$ .

Design							Embodied carbon				Self-weight
$t$	$d$	$a$	$b$	$\epsilon_{tie}$	$f_{ck}$	$A_t$	Conc.	Reinf.	Ties	Total	
[mm]	[mm]	[-]	[-]	[mm/m]	[MPa]	[mm <sup>2</sup> /m]	[kgCO <sub>2</sub> e/m <sub>2</sub> ]			[kN/m <sup>2</sup> ]	
50	30	0.477	0.346	1.47	95*	308	106.3	10.1	5.5	122.0	2.36
50	40	0.458	0.358	0.82	78	255	52.9	8.4	9.8	71.2	2.37
50	50	0.442	0.366	0.53	68	225	36.4	7.4	15.4	59.2	2.37
50	60	0.442	0.366	0.38	69	209	37.7	6.9	22.1	66.8	2.37
50	70	0.442	0.365	0.29	69	200	37.7	6.6	30.1	74.5	2.37
60	30	0.463	0.350	1.56	84	259	80.8	8.5	5.5	94.9	2.59
60	40	0.471	0.346	0.88	58	217	31.7	7.2	9.8	48.7	2.59
60	50	0.451	0.358	0.56	49	190	24.8	6.3	15.4	46.5	2.59
60	60	0.438	0.357	0.40	46	172	23.1	5.7	22.1	50.9	2.61
60	70	0.439	0.364	0.30	46	159	23.1	5.2	30.1	58.4	2.60
70	30	0.454	0.356	1.63	78	216	74.1	7.1	5.5	86.7	2.81
70	40	0.457	0.350	0.93	42	185	24.4	6.1	9.8	40.4	2.82
70	50	0.456	0.351	0.60	41	156	23.8	5.1	15.4	44.4	2.82
70	60	0.441	0.358	0.42	38	142	22.2	4.7	22.1	49.0	2.82
70	70	0.436	0.364	0.31	37	132	21.6	4.4	30.1	56.1	2.82
80	30	0.435	0.380	1.69	76	177	78.3	5.8	5.5	89.7	3.02
80	40	0.450	0.356	0.97	39	157	26.0	5.2	9.8	41.0	3.03
80	50	0.454	0.350	0.63	35	136	23.5	4.5	15.4	43.4	3.04
80	60	0.443	0.357	0.44	34	121	23.0	4.0	22.1	49.1	3.04
80	70	0.433	0.361	0.33	34	110	23.0	3.6	30.1	56.7	3.05
90	30	0.439	0.374	1.75	76	172	88.1	5.7	5.5	99.3	3.24
90	40	0.437	0.366	1.01	38	130	28.5	4.3	9.8	42.6	3.25
90	50	0.445	0.354	0.66	33	114	25.2	3.8	15.4	44.3	3.26
90	60	0.445	0.352	0.47	31	99	23.9	3.3	22.1	49.3	3.26
90	70	0.439	0.356	0.35	31	90	23.9	3.0	30.1	57.0	3.27

\*concrete strength exceeds Eurocode limit (design is approximate)



The individual carbon contributions from the concrete, reinforcement and ties are shown graphically in Figure 7.4. The shell concrete typically makes the largest contribution to total embodied carbon, with the fill ignored. The required concrete strength ( $f_{ck}$ ) is inversely correlated with both shell thickness and tie diameter. The carbon contribution, which also takes shell thickness into account, is therefore approximately uniform across a wide range of  $t$  and  $d$  values. Only at the lowest thicknesses and diameters does the embodied carbon increase due to large increases in the required concrete strength.

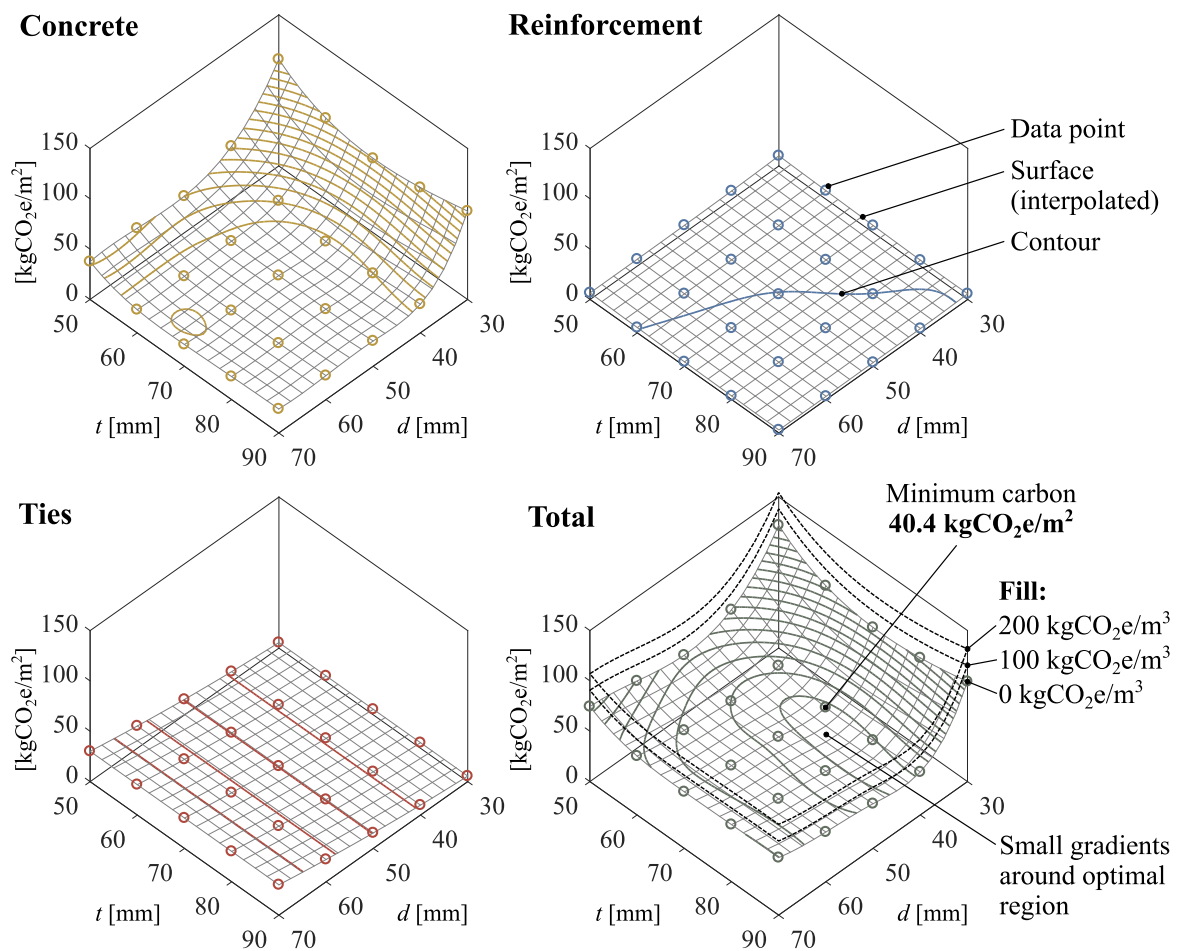


Figure 7.4: Variation of embodied carbon with shell thickness  $t$  and tie diameter  $d$  for a span of 8m and depth of  $h=800\text{mm}$ .

The contribution from the reinforcement is typically very small. Increasing both  $t$  and  $d$  reduces the required area of reinforcement, due to a greater lever arm and reduced mid-span bending respectively. This creates a highly variable reinforcement ratio, which might be problematically small in some cases. As well as providing the necessary strength, the reinforcement ratio must also be sufficiently large to ensure that cracks are small and closely

spaced, and that there is sufficient post-cracking deformation capacity to provide robustness. This topic is discussed in more detail in Section 7.4.1, where a minimum reinforcement ratio is introduced.

The embodied carbon of the ties scales with the square of the diameter, and therefore varies considerably across the range of sizes considered. At  $d = 70\text{mm}$ , it can overtake concrete as the largest carbon contributor. The fill volume is approximately constant across all values of  $t$  and  $d$ , varying only due to small fluctuations in the parameters  $a$  and  $b$ , and its carbon contribution therefore depends only on the material itself. The bottom right surface of Figure 7.4 shows the total embodied carbon, and indicates the additional contribution of a fill materials with  $100\text{kgCO}_2\text{e/m}^3$  and  $200\text{kgCO}_2\text{e/m}^3$ . These add an average of  $16.4\text{kgCO}_2\text{e/m}^2$  and  $32.7\text{kgCO}_2\text{e/m}^2$  respectively to each design.

The lowest carbon design features a 70mm thick shell with 40mm diameter ties, and has a total embodied carbon of  $40.4\text{kgCO}_2\text{e/m}^2$ , with the fill ignored, or  $56.8\text{kgCO}_2\text{e/m}^2$  and  $73.2\text{kgCO}_2\text{e/m}^2$  with fill materials of  $100\text{kgCO}_2\text{e/m}^3$  and  $200\text{kgCO}_2\text{e/m}^3$  respectively. It can be seen that the fill potentially makes up a significant proportion of the total embodied carbon. For this design, serviceability deflections of  $\delta_{tot} = 5.0\text{mm}$  and  $\delta_{live} = 16.4\text{mm}$  were calculated. These are both well within the respective limits of 40.0mm and 22.2mm, and the design is therefore governed by strength, rather than serviceability.

The topography of the total embodied carbon surface dictates how a methodology for minimising this might be best approached. The total embodied carbon is relatively consistent across a wide range of  $t$  and  $d$  values. This is a useful result for design, since a near-optimal solution will have a similar embodied carbon to the optimal. For example, choosing a smaller shell thickness than optimal might be desirable since the self-weight and total height are reduced. Alternatively, the thickness could be increased to maximise stiffness and natural frequency. Furthermore, the optimal shell thickness is approximately constant across all values of tie diameter, and vice versa, which means that each parameter could be optimised independently in order to simplify the design process.

### Minimal carbon design sequence

The previous investigation has shown the influence of  $t$  and  $d$  on embodied carbon. For each combination, the groin vault profile was optimised to ensure the most efficient operation of the shell. In order to correctly assess the influence of other variables, such as span, depth and column size, optimal values of  $t$  and  $d$  should also be found in each case. This could be done by exploring wide ranges of  $t$  and  $d$ , generating plots as shown in Figure 7.4. However, since each data point requires shape optimisation as well as ULS design of the section, with all load

patterns being analysed at all times, this is potentially impractical in terms of computation time and design effort.

A repeatable strategy for finding values of  $t$  and  $d$  which are acceptably close to optimal was therefore proposed, which includes the following steps:

**1. Predefine span, depth and column size.**

**2. Estimate initial values of  $t$  and  $d$ .**

- (a) Based on previous experience, or simplified analytical relationships (described in Section 3.3) based on expected values of concrete strength and tie stress.

**3. Optimise vault profile approximately, using a rigid tie.**

- (a) Create rigid tie with zero pre-strain (to eliminate  $d$  and  $\varepsilon_{tie}$  variables).
- (b) Set the geometric parameters  $a$  and  $b$  using genetic optimisation algorithm (see Section 3.5.4).

**4. Optimise shell thickness.**

- (a) Increment  $t$  by 5mm.
- (b) Calculate required  $f_{ck}$  and  $A_t$  values using the ULS design approach.
- (c) Calculate embodied carbon, considering concrete and reinforcement contributions only.
- (d) Repeat steps (a) to (c) until value of  $t$  is found which minimises embodied carbon.

**5. Optimise tie diameter.**

- (a) Reinstate tie with finite stiffness.
- (b) Increment  $d$  by 5mm.
- (c) For each value of  $d$ , set  $\varepsilon_{tie}$  to minimise bending strain energy envelope, then calculate required  $f_{ck}$  and  $A_t$  values using the ULS design approach.
- (d) Calculate total embodied carbon.
- (e) Repeat steps (b) to (d) until value of  $d$  is found which minimises embodied carbon.

**6. Final design.**

- (a) Redefine  $a$  and  $b$  using genetic optimisation algorithm, for chosen values of  $t$  and  $d$ .

- (b) Calculate required  $f_{ck}$  and  $A_t$  values using the ULS design approach.
- (c) Calculate total embodied carbon.
- (d) Verify serviceability performance.

This is a linear and repeatable process. Simultaneous optimisation of  $a$ ,  $b$  and  $\epsilon_{tie}$  is avoided, since this is the costliest procedure in terms of computational time. The additional complexity of a non-rigid tie, which requires adjustment of pre-strain in every new scenario, is introduced only after the thickness has already been set.

Several approximations and assumptions are relied upon. Firstly, it is assumed that the optimal shell thickness is independent of tie stiffness, and can therefore be set using an infinitely stiff tie. Constant values of  $a$  and  $b$  are also used throughout steps 4 and 5, meaning that the shell profile is not always optimal. It is also proposed that steps 3 to 5 are carried out at a lower element density to further increase speed.

The procedure was implemented for the scenario previously shown in Figure 7.4 in order to compare its prediction of optimal  $t$  and  $d$  values with those previously found. The resulting design features  $t = 80\text{mm}$  and  $d = 40\text{mm}$ , corresponding to a total embodied carbon of  $41.0\text{kgCO}_2\text{e/m}^2$  (ignoring fill). Four neighbouring solutions were also assessed with  $t$  and  $d$  modified by  $\pm 5\text{mm}$ , revealing small fluctuations in total carbon ( $<1.6\%$ ). However, the lowest solution remained that shown in Figure 7.4, with  $t = 70\text{mm}$ ,  $d = 40\text{mm}$  and  $40.4\text{kgCO}_2\text{e/m}^2$ . This is  $2.4\%$  smaller than the value found using the proposed methodology. In this case, the method does not find the lowest carbon solution, but one which is very close to it.

A second scenario was also investigated, again to test the proposed method, featuring the same span and rise but with the column size doubled to  $b = 1000\text{mm}$  to create a significant difference to the first test. In this case, the chosen design was  $t = 75\text{mm}$  and  $d = 45\text{mm}$  with an embodied carbon of  $34.2\text{kgCO}_2\text{e/m}^2$ . Again, neighbouring solutions were explored within  $\pm 5\text{mm}$  for both parameters, showing that the chosen solution was (in this case) optimal in terms of embodied carbon. The maximum variation was  $5.4\%$ , indicating again that the embodied  $\text{CO}_2$  solution surface is flat.

These small fluctuations are well within the expected tolerance for total embodied carbon, considering rounding errors on design parameters as well as the approximate nature of the material  $\text{CO}_2$  values themselves. This design procedure was therefore adopted for future investigations.

### 7.3.2 Influence of column dimensions

Previous investigations have assumed a shell-column interface width of 250mm, corresponding to a column size (or column head) of  $b_{col} = 500\text{mm}$ . As this length increases, so does the area of concrete at the shell-column interface. The required concrete strength might therefore be expected to be inversely related to column size. However, since the forces at the interface will also vary with the changing geometry, the precise relationship cannot be readily predicted.

An investigation was therefore undertaken to determine the effect of the column size in detail. For a constant span of  $l = 8\text{m}$  and rise of  $h = 800\text{mm}$ , the column (or column-head) size was varied from 320mm to 1600mm. The choice of column sizes is restricted by the use of a regular mesh, since the span must be divisible by the element length. There is therefore some variation of mesh density between designs.

For each column size, the shells were designed according to the procedure outlined in Section 7.3.3. Figure 7.5 compares the resulting shell forms graphically, highlighting the variation in column size and possible inclusion of a column-head to accommodate this. A summary of the design parameters found in each case is given in Table 7.4, and Figure 7.6 shows the corresponding embodied carbon values. As in previous investigations in this Chapter, it should be noted that some of the calculated reinforcement areas might be below a practical minimum. This issue is discussed in detail in Section 7.4.1.

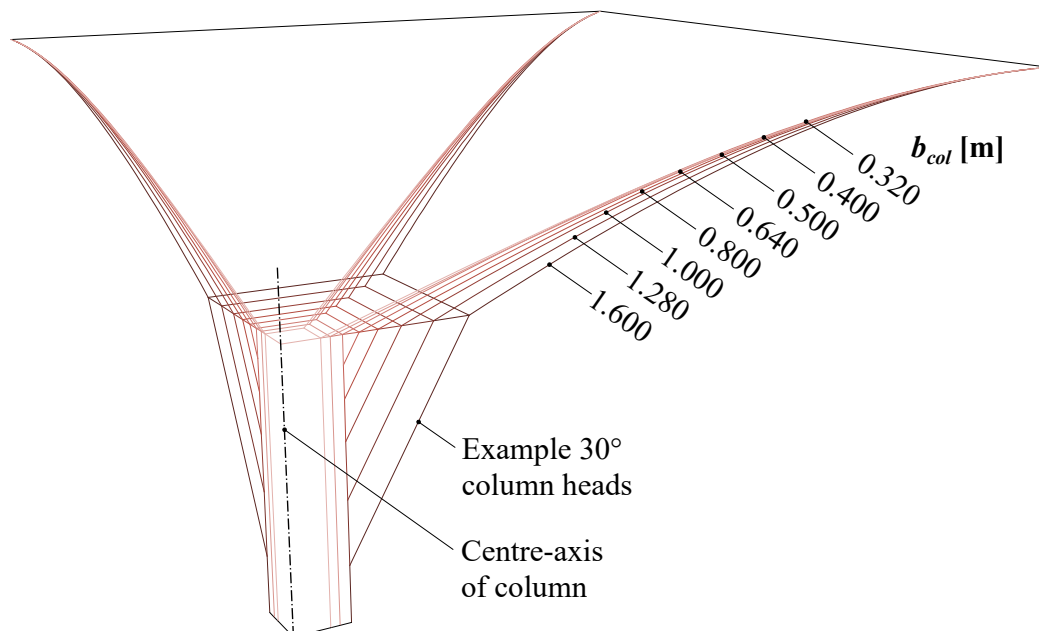


Figure 7.5: Graphical comparison of shell geometries with variable column size  $b_{col}$ , for constant span of 8m and depth of 800mm, as described in Table 7.4.

Table 7.4: Summary of optimal designs for various column sizes. In each case, the span is 8m and depth 800mm.

Column size $b_{col}$ [m]	t [mm]	d [mm]	a [-]	b [-]	$\epsilon_{tie}$ [mm/m]	$f_{ck}$ [MPa]	$A_t$ [mm <sup>2</sup> /m]	Critical load pattern [-]
0.320	130	75	0.398	0.355	0.38	49	70	7
0.400	120	70	0.413	0.343	0.41	43	74	7
0.500	80	45	0.446	0.353	0.78	37	143	7
0.640	85	60	0.465	0.344	0.44	36	104	2
0.800	85	60	0.474	0.340	0.43	30	96	2
1.000	75	45	0.510	0.322	0.68	26	126	1
1.280	80	50	0.539	0.305	0.53	25	98	1
1.600	85	50	0.563	0.295	0.49	23	78	1

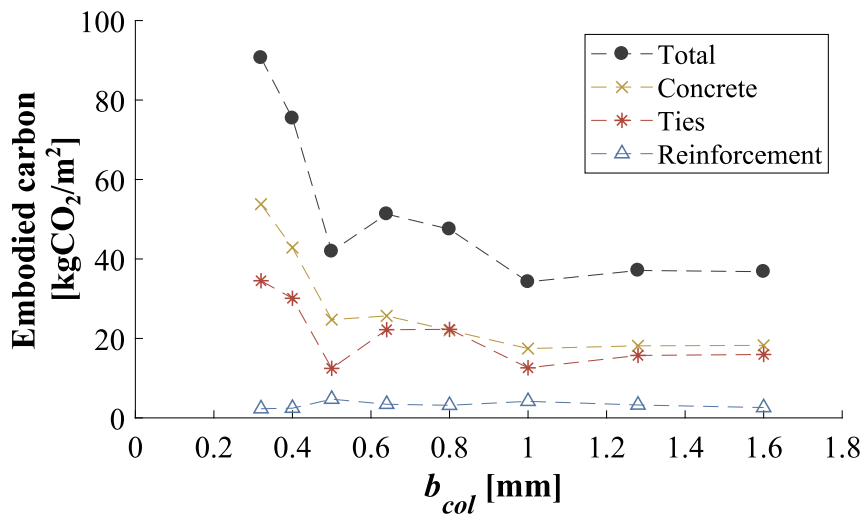


Figure 7.6: Variation of embodied carbon with column size, for constant span (8m) and depth (800mm).

The results show an inverse trend between column size and embodied carbon. This is to be expected, since a smaller column interface results in higher stresses. However, the relationship between column size and total embodied carbon is not smooth. This reflects the complex interaction of force, geometry and materials at this location.

The variable mesh density was investigated and found not to be the cause of these inconsistencies. Instead, it is postulated that variation of the critical load pattern (which determines the strength requirements at the shell-column interface) with column size is the cause of this non-smooth relationship.

For the smallest columns, compressive forces are highly concentrated and the concrete is at risk of crushing. The critical loading pattern is therefore that which maximises the compressive force: a full uniform load (Pattern 7 in Figure 3.6). Conversely, for the largest columns, the design is governed by the minimum loading (Pattern 1). This is because the compressive forces lie significantly below the 'nose' of the utilisation envelope, meaning that the bending capacity is below the peak for a given section. In this case, columns of intermediate size result in load Pattern 2 (asymmetric loading) being critical, in which bending at the shell-column interface is maximised. This points to each particular load pattern having a unique relationship with column size, thus creating a non-smooth overall behaviour.

The two column sizes which stand out as giving a low thickness, tie diameter and embodied carbon are  $b_{col} = 0.5\text{m}$  and  $b_{col} = 1.0\text{m}$ . In these cases, the utilisation was similar for several loading patterns. They exist at crossover points between critical load patterns, and therefore give a more 'balanced', and hence more efficient, solution.

The behaviour at the shell-column interface is complex, and this is reflected in the results of this investigation. This could be explored further in future work. Further investigation might also be required to verify that the design approach introduced in Section 7.2.1, which assumes uniform forces at the shell-column interface, is valid for large column sizes.

For present purposes however, it is acceptable to choose a span to column size ratio which gives an efficient design. The ratio of 16, corresponding to  $b_{col} = 0.5\text{m}$  in this case, is therefore used in the investigations that follow. Should this cause the column to be larger than would otherwise be required, it is proposed that a column head could be used to create an increased width at the shell-column interface.

### 7.3.3 Span, depth and embodied carbon

An investigation was carried out with variable spans of 6-18m. Three different depth to span ratios were investigated:  $h/l=0.125$ ,  $0.100$  and  $0.075$ . A span to column size ratio of 16 was assumed throughout, as shown in Figure 7.7. This allowed the same number of elements to be used in all FE models (a total of 4080 for optimisation procedures, and 16320 for each final design). The thickness, tie diameter and vault profile were then determined using the optimisation procedure described in Section 7.3.1.

The resulting designs are shown in Table 7.5. The optimal shell thickness ( $t$ ) is approximately proportional to the span, but is not significantly influenced by the depth. In contrast, the optimal tie diameter ( $d$ ) is related to both span and depth, since these both influence the thrust. An approximately constant maximum ULS tie stress (of 180-240MPa) is therefore maintained, and the optimal tie pre-strain accordingly shows little variation.

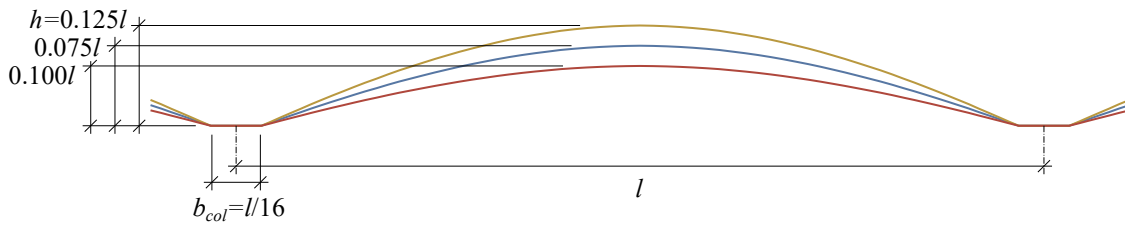


Figure 7.7: Geometric relationships between span, column size and depth for the designs considered, and shown in Table 7.5.

Table 7.5: Summary of design parameters determined for a range of spans and depths.

Geometry input			Design						
Span $l$ [m]	Depth $h$ [mm]	$b_{col}$ [m]	$t$ [mm]	$d$ [mm]	$a$ [-]	$b$ [-]	$\epsilon_{tie}$ [mm/m]	$f_{ck}$ [MPa]	$A_t$ [mm <sup>2</sup> /m]
<b><math>h/l = 0.125</math></b>									
6	750	0.375	65	30	0.446	0.337	0.76	28	110
8	1000	0.500	80	45	0.471	0.352	0.62	33	148
10	1250	0.625	90	50	0.487	0.354	0.83	41	205
12	1500	0.750	115	65	0.481	0.362	0.80	38	202
14	1750	0.875	130	75	0.487	0.365	0.88	42	224
16	2000	1.000	160	90	0.486	0.368	0.90	41	197
18	2250	1.125	175	105	0.488	0.371	0.88	43	217
<b><math>h/l = 0.100</math></b>									
6	600	0.375	70	35	0.424	0.345	0.69	31	97
8	800	0.500	80	45	0.446	0.353	0.78	37	143
10	1000	0.625	90	55	0.457	0.354	0.87	42	184
12	1200	0.750	110	70	0.464	0.357	0.85	43	189
14	1400	0.875	125	85	0.473	0.359	0.84	47	204
16	1600	1.000	150	100	0.469	0.364	0.88	48	208
18	1800	1.125	170	120	0.474	0.365	0.83	49	210
<b><math>h/l = 0.075</math></b>									
6	450	0.375	65	35	0.413	0.348	0.87	43	102
8	600	0.500	80	55	0.421	0.339	0.71	45	115
10	750	0.625	95	65	0.426	0.348	0.85	52	149
12	900	0.750	115	85	0.431	0.355	0.79	53	165
14	1050	0.875	135	100	0.432	0.355	0.84	58	182
16	1200	1.000	160	120	0.435	0.363	0.84	59	189
18	1350	1.125	185	140	0.437	0.366	0.85	61	201

There is a positive correlation between the required concrete strength and span, and a negative correlation with depth. The designs which generate more thrust require stronger



concrete, in addition to a thicker shell. This indicates a more complex scaling relationship than predicted by the simplified compression-only model. The required reinforcement area also correlates with span, although some inconsistency arises due to the specific choices of thickness and tie diameter for each design.

Figure 7.8 shows the calculated embodied carbon for each design, with separate curves plotted for each depth to span ratio. Two sets of results are shown; firstly with the fill ignored and secondly assuming a fill material with  $200\text{kgCO}_2\text{e/m}^3$ .

Should all dimensions be scaled proportionally with span, the expected change in total embodied carbon, per unit floor area, would be linear. However, the results do show some non-linearity, which arises primarily due to the changing concrete strength.

With the fill ignored, there is consistently a reduction in total embodied carbon with increasing depth ( $h$ ). This appears to be a non-linear relationship, with a greater discrepancy visible for smaller  $h$ . The difference also appears to grow larger with increasing span.

The influence of depth is affected by the inclusion of the fill. Since the fill volume is proportional to depth, the result is that the shallower vaults perform comparatively better when the fill material has a higher carbon content. At  $200\text{kgCO}_2\text{e/m}^3$ , lowest carbon solution is given by the intermediate depth to span ratio of 0.100 for all spans above 6m. This implies that the optimal depth is not necessarily the highest, but depends on the fill material being used.

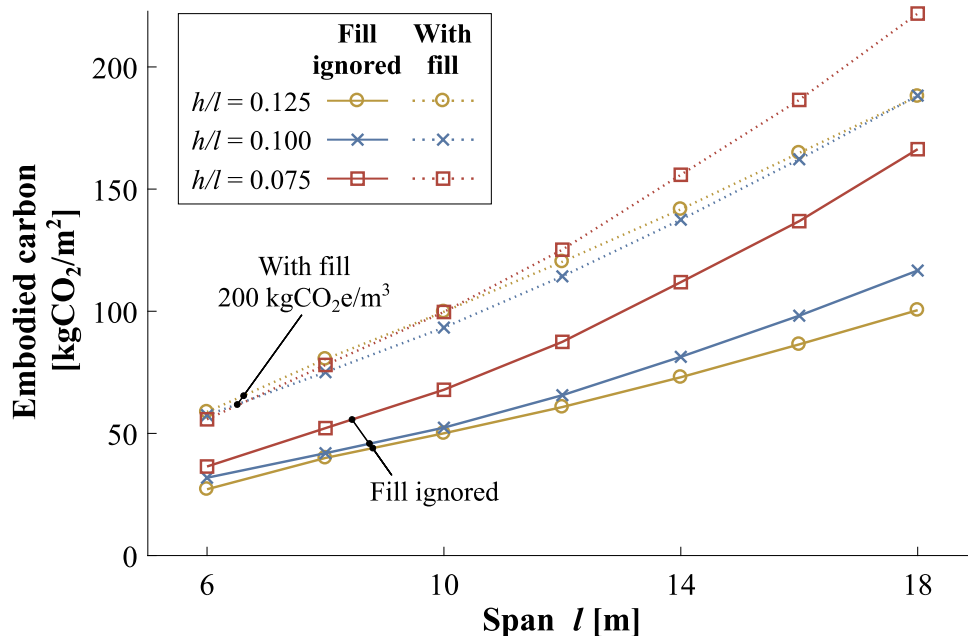


Figure 7.8: Relationship between total embodied carbon and span for various ratios of depth to span.

This investigation featured a constant span to column size ratio of 16. In Section 7.3.2, this was found to give efficient solutions by ensuring that the average compressive stress at the shell-column interface is of the correct magnitude to maximise the bending capacity of the section. Based on this argument, it might therefore be advisable to increase the column size, not only in proportion to the span (as in this investigation), but also inversely with depth. This is because a lower depth increases the compressive shell forces. In this investigation it was found that, for the lowest depth to span ratio of 0.075, the maximum load (Pattern 7) became dominant at the shell interface. The indication is that the shallower vaults could have been made more efficient by using a larger support perimeter. This result might be expected, since there is an intuitive geometric equivalence between a shallow vault with column head and a deeper vault without.

This investigation has shown that the variation of embodied carbon with depth is not simple. Although a greater depth reduces the tie forces and concrete strength requirements, a shallower vault can give a more efficient solution due to the reduction in fill volume, in some circumstances. This has potentially has positive economic implications, since minimising the depth also reduces inter-storey height.

## 7.4 Further design considerations

### 7.4.1 Minimum reinforcement

For the designs generated in the studies so far (given in Tables 7.3, 7.4 and 7.5), the reinforcement area ( $A_t$ ) is typically determined by the bending strength requirements in regions near the mid-span. In some of these cases, particularly when the shell is thick, the resulting reinforcement ratio is very low. This potentially leads to issues of under-reinforcement where, in extreme cases, the tensile capacity of the reinforcement may be smaller than that of the concrete. In this case, the section would fail at first cracking and no additional strength or robustness is provided by the reinforcement.

For steel-reinforced concrete, Eurocode 2 (BSI, 2004a) defines the minimum reinforcement in proportion to the ratio of the tensile strengths of the concrete and reinforcement. A similar approach is proposed in this case, whereby the minimum reinforcement area of each of the top and bottom mesh ( $A_{t,min}$ ) has the same tensile strength as half of the concrete section, according to Equation 7.5:

$$A_{t,min} = \frac{f_{ctm}}{f_{tc}/\sqrt{2}} \frac{t}{2} \quad (7.5)$$

This is analogous to the critical fibre volume fraction commonly discussed for composite materials, including TRC (Brameshuber, 2006). Note that the textile strength is conservatively reduced by a factor of  $\sqrt{2}$ , which corresponds to cracking at  $45^\circ$ , with equal reinforcement in both the  $0^\circ$  and  $90^\circ$  directions (according to Equation 4.10). It is proposed to calculate  $f_{ctm}$  according to Equation 4.12, for consistency with the adoption of the Eurocode concrete model.

For the designs shown in Table 7.5, applying this method results in a considerable increase in prescribed reinforcement in all cases, by between 33% for the thinnest shells and 249% for the thickest. However, the resulting change in total embodied carbon is small, between 4.1% and 11.3% (with fill ignored), since the initial reinforcement contribution is low.

### 7.4.2 Point loads

Until now, only floor area loadings have been considered. Point loads are however also specified for floor design in Eurocode 1 (BSI, 2002a). These are rarely a consideration for slabs, however it is possible that the proposed shells might be susceptible to point loads due to their comparatively low bending strength.

Values of imposed point loads are specified in the UK national annex to Eurocode 1 (BSI, 2002c) for various floor uses. A typical office requires 2.7kN, whilst corridors, landings and staircases must resist a load of 4.5kN. These can be applied at any point on the floor.

An investigation was carried out to determine the possible implications of point loadings on the proposed shells. A single point load of 6.75kN (representing a 4.5kN load with ULS partial factor of 1.5) was applied at various locations on the shell, and the resulting utilisation distributions calculated. The remainder of the shell supported factored dead loading only. It was found that the effect of point loadings were maximised for thinner and shallower shells, and correspondingly the shell with  $l=6\text{m}$ ,  $h=450\text{mm}$  and  $t=65\text{mm}$  was selected from the previous investigation as a worst-case scenario. The reinforcement area was increased from  $102\text{mm}^2/\text{m}$  to  $195\text{mm}^2/\text{m}$  in accordance with Equation 7.5. Any load-spreading effect of the fill was conservatively ignored.

Figure 7.9 shows the envelope of maximum utilisation for a total of 44 possible point load locations, analysed separately, applied over an eighth segment of the shell. In some cases, a local increase in utilisation is visible due to a concentration of bending forces beneath the point load. These are caused principally by local bending forces, however in no case are these large enough to exceed the section strength. The effect of the point loads increases towards the corner where, in reality, the depth of the fill would create significant load-spreading.

By considering a worst-case scenario, this investigation has shown that point loads would not be expected to influence the design of the shell regardless of their location.

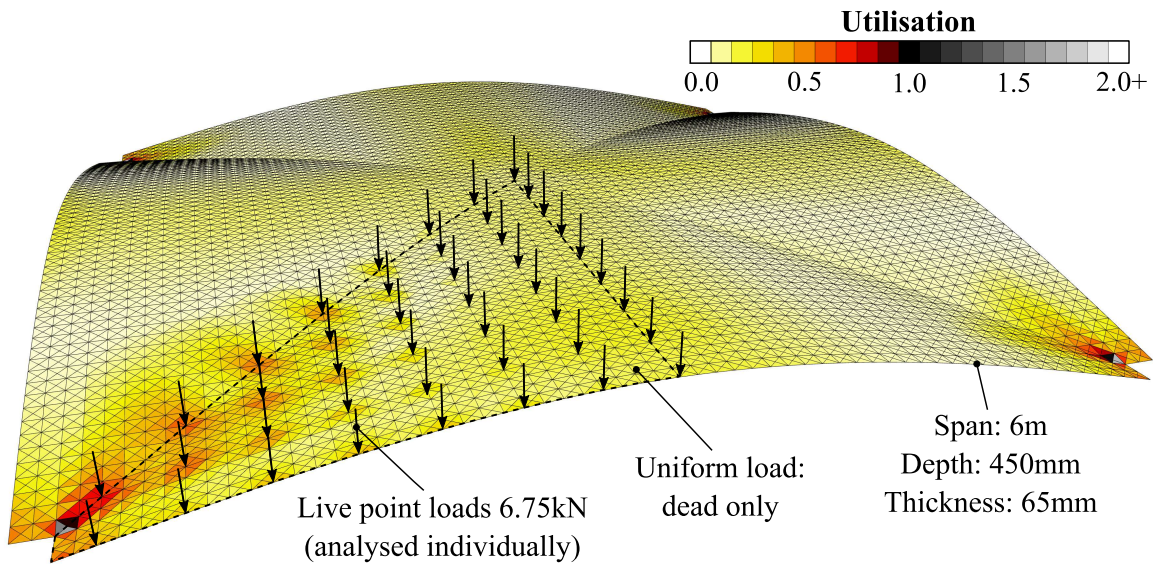


Figure 7.9: Utilisation envelope for multiple point load locations. The thinnest and lowest design featured in Table 7.5 is considered as a worst-case scenario.

### 7.4.3 Differential settlement

Previous investigations in this chapter have considered the supporting nodes at the shell-column interface to be vertically fixed. However, in Section 6.2.3 a high sensitivity to small vertical support displacements was demonstrated in the FE model, particularly regarding shell forces in this region. One means by which support displacement might occur in a real building is through differential settlement of columns, which can arise due to variable ground conditions, uneven loading on foundations or axial column shortening.

An investigation was therefore carried out to determine the possible impact of column settlement on the shell design. An 8m span and 800mm depth was chosen as a typical representative geometry, with the corresponding design parameters included in Table 7.5. Four possible differential settlement patterns were analysed, as shown in Figure 7.10. In each case, the magnitude of settlement was increased from 0-16mm in 2mm increments, and the shell section re-designed using the ULS design methodology. This involved adjusting the concrete cylinder strength to satisfy requirements at the shell-column interface. No changes were made to the thickness, tie diameter, pre-strain or shell geometry. Rotation of the column head about both horizontal axes was restricted, maximising the additional bending moments applied to the shell and therefore representing a worst-case scenario.

Figure 7.10 shows the relationship between required concrete strength and settlement magnitude for each pattern. In all cases, increasing settlement creates additional bending moments at the shell-column interface and therefore a higher concrete strength is required.

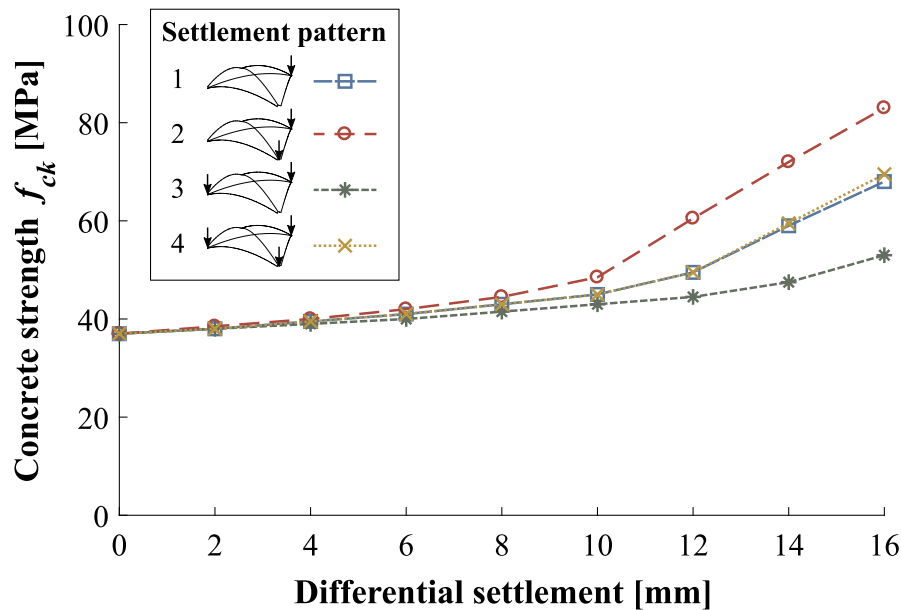


Figure 7.10: Variation of required concrete cylinder strength with the magnitude differential settlement in four patterns.

The reinforcement ratio remains dictated by minimum requirements (Equation 7.5) in all cases. The required concrete strength increase was greatest for settlement pattern 2, where two columns on the same side were displaced. The critical loading pattern switched from maximum (Pattern 7) to minimum (Pattern 1) uniform loading as the settlement was increased, due largely to the changing shape of the failure envelope as concrete strength increases. This is the cause of the non-linearity visible in the results, whereby the required strength begins to increase more rapidly with increasing settlement at approximately 10mm.

These results therefore appear to indicate that small differential settlements could be accommodated with only a moderate increase in concrete strength, but that issues may arise for larger settlements. The significance of this result will vary between projects, but it is possible that more stringent settlement limits (requiring more foundation material) might be required compared to traditional floor structures.

This investigation is, however, preliminary and based on worst-case assumptions. In reality, it is likely that rotation of the columns would attenuate the bending moments arising from differential settlement, as would the non-rigidity of the shell-column interface. Cracking of the concrete would also help to redistribute concentrated forces and accommodate deformation. In flat slab design, differential settlement is rarely considered explicitly since the use of plasticity theory enables redistribution of these forces at the ultimate limit state. It is possible that a similar approach could be justified for the proposed structure, however this would require further investigation.

#### 7.4.4 Stability

As well as supporting vertical loads, floor structures also form part of the load path for resisting lateral forces including wind, geometric imperfections or seismic activity. By acting as a diaphragm, floors transfer these loads to vertical stability structures such as cores, shear walls or external bracing.

Flat slabs have a high in-plane shear stiffness and as such a typical design almost always satisfies these requirements. This is also true of composite floors, with Eurocode 4 simply stating that a minimum total concrete depth of 90mm (with at least 50mm above the steel profile) allows diaphragm action to be assumed (BSI, 2004b). For a curved shell however, this diaphragm strength and rigidity is not guaranteed. The question therefore arises of how this structural requirement can be satisfied using the proposed system.

#### Analysis model

If the diaphragm strength of the shells is to be relied upon, then lateral loads must be considered in design alongside the vertical loads included so far. In preliminary FE analysis, it was found that lateral loads affect the forces at the critical shell-column interface, thereby increasing the required strength of the shell. This effect would vary depending on the location of the shell within the floor-plan, and between storeys, potentially preventing repetition of designs. Instead, an alternative force-path is proposed in Figure 7.11, whereby lateral forces are instead resisted by a truss structure formed by both pre-existing and additional diagonal ties. This is consistent with a lower-bound design approach, and enables diaphragm forces to be ignored in the design of the TRC shell. The truss cantilevers out from the core, and thus the additional diagonal ties are only required in certain locations.

A force ( $F$ ) is applied at each bay of the truss, which is a function of both the wind ( $\omega_w$ ,  $\omega_l$ ) and geometric imperfection ( $W_g$ ) forces, and the number of bays in the y-direction ( $n_y$  in Figure 7.11), as defined in Equation 7.6:

$$F = (\omega_w + \omega_l) l_x + W_g n_y \quad (7.6)$$

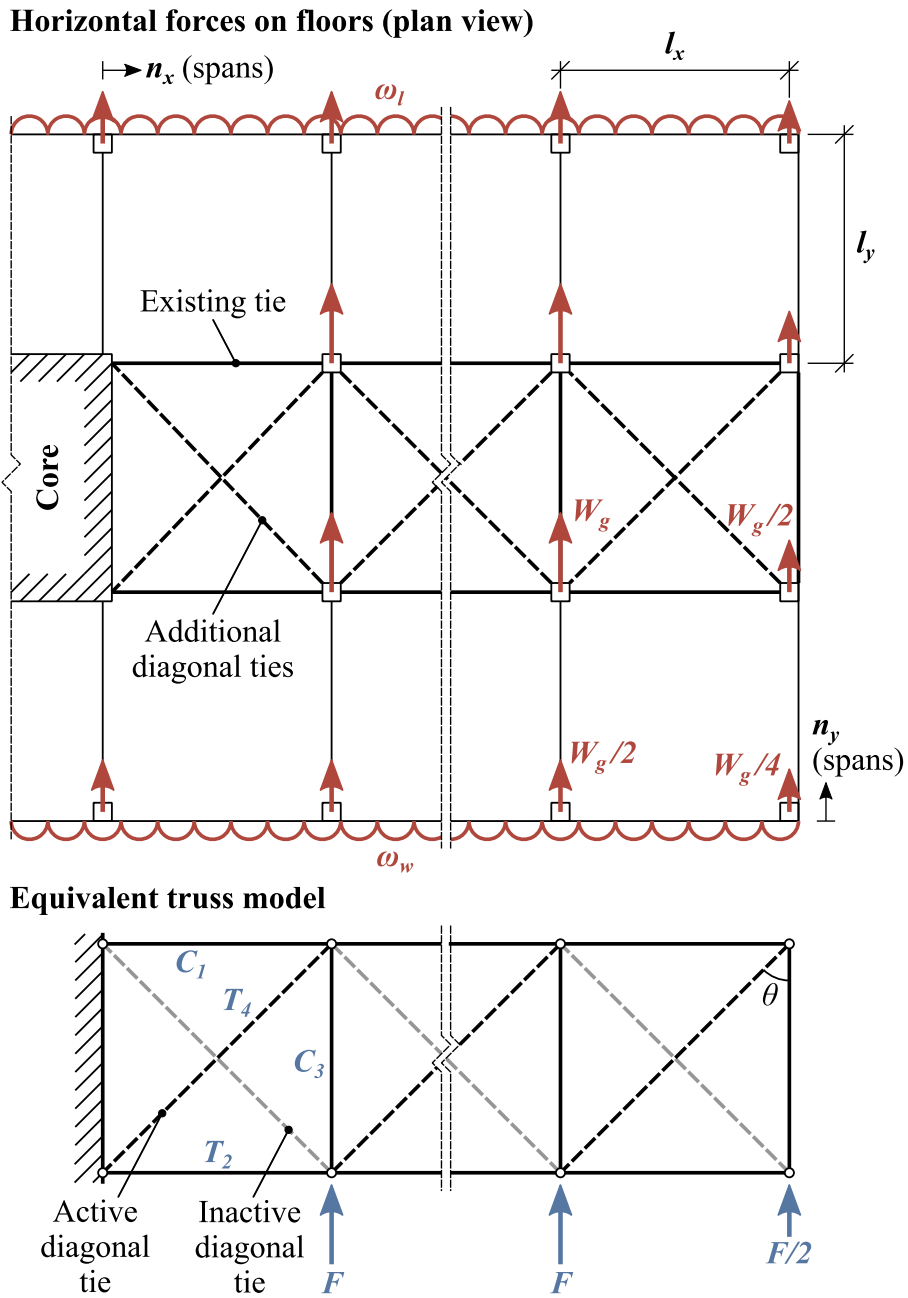


Figure 7.11: Lateral loads acting on a floor (top) and a proposed model for lateral stability using pre-existing ties and additional diagonal ties (bottom).

The resulting forces in the truss members are dependent on the force ( $F$ ) as well as the floor geometry shown in Figure 7.11, calculated as follows:

$$\begin{aligned}
 C_1 &= F \frac{n_x^2}{2} \tan \theta \\
 T_2 &= F \frac{(n_x - 1)^2}{2} \tan \theta \\
 C_3 &= F (n_x - 0.5) \\
 T_4 &= \pm F \frac{(n_x - 0.5)}{\cos \theta}
 \end{aligned} \tag{7.7}$$

Where:

$$\theta = \tan^{-1} \left( \frac{l_x}{l_y} \right)$$

In the pre-existing ties, the forces  $C_1$ ,  $T_2$  and  $C_3$  are superimposed onto the tensile force which already exists from the thrust. For  $T_2$ , the tie must be sufficiently strong to resist the additional tension. For the compressive forces ( $C_1$  and  $C_3$ ), the pre-existing tension must be sufficient to avoid slackening of the tie, and it is therefore conservative to assume a minimum tensile force due to gravity loads (unfactored dead loads only). The diagonal ties carry a tensile force of  $T_4$ , assuming that only one of each pair is active under a particular loading direction.

### Case-studies

This model was tested under a variety of scenarios to assess its validity and implications for design. Wind loads were calculated according to BS EN 1991-1-4 BSI (2002b), assuming a basic wind velocity of 23m/s and suburban terrain (representative of a typical project in Cambridge). Wind pressures depend on height above ground level, with the windward pressure ranging from 0.30kPa at 4m to 0.96kPa at 120m and the leeward pressure from -0.27kPa to -0.84kPa respectively. These pressures were converted to the line loads ( $\omega_w$  and  $\omega_l$ ) using an assumed storey-to-storey height of 4m.

The loads arising from geometric imperfections are proportional to the total axial column forces. These therefore depend on the number of storeys above the floor being analysed, the area supported by each column and the total ULS floor loading. The latter was determined using the same office loadings used in previous investigations, and self-weight values calculated for the shell designs shown in Table 7.5 with a depth to span ratio of 0.1. To find  $W_g$ , this column force is multiplied by the imperfection angle, which was calculated according to Eurocode 2 (BSI, 2004a).

The wind pressure increases with height, dominating at the top of the building, whilst the imperfection force increases with the number of storeys above, and is therefore largest at the



bottom of a building. As a result, the critical floor is either at the top or the bottom of the building, both of which were therefore assessed in each study.

The results from three case studies are summarised in Figure 7.12. Two low-rise buildings were investigated, the first with four storeys and two bays from the core to the edge ( $n_x=2$ ) and the second with an additional storey and bay. The third case study was a 120m tall building with 30 storeys, featuring perimeter columns only. In each case, the maximum tie forces due to lateral loads were calculated for the top and bottom floors for spans ranging from 6-18m. The minimum force in the ties (with lateral loading) are also included, which correspond to the shell designs given in Table 7.12 with depth to span ratios of 0.1. If the compressive forces  $C_1$  or  $C_3$  exceed this force, the tie becomes slack and the stability of the structure is lost.

In all three cases, the tie forces are greater at the bottom floor than the top, showing that geometric imperfections are the dominant lateral loading for diaphragm strength in this case. Both the tie forces caused by lateral forces and the minimum from gravity loads increase with span, however the latter increases more rapidly in all cases. The result is that the risk of tie slackening reduces for larger spans.

The maximum tie forces are highly dependent on the number of bays from the building edge to the core ( $n_x$ ). In Study 2,  $C_1$  exceeds the minimum tie tension for spans below 16m, and thus tie slackening is predicted. This indicates that  $n_x=3$  is too large for this stability system, when cantilevering from a core. A building with a large number of spans may therefore require additional shear walls between which the tie trusses can span. In Study 3, tie slackening is avoided at all spans despite the higher wind loads (top) and column forces (bottom), largely because the truss only extends for one column bay ( $n_x=1$ ). The other compressive force,  $C_3$ , is always smaller than or equal to  $C_1$  and is therefore not critical for design. This is generally true except where  $l_y \gg l_x$ .

The tensile force  $T_2$  creates additional load in the tie. The largest  $T_2$  values are again found for the bottom floor of case-study two, and range from 69-521kN for 6-18m spans. Using the corresponding tie diameters of 35mm and 120mm (from Table 7.5), the increases in tie stress are 72MPa and 45MPa respectively. The maximum ULS stresses in the ties under gravity loading are in the range of 180-240MPa, as noted in Section 7.3.3. This increase is therefore unlikely to affect the required tie diameter, since the total stress remains lower than a typical steel cable or reinforcing bar.

The tensile force  $T_4$  acts in the additional diagonal ties. The maximum value of 1316kN occurs at the bottom floor of case-study three for an 18m span, and corresponds to a tie diameter of 62mm for a yield strength of 500MPa, with partial factor of 1.15. Compared to the designed tie diameter of 120mm, the cross-sectional area is approximately four times

smaller. Since the diagonal ties are only present in half the bays, the total impact on the embodied carbon of the system is therefore likely to be small.

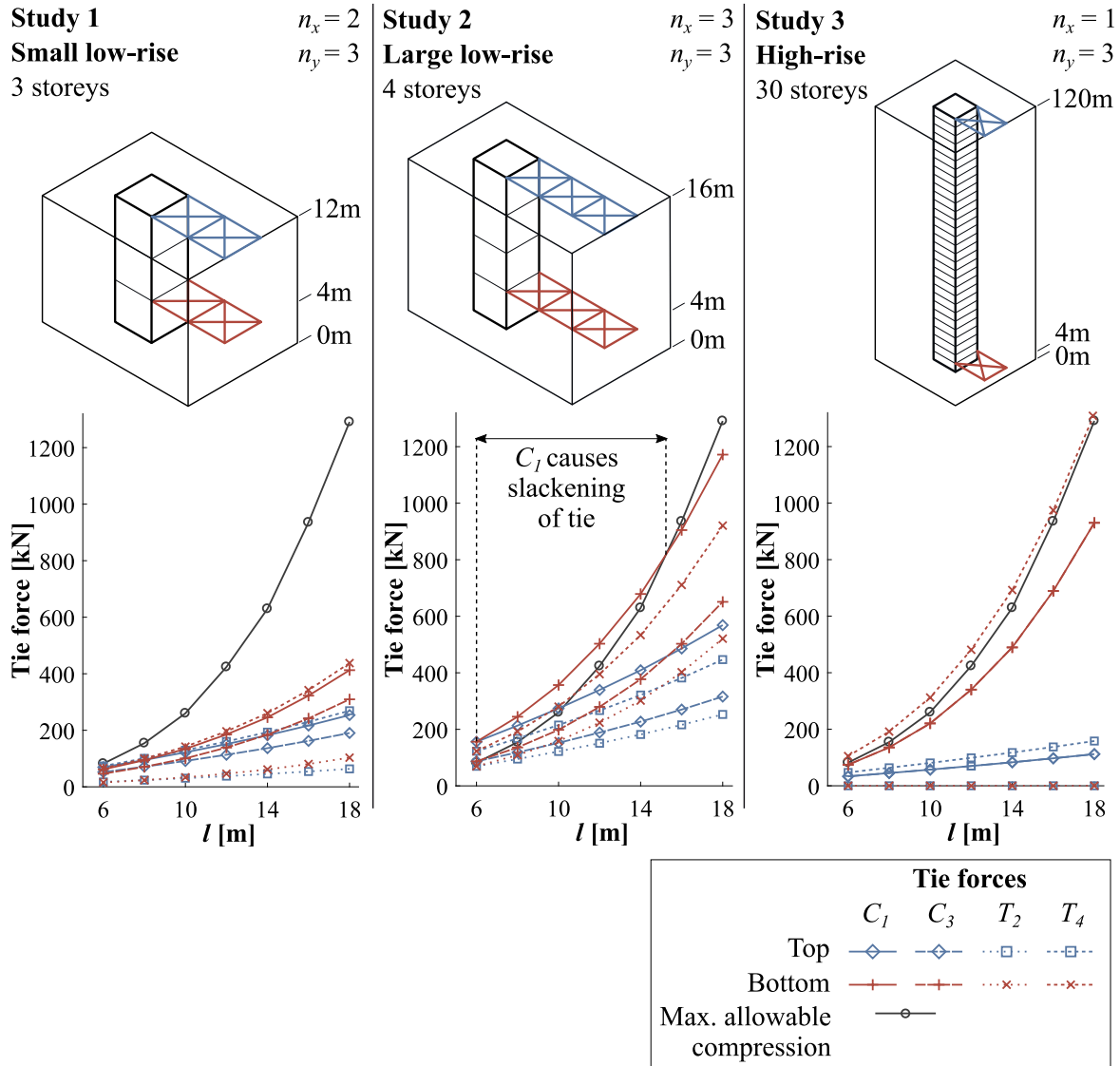


Figure 7.12: Lateral loading case studies, showing maximum additional tie forces due to lateral loading for three buildings of variable span based on the truss model shown in Figure 7.11.

**Conclusions: Lateral stability**

Designing curved shells for diaphragm action is not as straightforward as it is for slabs. However, this preliminary investigation has demonstrated that, in many building scenarios, additional diagonal ties could be an effective means of satisfying lateral strength require-

ments under horizontal loads. In other cases (depending principally on building geometry), additional lateral support structures (e.g. shear walls) might be required compared to an equivalent building with concrete slabs. The applicability of this approach is limited by slackening of existing ties, and therefore larger spans or higher dead loads are, in this instance, favourable.

## 7.5 Comparative case-study

This section compares the proposed system with common alternative floor structures, including reinforced concrete flat slabs and composite floors, which make use of similar materials (concrete and steel). The original hypothesis that greater efficiency can be achieved using shell structures in place of bending elements is therefore tested.

Similar loading and deflection requirements were considered in each case, matching those detailed previously in Section 7.2.2. A simplified floor-plan for a tall tower was assumed, with a central core surrounded by perimeter columns. This creates eight similarly sized bays, as shown in Figure 7.13. Each floor system was designed for spans from 6m to 18m, always equal in both directions. The floor area within the core was ignored in the comparison, as well as the contribution from columns and walls.

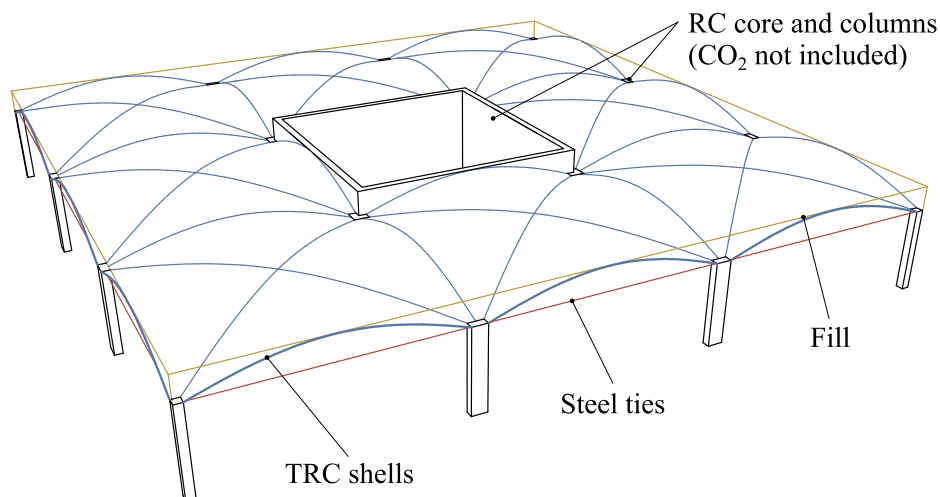


Figure 7.13: Simplified floor-plan for a tower featuring thin-shell concrete floors, showing eight identical pre-cast units spanning onto a reinforced concrete core and peripheral columns.

### 7.5.1 Thin concrete shells

The designs representing the proposed thin-shell system are those previously developed in Section 7.3.3 and given in Table 7.5, with depth to span ratios of 0.1, albeit with the reinforcement increased to satisfy the minimum requirements according to Equation 7.5. The corresponding material quantities and embodied carbon contributions are summarised in Table 7.6. The same design was repeated across all bays, and it was assumed that ties around the periphery of the core were not required. Diagonal ties, which might be used for building stability as described in Section 7.4.4, were not included.

Table 7.6: Summary of material quantities and embodied carbon for representative thin-shell designs, based on those given in Table 7.5 with  $h/l=0.1$ .

Span [m]	Total depth [mm]	$A_f$ [mm/m]	Fill volume [m <sup>2</sup> /m <sup>3</sup> ]	Total Mass [kg/m <sup>2</sup> ]	Embodied carbon			
					Conc.	Reinf.	Ties	Total [kgCO <sub>2</sub> e/m <sup>2</sup> ]
6	670	169	0.127	264	18.5	5.6	10.0	34.1
8	880	218	0.165	318	24.6	7.1	12.5	44.2
10	1090	266	0.204	373	31.3	8.7	14.9	54.9
12	1310	331	0.242	451	39.2	10.9	20.1	70.1
14	1525	399	0.280	517	49.0	13.1	25.4	87.5
16	1750	485	0.319	607	60.3	15.9	30.8	107.0
18	1970	558	0.357	687	70.1	18.3	39.4	127.8

For each span, the proportions of the embodied carbon contributions from each material remain approximately constant. The concrete in the shell makes the largest contribution, followed by the ties and finally the fibre reinforcement. A foamed concrete material with an embodied carbon of 200kgCO<sub>2</sub>e/m<sup>3</sup> would increase the totals given in Table 7.6 by 75-56%, with the greatest increase at smaller spans.

The total ( $\delta_{tot}$ ) and live load ( $\delta_{live}$ ) deflections were also calculated for each design, based on the approach described in Section 7.2.2, and are shown in Figure 7.14. In this case, the total deflection is actually smaller than that under the live loading because of the uplift caused by pre-strain in the ties. In all cases, the live load deflection is significantly smaller than the limit of span/360.

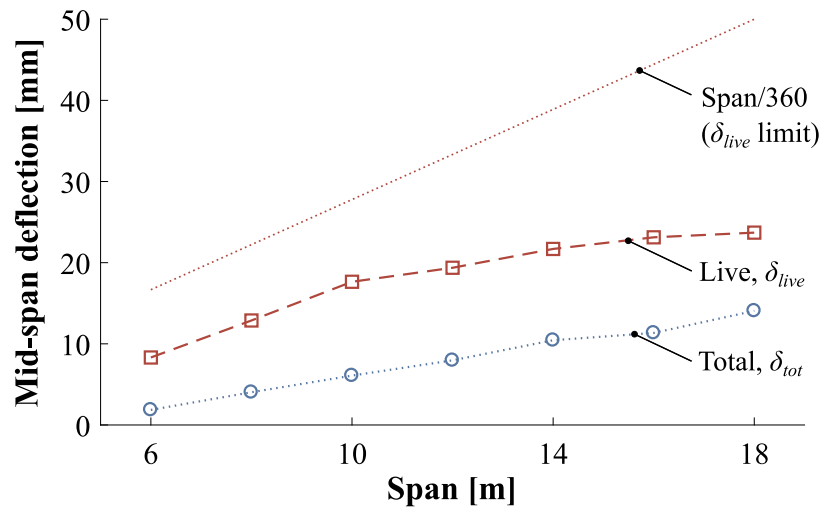


Figure 7.14: Variation of total  $\delta_{tot}$  and live load  $\delta_{live}$  deflections with span for the representative thin-shell floor designs. Both are smaller than the specified limits in all cases.

### 7.5.2 Concrete flat slab

Flat slabs must satisfy bending strength, punching shear, deflection and durability requirements. Although often verified using FE analysis, analytical approaches are commonly used to design flat slabs with regular column arrangements.

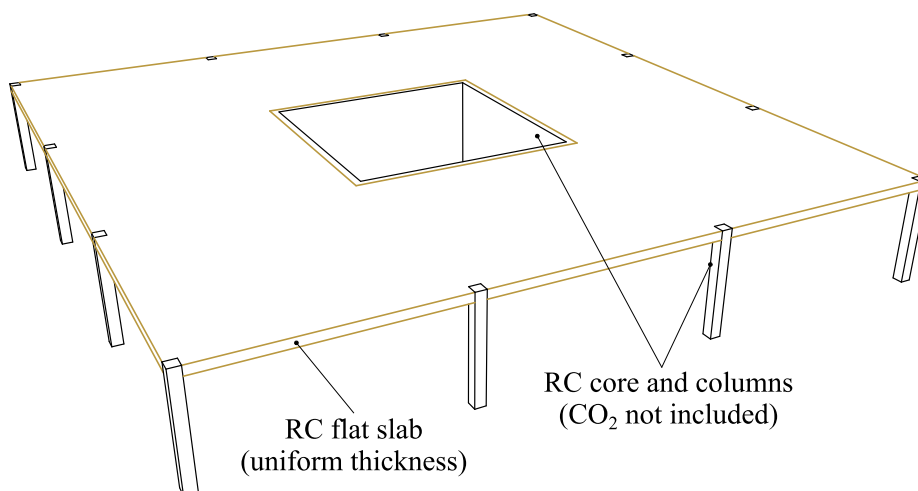


Figure 7.15: Reinforced concrete flat slab layout showing locations of columns and core.

### Design methodology

Each flat slab option was designed according to Eurocode 2 (BSI, 2004a), with guidance from a technical report published by the Concrete Society (2007). The following steps show the process and assumptions, which were implemented in a spreadsheet:

1. **Initial depth estimate:** This was based on a span to depth ratio of 24 (Eurocode 2, Table 7.4N).
2. **Moment distribution calculation:** The equivalent-frame method was employed, which splits the slab into column and middle strips of uniform moment. For self-weight calculation, the assumed density of reinforced concrete was  $2500\text{kg/m}^3$ .
3. **ULS design of reinforcement:** For each region of the slab, the required reinforcement area was calculated assuming full steel yielding and a rectangular concrete stress distribution. Where necessary, this was increased to the minimum value given by Eurocode 2 (Equation 9.1N). The prescribed steel was then found by rounding up to the nearest realistic value based on standard bar diameters spaced at 150, 175 or 200mm. A concrete cylinder strength of  $f_{ck} = 30\text{MPa}$  was assumed for all designs, along with a reinforcement yield strength of 500MPa, each reduced by relevant partial factors. The assumed cover was 25mm.
4. **Serviceability check:** A simplified analysis was used, based on the procedure described in Eurocode 2 (Section 7.4.2), whereby a maximum ratio of span to effective depth is calculated as a function of the concrete strength and the designed mid-span reinforcement. The approach taken was to minimise the slab depth whilst satisfying serviceability, reflecting typical design practice for a tall building. Where necessary, steps 2 and 3 were repeated until the lowest suitable depth was found, to the nearest 10mm.

This approach was quick to implement and provides a code-compliant design, however several limitations should be noted. A buildable design would feature a higher total reinforcement quantity for several reasons. Laps between bars have been ignored, as has punching shear reinforcement at columns. The designs feature different bar sizes and spacings in each direction, layer and region of the slab. In a real design, rationalisation of bar sizes and spacings would further increase the total steel quantity.

It might be possible to achieve depth reductions using a detailed finite element analysis, although whether this would give a lower embodied carbon is uncertain. Optimisation of the concrete strength was not carried out, however it was noted that repeating the design

with stronger concrete resulted in a small increase in total embodied carbon. C30/37 was therefore chosen as a lower-bound of common mixes used in superstructure construction, representing a conservative assumption for comparison.

## Results

Table 7.7 summarises each flat slab design. The total embodied carbon includes contributions from concrete and longitudinal reinforcement only. As expected, the depth, mass and embodied carbon increase with span.

Table 7.7: Summary of design parameters and embodied carbon for each assumed span: flat slab.

Design				Embodied carbon		
Span	Slab depth	Reinforcement quantity	Total mass	Concrete	Steel	Total
[m]	[mm]	[kg/m <sup>3</sup> ]	[kg/m <sup>2</sup> ]	[kgCO <sub>2</sub> e/m <sup>2</sup> ]		
6	220	59.7	541	51.6	26.1	77.8
8	300	64.1	739	70.4	38.3	108.7
10	360	69.6	889	84.5	49.8	134.3
12	450	74.9	1114	105.6	67.1	172.7
14	550	81.6	1365	129.1	89.3	218.4
16	630	88.1	1567	147.9	110.4	258.3
18	760	83.2	1887	178.4	125.0	303.4

The calculated embodied carbon values are within the ranges given in literature. For example, Nadoushani and Akbarnezhad (2015) calculated a value of 59kgCO<sub>2</sub>e/m<sup>2</sup> for flat slabs in a tall building with 5m spans, using embodied carbon values from the first version of the ICE (Hammond and Jones, 2008). This is slightly lower than the equivalent value extrapolated from Table 7.7 (62.3kgCO<sub>2</sub>e/m<sup>2</sup>). At the upper range, De Wolf et al. (2016a) calculates a theoretical value for flat slabs of 230kgCO<sub>2</sub>e/m<sup>2</sup> for a building with 10m spans, 71% larger than the value in Table 7.7.

As noted in Section 2.4.1, there is evidence to suggest that the embodied carbon of flat slabs can be reduced through post-tensioning (Miller and Doh, 2015) or the incorporation of beams and ribs (Griffin et al., 2010).

### 7.5.3 Composite steel deck

Composite steel floors are a common high-rise construction typology, particularly for commercial buildings, favoured for their low weight, large spans, fast construction and simple service integration.

#### Design methodology

Design of composite floors is based on a lower bound approach, assuming load path from the floor to the columns. A single-spanning profiled steel deck transfers floor loads on to secondary beams, which in turn span onto primary beams supported by columns. All of these structures can act compositely with the concrete slab cast above, providing sufficient shear transfer is provided. Figure 7.16 shows the assumed layout of these elements for the floor-plan considered.

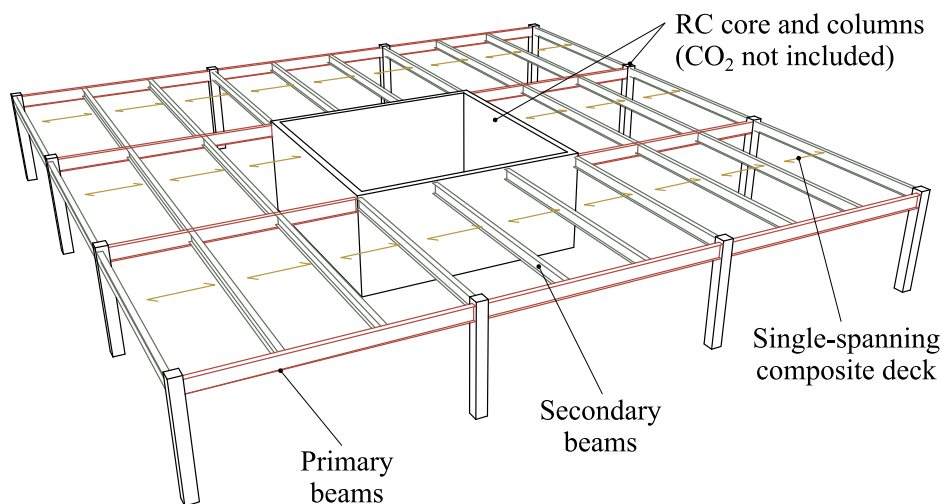


Figure 7.16: Example layout of structural elements for composite floor designs. Three secondary beams are shown per bay, however this number was varied depending on the span considered.

The design was carried out according to Eurocode 4 (BSI, 2004b), following guidance published by the Steel Construction Institute (Simms and Hughes, 2011). Key steps and assumptions are summarised below:

1. **Profile decking (temporary loading):** Firstly, the ability of the deck to support wet concrete during construction was considered. The behaviour of this thin-walled structure at the ultimate load is complex and typically determined through physical testing by the manufacturer, who then provides tables for design. The assumed product



was Multideck 60-V2 manufactured by Kingspan (2018), which has a trapezoidal profile of 60mm depth. This is available in sheet thicknesses from 0.9 to 1.2mm, chosen according to the required span and concrete depth. The number of secondary beams was chosen to provide a span below 4.2m, which is the limit for this type of decking.

2. **Profile decking (permanent loading):** The second design requirement for the decking is to carry the full ULS loads. In this case, the concrete acts compositely with the steel deck, and the design moment is calculated assuming simply supported spans between secondary beams. The minimum concrete depth is 120mm, dictated by cover, acoustic and stability (membrane) requirements. A concrete cylinder strength of 30MPa was assumed, along with a deck steel yield stress of 350MPa. A reinforcement mesh is provided for crack control, with the required area dictated by the concrete depth.
3. **Secondary beams:** These were assumed to be simply supported, carrying a uniform load proportional to the distance between adjacent beams. Section properties for standard hot-rolled universal beams were assumed throughout, with a steel yield strength of 355MPa.

**ULS design:** Ultimate plastic bending capacities were calculated for each beam section, and compared to the ULS mid-span moment. The contribution from the concrete slab depends on the degree of shear connection, which was calculated assuming a pair of 19mm diameter welded shear studs per rib (these studs were not included in CO<sub>2</sub> calculations).

**SLS (deflection):** The total and live load deflections were calculated and checked against the limits defined in Section 7.2.2. This involved using three stiffness values for each beam: construction (steel only), long-term (composite with full concrete stiffness) and short-term (composite with reduced stiffness, assuming a creep factor of 2.5). These were used for self-weight, superimposed dead-loads and live loads respectively. In all cases, the concrete was assumed uncracked.

**SLS (vibration):** A simple dynamic analysis was carried out according to guidelines by the Steel Construction Institute (Smith et al., 2009). Firstly, the static deflection under full permanent loading and 10% live loading was calculated, assuming an increased dynamic concrete stiffness of 38GPa. The natural frequency was then estimated from this value using a simplified formula, and considered acceptable if higher than 4Hz.

4. **Primary beams.** As for the secondary beams, these were assumed to be simply supported at each end. However, instead of uniformly distributed loads, the primary beams support point loads from secondary beams, in addition to self-weight. This affects the bending moment distribution and deflection calculation. Aside from this, the design process was similar to the secondary beams. In ULS design, it was however assumed that full shear connection with the concrete deck was possible in all scenarios, since the number of shear studs is not limited by the rib spacing of the deck.

This process was again implemented in a spreadsheet, and the lightest suitable steel sections were selected in all designs. This gives utilisation ratios close to 1.0, determined by either strength or serviceability.

The design method features several simplifications compared to a buildable design. Firstly, fire requirements were ignored for consistency with the design of the proposed TRC shells, where no equivalent fire consideration had been undertaken. However, the chosen slab thickness of 120mm would not be compliant with typical fire regulations for a high-rise building. For the decking system chosen, minimum slab thicknesses of 130, 140 and 150mm are required for fire resistance periods of 1.0, 1.5 and 2.0 hours respectively. In each case, the self-weight and embodied carbon would increase accordingly. Secondly, additional steel would also be required for connections and shear studs, which were not included in the total embodied carbon calculation. Finally, the simplified dynamic design is indicative only, and would require more detailed assessment in practice.

## Results

Table 7.8 shows each composite floor design, and corresponding quantities are shown in Table 7.9.

The required steel deck thickness varies with the secondary beam spacing, and is governed by the weight of wet concrete during construction (temporary loading). In all cases, the minimum concrete depth of 120mm provided sufficient strength in a composite state (permanent loading). The required steel sections become larger with increasing span. The criteria governing their design also changes, from strength at spans below 8m, through deflection, to vibration at spans above 14m.

The total depth is dictated by the slab thickness and the height of the primary beam. Self-weight is dominated by the concrete slab, and therefore the variation with span is relatively small. Similarly, the contribution to the total embodied carbon from the composite deck remains similar across all spans, whilst that of the steel beams increases considerably and quickly dominates the total value.

Table 7.8: Summary of composite floor designs for each span considered.

Span	Secondary beam spacing	Slab depth	Steel deck thickness	Secondary beam section	Primary beam section
[m]	[m]	[mm]	[mm]	[-]	[-]
6	3.00	120	0.9	254 x 102 x 22 UB	305 x 102 x 28 UB
8	4.00	120	1.1	305 x 127 x 48 UB	406 x 140 x 53 UB
10	3.33	120	0.9	406 x 140 x 53 UB	533 x 210 x 92 UB
12	4.00	120	1.1	457 x 152 x 82 UB	610 x 229 x 140 UB
14	3.50	120	0.9	533 x 210 x 92 UB	838 x 292 x 176 UB
16	4.00	120	1.1	610 x 305 x 149 UB	914 x 305 x 345 UB
18	3.60	120	0.9	762 x 267 x 173 UB	1016 x 305 x 584 UB

Table 7.9: Key quantities, including embodied carbon, for each design featured in Table 7.8.

Span	Total depth	Total Mass	Embodied carbon				Total
			Concrete	Reinforcement	Steel decking	Steel section	
[m]	[mm]	[kg/m <sup>2</sup> ]		[kgCO <sub>2</sub> e/m <sup>2</sup> ]			
6	429	235	20.6	3.1	23.9	21.9	69.5
8	527	245	20.6	3.1	29.2	33.9	86.7
10	653	250	20.6	3.1	23.9	44.7	92.3
12	737	260	20.6	3.1	29.2	57.1	109.9
14	955	265	20.6	3.1	23.9	67.7	115.2
16	1043	290	20.6	3.1	29.2	103.2	156.1
18	1176	312	20.6	3.1	23.9	141.1	188.6

Several studies were also found in literature which calculate the embodied carbon of steel composite floors, for comparison. As for flat slabs, significant variation was found between studies.

Eleftheriadis et al. (2018) measured the embodied carbon of multiple composite floor designs for a school with maximum span of 8.8m, obtaining values of 106-127kgCO<sub>2</sub>e/m<sup>2</sup> for various decking options of 120-125mm thickness. This used a similar design approach to that described in Section 7.5.3, and beams were also selected with utilisation ratios close to 1.0. Using linear interpolation, the corresponding value found in this investigation is 88.9kgCO<sub>2</sub>e/m<sup>2</sup>, 16% less than the minimum value found by Eleftheriadis et al. (2018). This might be a result of the higher live load of 4kN/m<sup>2</sup> considered. A composite floor spanning 5m in each direction was found to have 56kgCO<sub>2</sub>e/m<sup>2</sup> by Nadoushani and Akbarnezhad

(2015), which is approximately consistent with Table 7.9. However, another study by Gan et al. (2017) gave a value of approximately  $140\text{kgCO}_2\text{e/m}^2$  for the floor structure in a high-rise building with 10.5m maximum spans designed in Hong Kong. This is 45% larger than the equivalent (interpolated) value from Table 7.9.

Much of the variation in embodied carbon between real projects and theoretical designs concerns utilisation ratios. In this investigation, the minimum compliant beam section sizes were chosen, yielding utilisation ratios close to 1.0. In real structures however, average utilisation ratios are below 50% due to a combination of rationalisation, conservatism and the desire for design flexibility (Moynihan and Allwood, 2014). Dunant et al. (2018) showed that 35% additional steel mass is provided above what is required in a typical frame, with a significant corresponding impact on total embodied carbon. However, in this investigation, all three structural typologies have been designed to meet requirements as closely as possible to ensure a reliable comparison,

#### 7.5.4 Performance comparison

Figure 7.17 compares the mass, depth and embodied carbon for the three floor structures. The vaulted floor is significantly lighter than the equivalent flat slab, offering 51% and 63% weight savings at 6m and 18m spans respectively. However, the composite floor is the lightest solution and also has the smallest variation with span, since the self-weight is dominated by the concrete slab. At the smallest span, the TRC shell is only 12.3% heavier than the composite floor, however this discrepancy increases to 120% at 18m. Self-weight would also be expected to influence column and foundation requirements, and therefore a lighter floor system might create further reductions in the total embodied carbon of the building.

The total depth varies significantly between the three options, with the flat slab being the shallowest across all spans. However, a flat slab solution requires an additional depth of perhaps 500mm for services, whilst both other options allow service integration. In this scenario, the composite floor gives the lowest overall height. Whilst the total depth of the TRC shell is large, the floor to ceiling height is highly variable, being smallest at the columns only. For the designs considered, the average total depth is only 22-24% of the maximum. A direct comparison with other solutions is therefore potentially misleading. The depth of the vault might also be reduced (without a significant carbon penalty) by increasing the effective column size, as discussed previously in Section 7.3.3.

The flat slab is the costliest option in terms of embodied carbon in all designs. Assuming a fill material containing  $200\text{kgCO}_2\text{e/m}^3$ , matching that used in Shell 3 (Section 5.3.3), the proposed vaulted system contains 23-34% less embodied carbon. If a zero-carbon fill

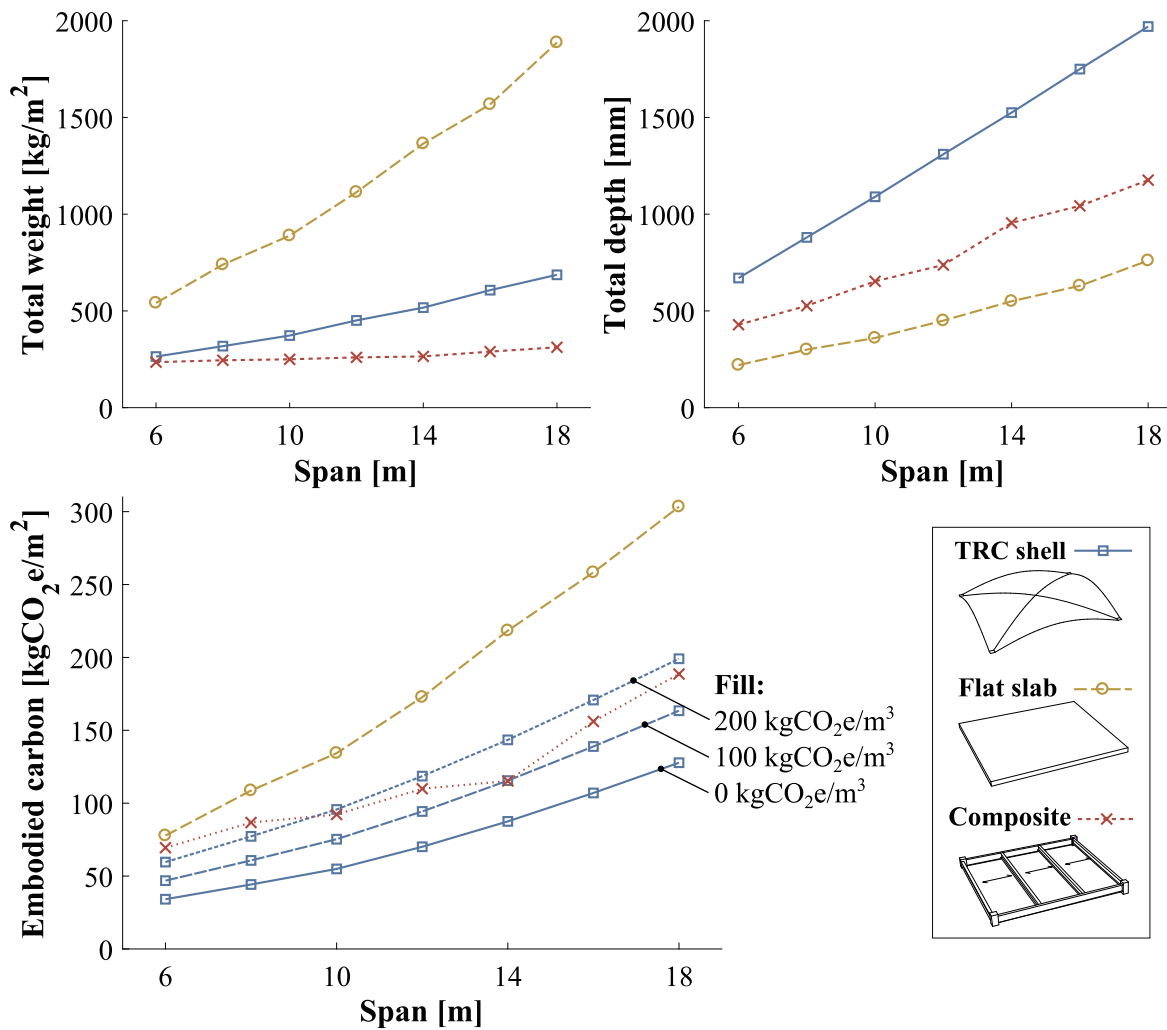


Figure 7.17: Comparison of the proposed flooring system with concrete flat slabs and composite floors, as shown in Figures 7.13 to 7.16, for spans of 6m to 18m.

material was used, the proposed vaulted structure would have 56-58% less embodied carbon than the flat slab. In both cases, the savings increase with span.

Compared to the composite floors, the potential savings are 51% at 6m span and 32% at 18m, with the fill excluded. For a fill material with 200 kgCO<sub>2</sub>e/m<sup>3</sup>, the embodied carbon of the proposed system is higher than the composite floors for spans greater than 8m. This suggests that the advantages of the vaulted system depend on the choice of fill material, with large potential savings possible using a low carbon material such as a geopolymer foam, gravel or recycled (crushed) rubble.

In this investigation, composite floors were found to have a lower embodied carbon than flat slabs across all spans. This result contrasts with some similar studies in literature, which show flat slabs more favourably in terms of embodied carbon or energy (Foraboschi et al.,

2014; Griffin et al., 2010; Kaethner and Burridge, 2012). As discussed in Section 7.5.3, this is likely due to the simplified approach taken in this investigation, which ignores issues of fire resistance and construction detailing. The proposed TRC shells might therefore be more advantageous compared to realistic steel designs than those of this investigation, where fire, serviceability and construction requirements are considered in more detail, although this is not guaranteed.

## 7.6 Summary, findings and conclusions

This chapter has built on the design methods, technical understanding and physical test observations of previous investigations to allow detailed assessment of the proposed structural system in practical use. A repeatable design methodology was developed based on the assumption of uniform forces at the shell-column interface. This was used to investigate the influence of various design parameters on total embodied carbon, leading to a linear design process for determining near-optimal solutions. A number of additional design scenarios and considerations were then examined, with the potential impact of each assessed. Finally, the proposed structural system was compared to reinforced concrete flat slabs and composite floors, using a realistic design scenario, for spans of 6-18m.

Key findings are outlined below:

- Using the proposed design methodology, the variation of total embodied carbon is small for a range of shell thicknesses and tie diameters. It is therefore possible to define a linear process for generating near-optimal designs.
- Maximising the structural depth of the shell does not necessarily lead to a lower total embodied carbon, as might be expected from the reduced thrust, due to the greater volume of fill material required.
- Point loads are unlikely to be critical in the design of any part of the shells.
- The use of thin-shells can impact overall building stability, since a high diaphragm stiffness is not guaranteed. In many scenarios, a small number of additional diagonal ties can be used to provide this structural function.
- The fill material, which is non-structural, has a greater impact on the total embodied carbon of the proposed system than initially anticipated.

- The proposed system shows potential for significant savings in embodied carbon compared to flat slabs and, to a lesser extent, composite steel floors. These can be maximised through the use of a low-carbon fill material.

**Conclusions: Chapter 7**

Thin-shells can satisfy the structural requirements of multi-storey buildings whilst considerably reducing embodied carbon compared to traditional flooring systems, despite the conservative assumptions of the design methodology established in this dissertation. Savings in the region of one half are feasible when using a low-carbon fill material.





# Chapter 8

## Conclusions and future work

The aim of this project was to explore the potential of thin shells as low-carbon and practical alternatives to typical floor structures in multi-storey buildings, switching the principal load-resisting mechanism from bending to membrane action.

Following an investigation into sustainable materials and construction methods, a solution was proposed consisting of pre-cast TRC shells with a foamed concrete fill and prestressed steel ties. A series of analytical, computational and experimental investigations were then carried out, leading to refinement of the system and the establishment of a design methodology incorporating a novel theoretical framework.

This final chapter summarises the conclusions of this dissertation, their implications and potential for future work. The initial objectives set out in Section 1.3 are also revisited.

### 8.1 Proposed structural system

**Objective:** *To understand the construction techniques, structural behaviour and environmental impacts of various materials, and thereby propose a practical and efficient structural system with sustainable potential.*

The materials and layout of the proposed system were established using the findings of the literature review, and maintained throughout the investigations of this dissertation. TRC was selected for its efficient use of reinforcement and suitability for the manufacture of thin shells, which was demonstrated by the successful construction of prototype shells. A high compressive strength, robustness and deformation capacity was achieved using TRC, making this a well suited material for this application. The system makes sparing use of materials with a higher embodied carbon, and thus the objective to create a practical, efficient and

sustainable system was met. However, several modifications might be explored in future work.

The quantity of reinforcement needed to satisfy strength at ULS was found to be very low compared to typical TRC applications, and less than a feasible minimum in most design scenarios. This under-utilisation of material is a potential inefficiency, and indicates that an unreinforced shell might be technically feasible. Whilst this would simplify construction and recycling, the risk of brittle failure would likely make this infeasible. Since the embodied carbon contribution of the reinforcement was low compared to the steel and cement used in the system, its inclusion remains recommended.

The fill is an essential component of the system for practical use, and was demonstrated to improve structural performance primarily through load spreading. However, for analysis and design, it can conservatively be ignored. Although foamed concrete is lightweight and can be applied quickly in large volumes, its contribution to the total embodied carbon of the system was greater than initially anticipated. This means that considerable savings could be made by switching to a low-carbon fill material such as mass-concrete, geopolymer or recycled rubble. Whilst this might add self-weight, an increased dead load could be structurally beneficial for the shell due to the reduced influence of variable loadings. A granular material might also provide vibration and acoustic damping, should these be of concern.

Detailed design considerations for practical application are yet to be considered, including impacts on building services, interior acoustics and architectural flexibility, which might be subjects of future investigations.

Detailed consideration of alternative materials was beyond the scope of this project, however these could be proposed based on the findings made. Timber can sometimes be a carbon-negative building material, and also balances good compressive strength with flexural capacity. This might make it suitable as a direct replacement for TRC in this application. Although timber is significantly less stiff than uncracked concrete, this would be unlikely to cause deflection problems (due to the low influence of shell stiffness on overall deformation). Assembly of smaller segments could also be easier in timber than concrete, facilitating road transportation of pre-cast sections from factory to site. This switch of material would alter the necessary analysis and construction approaches, although this dissertation could act as a starting point. From a sustainability perspective, the nature of the optimisation problem is fundamentally changed, or even inverted, when using a carbon-negative material. Rather than reducing the use of timber, it is possible that a vaulted system would create new possibilities for long-span timber floors.

## 8.2 Structural behaviour and design

**Objective:** *To explore and interpret the structural behaviour of thin-shell floors and thereby refine the proposal.*

Floors present a potentially unfavourable structural setting for shells, featuring non-rigid supports, variable loading arrangements and a low available depth. However, this project has demonstrated that their high structural efficiency can nevertheless be exploited by using an appropriate design. Several important observations were made regarding the structural behaviour of the system, and these were used to refine the design in line with the initial objective.

The shell geometry is critical to efficient structural performance. Whilst form-finding is an established means of generating efficient compression forms, in this scenario it does not provide the best solutions either for structural performance or fabrication simplicity. In contrast, groin vaults perform well across a broad range of structural criteria, and have further advantages for both construction (with simple formwork requirements) and design (being readily parametrised with a low number of variables). These assets were demonstrated through the successful design, construction and testing of physical prototypes, using an optimised groin vault geometry.

The proposed system derives its strength and stiffness primarily through compressive, arching action, as demonstrated by the high lateral thrust measured in both FE analysis and physical tests. However, bending forces were found to be of critical importance, dictating the peak stresses and the required section strength. Minimising bending forces is therefore an effective means of reducing material requirements. A horizontal restraint of high stiffness is key to limiting vertical deflections and bending stresses within the shell, and a system of prestressed steel ties is an effective means of achieving this. A stiffer tie reduces the bending strength requirements of the shell, and this interplay between compressive and tensile members has implications for efficient design. It leads to a wide range of near-optimal solutions in terms of total embodied carbon, with positive implications for practical design efficiency.

In all design scenarios explored in this project, strength governs the design rather than stiffness. However, other serviceability criteria such as vibration and acoustics were not investigated in detail, and would require further analysis. Since the fill material was found to be unimportant for strength or deflection, it might therefore be selected to provide vibration damping or acoustic absorption should these be of concern.

Future analytical investigations might focus on the behaviour at the ultimate load. The formation of a hinged collapse mechanism is reminiscent of unreinforced masonry structures,

albeit with many closely spaced cracks rather than isolated ones. Although this behaviour was replicated using a continuous FE model, this raises the possibility that an alternative approach to structural modelling, featuring rigid bodies with hinged mechanisms, might also provide insight at the ultimate load.

### 8.3 Construction

**Objective:** *To assess manufacturing methods through physical prototyping.*

Simplicity of construction was considered at the outset for the proposed system, and is one of the key advantages over many current examples of efficient concrete floor structures. Using a surface of uniform thickness, without ribs and with singly curved geometry, greatly simplifies formwork requirements, and the number of construction processes is minimised by using only two layers of reinforcement. This enabled prototype formwork and TRC shells to be constructed entirely by hand, albeit with some initial quality issues. Manual construction methods also led to geometric errors, but these were measured and shown to have only moderate structural consequences.

Significant improvements in construction speed and accuracy could be achieved for full-scale manufacture. Spraying can be used to create thin, uniform layers of fine-grained concrete, and the high speed and good compaction properties of this method have been demonstrated in preliminary tests using fabric formwork (Figure 8.1). If a concrete spraying nozzle was mounted on an automated movable gantry, then large surfaces could be quickly covered to a fine tolerance.

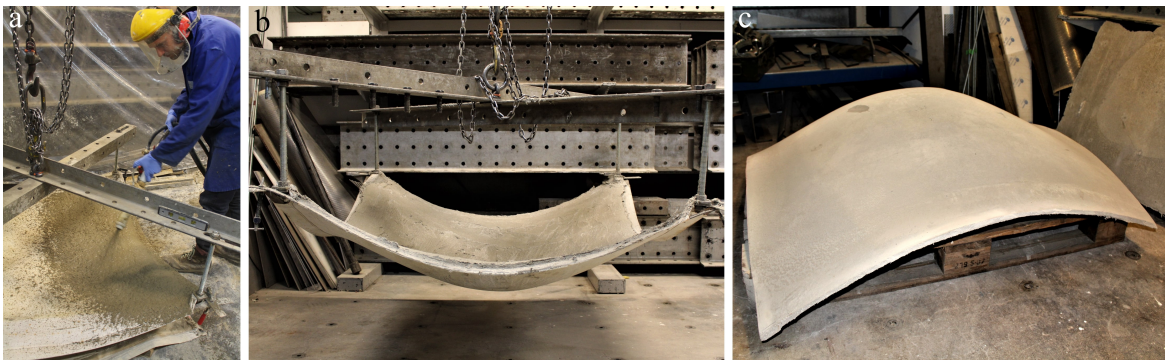


Figure 8.1: Preliminary experiments with sprayed TRC shells, showing a) fast application of material, b) hanging fabric formwork and c) completed shell of approximately 15mm thickness.

Applying the textile reinforcement layers by hand was fast and effective, with the groin vault geometry enabling simple use of pre-cut triangular segments. However, automated

placement of reinforcement might also improve construction speed, particularly at large scale, and could create opportunities for increased efficiency through selective positioning and variable orientation of reinforcement.

Pre-casting offers benefits of control, quality and high speed of assembly. However, since the proposed shells are monolithic over each column bay, their size is too great to be easily transported by road. The proposed solution is therefore to manufacture and store the shells on-site prior to superstructure assembly. It might be possible, however, to overcome this issue by deconstructing each shell into segments which are later connected together, perhaps along the diagonal creases. This would require some modification to both the construction and design methodologies.

## 8.4 Design methodology and theoretical models

**Objective:** *To create a safe, reliable and repeatable design methodology suitable for widespread application.*

Novel design and analysis methods were developed which could be readily applied to other projects featuring free-form TRC shells with large compressive forces and low reinforcement ratios, such as long-span canopies or thin-walled arches. The proposed analysis models offer not only improved accuracy over existing approaches, but also a reduction in physical testing requirements and familiarity to engineers with steel-reinforced concrete design knowledge.

A linear, repeatable design methodology has been developed for the proposed thin-shell flooring system. The simplifying assumptions were shown to create conservative, and therefore safe, predictions of strength compared to the experimental investigations of this project. This was a key component of the initial objective. However, since physical tests were limited to just one type of reinforcement and a small range of thicknesses, further physical testing would be required to determine the model's reliability and range of applicability, particularly at full scale.

Although the initial objectives were achieved, the proposed methodology has potential for further refinement and greater material efficiency. According to the model, the forces at the shell-column interface dictate the required concrete strength. However, the predicted crushing failure was not replicated in the physical tests. This indicates degree of conservatism which has not yet been reliably quantified. The proposed methodology might therefore be considered as a starting point, requiring further verification and with potential for refinement through more detailed modelling and testing.

The consideration of multiple live loading patterns, based on natural vibration modes, was integral to the design and optimisation processes. However, it was not determined explicitly whether the chosen patterns represent worst-case scenarios, or indeed if arbitrary load patterns can realistically arise in real buildings. This could be investigated using influence surfaces, in the former case, or by studying real buildings in the latter. The computational time required for design and optimisation is approximately proportional to the number of load patterns, and could therefore be reduced by analysing only those which are critical for design, and discarding others.

## 8.5 Thin-shell floors for sustainable buildings

**Objective:** *To quantify the potential embodied carbon reductions compared to existing alternatives.*

**Aim:** *To establish whether thin shells, harnessing membrane action, are a viable, practical and low-carbon alternative to typical floor structures in multi-storey buildings.*

The development of a repeatable design methodology enabled an embodied carbon comparison with typical floor structures. The proposed system was shown to offer considerable savings compared to equivalent flat slabs (by 56-58%, with a near zero-carbon fill) and composite floors (by 32-51%). This project has therefore successfully demonstrated that thin-shells are not only feasible and practical, but can offer environmental benefits through their high structural efficiency. The proposed structural system, and the findings made throughout its development, can therefore be steps towards a low-carbon future for building construction.

# References

- Abergel, T., Dean, B., and Dulac, J. (2017). Towards a zero-emission, efficient, and resilient buildings and construction sector: Global status report 2017. Technical report, UN Environment and International Energy Agency.
- Agustí-Juan, I. and Habert, G. (2017). Environmental design guidelines for digital fabrication. *Journal of Cleaner Production*, 142:2780 – 2791.
- Ahnert, R., Krause, K.-H., Maier, E., and Mönck, W. (1987). *Typische baukonstruktionen von 1860 Bis 1960: zur beurteilung d. vorhandenen bausubstanz; Grundlage, Wände, Decken, Dachtragwerke*. Verlag Fuer Bauwesen.
- Alexander, C., Ishikawa, S., and Silverstein, M. (1977). *A pattern language: towns, buildings, construction*, volume 2. Oxford University Press.
- Allwood, J. M., Ashby, M. F., Gutowski, T. G., and Worrell, E. (2011). Material efficiency: A white paper. *Resources, Conservation and Recycling*, 55(3):362–381.
- Allwood, J. M., Cullen, J. M., Carruth, M. A., Cooper, D. R., McBrien, M., Milford, R. L., Moynihan, M. C., and Patel, A. C. (2012). *Sustainable materials: with both eyes open*. UIT Cambridge, Cambridge.
- Allwood, J. M., Cullen, J. M., and Milford, R. L. (2010). Options for achieving a 50% cut in industrial carbon emissions by 2050.
- Anthony, E. J., Brunier, G., Besset, M., Goichot, M., Dussouillez, P., and Nguyen, V. L. (2015). Linking rapid erosion of the mekong river delta to human activities. *Scientific reports*, 5:14745.
- Antoni, M., Rossen, J., Martirena, F., and Scrivener, K. (2012). Cement substitution by a combination of metakaolin and limestone. *Cement and Concrete Research*, 42(12):1579–1589.
- Artec (2015). [www.artec3d.com](http://www.artec3d.com) (accessed June 2019).
- Ashby, M. F. and Jones, D. R. H. (2012). Chapter 15 - probabilistic fracture of brittle materials. In *Engineering Materials I (Fourth Edition)*, pages 219–228. Butterworth-Heinemann, Boston.
- Bahar, R., Benazzoug, M., and Kenai, S. (2004). Performance of compacted cement-stabilised soil. *Cement and Concrete Composites*, 26(7):811 – 820.

- Baker, D. A. and Rials, T. G. (2013). Recent advances in low-cost carbon fiber manufacture from lignin. *Journal of Applied Polymer Science*, 130(2):713–728.
- Banholzer, B., Brockmann, T., and Brameshuber, W. (2006). Material and bonding characteristics for dimensioning and modelling of textile reinforced concrete (trc) elements. *Materials and structures*, 39(8):749–763.
- Banichuk, N., Serra, M., and Sinitsyn, A. (2006). Shape optimization of quasi-brittle axisymmetric shells by genetic algorithm. *Computers & structures*, 84(29):1925–1933.
- Bannister, T. C. (1968). The roussillon vault: The apotheosis of a "folk" construction. *Journal of the Society of Architectural Historians*, 27(3):163–175.
- Bazant, Z. P. (2005). *Scaling of structural strength*. Elsevier.
- Bazant, Z. P. and Planas, J. (1997). *Fracture and size effect in concrete and other quasibrittle materials*, volume 16. CRC press, Florida.
- Beghini, L. L., Carrion, J., Beghini, A., Mazurek, A., and Baker, W. F. (2014). Structural optimization using graphic statics. *Structural and Multidisciplinary optimization*, 49(3):351–366.
- Bentur, A. (2000). Role of interfaces in controlling durability of fiber-reinforced cements. *Journal of materials in civil engineering*, 12(1):2–7.
- Bentz, E. C. (2019). Empirical modeling of cracking in reinforced concrete. *ACI Structural Journal*, 116(3).
- Bisby, L. (2016). Fire resistance of textile fiber composites used in civil engineering. In Triantafyllou, T., editor, *Textile Fiber Composites in Civil Engineering*, pages 169–183. Woodhead Publishing, Cambridge.
- Blaber, J., Adair, B., and Antoniou, A. (2015). Ncorr: open-source 2d digital image correlation matlab software. *Experimental Mechanics*, 55(6):1105–1122.
- Block, P., Ciblac, T., and Ochsendorf, J. (2006). Real-time limit analysis of vaulted masonry buildings. *Computers & structures*, 84(29-30):1841–1852.
- Block, P., DeJong, M., Davis, L., and Ochsendorf, J. (2010). Tile vaulted systems for low-cost construction in africa. *Journal of the African Technology Development Forum (ATDF)*, 7(1):4–13.
- Block Research Group (2019). HiLo - Research & innovation unit for NEST, Dübendorf, Switzerland. Online. <http://block.arch.ethz.ch/brg/project/hilo-research-innovation-unit-dest> (accessed June 2019).
- Bochmann, J., Curbach, M., and Jesse, F. (2017). Influence of artificial discontinuities in concrete under compression load—a literature review. *Structural Concrete*, 2017:1–9.
- Bosoaga, A., Masek, O., and Oakey, J. E. (2009). Co2 capture technologies for cement industry. *Energy Procedia*, 1(1):133 – 140. Greenhouse Gas Control Technologies 9.



- Boyd, S. E. and Rees, H. L. (2003). An examination of the spatial scale of impact on the marine benthos arising from marine aggregate extraction in the central english channel. *Estuarine Coastal and Shelf Science*, 57(1-2):1–16. Boyd, SE Rees, HL.
- Brameshuber, W. (2006). *Report 36: Textile Reinforced Concrete-State-of-the-Art Report of RILEM TC 201-TRC*, volume 36. RILEM publications.
- Brameshuber, W. (2016). Recommendation of rilem tc 232-tdt: test methods and design of textile reinforced concrete: Uniaxial tensile test: test method to determine the load bearing behavior of tensile specimens made of textile reinforced concrete. *Materials and Structures*, 49:4923–4927.
- BREEAM (2018). Technical manual sd5078: Breeam uk new construction 2018. *BRE Global Limited*.
- Brockmann, T. (2007). Mechanical and fracture mechanical properties of fine grained concrete for trc structures. In Grosse, C. U., editor, *Advances in Construction Materials 2007*, pages 119–129, Berlin, Heidelberg. Springer Berlin Heidelberg.
- BSI (2002a). Eurocode 1: Actions on structures (BS EN 1991-1-1:2005) Part 1-1: General actions - Densities, self-weight, imposed loads for buildings. British Standards Institution.
- BSI (2002b). Eurocode 1: Actions on structures (BS EN 1991-1-4:2005) Part 1-4: General actions - Wind actions. British Standards Institution.
- BSI (2002c). UK National Annex to Eurocode 1: Actions on structures. British Standards Institution.
- BSI (2004a). Eurocode 2: Design of concrete structures. British Standards Institution.
- BSI (2004b). Eurocode 4: Design of composite steel and concrete structures. British Standards Institution.
- BSI (2012a). BS EN 15804:2012: Sustainability of construction works. Environmental product declarations. Core rules for the product category of construction products. British Standards Institution.
- BSI (2012b). Fly ash for concrete. Definition, specifications and conformity criteria, BS EN 450-1:2012. British Standards Institution.
- Butcher, L. (2009). Lorry sizes and weights. <https://researchbriefings.files.parliament.uk/documents/SN00654/SN00654.pdf> (accessed June 2019).
- Butler, M., Mechtcherine, V., and Hempel, S. (2010). Durability of textile reinforced concrete made with ar glass fibre: effect of the matrix composition. *Materials and structures*, 43(10):1351–1368.
- CEN (2000). EN 206-1: Concrete - Part 1: Specification, performance, production, conformity. European Committee for Standardization.
- Chawla, K. K. (1998). *Fibrous materials / K.K. Chawla (Department of Materials & Metallurgical Engineering, New Mexico Institute of Mining and Technology)*. Cambridge solid state science series.

- Chilton, J. (2010). Heinz Isler's infinite spectrum: Form-finding in design. *Architectural Design*, 80(4):64–71.
- Chilton, J. and Isler, H. (2000). *Heinz Isler: The Engineer's Contribution to Contemporary Architecture*. Thomas Telford, London.
- Chiozzi, A., Milani, G., and Tralli, A. (2017). A genetic algorithm nurbs-based new approach for fast kinematic limit analysis of masonry vaults. *Computers & Structures*, 182:187–204.
- Christensen, J. (2018). *Emissions Gap Report 2018*. UNEP DTU Partnership. [www.unenvironment.org/resources/emissions-gap-report-2018](http://www.unenvironment.org/resources/emissions-gap-report-2018) (accessed June 2019).
- Chudoba, R., Sharei, E., and Scholzen, A. (2016). A strain-hardening microplane damage model for thin-walled textile-reinforced concrete shells, calibration procedure, and experimental validation. *Composite Structures*, 152:913–928.
- Chudoba, R., Sharei, E., Senckpiel-Peters, T., and Schladitz, F. (2019). Numerical modeling of non-uniformly reinforced carbon concrete lightweight ceiling elements. *Applied Sciences*, 9(11).
- Chudoba, R., Vořechovský, M., and Konrad, M. (2006). Stochastic modeling of multi-filament yarns. I. Random properties within the cross-section and size effect. *International Journal of Solids and Structures*, 43(3):413–434.
- Clarke, L. and Cope, R. (1984). *Concrete slabs: analysis and design*. CRC Press.
- Cole, R. J. and Kernan, P. C. (1996). Life-cycle energy use in office buildings. *Building and environment*, 31(4):307–317.
- Committee on Climate Change (2018). Reducing UK emissions – 2018 Progress Report to Parliament. [www.theccc.org.uk/publication/reducing-uk-emissions-2018-progress-report-to-parliament/](http://www.theccc.org.uk/publication/reducing-uk-emissions-2018-progress-report-to-parliament/) (accessed June 2019).
- Concrete Society (2007). Technical report no. 64: Guide to the design and construction of reinforced concrete flat slabs. *CCIP-022*.
- Couchman, G., Mullett, D., and Rackham, J. (2000). Composite slabs and beams using steel decking: Best practice for design and construction. *SCI PUBLICATION*.
- Crown Estate (2016). Energy, minerals & infrastructure. [www.thecrownestate.co.uk/energy-minerals-and-infrastructure/aggregates/](http://www.thecrownestate.co.uk/energy-minerals-and-infrastructure/aggregates/) (accessed June 2019).
- DAfStb, D. A. f. S. (2003). Din 1045-1:2008-08 concrete, reinforced and prestressed concrete structures - part 1: Design and construction. *Berlin: Beuth*.
- D'Antino, T., Carloni, C., Sneed, L., and Pellegrino, C. (2014). Matrix–fiber bond behavior in pbo frcm composites: A fracture mechanics approach. *Engineering Fracture Mechanics*, 117:94–111.
- Davidovits, J. (2005). *Geopolymer, green chemistry and sustainable development solutions: proceedings of the world congress geopolymer 2005*. Geopolymer Institute. 80-85

- Day, A. (1965). An introduction to dynamic relaxation. *The Engineer*, 219:218–221.
- De Silva, S. S. and Thambiratnam, D. P. (2009). Dynamic characteristics of steel–deck composite floors under human-induced loads. *Computers & Structures*, 87(17-18):1067–1076.
- De Wolf, C., Pomponi, F., and Moncaster, A. (2017). Measuring embodied carbon dioxide equivalent of buildings: A review and critique of current industry practice. *Energy and Buildings*, 140:68–80.
- De Wolf, C., Ramage, M., and Ochsendorf, J. (2016a). Low carbon vaulted masonry structures. *Journal of the International Association for Shell and Spatial Structures*.
- De Wolf, C., Yang, F., Cox, D., Charlson, A., Hattan, A. S., and Ochsendorf, J. (2016b). Material quantities and embodied carbon dioxide in structures. In *Proceedings of the Institution of Civil Engineers-Engineering Sustainability*, volume 169, pages 150–161. Thomas Telford Ltd.
- Deventer, J. S. V., Provis, J. L., and Duxson, P. (2012). Technical and commercial progress in the adoption of geopolymers. *Minerals Engineering*, 29:89 – 104. Sustainability through Resource Conservation and Recycling.
- Dey, V., Zani, G., Colombo, M., Prisco, M. D., and Mobasher, B. (2015). Flexural impact response of textile-reinforced aerated concrete sandwich panels. *Materials & Design*, 86:187 – 197.
- DIN, G. (2016). DIN EN 12602: Prefabricated reinforced components of autoclaved aerated concrete.
- Dini, E. (2006). Method and device for building automatically conglomerate structures. US patent No. US20080148683A1.
- Du, Y., Zhang, M., Zhou, F., and Zhu, D. (2017). Experimental study on basalt textile reinforced concrete under uniaxial tensile loading. *Construction and Building Materials*, 138:88 – 100.
- Duflo, J., Moor, J. D., Verpoest, I., and Dewulf, W. (2009). Environmental impact analysis of composite use in car manufacturing. *CIRP Annals*, 58(1):9 – 12.
- Dunant, C. F., Drewniok, M. P., Eleftheriadis, S., Cullen, J. M., and Allwood, J. M. (2018). Regularity and optimisation practice in steel structural frames in real design cases. *Resources, Conservation and Recycling*, 134:294–302.
- Duxson, P., Fernández-Jiménez, A., Provis, J. L., Lukey, G. C., Palomo, A., and van Deventer, J. S. J. (2007). Geopolymer technology: the current state of the art. *Journal of Materials Science*, 42(9):2917–2933.
- EAB Associates (2018). Foaming agent for lightweight foamed concrete production. [www.eabassoc.co.uk/Foamed-Concrete-Foaming-Agent.php](http://www.eabassoc.co.uk/Foamed-Concrete-Foaming-Agent.php) (accessed June 2019).
- EFCA (2015). *Environmental Product Declaration: Concrete admixtures – Plasticisers and Superplasticisers*. European Federation of Concrete Admixtures Associations Ltd.,

- Eisenbach, P. and Grohmann, M. (2017). Structural implementation of slender concrete shells with prefabricated elements. *Journal of the international association for shell and spatial structures*, 58(1):51–64.
- Elangovan, S. (1990). Analysis of funicular shells by the isoparametric finite element. *Computers & Structures*, 34(2):303 – 311.
- Eleftheriadis, S., Dunant, C. F., Drewniok, M. P., Rogers-Tizard, W., and Kyprianou, C. (2018). Comparative numerical analysis for cost and embodied carbon optimisation of steel building structures. *Advances in Computational Design*, 3(4):385–404.
- EPD International (2018). *EPD database*. Stockholm. [www.environdec.com/EPD-Search/](http://www.environdec.com/EPD-Search/) (accessed June 2019).
- European Parliament Council (2010). Directive 2010/31/EU on the energy performance of buildings.
- Fang, W., Yang, S., Wang, X.-L., Yuan, T.-Q., and Sun, R.-C. (2017). Manufacture and application of lignin-based carbon fibers (lcf) and lignin-based carbon nanofibers (lcnf). *Green Chemistry*, 19(8):1794–1827.
- FIB (2007). FRP reinforcement in RC structures. fib Bulletin 40.
- FIB (2012). Model Code 2010, Volume 1.
- Fitzgerald, R. (1988). The development of the cast iron frame in textile mills to 1850. *Industrial Archaeology Review*, 10(2):127–145.
- Flower, D. J. and Sanjayan, J. G. (2007). Green house gas emissions due to concrete manufacture. *The international Journal of life cycle assessment*, 12(5):282.
- Foraboschi, P., Mercanzin, M., and Trabucco, D. (2014). Sustainable structural design of tall buildings based on embodied energy. *Energy and Buildings*, 68:254–269.
- Foster, R. (2010). *Form Finding And Analysis Of Fabric Formed Concrete Beams*. Master's thesis, University of Bath, UK.
- Frenzel, M. and Curbach, M. (2017). Load-bearing behavior and efficiency of layered two-way slabs. In *Proceedings of the IASS Annual Symposium 2017, Hamburg*.
- Frischknecht, R., Jungbluth, N., Althaus, H.-J., Doka, G., Dones, R., Heck, T., Hellweg, S., Hischier, R., Nemecek, T., Rebitzer, G., and Spielmann, M. (2005). The ecoinvent database: Overview and methodological framework (7 pp). *The International Journal of Life Cycle Assessment*, 10(1):3–9.
- Funes, R. and del Cueto, J. I. (2011). Las bóvedas por arista de félix candela: variaciones sobre un mismo tema. *Bitácora arquitectura*, (23):38–47.
- Gan, V. J., Chan, C., Tse, K., Lo, I. M., and Cheng, J. C. (2017). A comparative analysis of embodied carbon in high-rise buildings regarding different design parameters. *Journal of Cleaner Production*, 161:663 – 675.

- Gardiner, J. B. and Janssen, S. R. (2014). Freefab. In *Robotic Fabrication in Architecture, Art and Design 2014*, pages 131–146. Springer.
- Gerard, R., Barber, D., and Wolski, A. (2013). *Fire safety challenges of tall wood buildings*. National Fire Protection Research Foundation.
- Gibson, L. J. and Ashby, M. F. (1999). *Cellular solids: structure and properties*. Cambridge University Press, UK.
- Giesekam, J., Barrett, J., Taylor, P., and Owen, A. (2014). The greenhouse gas emissions and mitigation options for materials used in uk construction. *Energy and Buildings*, 78:202–214.
- Gilbert, R. I. and Warner, R. F. (1978). Tension stiffening in reinforced concrete slabs. *Journal of the structural division*, 104(12):1885–1900.
- Goodchild, C; Webster, R. M. E. K. S. (2009). *Economic concrete frame elements to Eurocode 2*. The Concrete Centre, Surrey, UK.
- Graedel, T. E., Buchert, M., Reck, B., and Sonnemann, G. (2011). *Assessing Mineral Resources in Society: Metal Stocks and Recycling Rates*. United Nations Environmental Programme.
- Granta Design Ltd. (2018). The Cambridge Engineering Selector EduPack 2018 Version 18.1.1. Granta Design. [www.grantadesign.com/industry/products/ces-selector/](http://www.grantadesign.com/industry/products/ces-selector/) (accessed June 2019).
- Gries, T., Roye, A., Offermann, P., Engler, T., and Peled, A. (2006). Textiles. In Brameshuber, W., editor, *Textile Reinforced Concrete - State-of-the-Art Report of RILEM TC 201-TRC*. RILEM.
- Griffin, C. T., Reed, B., and Hsu, S. (2010). Comparing the embodied energy of structural systems in buildings. In *Proceedings of the 1st International Conference on Structures and Architecture, ICSA 2010*, pages 1367–1373.
- Guastavino, R. (1892). *Essay on the theory and history of cohesive construction applied especially to the timber vault*. Ticknor.
- Gudonis, E., Timinskas, E., Gribniak, V., Kaklauskas, G., Arnautov, A. K., and Tamulėnas, V. (2013). Frp reinforcement for concrete structures: state-of-the-art review of application and design. *Engineering Structures and Technologies*, 5(4):147–158.
- Gulentops, L., Mollaert, M., Adriaenssens, S., De Laet, L., and De Temmerman, N. (2009). Textile formwork for concrete shells. In *The International Association for Shell and Spatial Structures (IASS) Symposium*, pages 406–407, Valencia.
- Halpern, A., Billington, D., and Adriaenssens, S. (2013). The ribbed floor slab systems of pier luigi nervi. 54:127–136.
- Halpern, A. B. and Adriaenssens, S. (2013). Coupled form-finding and buckling optimization for stability-sensitive structures. In *Proceedings of IASS Annual Symposia*, volume 2013, pages 1–6. International Association for Shell and Spatial Structures (IASS).

- Hammond, G. P. and Jones, C. I. (2008). Embodied energy and carbon in construction materials. *Proceedings of the Institution of Civil Engineers-Energy*, 161(2):87–98.
- Hand, F. R., Pecknold, D., and Schnobrich, W. C. (1972). A layered finite element nonlinear analysis of reinforced concrete plates and shells. Technical report, University of Illinois Engineering Experiment Station. College of Engineering. University of Illinois at Urbana-Champaign., Engineering Experiment Station, College of Engineering, University of Illinois at Urbana-Champaign.
- Harilal, R. and Ramji, M. (2014). Adaptation of open source 2d dic software ncorr for solid mechanics applications. In *9th International Symposium on Advanced Science and Technology in Experimental Mechanics*.
- Hartig, J., Jesse, F., Schicktanz, K., and Häußler-Combe, U. (2012). Influence of experimental setups on the apparent uniaxial tensile load-bearing capacity of textile reinforced concrete specimens. *Materials and structures*, 45(3):433–446.
- Hawkins, W., Herrmann, M., Ibell, T., Kromoser, B., Michalski, A., Orr, J., Pedreschi, R., Pronk, A., Schipper, R., Shepherd, P., Veenendaal, D., Wansdronk, D., and West, M. (2016a). Flexible formwork technologies - a state of the art review. *Structural Concrete*, 17(6):911 – 935.
- Hawkins, W., Orr, J., Ibell, T., and Shepherd, P. (2018). An analytical failure envelope for the design of textile reinforced concrete shells. *Structures*, 15:56–65.
- Hawkins, W., Orr, J., Shepherd, P., and Ibell, T. (2016b). Fabric formed concrete: physical modelling for assessment of digital form finding methods. In *11th fib international PhD Symposium in Civil Engineering*.
- Hawkins, W., Orr, J., Shepherd, P., and Ibell, T. (2019). Design, construction and testing of a low carbon thin-shell concrete flooring system. *Structures*, 18:60–71.
- Hawkins, W., Orr, J., Shepherd, P., Ibell, T., and Bregulla, J. (2017). Thin-shell textile-reinforced concrete floors for sustainable buildings. In *IASS Annual Symposium 2017, Hamburg*.
- Hegger, J., Aldea, C., Brameshuber, W., and Curbach, M. (2006a). Applications of textile reinforced concrete. In Brameshuber, W., editor, *Textile Reinforced Concrete - State-of-the-Art Report of RILEM TC 201-TRC*. RILEM.
- Hegger, J. and Voss, S. (2005). Textile reinforced concrete–bearing behavior, design, applications. In *Third International Conference on Composites in Construction*, pages 1139–1146, Lyon.
- Hegger, J. and Voss, S. (2008). Investigations on the bearing behaviour and application potential of textile reinforced concrete. *Engineering structures*, 30(7):2050–2056.
- Hegger, J. and Will, N. (2016). Textile-reinforced concrete: design models. In Triantafyllou, T., editor, *Textile Fiber Composites in Civil Engineering*, pages 189–207.
- Hegger, J., Will, N., Bruckermann, O., and Voss, S. (2006b). Load–bearing behaviour and simulation of textile reinforced concrete. *Materials and structures*, 39(8):765–776.

- Hempel, S., Butler, M., and Mechtcherine, V. (2016). Bond behaviour and durability of basalt fibres in cementitious matrices. *Newsletter*.
- Herrmann, M. and Sobek, W. (2017). Functionally graded concrete: Numerical design methods and experimental tests of mass-optimized structural components. *Structural Concrete*, 18(1):54–66.
- Heyman, J. (1966). The stone skeleton. *International Journal of Solids and Structures*, 2(2):249 – 279.
- Heyman, J. (1969). The safety of masonry arches. *International Journal of Mechanical Sciences*, 11(4):363 – 385.
- Heyman, J. (1997). *The stone skeleton: structural engineering of masonry architecture*. Cambridge University Press.
- Heyman, J. (2000). An observation on the fan vault of Henry VII Chapel, Westminster. *Architectural Research Quarterly*, 4:357 – 372.
- Hills, T., Leeson, D., Florin, N., and Fennell, P. (2016). Carbon capture in the cement industry: Technologies, progress, and retrofitting. *Environmental Science & Technology*, 50(1):368–377. PMID: 26630247.
- Huerta, S. (2003). The mechanics of timber vaults: a historical outline. In *Essays on the History of Mechanics*, pages 89–134. Springer.
- Huerta, S. (2006). Structural design in the work of Gaudi. *Architectural science review*, 49(4):324–339.
- Ibell, T. and Burgoyne, C. (1994). A generalized lower-bound analysis of anchorage zones. *Magazine of Concrete Research*, 46(167):133–144.
- Ibn-Mohammed, T., Greenough, R., Taylor, S., Ozawa-Meida, L., and Acquaye, A. (2013). Operational vs. embodied emissions in buildings—a review of current trends. *Energy and Buildings*, 66:232 – 245.
- IEA, I. E. A. (2008). *Energy Technology Perspectives 2008: Scenarios & Strategies to 2050*. OECD/International Energy Agency.
- IEA, I. E. A. (2018). *Energy Technology Perspectives 2018: Scenarios & Strategies to 2050*. OECD/International Energy Agency.
- Intergovernmental Panel on Climate Change (2018). Special Report: Global Warming of 1.5 °C. [www.ipcc.ch/sr15/](http://www.ipcc.ch/sr15/) (accessed June 2019).
- International Energy Agency and The World Business Council for Sustainable Development (2009). Cement roadmap. [https://www.iea.org/publications/freepublications/publication/Cement\\_Roadmap\\_Foldout\\_WEB.pdf](https://www.iea.org/publications/freepublications/publication/Cement_Roadmap_Foldout_WEB.pdf) (accessed June 2019).
- Isler, H. (1994). Concrete shells derived from experimental shapes. *Structural Engineering International*, 4(3):142–147.

- ISO, I. (2006). Iso 14025:2006 - environmental labels and declarations - type iii environmental declarations - principles and procedures. International Organization for Standardization.
- Jackson, M. D., Landis, E. N., Brune, P. F., Vitti, M., Chen, H., Li, Q., Kunz, M., Wenk, H.-R., Monteiro, P. J. M., and Ingraffea, A. R. (2014). Mechanical resilience and cementitious processes in imperial roman architectural mortar. *Proceedings of the National Academy of Sciences*.
- Ji, Y., Li, K., Liu, G., Shrestha, A., and Jing, J. (2018). Comparing greenhouse gas emissions of precast in-situ and conventional construction methods. *Journal of Cleaner Production*, 173:124 – 134. Sustainable urban transformations towards smarter, healthier cities: theories, agendas and pathways.
- Jipa, A., Bernhard, M., Dillenburger, B., and Meibodi, M. (2016). 3d-printed stay-in-place formwork for topologically optimized concrete slabs. In *2016 TxA Emerging Design+ Technology conference*. Texas Society of Architects.
- Jones, C. and Hammond, G. (2019). Inventory of carbon & energy Version 3.0 (ICE V3.0). *Department of Mechanical Engineering, University of Bath, UK*.
- Jones, F., Rock, J., and Bailey, J. (1983). The environmental stress corrosion cracking of glass fibre-reinforced laminates and single e-glass filaments. *Journal of Materials Science*, 18(4):1059–1071.
- Jones, M. and McCarthy, A. (2005). Preliminary views on the potential of foamed concrete as a structural material. *Magazine of concrete research*, 57(1):21–32.
- Jones, M. R., Ozlutas, K., and Zheng, L. (2017). High-volume, ultra-low-density fly ash foamed concrete. *Magazine of Concrete Research*, 69(22):1146–1156.
- Jones, R. M. (1999). *Mechanics of Composite Materials*. Taylor & Francis.
- Kaethner, S. and Burrige, J. (2012). Embodied CO<sub>2</sub> of structural frames. *The structural engineer*, 90(5):33–40.
- Kapsalis, P., El Kadi, M., Vervloet, J., De Munck, M., Wastiels, J., Triantafillou, T., and Tysmans, T. (2019). Thermomechanical behavior of textile reinforced cementitious composites subjected to fire. *Applied Sciences*, 9:747.
- Kargin, A., Baev, V., and Mashkin, N. (2017). Fly-ash geo-polymer foamed concrete. *AIP Conference Proceedings*, 1800(1):020005.
- Kearsley, E. P. and Wainwright, P. J. (2002). The effect of porosity on the strength of foamed concrete. *Cement and Concrete Research*, 32(2):233–239.
- Kemna, R., van Elburg, M., Li, W., and van Holsteijn, R. (2011). Methodology study eco-design of energy-using products-MEEuP. *COWI*.
- Kennedy, J. and Eberhart, R. (1995). Particle swarm optimization. In *Proceedings of ICNN'95 - International Conference on Neural Networks*, volume 4, pages 1942–1948 vol.4.



- Khoshnevis, B. (2004). Automated construction by contour crafting – related robotic and information technologies. *Journal of Automation in Construction*, 13(1):5–19.
- Kilian, A. and Ochsendorf, J. (2005). Particle-spring systems for structural form finding. *Journal-international association for shell and spatial structures*, 148:77.
- Kim, J.-K. and Yi, S.-T. (2002). Application of size effect to compressive strength of concrete members. *Sadhana*, 27(4):467.
- Kim, T., Chae, C., Kim, G., and Jang, H. (2016). Analysis of CO<sub>2</sub> emission characteristics of concrete used at construction sites. *Sustainability*, 8(4):348.
- Kingspan (2018). *Multideck Technical Handbook*. Kingspan Structural Products, Sherburn, Malton, North Yorkshire. [https://az750602.vo.msecnd.net/netxstoreviews/assetOriginal/13181\\_Kingspan\\_Structural\\_KSP\\_Multideck\\_Technical\\_Handbook\\_LR\\_122018\\_EN\\_UK.pdf](https://az750602.vo.msecnd.net/netxstoreviews/assetOriginal/13181_Kingspan_Structural_KSP_Multideck_Technical_Handbook_LR_122018_EN_UK.pdf) (accessed June 2019).
- Kirkpatrick, S., Gelatt, C. D., and Vecchi, M. P. (1983). Optimization by simulated annealing. *Science*, 220(4598):671–680.
- Kisic, M., Ferguson, C., Clarke, C., and Smyth, J. (2018). Building pressure: Which cement companies will be left behind in the low-carbon transition? Technical report, CDP.
- Klemm, A. and Wiggins, D. (2016). Sustainability of natural stone as a construction material. In Khatib, J. M., editor, *Sustainability of Construction Materials (Second Edition)*, Woodhead Publishing Series in Civil and Structural Engineering, pages 283 – 308. Woodhead Publishing, second edition edition.
- Kloft, H., Hack, N., and Lindemann, H. (2019). Shotcrete 3D Printing (SC3DP) - 3D-Drucken von großformatigen Betonbauteilen. 1:54–57.
- Kotsovos, M. (1983). Effect of testing techniques on the post-ultimate behaviour of concrete in compression. *Materiaux et construction*, 16(1):3–12.
- Kotsovos, M. D. (1982). A fundamental explanation of the behaviour of reinforced concrete beams in flexure based on the properties of concrete under multiaxial stress. *Matériaux et Construction*, 15(6):529.
- Krüger, M. and Reinhardt, H. (2006). Composite materials - 6.4 Fire Resistance. In Brameshuber, W., editor, *Textile Reinforced Concrete - State-of-the-Art Report of RILEM TC 201-TRC*. RILEM.
- Kumbhar, S., Kulkarni, N., Rao, A. B., and Rao, B. (2014). Environmental life cycle assessment of traditional bricks in western maharashtra, india. *Energy Procedia*, 54:260 – 269. 4th International Conference on Advances in Energy Research (ICAER 2013).
- Langlois, V., Fiorio, B., Beaucour, A.-L., Cabrillac, R., and Gouvenot, D. (2007). Experimental study of the mechanical behavior of continuous glass and carbon yarn-reinforced mortars. *Construction and Building Materials*, 21(1):198–210.
- Larner, L., Speakman, K., and Majumdar, A. (1976). Chemical interactions between glass fibres and cement. *Journal of non-crystalline solids*, 20(1):43–74.

- Lee, D. S. H. (2011). *Study of construction methodology and structural behaviour of fabric formed form-efficient reinforced concrete beams*. PhD Thesis, University of Edinburgh.
- Leggatt, A. (1980). GRC and other laminar concretekim. In Neville, A. M. and Chatterton, M., editors, *New concrete technologies and building design*. Wiley, New York.
- Lehne, J. and Preston, F. (2018). *Making Concrete Change: Innovation in Low-carbon Cement and Concrete*. Chatham House Reports.
- Liebringshausen, A., Eisenbach, P., and Grohmann, M. (2017). Re-usable concrete formwork system made of sand and wax. In *Proceedings of IASS Annual Symposia*, volume 2017, pages 1–10. International Association for Shell and Spatial Structures (IASS).
- Liew, A., López, D. L., Van Mele, T., and Block, P. (2017). Design, fabrication and testing of a prototype, thin-vaulted, unreinforced concrete floor. *Engineering Structures*, 137:323–335.
- Liew, A., Stürz, Y., Guillaume, S., Mele, T. V., Smith, R., and Block, P. (2018). Active control of a rod-net formwork system prototype. *Automation in Construction*, 96:128 – 140.
- Lindemann, H., Fromm, A., Joscha, O., and Kloft, H. (2017). Digital prefabrication of freeform concrete elements using shotcrete technology. In *IASS Annual Symposium 2017, Hamburg*.
- Linkwitz, K. and Schek, H.-J. (1971). Einige bemerkungen zur berechnung von vorgespannten seilnetzkonstruktionen. *Ingenieur-Archiv*, 40(3):145–158.
- Liu, M., Xing, M., Yang, Q., and Yang, X. (2012). Computational morphogenesis of free form shell structures by optimization. *Procedia Engineering*, 31:608–612.
- Love, A. E. H. (1888). The small free vibrations and deformation of a thin elastic shell. *Philosophical Transactions of the Royal Society of London. A*, 179:491–546.
- López, D. L., Veenendaal, D., Akbarzadeha, M., and Block, P. (2014). Prototype of an ultra-thin, concrete vaulted floor system. In *IASS-SLTE 2014 Symposium*, Brasilia.
- López-Mesa, B., Ángel Pitarch, Tomás, A., and Gallego, T. (2009). Comparison of environmental impacts of building structures with in situ cast floors and with precast concrete floors. *Building and Environment*, 44(4):699 – 712.
- Lydon, G., Hofer, J., Svetozarevic, B., Nagy, Z., and Schlueter, A. (2017). Coupling energy systems with lightweight structures for a net plus energy building. *Applied Energy*, 189:310 – 326.
- MacKay, D. J., Cramton, P., Ockenfels, A., and Stoft, S. (2015). Price carbon—i will if you will. *Nature*, 526(7573):315–316.
- Mainka, H., Täger, O., Stoll, O., Körner, E., and Herrmann, A. S. (2013). Alternative precursors for sustainable and cost-effective carbon fibers usable within the automotive industry. In *Society of Plastics Engineers (Automobile Division)—Automotive Composites Conference & Exhibition*.

- Mainka, J., Kloft, H., Baron, S., Hoffmeister, H.-W., and Dröder, K. (2016). Non-waste-wachsschalungen: Neuartige präzisionsschalungen aus recycelbaren industriewachsen. *Beton-und Stahlbetonbau*, 111(12):784–793.
- Mark, R. and Hutchinson, P. (1986). On the structure of the Roman Pantheon. *The Art Bulletin*, 68(1):24–34.
- Massachusetts Institute of Technology (2019). Database for embodied quantity outputs. [www.carbondeqo.com](http://www.carbondeqo.com) (accessed June 2019).
- May, S., Michler, H., Schladitz, F., and Curbach, M. (2018). Lightweight ceiling system made of carbon reinforced concrete. *Structural Concrete*, 19.
- May, S., Steinbock, O., Michler, H., and Curbach, M. (2019). Precast slab structures made of carbon reinforced concrete. *Structures*, 18:20 – 27.
- McGrath, T., Nanukuttan, S., Basheer, P., and Long, A. (2012). Embodied energy and carbon footprinting of concrete production and use. In *32nd Cement and Concrete Science Conference*.
- McLaren, D., Bullock, S., and Yousuf, N. (1998). *Tomorrow's world: Britain's share in a sustainable future*, volume 15. Earthscan.
- McManus, M. C. and Taylor, C. M. (2015). The changing nature of life cycle assessment. *Biomass and bioenergy*, 82:13–26.
- Mechtcherine, V. (2012). Towards a durability framework for structural elements and structures made of or strengthened with high-performance fibre-reinforced composites. *Construction and Building Materials*, 31:94–104.
- Mechtcherine, V., Grafe, J., Nerella, V. N., Spaniol, E., Hertel, M., and Füssel, U. (2018). 3d-printed steel reinforcement for digital concrete construction – manufacture, mechanical properties and bond behaviour. *Construction and Building Materials*, 179:125 – 137.
- Mechtcherine, V., Schneider, K., and Brameshuber, W. (2016). Mineral-based matrices for textile-reinforced concrete. In Triantafyllou, T., editor, *Textile fibre composites in civil engineering*. Woodhead Publishing.
- Meibodi, M. A., Bernhard, M., Jipa, A., and B, D. (2017). The smart takes from the strong: 3d printing stay-in-place formwork for concrete slab construction. UCL Press,.
- Miller, D. and Doh, J.-H. (2015). Incorporating sustainable development principles into building design: a review from a structural perspective including case study. *The Structural Design of Tall and Special Buildings*, 24(6):421–439.
- Miller, D., Doh, J.-H., and Mulvey, M. (2015). Concrete slab comparison and embodied energy optimisation for alternate design and construction techniques. *Construction and Building Materials*, 80:329–338.
- Ministerium für Wirtschaft und Aufbau (1952). Bekanntmachung über die zulassung der "kelling-decke". *Thuringen Legislativ & Exekutiv*.

- Miranda, H., Williams, C., and Orr, J. (2016). Peridynamics for concrete structures-a new explicit analysis method. In *CTU Congress, Dundee*. University of Dundee.
- Mobasher, B. (2016). Textile fibre composites: Testing and mechanical behaviour. In Triantafyllou, T., editor, *Textile Fiber Composites in Civil Engineering*, pages 101–147. Woodhead Publishing, Cambridge.
- Moncaster, A. and Symons, K. (2013). A method and tool for ‘cradle to grave’ embodied carbon and energy impacts of uk buildings in compliance with the new tc350 standards. *Energy and Buildings*, 66:514 – 523.
- Morrow, G. (2018). Practice-based research, testing and application of fabric formwork to build reinforced concrete buildings in cambodia. *Journal of the International Association for Shell and Spatial Structures*, 2018 Vol. 09:1–10.
- Moynihan, M. C. and Allwood, J. M. (2014). Utilization of structural steel in buildings. *Proceedings of the Royal Society of London A: mathematical, physical and engineering sciences*, 470(2168):20140170–20140170.
- Müller, D. B., Wang, T., Duval, B., and Graedel, T. E. (2006). Exploring the engine of anthropogenic iron cycles. *Proceedings of the National Academy of Sciences*, 103(44):16111–16116.
- Nadoushani, Z. S. M. and Akbarnezhad, A. (2015). Effects of structural system on the life cycle carbon footprint of buildings. *Energy and Buildings*, 102:337 – 346.
- Naik, T. R. and Ramme, B. W. (1987). Low cement content high strength concrete. *Cement and Concrete Research*, 17(2):283 – 294.
- Nath, P., Sarker, P. K., and Biswas, W. K. (2018). Effect of fly ash on the service life, carbon footprint and embodied energy of high strength concrete in the marine environment. *Energy and Buildings*, 158:1694–1702.
- Neudecker, S., Bruns, C., Gerbers, R., Heyn, J., Dietrich, F., Dröder, K., Ratz, A., and Kloft, H. (2016). A new robotic spray technology for generative manufacturing of complex concrete structures without formwork. *Procedia CIRP*, 43:333–338.
- Ochsendorf, J. (2010). *Guastavino vaulting: The art of structural tile*. Princeton Architectural Press.
- Ockleston, A. (1958). Arching action in reinforced concrete slabs. *The Structural Engineer*, 36(6):197–201.
- O’Connor, C. (1994). Development in roman stone arch bridges. *Endeavour*, 18(4):157 – 162.
- Ohno, S. and Hannant, D. (1994). Modelling the stress-strain response of continuous fiber reinforced cement composites. *ACI Materials Journal*, 91(3):306–312.
- Orr, J. (2018). Minimising energy in construction: Survey of structural engineering practice. <https://static1.squarespace.com/static/58f72c9a1b631bc0c1e1b84c/t/5b85fb334fa51a1080348b19/1535507448054/MEICON+Report+Online.pdf> (accessed June 2019).

- Orr, J. J., Darby, A. P., Ibell, T. J., Evernden, M. C., and Otlet, M. (2011). Concrete structures using fabric formwork. *The Structural Engineer*, 89(8):20–26.
- Ostle, N., Levy, P., Evans, C., and Smith, P. (2009). Uk land use and soil carbon sequestration. *Land Use Policy*, 26:S274 – S283. Land Use Futures.
- Otter, J. (1965). Computations for prestressed concrete reactor pressure vessels using dynamic relaxation. *Nuclear Structural Engineering*, 1(1):61–75.
- Pan, B. (2009). Reliability-guided digital image correlation for image deformation measurement. *Applied optics*, 48(8):1535–1542.
- Pereira, K. and Ratnayake, R. (2013). Water integrity in action: Curbing illegal sand mining in sri lanka. *Berlin, Germany: Water Integrity Network*.
- Pickering, S. (2006). Recycling technologies for thermoset composite materials—current status. *Composites Part A: Applied Science and Manufacturing*, 37(8):1206 – 1215. The 2nd International Conference: Advanced Polymer Composites for Structural Applications in Construction.
- Piker, D. (2013). Kangaroo: form finding with computational physics. *Architectural Design*, 83(2):136–137.
- Preisinger, C. (2013). Linking structure and parametric geometry. *Architectural Design*, 83(2):110–113.
- Pugnale, A. and Sassone, M. (2007). Morphogenesis and structural optimization of shell structures with the aid of a genetic algorithm. *Journal of the International Association for Shell and Spatial Structures*, 48(155):161–166. Cited By :10 Export Date: 12 February 2016.
- Purnell, P. and Black, L. (2012). Embodied carbon dioxide in concrete: Variation with common mix design parameters. *Cement and Concrete Research*, 42(6):874–877.
- PwC (2016). Life cycle assessment of CFGF – Continuous Filament Glass Fibre Products.
- Rajamane, N., Nataraja, M., Dattatreya, J., Lakshmanan, N., and Sabitha, D. (2012). Sulphate resistance and eco-friendliness of geopolymer concretes. *Indian Concrete Journal*, 86(1):13.
- Ramage, M., Hall, T. J., Gatóo, A., and Asali, M. W. A. (2019). Rwanda cricket stadium: Seismically stabilised tile vaults. *Structures*, 18:2 – 9.
- Ramage, M. H., Ochsendorf, J., Rich, P., Bellamy, J. K., and Block, P. (2010). Design and construction of the mapungubwe national park interpretive centre, south africa. *ATDF journal*, 7(1/2).
- Ramaswamy, G. and Chetty, S. (1960). A new form of doubly curved shell for roofs and floors. *International Association for Shell Structures*, 1:49–56.
- Ramm, E. and Mehlhorn, G. (1991). On shape finding methods and ultimate load analyses of reinforced concrete shells. *Engineering structures*, 13(2):178–198.

- Raouf, S. M., Koutas, L. N., and Bournas, D. A. (2016). Bond between textile-reinforced mortar (trm) and concrete substrates: experimental investigation. *Composites Part B: Engineering*, 98:350–361.
- Rasch, B. and Otto, F. (1996). *Finding Form: Towards an Architecture of the Minimal*. Axel Menges.
- Rege, A. (2016). Not biting the dust: using a tripartite model of organized crime to examine india's sand mafia. *International Journal of Comparative and Applied Criminal Justice*, 40(2):101–121.
- Richardson, J., Adriaenssens, S., Filomeno Coelho, R., and Bouillard, P. (2013). Coupled form-finding and grid optimization approach for single layer grid shells. *Engineering Structures*, 52:230–239.
- Rippmann, M., Lachauer, L., and Block, P. (2012). Interactive vault design. *International Journal of Space Structures*, 27(4):219–230.
- Rutten, D. (2013). Galapagos: On the logic and limitations of generic solvers. *Architectural Design*, 83(2):132–135.
- Scheerer, S., Chudoba, R., Garibaldi, M. P., and Curbach, M. (2017). Shells made of textile reinforced concrete-applications in germany. *Journal of the international association for shell and spatial structures*, 58(1):79–93.
- Schipper, H. (2015). *Double-curved precast concrete elements: Research into technical viability of the flexible mould method*. PhD thesis, TU Delft, Delft University of Technology.
- Schneider, M., Romer, M., Tschudin, M., and Bolio, H. (2011). Sustainable cement production—present and future. *Cement and concrete research*, 41(7):642–650.
- Scholzen, A., Chudoba, R., and Hegger, J. (2015a). Thin-walled shell structures made of textile-reinforced concrete: Part i. *Structural Concrete*, 16(1):106–114.
- Scholzen, A., Chudoba, R., and Hegger, J. (2015b). Thin-walled shell structures made of textile-reinforced concrete: Part ii. *Structural Concrete*, 16(1):115–124.
- Scholzen, A., Chudoba, R., and Hegger, J. (2015c). Ultimate limit state assessment of trc shell structures with combined normal and bending loading. In *11th International Symposium on Ferrocement and 3rd ICTRC International Conference on Textile Reinforced Concrete (Ferro-11)*, volume 710.
- Seracino, Dr. R., Cauberg, N., Tysmans, T., Adriaenssens, S., Wastiels, J., Mollaert, M., and Belkassam, B. (2012). Shell elements of textile reinforced concrete using fabric formwork: a case study. *Advances in Structural Engineering*, 15(4):677–690.
- Shanks, W., Dunant, C., Drewniok, M. P., Lupton, R., Serrenho, A., and Allwood, J. M. (2019). How much cement can we do without? lessons from cement material flows in the uk. *Resources, Conservation and Recycling*, 141:441 – 454.
- Sharei, E., Scholzen, A., Hegger, J., and Chudoba, R. (2017). Structural behavior of a lightweight, textile-reinforced concrete barrel vault shell. *Composite Structures*, 171:505–514.

- Sim, J., Park, C., et al. (2005). Characteristics of basalt fiber as a strengthening material for concrete structures. *Composites Part B: Engineering*, 36(6-7):504–512.
- Simms, W. and Hughes, A. (2011). *Composite Design of Steel Framed Buildings*. SCI.
- Smith, A. L., Hicks, S. J., and Devine, P. J. (2009). *Design of floors for vibration: A new approach*. Steel Construction Institute.
- Sneed, L., D'Antino, T., Carloni, C., and Pellegrino, C. (2015). A comparison of the bond behavior of pbo-frcm composites determined by double-lap and single-lap shear tests. *Cement and Concrete Composites*, 64:37–48.
- SOFiSTiK (2019). Finite Element Software. [www.sofistik.com](http://www.sofistik.com) (accessed June 2019).
- Song, P. and Hwang, S. (2004). Mechanical properties of high-strength steel fiber-reinforced concrete. *Construction and Building Materials*, 18(9):669–673.
- Steffen, W., Rockström, J., Richardson, K., Lenton, T. M., Folke, C., Liverman, D., Summerhayes, C. P., Barnosky, A. D., Cornell, S. E., Crucifix, M., Donges, J. F., Fetzer, I., Lade, S. J., Scheffer, M., Winkelmann, R., and Schellnhuber, H. J. (2018). Trajectories of the earth system in the anthropocene. *Proceedings of the National Academy of Sciences*, 115(33):8252–8259.
- Sturgis, S. and Roberts, G. (2010). Redefining zero: Carbon profiling as a solution to whole life carbon emission measurement in buildings. [www.isurv.com/downloads/download/1197/redefining\\_zero\\_carbon\\_profiling\\_as\\_a\\_solution\\_to\\_whole\\_life\\_carbon\\_emission\\_measurement\\_in\\_buildings\\_rics](http://www.isurv.com/downloads/download/1197/redefining_zero_carbon_profiling_as_a_solution_to_whole_life_carbon_emission_measurement_in_buildings_rics) (accessed June 2019).
- Tang, G. (2012). Deployable gridshells and their application as temporary, reusable and flexible concrete formwork.
- Tang, G. (2015). An overview of historical and contemporary concrete shells, their construction and factors in their general disappearance. *International Journal of Space Structures*, 30(1):1–12.
- Tayfur, Y., Darby, A., Ibell, T., Orr, J., and Evernden, M. (2019). Serviceability of non-prismatic concrete beams: Combined-interaction method. *Engineering Structures*, 191:766–774.
- Teychenné, D. C., Franklin, R. E., Erntroy, H. C., and Marsh, B. (1997). *Design of normal concrete mixes, 2nd edition*. Building Research Establishment Ltd, Garston, UK.
- Tikalsky, P. J., Pospisil, J., and MacDonald, W. (2004). A method for assessment of the freeze–thaw resistance of preformed foam cellular concrete. *Cement and concrete research*, 34(5):889–893.
- Timoshenko, S. P. and Woinowsky-Krieger, S. (1959). *Theory of plates and shells*. McGraw-hill.
- Tomás, A. and Martí, P. (2010a). Optimality of candela's concrete shells: A study of his posthumous design. *Journal of the International Association for Shell and Spatial Structures*, 51(1):67.

- Tomás, A. and Martí, P. (2010b). Shape and size optimisation of concrete shells. *Engineering Structures*, 32(6):1650–1658.
- Tomás, A. and Tovar, J. P. (2012). The influence of initial geometric imperfections on the buckling load of single and double curvature concrete shells. *Computers & Structures*, 96-97:34 – 45.
- Torelli, G. and Lees, J. M. (2019). Fresh state stability of vertical layers of concrete. *Cement and Concrete Research*, 120:227 – 243.
- Torsing, R., Bakker, J., Jansma, R., and Veenendaal, D. (2012). Large-scale designs for mixed fabric and cable net formed structures.
- Tukker, A. and Jansen, B. (2006). Environmental impacts of products: A detailed review of studies. *Journal of Industrial Ecology*, 10(3):159–182.
- Tully, D. (1979). Inverted, doubly-curved umbrella, hyperbolic paraboloid shells with structurally integrated upper diaphragm.
- Tysmans, T. (2010). *Design of anticlastic shells in innovative textile reinforced cement composites*. PhD thesis, PhD thesis, Vrije Universiteit Brussel.
- Tysmans, T., Adriaenssens, S., and Wastiels, J. (2011). Form finding methodology for force-modelled anticlastic shells in glass fibre textile reinforced cement composites. *Engineering Structures*, 33(9):2603–2611.
- UK Green Building Council (2015). Tackling embodied carbon in buildings. [www.ukgbc.org/sites/default/files/Tackling%20embodied%20carbon%20in%20buildings.pdf](http://www.ukgbc.org/sites/default/files/Tackling%20embodied%20carbon%20in%20buildings.pdf) (accessed June 2019).
- United Nations (2015). The paris agreement. <https://unfccc.int/process-and-meetings/the-paris-agreement/the-paris-agreement> (accessed September 2019).
- U.S. Geological Survey (2018). Mineral commodity summaries. [www.usgs.gov/centers/nmic/mineral-commodity-summaries](http://www.usgs.gov/centers/nmic/mineral-commodity-summaries) (accessed June 2019).
- Uysal, H., Gul, R., and Uzman, U. (2007). Optimum shape design of shell structures. *Engineering structures*, 29(1):80–87.
- Valore, R. C. (1954). Cellular concretes: Part 2, physical properties. *Journal of the American Concrete Institute*, 50(10):817–836.
- Van Mele, T. and Block, P. (2011). A novel form finding method for fabric formwork for concrete shells. *J. Int. Assoc. Shell and Spatial Structures*, 52:217–224.
- Vatopoulos, K. and Tzimas, E. (2012). Assessment of CO2 capture technologies in cement manufacturing process. *Journal of Cleaner Production*, 32:251 – 261.
- Veenendaal, D., Bakker, J., and Block, P. (2017). Structural design of the flexibly formed, mesh-reinforced concrete sandwich shell roof of nest hilo. *Journal of the international association for shell and spatial structures*.



- Veenendaal, D. and Block, P. (2014). Design process for prototype concrete shells using a hybrid cable-net and fabric formwork. *Engineering Structures*, 75:39–50.
- Venkatarama Reddy, B. V. and Jagadish, K. S. (2003). Embodied energy of common and alternative building materials and technologies. *Energy and Buildings*, 35(2):129–137. Cited By :196 Export Date: 13 December 2015.
- Verwimp, E., Tysmans, T., Mollaert, M., and Berg, S. (2015). Experimental and numerical buckling analysis of a thin trc dome. *Thin-Walled Structures*, 94:89–97.
- Verwimp, E., Tysmans, T., Mollaert, M., and Wozniak, M. (2016). Prediction of the buckling behaviour of thin cement composite shells: Parameter study. *Thin-Walled Structures*, 108:20 – 29.
- Von Neumann, J. and Burks, A. W. (1966). Theory of self-reproducing automata. *IEEE Transactions on Neural Networks*, 5(1):3–14.
- Voss, S. and Hegger, J. (2006). Dimensioning of textile reinforced concrete structures. RILEM.
- Vukotic, L., Fenner, R., and Symons, K. (2010). Assessing embodied energy of building structural elements. In *Proceedings of the Institution of Civil Engineers-Engineering Sustainability*, volume 163, pages 147–158. Thomas Telford Ltd.
- Wang, Q., Kim, M.-K., Cheng, J. C., and Sohn, H. (2016). Automated quality assessment of precast concrete elements with geometry irregularities using terrestrial laser scanning. *Automation in Construction*, 68:170–182.
- Wang, T., Müller, D. B., and Graedel, T. (2007). Forging the anthropogenic iron cycle. *Environmental science & technology*, 41(14):5120–5129.
- Weight, D. H. (2011). Embodied through-life carbon dioxide equivalent assessment for timber products. *Proceedings of the Institution of Civil Engineers - Energy*, 164(4):167–182.
- Wermiel, S. (2017). The development of fireproof construction in Great Britain and the United States in the nineteenth century. In *Structural Iron and Steel, 1850–1900*, pages 101–124. Routledge.
- West, M. (2009). Thin shell concrete from fabric molds. [http://fabwiki.fabric-formedconcrete.com/lib/exe/fetch.php?media=chile:thin\\_shell\\_panels.pdf](http://fabwiki.fabric-formedconcrete.com/lib/exe/fetch.php?media=chile:thin_shell_panels.pdf) (accessed June 2019).
- West, M. and Araya, R. (2012). Recent fabric formwork construction projects. In *Proceedings of The Second International Conference on Flexible Formwork*, University of Bath, UK.
- Williams, M. (1952). Stress singularities resulting from various boundary conditions in angular corners of plates in extension. *Journal of applied mechanics*, 19(4):526–528.
- Williams-Portal, N., Lundgren, K., Wallbaum, H., and Malaga, K. (2014). Sustainable potential of textile-reinforced concrete. *Journal of Materials in Civil Engineering*, 27(7).
- Wimpenny, D. (2009). Low carbon concrete—options for the next generation of infrastructure. *Concrete Solutions*, 9:41–41.

- Wolfs, R., Bos, F., and Salet, T. (2018). Early age mechanical behaviour of 3d printed concrete: Numerical modelling and experimental testing. *Cement and Concrete Research*, 106:103 – 116.
- Worldsteel (2018). *Steel Statistical Yearbook*. World Steel Association. [www.worldsteel.org/steel-by-topic/statistics/steel-statistical-yearbook.html](http://www.worldsteel.org/steel-by-topic/statistics/steel-statistical-yearbook.html) (accessed June 2019).
- Xi, F., Davis, S. J., Ciais, P., Crawford-Brown, D., Guan, D., Pade, C., Shi, T., Syddall, M., Lv, J., Ji, L., et al. (2016). Substantial global carbon uptake by cement carbonation. *Nature Geoscience*, 9(12):880.
- Zadeh, H. J. and Nanni, A. (2012). Design of RC columns using glass FRP reinforcement. *Journal of Composites for Construction*, 17(3):294–304.
- Zhang, Z., Provis, J. L., Reid, A., and Wang, H. (2014). Geopolymer foam concrete: An emerging material for sustainable construction. *Construction and Building Materials*, 56:113 – 127.
- Zhang, Z., Provis, J. L., Reid, A., and Wang, H. (2015). Mechanical, thermal insulation, thermal resistance and acoustic absorption properties of geopolymer foam concrete. *Cement and Concrete Composites*, 62:97–105.